THÈSE

Délivrée par

L'Université de Lille – Faculté des Sciences et Technologies
École Doctorale des Sciences de la Matière, du Rayonnement et de l'Environnement

Pour l'obtention du grade de

Docteur en Chimie des matériaux

Présentée par

Céline MOUSSA

Observation des sites actifs catalytiques par spectroscopie RMN du solide à hauts champs

Observation of catalytic actives sites by high-field solid-state NMR spectroscopy

Soutenance prévue le 24 Octobre 2025

Composition du jury:

Mme Anne LESAGE	Ingénieur de Recherche, Université Claude Bernard Lyon	*Rapportrice*
M. Eddy DIB	Chargé de recherche, HDR, CEMHTI Orléans	*Rapporteur*
Mme Claire MARICHAL	Professeure, Université de Haute Alsace	*Examinatrice et Présidente*
M. Olivier LAFON	Professeur, Université de Lille	*Co-directeur de thèse*
M. Laurent DELEVOYE	Directeur de recherche, Université de Lille	*Directeur de thèse*

Acknowledgements

This thesis could not have been accomplished without the constant support and encouragement of my supervisors, family, colleagues, and friends. I am deeply grateful to all those whose contributions have, in different ways, made this journey both memorable and meaningful.

I would first like to extend my sincere thanks to the members of the jury, Mme. Anne LESAGE, M. Eddy DIB and Mme. Claire MARICHAL for kindly accepting to evaluate my doctoral work.

I would like to express my foremost gratitude to Laurent Delevoye, my supervisor, for his invaluable guidance and constant support throughout my doctoral studies. His trust in my abilities has been a true source of motivation, encouraging me to persevere and aim higher. I am especially grateful for the opportunities he gave me to participate in national and international conferences, which greatly enriched my knowledge and professional experience. What I deeply value is his remarkable optimism and positive outlook, which he has consistently maintained even in the most demanding moments. His attitude has taught me that, regardless of the difficulties one may face, it is always possible to remain hopeful and supportive of others. It has truly been a privilege to be guided by him, and I could not have wished for a more dedicated and inspiring mentor throughout this journey.

I would also like to express my sincere gratitude to Olivier Lafon, my co-supervisor, for his exceptional guidance and support. His professionalism and sharp scientific insight have been a true source of inspiration throughout my doctoral journey. Under his supervision, I have learned the importance of working with rigor and precision, as well as the value of paying close attention to every detail. His remarkable scientific knowledge and clarity of thought have not only enriched my research but have also shaped the way I approach challenges in science. I am also deeply thankful to him for the numerous collaborations he made possible, which allowed me to explore diverse scientific topics, broadened my knowledge and strengthened my ability to adapt to different subjects. I am privileged to have benefited from his expertise and high standards, which will continue to guide me in my future career.

Special thanks to the one and only Jean-Paul Amoureux. It has been a real pleasure working with such a brilliant mind. You taught me so much and constantly encouraged me to push my understanding, even of the most difficult concepts. I must admit, I did not always catch every single word, but I was able to understand much of it! And of course, I cannot forget your unforgettable jokes, which may have “traumatized” me a little, but always made the atmosphere better. You truly are a phenomenon.

My gratitude extends also to the RM2I team at the University of Lille. I am especially grateful to the brilliant Julien Trébosc for his invaluable help in overcoming practical NMR challenges. His expertise in experiments and analysis has been essential to the progress of my work. I would also like to thank Andrew Rankin for his assistance with NMR experiments, for generously sharing his knowledge, and for his constant encouragement throughout my research. I am particularly grateful for the many Friday afternoons we spent by the spectrometer, the Mondays spent troubleshooting without signal, the patience with non-spinning rotors, and of course, the “VIP treatment” at the 1200. My gratitude also goes to Bertrand Doumert and Bertrand Revel for their dedication in maintaining the outstanding NMR facility in Lille and for their valuable technical support. Special thanks to Yury Kolyagin. It was a lot of fun working with you on these sophisticated pulse sequences, and I am grateful for all the thoughtful discussions we had. Thanks to Frédérique Pourpoint, for the memorable treasure hunt, her wonderful sense of humor, and the positive, youthful energy she brought along the way.

I sincerely thank all my current and former colleagues from the RM2I team for their constant support, engaging discussions, shared laughter, and the many memorable moments we spent together. Special thanks to Lama Hamdouna for her warm welcome and valuable support. I’m also thankful to my colleagues Diane, Racha, Athulya, Neethu and to Nadine, Abbas, Gisel, Leonardo, Tamali, Kouakou, Imane, Lilia, Thomas for creating a positive and motivating atmosphere that made my journey smoother.

I am especially grateful to the future Drs. Pierre and Raphael, the best bad influences. You two are always bringing good humor, and I truly enjoyed our office moments and side conversations. Raphaël, thank you for the countless coffees we shared, for the office hours till 8 p.m. that were supposed to be for work… but turned into chatting, and demotivation, and naturally thanks for the daily dose of bullying. Pierre, thank you for always defending

me against him, for always answering my “Pierre, il faut qu’on parle” with genius ideas, but will you survive without my daily “Tu quittes” at 2 p.m.?

A special thanks goes to my Lebanese colleagues, whose presence made my days so much easier and brighter. To Nabil, my university buddy since 2017, thank you for always being there along this journey. To Maria, for your love, constant care and support. To Mira, for your wonderful sense of humor even in the toughest moments. And to Krystel, for your kindness and tenderness, which I will always cherish.

Lastly, I would like to dedicate a special acknowledgment to my family, whose unwavering support, love, encouragement, and belief in me have made this achievement possible. To my incredible mom, your boundless love, tenderness, faith, prayers, and attentive ear to both my successes and my struggles are mu true blessing. Your continuous encouragement has truly been the driving force that kept me moving forward. To my sisters, Christy-Bel and Mary-Lynn, my true soulmates, thank you for always standing by me and sharing in both my joys and challenges. To my little brother, Jean-Paul, my pride and strength, your presence has always been a source of light and happiness. And to my Joy, thank you for your presence, I love you always.

Abstract

Rational inorganic synthesis methods enable the rapid development of new materials with innovative properties by employing a wide range of structural characterization techniques at the atomic scale. These techniques typically rely on the periodic arrangement of atoms in a crystal structure. However, many physical and chemical properties of materials only emerge through structural defects. In particular, these defects strongly influence the activity of heterogeneous catalysts. Solid-state nuclear magnetic resonance (NMR) spectroscopy, unlike diffraction-based techniques, allows probing the local environment of nuclei and hence, is well suited to characterize the atomic-level structure of defects, including active sites of heterogeneous catalysts. This PhD work focuses on the solid-state NMR characterization of active sites in two types of heterogeneous catalysts: molybdenum-based catalysts used for olefin metathesis and a new type of acid photocatalyst based on amorphous acidic aluminosilicate (AAS) functionalized by gold nanoparticles (Au/AAS). The rational improvement of the performances of these catalysts with numerous applications in sustainable chemistry is limited by the lack of knowledge about the atomic-level structure of their active sites. In the first part of this work, we explored how the local environment of Mo atoms in molybdenum-based catalysts can be probed by solid-state NMR of the ^{95}Mo isotope. Despite the inherently low receptivity of this nucleus, we were able to record ^{95}Mo NMR spectra of model Mo complexes with a wide range of chemical shifts and quadrupolar coupling constants. These experimental NMR parameters were compared to those calculated using Density Functional Theory (DFT) to investigate further the links between the local environment of ^{95}Mo nuclei and their NMR spectra. These results support the use of ^{95}Mo NMR for the structural analysis of complex molybdenum-based molecular systems. Furthermore, the obtained database of NMR parameters and optimal acquisition conditions will be useful to determine the structure of catalytic active sites in industrial Mo-containing heterogeneous catalysts, particularly molybdenum complexes grafted onto silica supports. The second part focuses on solid-state NMR characterization of Au/AAS acid photocatalysts, which exhibit increased Brønsted acidity when exposed to light. This effect has been attributed to localized surface plasmon resonance (LSPR) of gold nanoparticles, which could generate in their vicinity electric fields capable of inducing changes in the

structure of Brønsted acid sites of AAS. However, there was a lack of experimental data about these structural changes. During my PhD, we developed and applied multinuclear (^{1}H and ^{27}Al) solid-state NMR experiments under light irradiation to evidence these structural changes due to LSPR in Au/AAS. In conclusion, this PhD work opens new avenues for the solid-state NMR characterization of two classes of heterogeneous catalysts: those containing molybdenum and plasmonic photocatalysts.

Résumé

Les méthodes de synthèse inorganique raisonnées permettent le développement rapide de nouveaux matériaux aux propriétés innovantes, en faisant appel à de nombreuses techniques de caractérisation structurale à l'échelle atomique. La plupart de ces techniques nécessitent un agencement périodique des atomes dans la structure. Cependant, de nombreuses propriétés physiques ou chimiques des matériaux proviennent de défauts structuraux. En particulier, ces derniers influencent fortement l'activité des catalyseurs hétérogènes. La spectroscopie de résonance magnétique nucléaire (RMN), contrairement aux techniques de diffraction, permet de sonder l'environnement local des noyaux et donc bien adaptée pour caractériser la structure à l'échelle atomique des défauts, dont les sites actifs de catalyseurs hétérogènes. Ce travail de thèse porte sur la caractérisation par spectroscopie RMN du solide de sites actifs de deux types de catalyseurs hétérogènes : des catalyseurs à base de molybdène utilisés pour la synthèse des oléfines et un nouveau type de photocatalyseurs basés sur des silices-alumines amorphes acides (*amorphous acidic aluminosilicate*, AAS, en anglais) fonctionnalisés avec des nanoparticules d'or (Au/AAS). L'amélioration raisonnée des performances de ces catalyseurs est limitée par notre manque de connaissance de la structure à l'échelle atomique de leurs sites actifs. Un premier pan de notre travail a consisté à explorer comment l'environnement local des atomes de Mo dans les catalyseurs à base de molybdène peut être sondé par spectroscopie RMN du molybdène. En dépit de la faible réceptivité de ce noyau, nous avons pu acquérir les spectres RMN ^{95}Mo de différents complexes de molybdène modèles présentant une large gamme de déplacements chimiques et de constantes quadripolaires. Ces paramètres RMN expérimentaux ont été comparés à ceux calculés par la théorie de la fonctionnelle de la densité (*Density Functional Theory*, DFT, en anglais) pour étudier plus avant les relations

entre l'environnement local des noyaux ^{95}Mo et leur signature RMN. De plus, la base de données obtenus de paramètres RMN et de conditions expérimentales optimisées sera utile pour déterminer la structure des sites actifs de catalyseurs hétérogènes industriels contenant du molybdène, et notamment ceux à base de complexes de molybdène greffés sur silice. La seconde partie de ces travaux de thèse a porté sur la caractérisation par RMN des solides des photocatalyseurs acides à base de Au/AAS, qui présentent une acidité de Brønsted lorsqu'ils sont exposés à la lumière. Cet effet a été attribué à la résonance des plasmons de surface des nanoparticules d'or, qui produisent autour d'elle des champs électriques capables de modifier la structure des sites acides de Brønsted des AAS. Cependant, cette hypothèse n'était pas étayée par des données expérimentales. Au cours de cette thèse, nous avons développé et appliqué des expériences RMN multinucléaires (^{1}H et ^{27}Al) sous irradiation lumineuse pour mettre en évidence ces changements structuraux dus aux résonances des plasmons de surface. En conclusion, ces travaux de thèse ouvrent de nouvelles perspectives pour la caractérisation par RMN des solides de deux classes de catalyseurs hétérogènes : ceux à base de molybdène et les photocatalyseurs plasmoniques.

Table of Contents

List of Figures

List of Tables

List of Schemes

General Introduction

Catalysis is central to modern chemistry, providing efficient and sustainable methods for molecular transformation. Catalysts make operations that would otherwise be too slow or energy-intensive possible by decreasing the energy barriers of chemical reactions. Heterogeneous catalysis is a key type of catalysis because it involves catalysts in a different phase than the reactants, which are typically solids that interact with gaseous or liquid substrates. In such reactions, the phase separation enables more efficient catalyst recovery and reuse, which is critical for large-scale industrial processes. As a result, heterogeneous catalysis is useful in a variety of applications, including ammonia synthesis, energy generation, and petrochemistry, as well as fine chemicals, pharmaceuticals, and environmental protection. Therefore, heterogeneous catalysis plays a pivotal role in industry and is considered as a key technology for sustainable development since it reduces the use of energy and raw matters as well as the amount of waste.

A powerful approach to improve the performances of heterogeneous catalysts in a rational way consists in the determination of the structure-activity relationships. Nevertheless, this approach is still limited for many classes of heterogeneous catalysts by our lack of understanding of their atomic-level structure and especially, that of catalytic sites, which strongly influence their catalytic performances. Nevertheless, the catalytic sites generally reside on the surfaces and often lacks long-range order. Therefore, they cannot be characterized by diffraction techniques. As a local characterization technique endowed with atomic resolution, solid-state NMR spectroscopy can provide unique insights into the atomic-level structure and dynamics of heterogeneous catalysts.[1–6] Nevertheless, the advent of novel NMR instruments and techniques provide access to novel information about the structure and dynamics of catalytic sites. In the frame of this PhD, we investigated using solid-state NMR spectroscopy the structure of active sites in heterogeneous catalysts used for two classes of reaction: (i) olefin metathesis and (ii) acid-catalyzed reactions.

Olefin metathesis developed in the 1950s consists in the breaking of carbon-carbon double bonds and their recombination to form new alkenes. This reaction allows for the production of tiny and medium-sized rings, large macromolecules, polymers, and even complicated natural products. Heterogeneous metathesis catalysts are often composed of

transition metals such as molybdenum, tungsten, or rhenium grafted on amorphous supports. In the frame of this PhD, we investigated how high-field NMR spectroscopy, notably using the 1.2 GHz NMR spectrometer, which was recently installed in Lille, can be instrumental to characterize the local environment of Mo atoms in molybdenum-based heterogeneous catalysts of olefin metathesis. The observation of Mo element by solid-state NMR spectroscopy is challenging owing to the unfavorable properties of its NMR-active isotopes, ^{95}Mo and ^{97}Mo, which have low gyromagnetic ratios and natural abundances as well as nuclear spin I = 5/2 yielding transitions broaden by quadrupolar interaction. Therefore, high magnetic fields, which enhance sensitivity and resolution, are beneficial for the NMR detection of molybdenum.

In the frame of this PhD, we also investigated solid-acid catalysts, which are widely employed in petroleum refining, biomass conversion and organic synthesis.[7,8] Among the existing solid-acid catalysts, zeolites, which are microporous crystalline aluminosilicates, are widely employed because of their high Brønsted acidity and thermal stability. Nevertheless, their application in many industrial processes involving large molecules is limited by their microporosity, which induces diffusion constraints. Alternatively, amorphous silica-aluminas (ASAs), although exhibiting lower Brønsted acidity than zeolites, offer improved mass transfer because they do not contain micropores. More recently, novel nanosponges made of amorphous acidic aluminosilicate (AAS) have been introduced which possesses Brønsted acid sites similar to those found in zeolites but textural properties like ASAs.[9] These AAS catalyze several reactions with better performance than state-of-the-art zeolites and ASAs. It has also been observed that the Brønsted acidity of AAS can be increased by functionalizing them with gold nanoparticles and irradiating them with light. These Au/AAS materials represent promising solid-acid photocatalysts, which could use sunlight as the energy source to drive chemical reactions. It has been hypothesized that this acidity enhancement stems from localized surface plasmon resonance (LSPR) process, which produces localized electric fields near gold nanoparticles in the presence of light. These local electric fields could lengthen the O-H bonds of silanol groups, thus enhancing their Brønsted acidity. Nevertheless, this structural modification has not been evidenced so far. In the frame of this PhD, we have tried to evidence this

structural change using multinuclear (^{1}H and ^{27}Al) using solid-state NMR spectroscopy under light irradiation.

In this manuscript, the first chapter presents the investigated heterogeneous catalysts, the state-of-the art for their characterization using solid-state NMR spectroscopy as well as the solid-state NMR techniques and quantum mechanical modelling methods we employed in the manuscript. Then the second chapter focuses on the high-field solid-state NMR characterization of molybdenum-based heterogeneous catalysts for olefin metathesis. Finally, the NMR results on solid-acid photocatalysts are presented in the last chapter.

References

(1) Blanc, F.; Berthoud, R.; Salameh, A.; Basset, J.-M.; Copéret, C.; Singh, R.; Schrock, R. R. Dramatic Improvements of Well-Defined Silica Supported Mo-Based Olefin Metathesis Catalysts by Tuning the N-Containing Ligands. *J. Am. Chem. Soc.* **2007**, *129* (27), 8434–8435. https://doi.org/10.1021/ja073095e.

(2) Jiang, Y.; Huang, J.; Dai, W.; Hunger, M. Solid-State Nuclear Magnetic Resonance Investigations of the Nature, Property, and Activity of Acid Sites on Solid Catalysts. *Solid State Nucl. Magn. Reson.* **2011**, *39* (3), 116–141. https://doi.org/10.1016/j.ssnmr.2011.03.007.

(3) Copéret, C.; Liao, W.-C.; Gordon, C. P.; Ong, T.-C. Active Sites in Supported Single-Site Catalysts: An NMR Perspective. *J. Am. Chem. Soc.* **2017**, *139* (31), 10588–10596. https://doi.org/10.1021/jacs.6b12981.

(4) Zheng, M.; Chu, Y.; Wang, Q.; Wang, Y.; Xu, J.; Deng, F. Advanced Solid-State NMR Spectroscopy and Its Applications in Zeolite Chemistry. *Prog. Nucl. Magn. Reson. Spectrosc.* **2024**, *140–141*, 1–41. https://doi.org/10.1016/j.pnmrs.2023.11.001.

(5) Gutmann, T.; Groszewicz, P. B.; Buntkowsky, G. Chapter One - Solid-State NMR of Nanocrystals. In *Annual Reports on NMR Spectroscopy*; Webb, G. A., Ed.; Academic Press, 2019; Vol. 97, pp 1–82. https://doi.org/10.1016/bs.arnmr.2018.12.001.

(6) Grekov, D.; Vancompernolle, T.; Taoufik, M.; Delevoye, L.; Gauvin, R. M. Solid-State NMR of Quadrupolar Nuclei for Investigations into Supported Organometallic Catalysts: Scope and Frontiers. *Chem. Soc. Rev.* **2018**, *47* (8), 2572–2590. https://doi.org/10.1039/c7cs00682a.

(7) Wang, Z.; Jiang, Y.; Baiker, A.; Huang, J. Pentacoordinated Aluminum Species: New Frontier for Tailoring Acidity-Enhanced Silica–Alumina Catalysts. *Acc. Chem. Res.* **2020**, *53* (11), 2648–2658. https://doi.org/10.1021/acs.accounts.0c00459.

(8) Busca, G. Silica-Alumina Catalytic Materials: A Critical Review. *Catal. Today* **2020**, *357*, 621–629. https://doi.org/10.1016/j.cattod.2019.05.011.

(9) Maity, A.; Chaudhari, S.; Titman, J. J.; Polshettiwar, V. Catalytic Nanosponges of Acidic Aluminosilicates for Plastic Degradation and CO_2 to Fuel Conversion. *Nat. Commun.* **2020**, *11* (1), 3828. https://doi.org/10.1038/s41467-020-17711-6.

CHAPTER 1.
State of the art

Chapter 1: State of the art

1. Heterogeneous Catalysis

1.1. Principle of Heterogeneous Catalysis

Major advances in catalysis began in the 19th century when Johann Wolfgang Döbereiner first discovered in 1823 that platinum could be used as a catalyst to burn hydrogen. Later, in 1835, Jöns Jacob Berzelius formalized the concept of catalysis. In the 20th century, Fritz Haber developed the ammonia synthesis process in 1909, and by 1913, Carl Bosch provided iron-based catalysts that enabled its industrial application, resulting in what is now known as the Haber-Bosch process. This era also saw the introduction of catalytic cracking in oil refining with amorphous aluminosilicates in the 1930s and synthetic zeolites in the 1950s. In the 1970s, platinum, palladium, and rhodium metal-based catalysts were developed for automotive catalytic converters. Later developments in nanocatalysis and sustainable processes were exemplified by Nobel laureates such as Gerhard Ertl, who was awarded the Nobel prize in chemistry in 2007 for his contribution to surface reactions and advances in catalyst design. Today, it is estimated that the production of about 85% of all industrial chemicals such as plastics, pharmaceuticals, and fertilizers involves catalysis.[1]

Catalysts can be liquids, gases, or solids. They are often classed based on their physical features or the type of reaction they catalyze. The catalyst in homogeneous catalysis occurs in the same physical state as the reacting species, typically gases or liquids. However, the majority of catalytic processes employed in industrial manufacturing processes today use heterogeneous catalysts. In contrast to homogeneous catalysis, the catalyst and reaction substrate in heterogeneous catalysis are in separate phases. The catalyst is usually solid, while the reactants and products are liquids or gases. The simplicity with which the catalyst can be separated from the reaction mixture is a significant advantage of heterogeneous catalysis.

In the 21st century, heterogeneous catalysis has become the predominant reaction mechanism in industrial processes because of its diverse applications, which range from the manufacture of fuels, chemicals, and products to environmental protection and

chemical applications. The synthesis of catalysts with high activity, selectivity, and stability, remains an important field of research. In fact, heterogeneous catalysis generally takes place near the surface of solids. Therefore, solids with high surface area, such as nanoparticles or porous solids, are typically employed. Porous materials employed for catalysis include zeolites, aluminosilicates, alumino-phosphates, and double layered hydroxides, but also carbon nanotubes and metal-organic frameworks (MOFs).[2–6] In the past thirty years, significant efforts have been made to design catalytic materials with precisely controlled active site structures and dispersion to enhance their catalytic activity and selectivity.[7]

Transition metals, such as iron (Fe), nickel (Ni), cobalt (Co), copper (Cu), molybdenum (Mo), tungsten (W) and ruthenium (Ru), are widely used in heterogeneous catalysis. These metals have changeable oxidation states, which allow them to easily donate or take electrons in redox reactions occurring in many industrial processes, such as hydrogenation and oxidation. Moreover, metal catalysts have exceptional thermal stability, allowing them to function under high temperatures without considerable degradation. In particular, molybdenum and tungsten catalysts are essential in hydrotreating, where they catalyze the removal of sulfur and nitrogen from fuel to meet environmental regulations and improve fuel quality.[8] Both metals have also recently shown a good catalytic activity in Fischer-Tropsch synthesis (FTS), which converts non-oil resources, such as coal, natural gas, and biomass into more valuable fuels or chemicals through the use of syngas.[9] Additionally, molybdenum-based electrocatalysts with controllable nanostructures and diverse compositions have been demonstrated to be promising candidates for Overall Water Splitting exhibiting high catalytic performance comparable to that of platinum-based catalysts.[10] Most of these materials show improved stability, activity, and selectivity when supported on oxide supports such as alumina, silica, or titania.[11]

1.2. Key Applications

Because of its efficiency, selectivity, and adaptability to a wide range of operating conditions, heterogeneous catalysis plays a key role in many industrial sectors. It is widely used in the energy industry, including petroleum refining, natural gas conversion, and the generation of cleaner energy carriers, such as hydrogen. In bulk chemical manufacturing, it allows for large-scale synthesis of important chemicals, such as ammonia and olefins. It is

critical in fine chemistry to produce high-value products such as pharmaceutical intermediates. Heterogeneous catalysis is also important for environmental applications like exhaust gas treatment and water purification. Furthermore, it finds use in the agri-food industry, for example, in the hydrogenation of oils and the conversion of sugars, emphasizing its adaptability and strategic importance across a wide range of fields.

1.3. Different types of heterogeneous catalysts

1.3.1. Molybdenum Based Catalysts

1.3.1.1. Principle applications of molybdenum-based catalysts

Molybdenum is a chemical element with the symbol Mo and the atomic number 42 and classified as Group 6 transition metal. It has an electrical configuration is [Kr] $4d^5$ $5s^1$, allowing for multiple oxidation states, most typically +IV, +V, and +VI, with the latter being the most stable. Molybdenum is a silvery-gray hard metal with a high melting point of 2623 °C, making it useful in high-temperature alloys. Molybdenum is the 54th most prevalent element in the Earth's crust with a concentration of about 1.2 ppm. It is mined primarily from the mineral molybdenite (MoS2). It can also be obtained from minerals such as powellite (calcium molybdate) and wulfenite (lead molybdate). An important advantage of molybdenum is that it is more abundant and affordable than nobel metals like platinum, palladium and ruthenium. Therefore, molybdenum-based catalysts represent a more economically feasible solution for industrial applications requiring large quantities and subject to budget constraints than those containing noble metals.

As a transition metal, Mo can easily form compounds with other elements, which makes it particularly useful in catalysis. Molybdenum-based catalysts are recognized for their high efficiency and selectivity in a variety of chemical processes, including hydrogenation, dehydrogenation, and oxidation reactions.[12] In these processes, the main class of catalysts used is molybdenum oxide-based catalysts. Their high performance is especially significant in operations like hydrodesulfurization (HDS), which removes sulfur from fuels while ensuring that the finished product passes stringent environmental regulations.[8] Molybdenum-based oxide catalysts are also highly effective in the selective oxidation of cycloalkanes, notably cyclooctane, with molecular oxygen. These catalysts produce important products that are cycloalkanones and cycloalkanols with low byproducts and a

high turnover rate. Furthermore, their reusability and thermal stability increase their practical utility. The appropriate interlayer spacing in 2D structures improves substrate access and reactivity. Overall, Mo-based catalysts provide a green and efficient approach for alkane oxidation that does not require severe conditions or co-reagents.[13]

Another widely used category is sulfur-based Mo catalysts. They are essential in hydrotreatment processes due to their extraordinary ability to activate hydrogen and cleave C-S, C-N, and C-O bonds. When stimulated with Co or Ni, their performance improves dramatically, resulting in highly active CoMoS or NiMoS phases. These catalysts are frequently utilized in the hydrodesulfurization (HDS), hydrodenitrogenation (HDN), and hydrodeoxygenation (HDO) processes, all of which are critical for creating cleaner fuel. Their distinctive edge sites, which are stabilized by sulfur ligands, aid in critical hydrogenation and bond-scission processes. Overall, sulfided Mo catalysts remain crucial for converting fossil feedstocks into environmentally friendly fuel.[14]

Molybdenum nitride-based complexes are also considered as promising catalysts to reduce the consumption of energy during the synthesis of ammonia. The mechanism of this catalytic reaction is not fully understood. Nevertheless, well-defined molybdenum nitride catalysts have been used as a model to understand the links between the electronic structure of molybdenum and intrinsic activity understand these properties.[15] Carbides-based Mo catalysts are also utilized for numerous applications related to sustainable and renewable energy.[16] In particular, molybdenum carbides catalysts have been proposed for the production of hydrogen by catalyzing the steam reforming methanol process.[17]

Besides all these diverse applications, molybdenum-based catalysts are also found to be very efficient in the olefin's metathesis reactions. Today, there are four main metals, *i.e.,* tungsten, molybdenum, ruthenium, and rhenium, used in the preparation of the olefins metathesis catalysts. The latter has already been exploited by IFPEN through the Meta-4 process, which is devoted to the production of propylene. This process involves the reaction between ethylene and 2-butene in the liquid phase. In the presence of Re_2O_7/Al_2O_3, it has been demonstrated to be capable of converting 63% of the charge introduced.[18] However, due to its rarity and high cost (around \$3,165 per kg[19] instead of \$71 per kg for molybdenum[20]), it is less commonly used in today's industrial processes. Ruthenium, owing to its high affinity towards olefins, as seen in Table 1, would be the most

suitable metal for the development of novel catalysts. However, it is quite costly, at around $29,000 per kg.[21] Tungsten catalysts are also used for this purpose. This metal is more affordable ($38 per kg)[22] than molybdenum, but the tungsten-based catalysts are more sensitive to oxygenated derivatives and less active for metathesis than their molybdenum-based counterparts.

Table 1: *Functional group tolerance towards olefin metathesis catalysts.* [23]

Re	W	Mo	Ru
Acids	Acids	Acids	**Olefins**
Alcohol, Water	Alcohol, Water	Alcohol, Water	Acides
Aldehydes	Aldehydes	Aldehydes	Alcohol, Water
Ketones	Ketones	**Olefins**	Aldehydes
Olefins	**Olefins**	Ketones	Ketones
Esters, Amides	Esters, Amides	Esters, Amides	Esters, Amides

Increased Reactivity

Molybdenum catalysts are, in addition, active at room temperature and their metallacycle, an organometallic intermediate where the metal atom is part of a cyclic structure, is unstable, leading to the loss of an olefin, which favors the metathesis reaction. Numerous metathesis catalysts were generated in situ from molybdenum derivatives and a co-catalyst. $MoCl_6/AlEt_3$ (where Et denotes ethyl groups) were developed around the mid-1960s for the polymerization of cyclopentene.[24] For these ill-defined systems, the active sites have never been characterized so far. However, Schrock in 1987 pioneered the synthesis of molybdenum-based imido alkylidene complexes that have a well-defined structure and considerable activity in olefin metathesis.[25] Within those systems, the nature of the different ligands (imido, alkoxy, aryloxy, carbene, etc.) is closely linked to the catalytic performance of complexes, especially with respect to the substrate compatibility (functionalized, cyclic, etc.) and the stereoselectivity of the reaction (*Z* or *E* isomers).

1.3.1.2. Olefins Metathesis Reaction

Olefins metathesis reaction discovered in 1956 and so named in 1967 is a process where the carbon-carbon double bond is broken in order to redistribute the olefins' carbon chains.[26] This reaction is a powerful tool used in diverse domains mainly oleo chemistry, petrochemistry and polymers as well as the synthesis of pharmaceuticals and variety of organic complexes.[27–29]

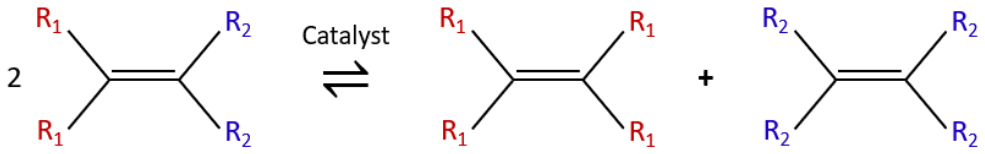

Figure 1: *Simplified representation of the olefin metathesis reaction.*[30]

Types of metathesis reaction include ring closure metathesis (RCM), acyclic diene metathesis (ADMET),[31] ring-opening polymerization by metathesis (ROMP),[32] cross-metathesis (CM),[33] and ring-opening metathesis (ROM)[34]. These reactions enable access to a large range of unsaturated compounds that are otherwise challenging to manufacture.[35,36] Industrial processes have benefited to a great extent from this catalytic reaction. The well-known Shell Higher Olefin and Phillips Triolefin processes depend on cross-metathesis for the production of olefins.[37,38] The foremost costly step of this manufacturing process is the olefin metathesis, because of the high cost of the metal catalyst. Therefore, there have been search for well-defined olefin metathesis catalysts that are less expensive yet extremely reactive.

The earliest catalysts used for metathesis classified as "ill-defined," meaning that their structure and mechanism of action are not fully understood. Some were employed for years without understanding of why they were active, and little has changed since the discovery of the first tantalum-based compounds with a high degree of oxidation by Schrock.[39,40]

Multiple mechanisms were proposed to explain the metathesis reaction. Calderon *et al.* considered a mechanism passing through a cyclobutane intermediate complexed on the metal in 1968.[41] In 1971, Pettit proposed an intermediate complex of the tetramethylene type to explain the reaction.[42] Grubbs also offered a technique that involved the rearranging of metallacyclopentane[43]. Nevertheless, only the mechanism proposed by Hérisson and Chauvin in 1971 were tested.[44]

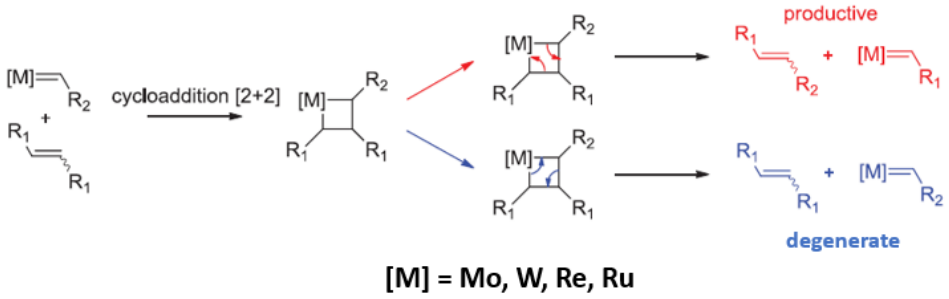

***Figure 2**: Mechanism proposed by Chauvin in 1971.*

A more detailed mechanism proposed by Chauvin is shown in Figure 2. It involves a [2+2] cycloaddition that occurs after the olefin is coordinated with the metal. The resulting metallacyclobutane can be rearranged in two ways: by forming a new olefin and carbenic complex representing a productive metathesis, or by recovering the olefin and the initial carbenic complex, resulting in a degenerate metathesis.

1.3.1.3. Molybdenum-Based Catalysts for Olefins metathesis

While ruthenium-based olefin metathesis catalysts are the most widely used, the high cost of ruthenium as a starting material compared to other metals such as molybdenum, necessitates the quest for less expensive olefin metathesis catalysts. For that reason, molybdenum was used to create one of the first well-defined catalysts in this sector. However, one major disadvantage is that it is sensitive to heat, air, moisture, and some common organic functional groups.[25,45] The reactivity toward oxygen and water is related to molybdenum's "hard" character, which causes it to react with "hard" bases like oxygen and water. Ruthenium, as a "soft" metal, is less sensitive to these air components but more reactive to "soft" bases, such as olefins.[46]

The majority of these early molybdenum alkylidene complexes have 14 electrons, which causes them to be electrically starved (Figure 3). As a result, the positioning of very bulky ligands must inhibit both bimolecular degradation and unimolecular ligand rearrangement, also called shuffling. While these complexes suffer from electron deficit, they are known for their great metathesis activity, particularly in the ROMP process.

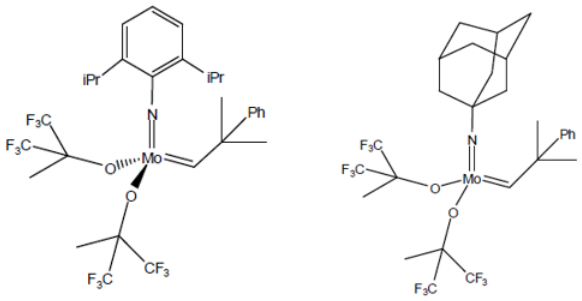

Figure 3: *Molybdenum-based catalysts with 14 electrons*

In 1987, the first well-characterized olefin metathesis catalysts based on molybdenum were created by adding ArNH(TMS) (TMS = trimethylsilyl) to $Mo(C^tBu)(dme)Cl_3$ (dme = dimethoxyethane), followed by catalytic triethylamine (NEt_3). After that, the dme ligand was replaced with bisalkoxy derivatives. The $Mo(CHEt)(NAr)[OCMe(CF_3)_2]_2$ complex showed a considerable activity in self-metathesis of cis-2-pentene. Since then, a lot of work has been done to optimize the ROMP reaction using molybdenum catalysts.[47] In 1998, Schrock created his first chiral molybdenum olefin metathesis compound.[48] Schrock leveraged the ligand-substrate interaction by creating catalysts that caused the substrate to approach the metal center in a controlled manner. While altering the substituents in his complex to address tacticity control during ROMP, he created a catalyst capable of creating enantiomerically pure metathesis products.

1.3.1.4. Molybdenum complexes grafted on silica support

Heterogeneous catalysis at the industrial level requires the grafting of solid precursors of the catalyst. Thus, olefin metathesis catalysts must be functionalized on amorphous supports in order to be efficiently activated. The functionalization process generally includes grafting molecular precursors onto the amorphous surface, followed by activation steps including heat treatment or exposure to reducing agents. Silica and alumina provide stable and inert nanoparticles for the dispersion of active catalytic sites, thereby increasing their number per unit mass of catalyst. This amorphous environment prevents the aggregation of energetic species, thus maintaining the overall performance of the catalyst at any point in the reaction. Although the concentration of the catalyst on the support will be less than 5%, its activity can be significantly improved by regulating the density of the active site, which means reducing clustering and site isolation during

deposition. Additionally, the metal loading level should ideally be optimized to avoid overcrowding or underutilization of active sites.

Previously, Amakawa *et al*. studied how configuration strain affects the reactivity of MoO_4 species supported on mesoporous silica (SBA-15) during propene metathesis.[49] As the molybdenum loading exceeds the ideal level of around 1 Mo atom per nm^2, strain arises due to the limited number of silanol anchoring sites. The strain induces distorted configurations of the MoO_4 species, increasing their catalytic activity. A considerable boost in performance is seen at 8% Mo loading, which correlates with enhanced reducibility as indicated by temperature-programmed reduction (H_2-TPR). These findings indicate that, while strain is often considered as a challenge in catalyst design, it can play a beneficial role in optimizing catalytic performance in this system.

The catalytic performance of grafted catalysts is significantly affected by the activation mechanism used. For example, recent study showed that the use of methane pretreatment at 650 °C significantly improves the activity of MoO_3-based catalysts for low-temperature olefin metathesis reactions.[50] Methane pretreatment increases propene metathesis activity by 1-2 orders of magnitude, with values ranging from 144 to 167 $mmol \cdot g_{cat}^{-1} \cdot h^{-1}$ and turnover frequencies (TOF which defines the number of reaction products generated per active site per unit of time) from 120 to 2066 h^{-1}, depending on MoO_3 loading (20 to 1 wt%, respectively). The process is separated into two steps: Mo(VI) is mainly reduced to carbide-like species (MoC_x), which then combine with ethene to produce metathesis-active carbenes. Methane pretreatment outperforms argon pretreatment that has a specific activity as low as 6.9 $mmol \cdot g_{cat}^{-1} \cdot h^{-1}$. A 30-minute methane treatment provides optimal results, whereas prolonged durations result in coke production and decreased activity.

The aim of this research is to study how local ligands surrounding metallic molybdenum influence the NMR parameters of grafted molybdenum-based catalyst for olefins metathesis. Additionally, DFT simulations will be performed to explain the observed changes in NMR parameters, providing comprehensive insight into the catalytic behavior and properties of these compounds.

1.3.2. Amorphous silica-alumina (ASA) catalysts

1.3.2.1. Application of ASA in heterogeneous catalysis

The use of amorphous silica-alumina (ASA) as solid acid catalysts dates back to the 1940s.[51] They are also used as supports for metal active sites. However, synthesizing ASAs with zeolite-like acidity remains a challenge. Zeolites are microporous crystalline materials with exceptionally high Brønsted acidity and thermal stability. Nevertheless, their application in many industrial processes involving large molecules is limited by their microporosity, which induces diffusion constraints.[52–54] Alternatively, ASAs, although exhibiting lower Brønsted acidity than zeolites, offer improved mass transfer and better performance towards large molecules.[55] In addition, the production of ASAs is ecofriendly and cost-effective, supporting a wide range of applications in biomass conversion, biorefining industries and renewable chemicals.[56–59] Aluminosilicates are also used in the dehydrochlorination of halogenated hydrocarbons and as supports for metals for ring-opening reactions.[60]

In addition to conventional silica-alumina, other types of amorphous aluminosilicates are used: aluminum-rich aluminosilicates can produce dimethylether (DME) or co-produce methanol and DME from syngas.[60] Silicate alumina, prepared by grafting tetraethyl orthosilicate (TEOS) on alumina, yields acidic sites suitable for dehydration reactions and can thus be used to dehydrate terbutyl alcohol to isobutylene. Alternatively, aluminated silica, made by adding alumina precursors to preformed silica, is commonly used as a catalyst for the cracking of methyl tert-butyl ether (MTBE) to isobutylene.[60]

Another distinguishing feature of ASA is their high density of Lewis sites, which makes them suitable for Lewis-acid catalyzed reactions, such as the Meerwein-Ponndorf-Verley (MPV) reduction of carbonyl compounds.[61]

1.3.2.2. Brønsted Acidity in ASA

Controlling acidic properties is critical for understanding reaction mechanisms and developing effective acidic catalysts. Zeolites' Brønsted acid sites (BAS) have been extensively studied both experimentally and theoretically. The bridging hydroxyl group is generated by substituting a Si^{4+} atom in the crystal structure with an Al^{3+} [≡Al-(OH)-Si≡].[62] Zeolites' acidity is determined by the proportion of aluminum and the local environment of OH groups. Specifically, when the number of Al^{3+} atoms in the second coordination sphere

grows, the strength of acid sites steadily declines.[63] Zeolites with high Al^{3+} concentration have a high density of acid sites with low strength, whereas dealuminated zeolites have a low density of acid sites but with stronger acidity. Furthermore, increased Al^{3+} content promotes zeolites' ability to create extra framework aluminum species (EFAL), resulting in Lewis acid sites.[63] These Lewis acid sites can further improve Brønsted acidity through a synergistic effect.[64] The acidity of the zeolites is also affected by the size of the cavities: for equal chemical composition, medium-pore zeolites display stronger acid sites than large-pore zeolites.[65]

Due to their amorphous nature, the acid sites of aluminosilicates are less well-defined than those of zeolites, and their structure remains unclear despite their importance in many catalytic processes. Early models of ASA suggested that BAS arise from protons compensating for the electrical charge on the surface. Back in 2005, Góra-Marek *et al*. reported weak infrared bands at 3600-3610 cm^{-1} in several aluminosilicates, which they attributed to Si–OH–Al bridges in ASA responsible for strong Brønsted acid sites.[66] Although ASA contain considerable numbers of BAS, detecting the OH band around 3600-3610 cm^{-1} remains challenging because weakly acidic hydroxyl groups have a low extinction coefficient, making their bands weak and difficult to identify. In 2006, Busca *et al*. challenged this interpretation by proving that aluminated silica contains equivalent catalytic sites regardless of the presence of a specific spectral band.[67] They presented a new "drawbridge" model, in which an Si–OH and Al^{3+} pair forms a structure that may be "closed" in the hard framework of zeolites and "open" in the flexible amorphous silica-alumina (ASA). The stiffness of the zeolite framework stabilizes the closed drawbridge, which cannot be achieved with ASA.

In 2009, Chizallet and Raybaud proposed the first theoretical model for amorphous silica-alumina.[68] This model utilized periodic density functional theory (DFT) to optimize a γ-alumina surface coated with a silica monolayer. They identified pseudo-bridging silanols (PBS), which interact electrostatically with aluminum (PBS-Al) but are not covalently bonded as in zeolites (see figure 4). When a strong base is adsorbed, the pseudo-bridge, previously called drawbridge by Busca *et al*., becomes stable. Their calculations showed that a strong base (such as 2,6-dimethylpyridine) can close the drawbridge but a weak base (such as carbon dioxide) cannot. Complementary studies by the Huang group revealed that

silanols which interact with tetra- and penta-coordinate aluminum exhibit high Brønsted acidity.[69] Solid state NMR evidence for these interactions is discussed in section 5.

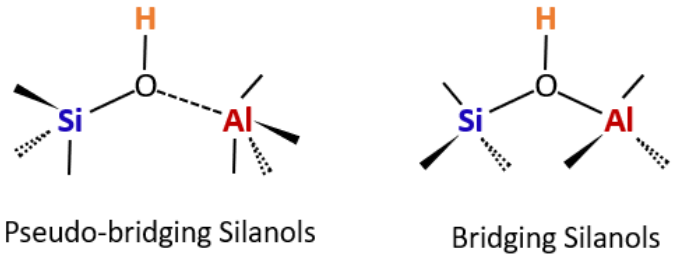

Figure 4: *Structure of pseudo-bridging (left) and bridging (right) silanols*

As a conclusion, the recent common hypothesis for acidity in amorphous silica-aluminas (ASAs) is caused by pseudo-bridging silanols formed between silicon and either tetracoordinate (IV) or pentacoordinate (V) aluminum. The silanol oxygen to aluminum bond distance in ASAs (2.94-4.43 Å)[70] is significantly longer than in zeolites (1.8-2 Å)[70], resulting in weaker acidic sites. Synthesizing ASAs with zeolite-like bridging silanols could result in materials with high acidity and surface area, although their existence is still contested.

1.3.2.3. Plasmonic photocatalysis properties

Metallic nanoparticles such as gold and silver, when exposed to light in the visible and near-infrared regions, experience coherent oscillation of conduction electrons. This phenomenon called localized surface plasmon resonance (LSPR) enhances electric field near the surface of metal nanoparticles. This electric field can trigger chemical reactions with selective pathways, thus offering an alternative to classic thermal catalysis.[71] Typically, metal nanoparticles are deposited on the surface of a catalyst that enables the LSPR phenomenon under light irradiation, giving rise to so-called “plasmonic photocatalysts”. The structure of plasmonic photocatalysts, such as the size, shape, and composition of the nanoparticles, influences their LSPR properties, modifying the catalytic efficiency and enabling reactions that would be impossible under moderate temperature conditions. Multi-metallic designs, which integrate both plasmonic and catalytic metals, extend the application of plasmonic catalysis to reactions that previously required non-plasmonic metals. Such materials hold significant promise for the conversion of solar-to-chemical energy and for advanced green chemistry.[71]

Recently, Verma *et al.* explored the application of plasmonic photocatalyst for the conversion of CO_2 into chemicals and fuels.[72] Combining gold and silver nanoparticles with metals, such as platinum or palladium, improves charge transfer, enabling CO_2 reduction and dry methane reforming. In their recent study, they found that the combination of gold nanoparticles with platinum shells can oxidize CO at low temperatures between 130 and 180 °C using visible light (400 mW/cm^2), thereby surpassing the monometallic Ag at 200-260 °C. Various mechanisms, including direct charge carrier transfer and photothermal effects, were investigated, with results revealing up to a seven-fold increase in CH_4 generation rate for Rh/Al_2O_3 under UV light from 365 nm to 623 K. The article highlights the importance of tailored plasmonic catalysts in achieving improved selectivity and efficiency in the conversion of CO_2 by solar energy by considering design parameters including particle composition, thickness of the shell and the excitation wavelength.

In the frame of this PhD, we investigated amorphous aluminosilicates functionalized with gold nanoparticles, which can also serve as plasmonic photocatalysts. These catalysts revealed increased acidity when exposed to light, encouraging us to investigate how light irradiation affects the nature and structure of the acid sites. This observation raised the crucial question: what precise changes occur at these sites when illuminated, and how can we characterize them? The structure of these materials was studied by solid-state NMR with and without light irradiation. This study will be presented in the chapter 3.

2. Characterization of heterogeneous catalysts by solid-state NMR

2.1. Solid-state NMR spectroscopy

2.1.1. Principle of solid-state NMR

Structural characterization is a key to understand the reactivity of active sites at the surface of solid catalysts and hence, to improve their performances in a rational way. In the case of grafted catalytic systems and ASAs, which lack long-range order, the structure of active sites cannot be determined using diffraction techniques. Therefore, probing of the structure of these sites requires the use of local characterization techniques.

NMR spectroscopy is one of the most powerful, adaptable, and commonly used analytical technique for determining local atomic-level structure. This technique is element-specific, with practically all elements having accessible spin-active isotopes, and it may be applied to a wide range of samples, both solid and liquid, with no need for long- or short-range ordering. Solid materials exhibit constrained molecular dynamics, which do not avergae anisotropic interactions to their isotropic values, as in solution. As a result, NMR spectra of solids are broader than those of solutions and often more difficult to interpret. However, these anisotropic interactions provide additional information regarding structure and bonding.

The intrinsic nuclear spin angular momentum, denoted by the vector **I**, is described by the nuclear spin quantum number *I*, which can be a positive or half-integer number. The projection of **I** on z-axis is equal to $m_I\hbar$, where m_I is the magnetic quantum number and can take values ranging from $+I$ to $-I$, resulting in $2I+1$ degenerate spin states and $\hbar$ is the reduced Planck's constant. The nuclear magnetic dipole moment $\boldsymbol{\mu}$ is proportional to **I**

$$\boldsymbol{\mu} = \gamma\hbar\mathbf{I} \qquad \text{(Eq. 1)}$$

where γ is the gyromagnetic ratio, which depends on the isotope.

In the absence of an external magnetic field, the orientation of the magnetic moments is random and NMR signal cannot be detected. In the presence of an external magnetic field $\mathbf{B}_0$, the nuclear spins tend to align with the field due to the Zeeman interaction, resulting in nuclear magnetization parallel to the field B_0 at equilibrium.

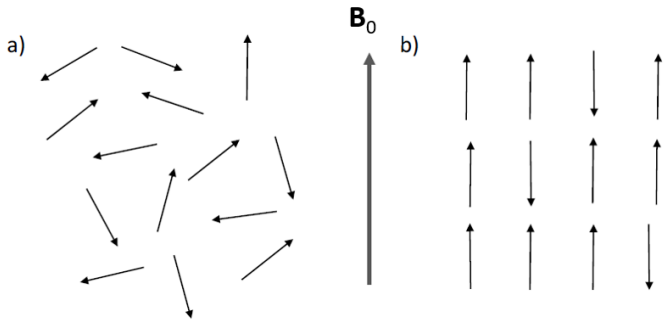

Figure 5: *a) In the absence of external magnetic field B_0, all orientations of the nuclear magnetic moment have the same probability. (b) An external magnetic field aligns nuclear spins removing the degeneracy of their energy levels.*

In the presence of an external magnetic field $\mathbf{B}_0$, the energy difference between adjacent energy levels, m_I and $m_I + 1$ is equal to $h|\nu_0|$ where h denotes the Planck's constant and ν_0 the Larmor frequency

$$\nu_0 = -\frac{\gamma B_0}{2\pi} \qquad \text{(Eq. 2)}$$

A transverse radiofrequency (rf) field, $\mathbf{B}_{rf}$, oscillating at ν_0 can be employed to change the orientation of nuclear spins with respect to $\mathbf{B}_0$ and transfer spins between adjacent energy levels. This phenomenon is called resonance.

2.1.2. Spin interactions in solids

Nuclear spins are subject to various interactions that can occur between two spins or between a spin and its local environment. In addition to the Zeeman interaction, NMR interactions in solids are classified according to their nature. Nuclei with spin 1/2 can be subject to three purely magnetic interactions, while nuclei with spin $I > 1/2$, also called quadrupolar nuclei, can be subject to an additional interaction of electric nature called the quadrupolar interaction. The total interaction energy of a spin system is described by the spin Hamiltonian H:

(Eq. 3)

$$H = H_Z + H_{CSA} + H_D + H_J + H_Q$$

where:

H_Z: Zeeman Hamiltonian

H_{CSA}: Chemical Shift Hamiltonian

H_D: Direct spin-spin coupling Hamiltonian

H_J: Indirect spin-spin coupling Hamiltonian

H_Q: Quadrupolar coupling Hamiltonian

2.1.2.1. Zeeman Interaction

The Zeeman Hamiltonian describes the interaction between the nuclear magnetic moment and the external static magnetic field, $\mathbf{B}_0$. Because of this interaction, the states

for which the magnetic moments are in the same direction as the field $\mathbf{B}_0$ have a lower energy than those where the magnetic moments are in the opposite direction to the field $\mathbf{B}_0$.

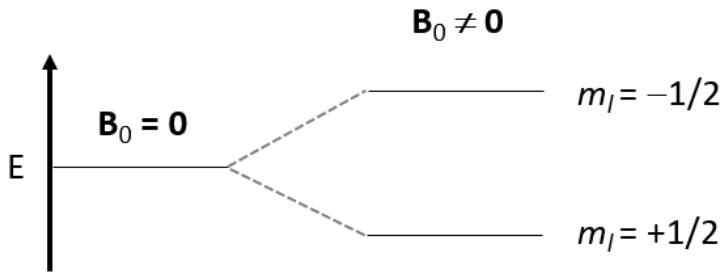

Figure 6: *Lifting of degeneracy of energy levels for a spin-1/2 nucleus subject only to the Zeeman interaction.*

The Zeeman Hamiltonian H_Z can be written as:

$$H_Z = -\gamma B_0 I_z \qquad \text{(Eq. 4)}$$

where I_z denotes the operator corresponding to the z-component of nuclear spin. The Zeeman interaction is usually more than one order of magnitude greater than the internal spin interactions, which can therefore be considered as perturbations of Zeeman energy levels.

2.1.2.2. Chemical shift interaction

When a molecule is placed in a magnetic field $\mathbf{B}_0$, the electric current induced in the electron cloud surrounding the nucleus create an induced magnetic field, $\mathbf{B}_{ind}$, which modifies the local magnetic field, $\mathbf{B}_{loc}$, at the position of the nucleus. The induced magnetic field being proportional to $\mathbf{B_0}$, the $\mathbf{B}_{loc}$ field is equal to:

$$\mathbf{B}_{\mathrm{loc}} = \mathbf{B}_0 + \mathbf{B}_{\mathrm{ind}} = \mathbf{B}_0(1 + \boldsymbol{\delta}) \qquad \text{(Eq. 5)}$$

where $\boldsymbol{\delta}$ denotes chemical shift tensor. It is a 3x3 symmetric matrix, since the direction of the B_{ind} field depends on the orientation of the solid with respect to $\mathbf{B}_0$. In other words, the chemical shift is anisotropic. The $\boldsymbol{\delta}$ matrix depends on the electron cloud around the nucleus and therefore the isotropic and anisotropic chemical shifts depend on the electronic environment of the nucleus. The matrix $\boldsymbol{\delta}$ can be diagonalized in a system of principal axes {X, Y, Z}. The isotropic chemical shift (δ_{iso}) corresponds to the average of the three eigenvalues of the matrix $\boldsymbol{\delta}$:

$$\delta_{\mathrm{iso}} = \frac{1}{3}\left(\delta_{\mathrm{XX}} + \delta_{\mathrm{YY}} + \delta_{\mathrm{ZZ}}\right) \qquad \text{(Eq. 6)}$$

while the chemical shift anisotropy (δ_{aniso}) quantifies the largest deviation from the isotropic value:

$$\delta_{\mathrm{aniso}} = \delta_{\mathrm{ZZ}} - \delta_{\mathrm{iso}} \qquad \text{(Eq. 7)}$$

The asymmetry parameter of CSA tensor, η_{CSA}, is defined as:

$$\eta_{\mathrm{CSA}} = \frac{\delta_{\mathrm{YY}} - \delta_{\mathrm{XX}}}{\delta_{\mathrm{ZZ}} - \delta_{\mathrm{iso}}} \qquad \text{(Eq. 8)}$$

and can range from 0 to 1.

2.1.2.3. Dipolar interaction

Each nuclear magnetic moment produces a local magnetic field which interacts with the magnetic moments of neighboring nuclei. This direct spin-spin coupling interaction through space, also called dipolar interaction, between two spins *I* and *S* with gyromagnetic ratio γ_I and γ_S is characterized by the dipolar coupling constant b_{IS} in Hz

$$\frac{b_{IS}}{2\pi} = -\frac{\hbar\,\mu_0\,\gamma_I\gamma_S}{8\pi^2 r_{IS}^3} \qquad \text{(Eq. 9)}$$

where μ_0 denotes the magnetic permeability of the vacuum, and r_{IS} the internuclear distance. This interaction can provide unique information about the distances between nuclei.

2.1.2.4. J-coupling

Besides dipolar interaction, nuclear spins can also be coupled indirectly through shared electron density (*J*-coupling). In the latter situation, spin-spin coupling occurs via covalent bonds and can thus provide useful information on the connectivity between atoms and the conformation of molecules. This coupling can be described by a tensor ***J*** with isotropic value J_{iso}. For isotopes in the first part of the periodic table of light elements, the dipolar couplings are usually larger than the *J*-couplings. Nevertheless, for some heavy elements, the amplitude of *J*-coupling can exceed that of dipolar interactions.

2.1.2.5. Quadrupolar interaction

75% of NMR-active isotopes (e.g., ^{27}Al, ^{95}Mo, ^{17}O) are quadrupolar nuclei with a spin $I > 1/2$, which presents a non-spherical distribution of charge in the nucleus and hence, possess an electric quadrupole moment, eQ. This electric quadrupole moment interacts with the surrounding electric field gradient (efg) (see figure 7a). This quadrupolar interaction is anisotropic.

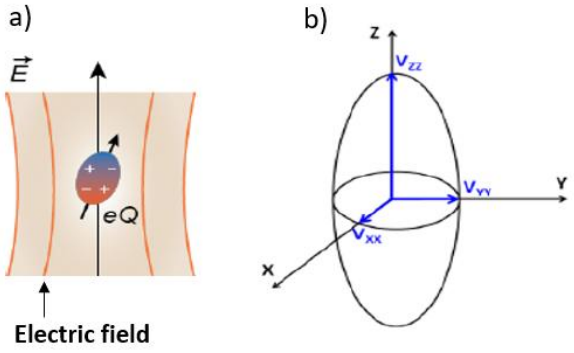

Figure 7: *a) Representation of the nuclear quadrupolar interaction, which arises from the coupling between the electric quadrupolar moment eQ and the electric field gradient. b) Representation as an ellipsoid of efg tensor.*

The quadrupolar interaction provides information about the local symmetry around the quadrupolar nucleus. The efg is described by a tensor, V, which can be diagonalized in a principal axis system (PAS)

$$\mathbf{V}^{\mathrm{PAS}} = \begin{pmatrix} V_{\mathrm{XX}} & 0 & 0 \\ 0 & V_{\mathrm{YY}} & 0 \\ 0 & 0 & V_{\mathrm{ZZ}} \end{pmatrix} \qquad \text{(Eq. 10)}$$

with $|V_{ZZ}| \geq |V_{YY}| \geq |V_{XX}|$. The quadrupolar interaction is usually described by the quadrupolar coupling constant

$$C_Q = \frac{e\,Q\,V_{\mathrm{ZZ}}}{h} \qquad \text{(Eq. 11)}$$

expressed in frequency units, and the asymmetry parameter of efg tensor

$$\eta_Q = \frac{V_{\mathrm{XX}} - V_{\mathrm{ZZ}}}{V_{\mathrm{YY}}} \qquad \text{(Eq. 12)}$$

which is dimensionless and ranges between 0 and 1.

In NMR experiments, the amplitude of the quadrupolar interaction remains lower than that of the Zeeman interaction. Therefore, its effect on spin dynamics can be described as a perturbation of the Zeeman Hamiltonian. However, the amplitude of the quadrupolar coupling is equal to several megahertz and hence, is significant with respect to the Larmor frequency. Hence, the first-order perturbation theory is often not sufficient and the second-order terms must be considered. In other words, the quadrupolar Hamiltonian H_Q can be written as:

$$H_Q = H_Q^{(1)} + H_Q^{(2)} \qquad \text{(Eq. 13)}$$

where $H_Q^{(1)}$ and $H_Q^{(2)}$ denote the first- and second-order quadrupolar Hamiltonians

Figure 8 depicts the effects of these two terms on the energy levels of a spin-5/2 nucleus. This isotope has (2×5/2 + 1) = 6 energy levels and exhibits 2×5/2 = 5 single-quantum (SQ) transitions between adjacent energy levels. For a spin-5/2 nucleus in an isotropic liquid or a site with cubic symmetry, the five SQ transitions are degenerate and resonate at the angular Larmor frequency, ω_0. The first-order quadrupolar interaction affects the frequencies of all satellite transitions (ST) between energy levels m_I and $m_I + 1$ with $m_I \neq -1/2$, where m_I denotes the magnetic spin quantum number but it does not affect that of central transition (CT) between energy levels $m_I = -1/2$ and $+1/2$. Conversely, the second-order quadrupolar interaction, which is several orders of magnitude smaller, affects the frequencies of all SQ transitions.

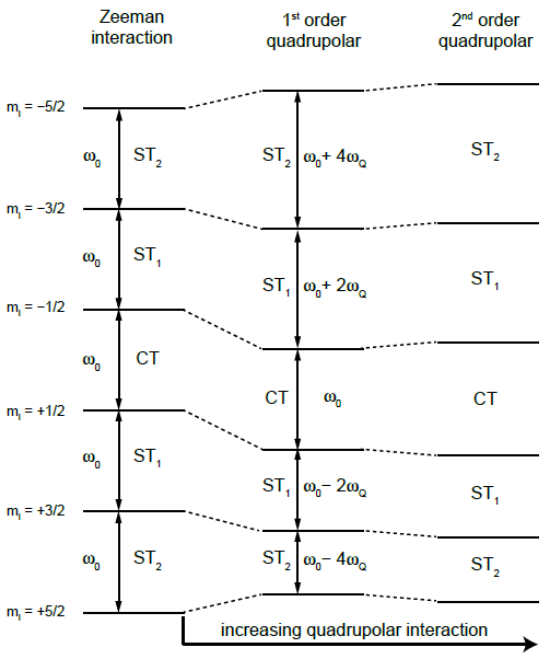

Figure 8: *Schematic energy level diagram for a spin I = 5/2 nucleus showing the effect of the Zeeman, first-order and second-order quadrupolar interactions.*

2.2. Sensitivity and resolution enhancement

The NMR signal of quadrupolar nuclei in powders are broadened by first- and second-order quadrupolar interactions. This broadening reduces the resolution and the sensitivity compared to spin-1/2 nuclei. In particular, quadrupolar nuclei with low gyromagnetic ratios (γ), low natural abundances or subject to large quadrupolar interaction are especially challenging to detect. For this reason, many NMR methods have been developed to improve the resolution and sensitivity of NMR experiments on quadrupolar nuclei. Some of the methods employed during this PhD are presented below.

2.2.1. High Field

High magnetic fields reduce the second-order quadrupolar broadening, which is not fully averaged under magic-angle spinning (MAS)[73] but is inversely proportional to the strength of the field ($\propto B_0^{-1}$). Hence, the resolution and sensitivity of 1D NMR spectra of half-integer spin quadrupolar nuclei are proportional to B_0^2 and $B_0^{11/4}$, respectively.[74,75] Recently, the advent of ultra-high magnetic field magnet with B_0 field higher than 23 T, *i.e.* ^{1}H Larmor frequencies higher than 1 GHz, has improved the resolution and the sensitivity for the NMR detection of quadrupolar nuclei in solids, opening new avenues for the observation of low-γ weakly abundant quadrupolar nuclei, such as ^{95}Mo and ^{67}Zn. [76–78]

2.2.2. Magic-Angle Spinning

In the liquid phase, the rapid molecular motions average out the anisotropic part of NMR interactions, resulting in spectra with narrow lines. On the contrary, in the solid phase, these interactions persist and can cause significant peak broadening. This broadening reduces sensitivity and resolution, making it more difficult to distinguish between different chemical environments. However, the anisotropic NMR interactions, which include chemical shift anisotropy, dipolar interaction, and first-order quadrupolar interaction, can be averaged to zero by rotating the sample around an axis tilted by 54.74°, the so-called magic angle (figure 9), with respect to the stationary field $\mathbf{B}_0$ at frequencies much higher than the strength of the anisotropic interactions.[82,79] Thus, this approach, known as magic-angle spinning (MAS), greatly improves the sensitivity and resolution of solid-state NMR measurements.

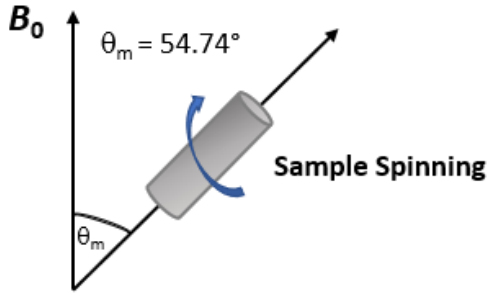

Figure 9: *Representation of magic angle spinning*

2.2.3. Population Transfer - DFS

Population transfer is another strategy for increasing the sensitivity of quadrupolar nuclei. This approach is employed to enhance the CT of a quadrupolar nucleus by increasing population difference across CT through the irradiation of STs.[80] This population transfer is based either on the saturation or the inversion of STs. ST saturation cancels population difference across STs. Through this approach, the CT signal can be improved by a factor of (I + 1/2) = 2, 3, 4, and 5 for nuclei with spins of 3/2, 5/2, 7/2, and 9/2, respectively.[81] Higher enhancements equal to 2I = 3, 5, 7, and 9 for I = 3/2, 5/2, 7/2, and 9/2, respectively, can be achieved in principle by inverting all the outer STs before the inner ones.[81] Various population transfer strategies through saturation or inversion of spin populations have been proposed. DFS (Double Frequency Sweeps) and HS (adiabatic inversion with Hyperbolic Secant pulses) are two examples.[82]

DFS enhances the signal by adiabatically inverting the STs, transferring the population of the outer spin levels to the CT energy level before selectively exciting them.[83] Sweeping a continuous rf-field across the whole spectrum while keeping the pulse's amplitude constant allows for population inversion between two energy levels.[82] Using waveform generators, it is possible to design pulses, which irradiate both high and low frequencies at the same time.[82] DFS techniques with a large sweep range provide the optimum signal enhancement for the NMR spectra of stationary powdered materials.[84]

2.2.4. QCPMG

The quadrupolar Carr-Purcell-Meiboom-Gill (QCPMG) method,[85] derived from the CPMG sequence, is widely employed in solid-state NMR to improve the sensitivity of half-integer quadrupolar nuclei. The QCPMG pulse sequence (figure 10) consists of two main parts: a π/2 pulse for excitation and a train of *N* consecutive CT selective π pulses separated by 2τ refocusing delays. Multiple spin-echoes are recorded for every free-induction decay (FID) until the echo intensities decay to zero. The Fourier transformation of the echo train produces a spectrum consisting of small peaks, called spikelets, whose manifold reproduces that of the powder spectrum under static conditions.[86] The spikelet envelope carries information on anisotropic interactions, such as CSA, quadrupolar coupling, and heteronuclear dipolar coupling.[81] For the QCPMG method to be effective, the decay of the echo envelope, T_2', must be significantly greater than the duration of the echo, T_{off}.[87] The gain in sensitivity achieved with QCPMG, compared to a regular echo experiment, is given by $G_{S/N} = 2\sqrt{T_2' T_{\text{off}}}\,(2\tau)^{-1}$.[88]

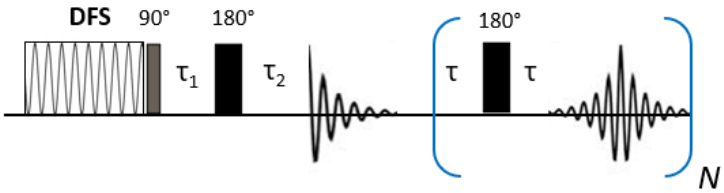

Figure 10: *Representation of DFS-QCPMG pulse sequence*

2.2.5. UDEFT

The uniform driven equilibrium Fourier transform (UDEFT) is a direct-excitation technique used to improve the sensitivity of spin-1/2 nuclei having long longitudinal relaxation T_1.[89] As seen in Figure 11, it consists in a spin-echo, at the end of which rf pulses

brings back the remaining transverse magnetization onto the *z*-axis. This approach reduces the recovery delay, hence enhancing the sensitivity.

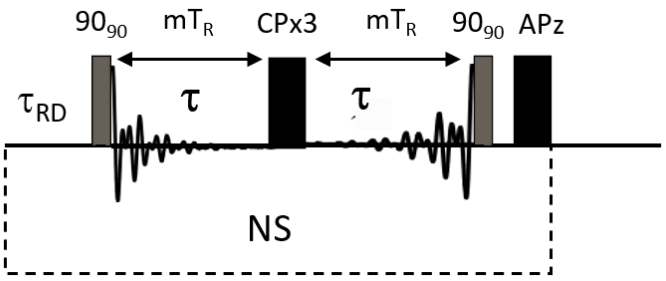

Figure 11: *Representation of UDEFT pulse sequence*

2.3. Two-dimensional heteronuclear correlation experiments

2.3.1. CP-HETCOR

Cross-polarization heteronuclear correlation (CP-HETCOR) displayed in Figure 12a is a 2D experiment used to probe through-space proximities between two distinct spin-1/2 isotopes, *I* and *S*. The excitation 90° pulse on *I* channel produces transverse magnetization for *I* nuclei, which is encoded by the isotropic chemical shift during the period t_1. This transverse magnetization is then transferred to *S* isotope using cross-polarization (CP) transfer. During this transfer, rf fields maintain the transverse magnetization of the two isotopes along a specific direction in the rotating frame. The nutation frequencies of both isotopes denoted ν_{1I} and ν_{1S} must fulfill the Hartmann-Hahn condition under MAS (ν_R) to produce an effective CP transfer:[90]

(Eq. 14)

$$\nu_{1I} + \varepsilon\nu_{1S} = n\nu_R$$

where the coefficient ε is equal to −1 for zero-quantum (0Q) CP and +1 for double-quantum (2Q) CP and *n* = ±1 or ±2.

2.3.2. *D*-HMQC

However, CP transfer lacks robustness for quadrupolar nuclei since the use of rf irradiation selective of the CT leads to a high sensitivity to the strength of the quadrupolar interaction and offset.[91] The sensitivity to offset is a major limitation for its use at high magnetic fields, which produce larger chemical shift dispersions.

Dipolar-mediated heteronuclear multi-quantum coherence (*D*-HMQC) experiment represents an alternative to CP-HETCOR technique to observe through-space heteronuclear proximities, notably between spin-1/2 and quadrupolar nuclei.[90] As seen in Figure 12b, in the *D*-HMQC pulse sequence, a π/2 pulse is initially applied on the *S* channel generating in-phase transverse magnetization. Then, *I*-*S* dipolar interactions are reintroduced under MAS conditions during the defocusing and refocusing delays by the application of heteronuclear dipolar recoupling scheme. If possible, the recoupling scheme must be applied to the indirectly detected isotope, *I*, to limit t_1-noise.[92] When *I* = ^{1}H, symmetry-based recoupling blocks $\mathrm{SR4}_1^2$ can be employed since it reintroduces the ^{1}H-*S* dipolar interactions, while suppressing the contribution of ^{1}H-^{1}H dipolar couplings to the first-order Hamiltonian. The first π/2 pulse on *I* channel creates heteronuclear multiple-quantum coherences, which are encoded by isotropic shifts of *I* nuclei during the indirect evolution period, t_1, while the π pulse on *S* channel refocuses their evolution under isotropic shifts of *S* nuclei. The second π/2 pulse on *I* channel and the refocusing delay reconvert heteronuclear multiple-quantum coherences into transverse magnetization of *S* isotope, which is detected during the acquisition.

2.3.3. *D*-RINEPT

Dipolar-mediated Refocused Insensitive Nuclei Enhanced by Polarization Transfer (*D*-RINEPT) is another 2D through-space heteronuclear correlation experiment, which can be used to probe proximities between distinct isotopes. Whereas *D*-HMQC experiment employs two consecutive coherence transfer $^1\mathrm{H} \rightarrow I \rightarrow {}^1\mathrm{H}$, where *I* denotes the indirectly detected quadrupolar nucleus, *D*-RINEPT sequence relies on a single magnetization transfer $^1\mathrm{H} \rightarrow I$. Like in *D*-HMQC sequence, the coherence transfer in *D*-RINEPT technique is mediated by the ^{1}H-*I* dipolar interactions, which are reintroduced by the application of heteronuclear dipolar recoupling during the defocusing and refocusing delays, τ. In the case of *D*-RINEPT sequence, those interactions are reintroduced by applying a non-γ-encoded two-spin order dipolar recoupling to the ^{1}H channel. The dipolar recoupling blocks used in this work are $\mathrm{SR4}_1^2$ built from tanh/tan adiabatic inversion pulses.[90,93,94] As this recoupling is non-γ-encoded, the blocks must be rotor-synchronized, *i.e.* separated by an integer number of rotor periods. Furthermore, to improve the robustness towards the ^{1}H rf inhomogeneity and ^{1}H-^{1}H dipolar interactions, composite ($90_0180_{90}90_0$) and ($90_{90}90_0$)

pulses incorporating continuous wave (CW) irradiation, are applied as refocusing or 90° pulses, respectively.[93,95–97] His variant is termed *D*-RINEPT-CWc sequence.

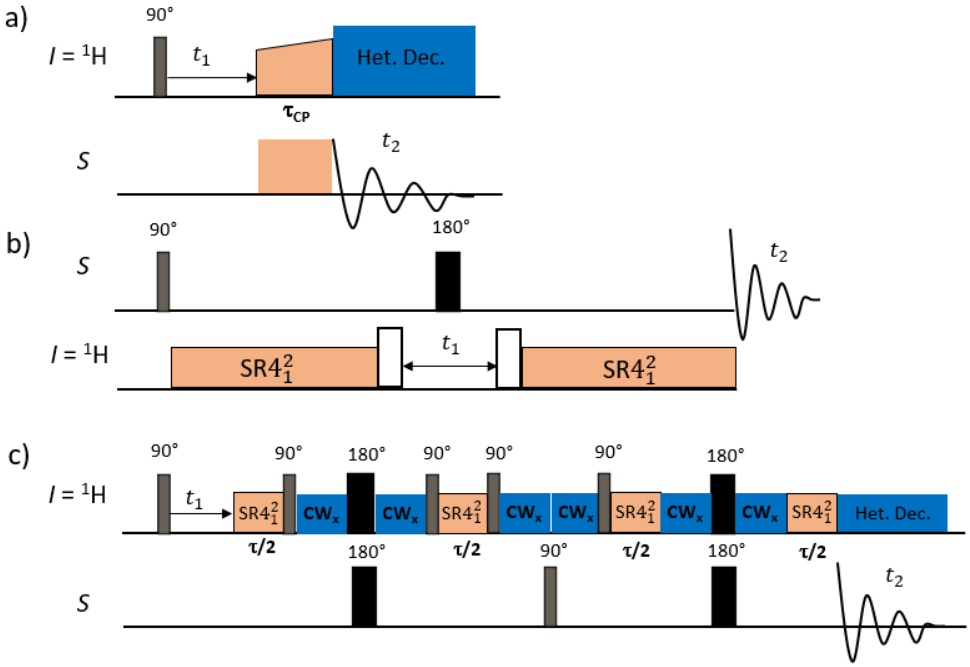

Figure 12: *Representation of 2D S{¹H} (a) CP-HETCOR, (b) D-HMQC and (c) D-RINEPT pulse sequences, in which the S nuclei are detected, whereas the protons are indirectly observed* [90]

3. Calculation of NMR parameters

3.1. Basics of the quantum chemistry

Quantum mechanics was developed to overcome classical mechanics' incapacity to describe certain aspects of matter-radiation interactions. This theory introduces a complex wave function, Ψ, which encompasses all physical features of a system. Solving the time-independent Schrödinger equation (Eq. 15) provides the wave function and the various energy levels associated with state *i*.

(Eq. 15)

$$H\Psi_i(\mathbf{r},\mathbf{R}) = E_i\,\Psi_i(\mathbf{r},\mathbf{R})$$

Here, **r** denotes electron coordinates, while **R** represents those of nuclei. The non-relativistic Hamiltonian operator H of a molecular system can be expressed as

(Eq. 16)

$$H = T_{\mathrm{N}} + T_{\mathrm{e}} + V_{\mathrm{NN}} + V_{\mathrm{Ne}} + V_{\mathrm{ee}}$$

The terms T_{N} and T_{e} denote the kinetic energy operators of nuclei and electrons, respectively, while V_{NN}, V_{ee}, and V_{Ne} refer to the potential energy operators stemming from repulsion between nuclei, electrons, and attraction between electrons and nuclei, respectively. For hydrogen-like atoms, such as He^{+}, Li^{2+}, and Be^{3+}, the Schrödinger equation can be solved analytically. For other chemical compounds, it can be solved numerically using approximate wave functions. For systems containing more than two nuclei, such as H_2^+, the Born-Oppenheimer approximation, which assumes that the wave functions of atomic nuclei and electrons in a molecule can be treated separately, is usually valid since the mass of nuclei is much higher than that of an electron (for instance, a proton is 1836 heavier than an electron). Under this approximation, the nuclei can be considered as stationary in their equilibrium positions, while the electrons move. The electronic wave function determines the density of the *N* electrons. Nevertheless, for systems containing a large number of atoms, additional approximations are required to solve the Schrödinger equation. One of the most widely used approaches is density functional theory (DFT), which will be discussed in the following section.

3.2. Density functional theory

DFT is appealing because it provides an effective and reliable approach to accurately and efficiently treat large systems, including transition metal complexes and compounds containing heavy elements. Furthermore, DFT is commonly used to simulate the electronic structure of solid materials. It is based on the model proposed by L. H. Thomas [98] and E. Fermi [99], who demonstrated that the electronic properties of a system can be derived from its electronic density. Such a density, $\rho(\mathbf{r})$, may be calculated using only three spatial variables, regardless of the number of electrons (*N*).

The Hohenberg-Kohn theorem[100] is pivotal to the density functional theory. This theorem shows that the electron density $\rho(\mathbf{r})$ is the only determinant of the external potential V_{ext} in a ground state system. The ground state energy is expressed uniquely as a function of electron density:

(Eq. 17)

$$E_0[\rho_0] = T[\rho_0] + E_{\mathrm{ee}}[\rho_0] + \int \rho_0(\mathbf{r})\, V_{\mathrm{ext}}\, \mathrm{d}\mathbf{r} = F_{\mathrm{HK}}[\rho_0] + \int \rho_0(\mathbf{r})\, V_{\mathrm{ext}}\, \mathrm{d}\mathbf{r}$$

where $E_0[\rho_0]$ represents the system's total energy and serves as a density functional and $F_{HK}[\rho_0]$ is the universal functional that represents the sum of kinetic energy $T[\rho_0]$ and electronic repulsion energy $E_{ee}[\rho_0]$.

The second portion of the theorem explains how the variational principle can be used to calculate the energy of the ground state. This can be expressed mathematically as:

$$\frac{\partial E[\rho(\mathbf{r})]}{\partial \rho(\mathbf{r})} = 0 \qquad \text{(Eq. 18)}$$

In 1965, the Kohn-Sham theorem established a method for determining E_0 as a function of ρ_0. Kohn and Sham[101] propose that each real system can be represented by an imaginary system with independent electrons and the same electron density as the ground state. For the imaginary system, the Kohn-Sham Hamiltonian is written as the following:

$$h_{\mathrm{KS}} = -\frac{1}{2}\nabla_i^2 + V_s(\boldsymbol{r}_i) \qquad \text{(Eq. 19)}$$

where V_s denotes the effective potential imposed on the imaginary system.

The Kohn-Sham equation is defined by applying the Hamiltonian to spin-orbits Φ_i.

$$h_{\mathrm{KS}}\Phi_i = \varepsilon_i\Phi_i \qquad \text{(Eq. 20)}$$

The kinetic energy T_S of the imaginary system can be expressed using the monoelectronic spin-orbits Φ_i and electronic repulsion J in a mean field. The imaginary system and the real system have the same energy; thus, we can write:

$$E_0[\rho_0] = T_s[\rho_0] + J[\rho_0] + E_{\mathrm{eN}}[\rho_0] + E_{\mathrm{xc}}[\rho_0] \qquad \text{(Eq. 21)}$$

where $E_{xc}[\rho_0]$ is the exchange and correlation functional, which contains the difference between the treatment of electronic interactions in a mean field and the instantaneous correlation of electrons in a real system. The exchange term (E_{xc}) comes from Pauli's principle and applies to electrons with the same spin. E_{xc} has no equivalent in classical mechanics. The only approximation to the DFT is the expression of the exchange and correlation functions E_{xc}. This parameter determines the DFT's precision. The expressions of the remaining terms (T_s, J, and E_{eN}) in the ground state are accurate. The Kohn-Sham approach is equivalent to solving the Schrödinger equation for N single-electron orbitals. Electron density is calculated using a set of test orbitals. This is then sent into the

functionals, where the effective potential V_s is calculated, the Kohn-Sham Hamiltonian is defined, and the Schrödinger equation is resolved. This iterative approach continues until a convergence factor is reached.

3.3. Computational methods

The single-electron wave function Φ can be represented as a linear combination of base functions:

$$\Phi_i(\mathbf{r}) = \sum_i^N c_i \chi_i(\mathbf{r}) \quad \text{(Eq. 22)}$$

where c_i are the development coefficients, and $\{\chi_i(\mathbf{r})\}$ is the basis of functions of dimension *N*.

There are generally two sorts of basis:

- localized basis functions that are mostly employed for molecular systems,
- extended basis functions (plane waves) employed for condensed systems, such as crystalline solids, amorphous solids, and liquids.

It is worth noting that these two sets can be merged to characterize core regions (near the nucleus) with atomic orbitals, whilst extended basis are employed for interatomic space.

3.3.1. Periodic Approach

In the case of solid materials, the application of DFT is complicated by the unlimited number of electrons to address, resulting in an endless number of Kohn-Sham functions to solve. This problem can be solved using Bloch's theorems and the plane wave basis.

3.3.1.1. Bloch's theorem and sampling of the reciprocal space

A perfect crystal may always be described using a set of lattice translations **R**. The Bravais lattice consists of points in space related to the lattice's origin by a translation **R**. Bloch's theorem state that if a crystal is exposed to an external potential with the same periodicity as the Bravais network ($V(\mathbf{r}) = V(\mathbf{r}+\mathbf{R})$), the monoelectronic wave function $\Phi_{i,\mathbf{k}}(\mathbf{r})$ will have the following expression:

$$\Phi_{i,\mathbf{k}}(\mathbf{r}) = e^{i\mathbf{k}\cdot\mathbf{r}}\mu_{i,\mathbf{k}}(\mathbf{r}) \quad \text{(Eq. 23)}$$

where the Bloch functions $\mu_{i,\mathbf{k}}(\mathbf{r})$ satisfy the periodicity condition $\mu_{i,\mathbf{k}}(\mathbf{r}) = \mu_{i,\mathbf{k}}(\mathbf{r}+\mathbf{R})$ where **k** is a vector in the reciprocal space.

The periodicity of $\mu_{i,\mathbf{k}}(\mathbf{r})$ allows limiting assessment of the mono-electronic wave functions $\Phi_{i,\mathbf{k}}(\mathbf{r})$ to the vectors **k** of the first Brillouin zone. However, the initial Brillouin zone contains an infinite number of **k**-points. The issue of solving an infinite number of equations is thus replaced by solving a finite number of equations in an unlimited number of **k**-points. But, the Bloch functions $\mu_{i,\mathbf{k}}(\mathbf{r})$ vary slowly between two close **k**-points, so a fair sampling of the initial Brillouin zone suffices to limit the calculation to a finite number of **k**-points. The Monckhorst-Pack grid is the most used method for sampling the reciprocal space.[102] Furthermore, the number of **k**-points required can be lowered if the first Brillouin zone contains symmetry elements.

3.3.1.2. Basis of Plane waves

In reciprocal space, Bloch functions in Eq. 23 can be replaced by its Fourier transform:

$$\Phi_{\mathbf{k}}(\mathbf{r}) = \frac{1}{V} e^{i\mathbf{k}\cdot\mathbf{r}} \sum_{\mathbf{G}} C_{\mathbf{G}}\, e^{i\mathbf{G}\cdot\mathbf{r}} = \frac{1}{V} \sum_{\mathbf{G}} C_{\mathbf{G}+\mathbf{k}}\, e^{i(\mathbf{G}+\mathbf{k})\cdot\mathbf{r}} \qquad \text{(Eq. 24)}$$

where **G** is a set of translations in the reciprocal lattice and V the volume of the unit cell

Eq. 24 is the exact decomposition of the wave function $\Phi_{\mathbf{k}}(\mathbf{r})$ over an infinite base of plane waves. In practice, the basis must be truncated. Large values of $|\mathbf{G}+\mathbf{k}|$ result in relatively small Fourier coefficients $C_{\mathbf{G}+\mathbf{k}}$, allowing only a finite number of plane waves to be considered. When determining basis size, just the energy of truncation or cut-off ($E_{\text{cut-off}}$) should be considered. In fact, monoelectronic wave functions $\Phi_{\mathbf{k}}(\mathbf{r})$ consist of plane waves with lower kinetic energy than the cutoff energy. This can be expressed following the equation 25:

$$\frac{h^2}{4\pi m} \|\mathbf{k}+\mathbf{G}\|^2 < E_{\text{cut-off}} \qquad \text{(Eq. 25)}$$

where *m* is the electron's mass.

As the cutoff energy increases, so does the number of plane waves, resulting in a more accurate representation of electron density and a more reliable estimate. The downside is that when the cutoff energy increases, so does the calculation time.

3.3.1.3. Pseudopotentials Approach

The computational strategies ($E_{\text{cut-off}}$, **k**-point grid) previously stated for using the DFT formalism may not be sufficient to reduce calculation time. Indeed, electronic wave functions vary greatly near the cores, requiring a high number of plane waves to accurately describe this core region. The pseudopotential technique simplifies this by assuming that core electrons do not participate in chemical bonding and can be considered as frozen. The computation is simplified since the Kohn-Sham equations are only solved for the valence electrons, while the core states are substituted by a V^{PP} pseudopotential. The Kohn-Sham equation is redesigned by the following equation:

$$\left\{-\frac{1}{2}\nabla_i^2 + V^{\mathrm{PP}}(\mathbf{r})\right\}\widetilde{\Phi_l}(\mathbf{r}) = \varepsilon_i\widetilde{\Phi_l}(\mathbf{r}) \qquad \text{(Eq. 26)}$$

where V^{PP} represents the pseudo-potential, while $\widetilde{\Phi_l}(\mathbf{r})$ represents the pseudo monoelectronic wave function of valence.

The pseudo-potential should yield pseudo-wave functions $\widetilde{\Phi_l}(\mathbf{r})$ that are identical to real wave functions Φ_i in the valence areas and more linear in the core regions. If these limitations are followed, a plane wave base can effectively address this problem. A pseudopotential is referred to as soft when used with a small basis of plane waves and hard when used with an expanded base.

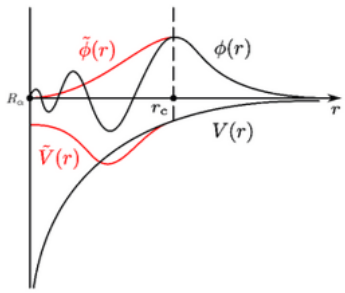

Figure 13: *A schematic illustration of the pseudo potential in the core region of an atom at position* ***R*** *and cutoff radius* $\mathbf{r_c}$*. The black lines represent the exact all-electron wave function and potential. The red lines* $\widetilde{\Phi}(\mathbf{r})$ *and* $\tilde{V}(\mathbf{r})$ *represent the pseudo wavefun.*[103]

3.3.1.4. PAW Method

Blöchl's PAW method combines the basic ideas of pseudopotentials and linearized augmented plane wave (LAPW) methods.[104] It is effective to calculate efg in both solids and molecules.[105] PAW utilizes ultra-soft pseudopotentials, which significantly save CPU time. The PAW approach represents the single-electron wave function $\Phi_{i,\mathbf{k}}(\mathbf{r})$ using a basis of pseudo-wave functions $\widetilde{\Phi_l}$ inside spheres Ω_i called "augmentation areas" and a basis of plane waves outside these spheres. A linear transformation operator (Γ) is used to convert wave functions into pseudo-wave functions, which are more computationally efficient.

$$|\Phi_i> = \Gamma \left|\widetilde{\Phi_l}\right> \qquad \text{(Eq. 27)}$$

Outside augmentation areas Ω_i, the linear operator is defined as the unit operator, as the mono-electronic wave functions Φ_i and pseudo-wave functions $\widetilde{\Phi_l}$ are identical in pairs. Inside the augmentation spheres, the pseudo-wave functions $\widetilde{\Phi_l}$ are simplified and the linear operator is expressed as a sum of local operators Γ_{Ω_i}. This yields the following equation:

$$\Gamma = 1 + \sum_i \Gamma_{\Omega_i} \qquad \text{(Eq. 28)}$$

The combination of equations 27 and 28 lead to

$$|\Phi_i> = \left(1 + \sum_i \Gamma_{\Omega_i}\right) |\widetilde{\Phi_l}> \qquad \text{(Eq. 29)}$$

Inside augmentation spheres, $|\widetilde{\Phi}>_{\Omega_i}$ can be developed on a basis of partial pseudo-waves $|\tilde{\chi}>_{\Omega_i}$. We then have:

$$|\widetilde{\Phi_l}>_{\Omega_i} = \sum_i |\tilde{\chi}_l>_{\Omega_i} c_i \qquad \text{(Eq. 30)}$$

Applying the linear operator Γ to the partial pseudo-waves $\left|\tilde{\chi}_l\right>$, we obtain the partial waves $\left|\chi_i\right>$ and extend the wave function Φ. Equation 31 defines the following transformation:

$$|\Phi>_{\Omega_i} = \sum_i |\chi>_{\Omega_i} c_i \qquad \text{(Eq. 31)}$$

Since the operator Γ is linear, the coefficients are linear functions as defined in equation 32:

$$c_i = \langle \tilde{p}_l | \widetilde{\Phi}_l \rangle \quad \text{(Eq. 32)}$$

The $\tilde{p}_l$ are projectors, with a projector function for each pseudo-partial wave $|\tilde{\chi}_l>$

We now obtain the expression for the real single-electron wave function $|\Phi>$ based on $|\widetilde{\Phi}\rangle$, $|\chi_i>$, and $|\tilde{\chi}_l>$

$$|\Phi_i> = |\widetilde{\Phi}_l> - \sum_i |\tilde{\chi}_l> c_i + \sum_i |\chi_i> c_i \quad \text{(Eq. 33)}$$

The final equation 33 is typical of the PAW approach. In the PAW spheres, the single-electron wave function Φ_i equals the pseudo-wave function $\widetilde{\Phi}_l$ with a local PAW correction. Figure 14 depicts a schematic of the PAW approach.

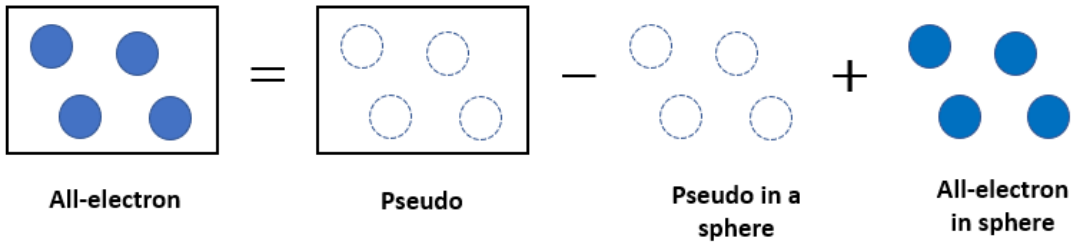

Figure 14: *An illustration of PAW method. The pseudo plane wave grid is represented in the entire space. The pseudo wave functions are reconstructed inside spheres and the corresponding one-center terms are subtracted. Finally, the all-electron wave functions are reconstructed and the corresponding one-center energies are added.* [103]

3.3.1.5. Code VASP

In this study, we used the VASP (Vienna Ab initio Simulation Package) computation code, developed at the University of Vienna by G. Kresse, J. Furthmuller, and J. Hafner.[106,107] Several density functionals can be employed in the VASP code, including the exchange and correlation functions of Perdew and Wang (PW91), Ceperley and Alder (CA)[108], and Vosko-Wilk-Nusair (VWN). For our calculations, we employed Perdew-Burke-Ernzerhoff's (PBE) GGA type functional. The code is organized around plane waves and pseudopotentials.

VASP is a popular software for calculating NMR parameters because it uses the PAW approach to reconstruct the all-electron response. This approach avoids the frozen-core approximation, which means that core electrons, typically treated as immobile and non-

interacting in most calculations, are here part of the system's dynamics, allowing their interactions with both nuclei and valence electrons to be considered. The Schrödinger equation is solved for a discrete number of **k**-points generated using the Monkhorst-Pack approach. The occupied states can be integrated using the tetrahedron approach.[109] The Davidson-Block approach solves the Kohn-Sham equations using iterative matrix diagonalization.[110] Charge density is updated using the Broyden-Pulay method during self-consistent iterations.[111,112] Therefore, the iterative process of self-consistent field (SCF) calculations used to identify the ground state of an electronic system works as follows: it begins with an initial estimate of the electron density ρ_{in} and associated wave functions. A new electron density, ρ_{out}, is then derived by constructing and diagonalizing the density-based Hamiltonian, which will lead to new electron occupations and energies. This new electron density is then combined with the previous estimate to help stabilize the process and promote convergence. Finally, convergence tests are carried out to ensure that the requirements are met, and once it is achieved, the ground state of the system is identified using the optimal electrical density and total energy.

3.3.2. Molecular Approach

Gaussian and Amsterdam Density Functional (ADF) are quantum chemistry packages designed to solve the Schrödinger equation and describe the electronic structure of molecules, as well as their properties and reactivity. These programs are based on the representation of a molecular wave function, which describes the quantum behavior of electrons within a molecule. This wave function is built with atomic orbitals (AOs) as fundamental building components. AOs are mathematical functions centered on atoms that describe the most probable locations of electrons. These atomic orbitals are combined to form molecular orbitals (MOs), which represent the distribution of electrons across the molecule, providing extensive information about chemical bonding and reactivity.

Two common mathematical functions are used to describe the atomic orbitals that form the wave function when using the molecular approach: Slater-type orbitals (STOs) and Gaussian-type orbitals (GTOs). STOs are suitable for representing hydrogen-like atomic orbitals but are difficult to integrate for molecules containing more than two atoms. In contrast, GTOs approximate the radial part decaying with increasing distance from the nucleus as Gaussian function ($e^{-\alpha r^2}$) where α determines the width of the function. Larger

α values result in more localized orbitals, while lower values result in more diffuse orbitals. Initially, atomic orbitals were represented by a sufficient number of basis functions to describe all the electrons in the neutral atom. Then all the basis functions were multiplied by two, three, etc… to form a double or triple zeta basis set (DZ and TZ). An extended database increases the precision of the results but also significantly increasing computational cost.

4. Solid-state NMR for molybdenum-based catalysts

4.1. NMR properties of NMR-active Mo isotopes

Molybdenum element is a transition metal occupying the group 6 in the periodic table and having an electronic structure of [Kr] $5s^1$ $4d^5$. In molecular complexes, mainly the olefin's metathesis catalysts, Mo has a high oxidation state of +VI, which is diamagnetic. The isotopes-95 and 97 of molybdenum are spin-5/2 quadrupolar nuclei, which can be observed by NMR spectroscopy (Table 2). Observation is generally done through ^{95}Mo isotope because it is more abundant (15.9%) than ^{97}Mo (9.6%) and gives narrower resonances because of its smaller electric quadrupolar moment, *Q*.

Table 2: *NMR properties of NMR-active Mo isotopes.*

Isotope	Spin	Natural Abundance (%)	Gyromagnetic Ratio (10^7 rad s^{-1} T^{-1})	Measured Frequency (Ref. ^{1}H = 800 MHz)	Measured Frequency (Ref. ^{1}H = 1200 MHz)
^{1}H	1/2	99.98	26.75	800	1200
^{95}Mo	5/2	15.9	−1.7514	−52.6	−78.9
^{97}Mo	5/2	9.6	−1.7884	−36.2	−54.3

4.2. State-of-the-art of ^{95}Mo solid-state NMR experiments

The activity of many Mo-containing catalysts is dependent on the molybdenum local environment, which can be probed by ^{95}Mo NMR. This information is crucial to optimize the catalytic performance in a rational way. Solid-state ^{95}Mo NMR was employed over different types of crystalline materials with a well-defined symmetry such as ionic

conductors, salts and phosphomolybdates.[113–115] It is also applicable for the characterization of amorphous complexes such as glass and disordered oxides.[116,117]

For instance, solid-state ^{95}Mo MAS NMR was applied to probe the local coordination environment of molybdenum species in ion conducting glasses.[118] In the AgI-Ag_2O-MoO_2 glass system, ^{95}Mo NMR distinguishes between tetrahedral monomeric MoO_4^{2-}units and more complicated polymeric molybdate species comprising octahedrally coordinated molybdenum. ^{95}Mo NMR spectra of glasses with a 1:1 Ag_2O/MoO_3 molar ratio exhibits a single and strong resonance near 70 ppm, similar to isolated MoO_4 tetrahedra, whereas samples with an excess of MoO_3 showed a broad resonance near −100 ppm, indicating disordered MoO_6 octahedra with polymeric or chain-like structural motifs. These findings demonstrate the sensitivity of ^{95}Mo NMR to coordination number and local symmetry. Yasui *et al.* group also used ^{95}Mo NMR to identify hidden chemical ordering in complicated oxide-ion conductors like $Ba_7Nb_4MoO_{20}{\cdot}0.15H_2O$.[119] Conventional diffraction techniques cannot discriminate between Mo^{6+} and Nb^{5+} cations in this material due to similar X-ray scattering factors and neutron scattering lengths. However, ^{95}Mo NMR gave direct spectroscopic evidence for the selective occupation of Mo atoms at the M2 site near the ion-conducting c' layer, demonstrating a high degree of chemical order in what was previously considered to be completely disordered. The ^{95}Mo MAS NMR spectra showed a single resonance, confirming the presence of Mo in a single crystallographic environment. This is compatible with DFT calculations and resonant X-ray diffraction data.

Mo sites in Mo-modified HZSM-5 zeolites used for methane dehydroaromatization (MDA) were also characterized using ultrahigh-field ^{95}Mo NMR spectroscopy.[120] To improve the sensitivity, Mo/HZSM-5 catalyst was isotopically enriched in ^{95}Mo isotope using crystalline $^{95}MoO_3$ as a precursor. One-dimensional ^{95}Mo Hahn-echo spectra of four catalysts with different molybdenum loadings were recorded at 21.1 T. These spectra revealed not only the presence of MoO_3 crystallites but also Mo atoms attached to the zeolite framework through the exchange with protons of Brønsted acid site. The latter species, referred to as exchanged Mo, are the active sites catalyzing the MDA reaction. In the course of this reaction, the exchanged species were converted into molybdenum carbides.

In 2012, Cuny *et al*. applied the ^{95}Mo solid-state NMR as a specific method to investigate molybdenum cluster compounds.[121] To improve the resolution and the sensitivity, the ^{95}Mo

NMR spectra were recorded at high magnetic fields (up to 19.6 T) under MAS conditions using QCPMG detection. The octahedral cluster compound $Cs_2Mo_6Br_{14}$, which contains a single crystallographic Mo site, exhibits an NMR signal with an isotropic chemical shift δ_{iso} = 3166 ppm and a quadrupolar coupling constant C_Q = 4.7 MHz. For the octahedral cluster $(Bu_4N)_2Mo_6Br_{14}$, δ_{iso} shifts and C_Q values of three ^{95}Mo sites range from 3204 to 3218 ppm and from 5.15 to 5.60 MHz, respectively. This variation in NMR parameters originates from different Mo–Br distances in the cluster. Furthermore, for this cluster, counter cation with larger size leads to smaller Mo–Br distances, which results in lower values of C_Q value. This direct relationship between the quadrupolar coupling constant and the Mo–ligand bond length was confirmed by the study of other clusters, such as $Mo_3S_7Cl_4$. DFT computations with periodic boundary conditions utilizing the PAW and GIPAW methods provided additional support for the analysis. GIPAW model showed a robustness towards large chemical shift range for all the molybdenum octahedral cluster compounds studied. It also evidenced another trend: the lower the oxidation degree of Mo element, the higher the isotropic chemical shift. The good agreement between experimental and theoretical results highlighted the complimentary role of ^{95}Mo solid-state NMR and computational modeling in elucidating the structure of molybdenum-based materials.

Advances in ^{95}Mo solid-state NMR techniques have made this technology a strong tool for investigating the structural and electronical properties of molybdenum-containing materials. From comprehensive research on Mo/HZSM-5 to complex molybdenum clusters, ^{95}Mo NMR has proven useful in illuminating local surroundings and capturing small structural distortions. These qualities are especially important in the context of supported molybdenum-based catalysts, where molybdenum sites frequently exhibit complex coordination geometries and dynamic alterations under catalytic conditions.

4.3. Insights from ^{95}Mo NMR on Supported Molybdenum-Based Catalysts

In addition to conventional ^{1}H, ^{13}C or ^{15}N NMR, solid-state ^{95}Mo NMR can offer valuable information on the local structure and active sites of supported catalysts. However, the low receptivity of this isotope poses a challenge for the characterization of these catalysts containing low amounts of Mo element. Therefore, acquiring high-quality

spectra with sufficient resolution and sensitivity requires advanced techniques and equipment, such as high-field NMR instruments and sophisticated pulse sequences.

In 1990, J. C. Edwards *et al.* first studied the supported polyoxomolybdates onto γ-alumina.[122] These compounds create distinct oxomolybdenum surface species that serve as precursors to the catalytically active sulfide phase, resulting in active HDS catalysts. When adsorbed at monolayer coverage, these polyoxomolybdates form different molybdenum environments, particularly distorted octahedral and tetrahedral geometries, which are required for successful sulfur removal. Solid-state ^{95}Mo NMR investigations show that the nature of the polyoxomolybdate species and their interaction with the alumina surface can be controlled by parameters such as pH during impregnation and subsequent calcination. Grafting stabilizes molybdenum species, preventing agglomeration into inactive bulk MoO_3 and promoting their transformation into polymeric oxomolybdenum structures with great dispersion. However, sulfidation increases the distribution of catalytically active MoS_2-like phases, enhancing HDS activity and selectivity of the catalyst. Another study by d'Espinose de Lacaillerie *et al.* showed that solid-state ^{95}Mo MAS NMR is an effective method for studying the local environment of molybdenum species grafted onto γ-alumina.[123] They found that ^{95}Mo NMR spectra of these catalysts show unique resonances associated with tetrahedral and distorted octahedral molybdenum environments, strongly connected to polymeric or monomeric molybdate surface species. Tetrahedral Mo sites normally produce signals between +100 and −50 ppm, while distorted octahedral Mo species are detected at lower fields, usually between −100 and −200 ppm. These chemical shifts and line morphologies depend on molybdenum coordination and interactions with the alumina surface.

A first attempt on supported molybdenum-based catalysts for olefins metathesis was made and published by the group of C. Coperet.[124] High-field DFS-QCPMG experiments at 14.1 T and 28.2 T, in combination with fast MAS rates of up to 50 kHz, have enabled the observation of distinct ^{95}Mo sites, each characterized by specific isotropic chemical shifts and quadrupolar coupling constants. The experiments were carried out at 100 K, which improves sensitivity, especially by enhancing the equilibrium magnetization and reducing the dynamics, leading to the observation of a larger number of echoes in QCPMG experiment. They observed a dominance of signal with δ_{iso} = −95 ppm and C_Q = 3.3 MHz for

catalysts prepared by surface-organometallic chemistry (SOMC). This signal was assigned to low-coordinate strained tetrahedral Mo dioxo sites, which have high reducibility and catalytic activity. A second site with δ_{iso} = −126 ppm and C_Q = 4 MHz were assigned to relaxed tetrahedral sites coordinated to one or two siloxane moieties. Third and fourth sites with {δ_{iso}, C_Q} = {−135 ppm, 6.1 MHz} and {−47 ppm, 7.3 MHz} corresponds to higher coordination of Mo sites and thus to aggregated or polymeric species, especially in the case of catalysts prepared by incipient-wetness-impregnation with high molybdenum loadings. The deshielded signals in the −80 to −100 ppm range corresponding to highly reactive Mo sites are more intense for SOMC-prepared catalysts. The signal assignment in this study was mainly based on DFT calculation of molecular complexes. Nevertheless, the experimental data for supported Mo catalysts are still limited and the relationship between ^{95}Mo NMR parameters and the local environment of that metal is still yet not fully understood.

High-field ^{95}Mo solid-state NMR spectroscopy has also been employed recently to study MoS_2 supported on alumina support.[125] This material catalyzes heterogeneous hydrodesulfurization (HDS) reaction at oil refineries. The ^{95}Mo NMR data of MoS_2/Al_2O_3 were compared to those of other MoS_2 nanostructures, including an exfoliated sample with 160 layers, a sample with 4 layers and a pseudo-amorphous sample. Sensitivity and resolution were improved by performing experiments at high magnetic fields up to 35.2 T. This study found that the use of higher magnetic fields greatly reduces T_1. The 160-layer sample had T_1 values of 10.9 s at 19.6 T and 2.8 s at 35.2 T. This reduction was due to relaxation caused by chemical shift anisotropy (CSA) and delocalized band-gap electrons in the MoS_2 lattice. At 35.2 T, Jakobsen *et al*. found a 60-fold increase in sensitivity for the 160-layer sample compared to 14.1 T, allowing high-resolution spectra to be obtained in hours rather than days. This sensitivity gain allowed for the first observation of ^{95}Mo local environment in MoS_2/Al_2O_3 catalyst, in spite of the low amount of molybdenum in this material. On the contrary, the 4-layer sample showed significant spectrum broadening and intensity loss at higher fields. This effect was attributed to greater isotropic chemical shift distribution, flaws, and edge-site contributions in thinner layers. The study emphasizes ^{95}Mo NMR at ultrahigh fields as a transformational technique for analyzing MoS_2 nanostructures. It provides exceptional sensitivity, faster data collecting, and the capacity

to characterize local structural and electronic environments in both multilayered and catalytic systems. In conclusion, the NMR study of ^{95}Mo for most heterogeneous catalysts (i.e., supported complexes), not only for olefin metathesis, seems difficult, but high fields and well-optimized pulse sequences can be instrumental to observe this isotope with low receptivity and provide insight into the local structure around the molybdenum center.

5. Overview of solid-state NMR for the amorphous silica alumina catalysts

5.1. NMR properties of ^{29}Si and ^{27}Al isotopes

In aluminosilicates, the nuclei of importance are ^{1}H (I = 1/2, natural abundance 99.98%), ^{27}Al (I = 5/2, natural abundance 100%, Q = 14.66×10^{-30} m^2) with a gyromagnetic ratio of $\gamma(^{27}\text{Al})/\gamma(^{1}\text{H}) \approx 0.26$, and ^{29}Si ($I$ = 1/2, natural abundance 4.7%) with a gyromagnetic ratio of $\gamma(^{29}\text{Si})/\gamma(^{1}\text{H}) \approx 0.2$. The first two isotopes are relatively easy to detect, whereas the latter has a lower receptivity.

^{27}Al isotropic chemical shifts provide valuable information about the Al coordination numbers, allowing to distinguish the signals of AlO_4, AlO_5 and AlO_6 local environments. The central transition of ^{27}Al nuclei is broadened by second-order quadrupole interaction. As a result, ^{27}Al NMR signals can be rather large, and some of them, subject to very large efg, may be invisible. This broadening is inversely proportional to the field strength, leading to narrower CTs at high field.

Acquiring ^{29}Si MAS NMR spectra is challenging due to the low natural abundance of this isotope. Therefore, ^{29}Si NMR experiments require longer acquisition times to achieve good signal-to-noise ratio compared to high-abundance spin-1/2 nuclei, such as ^{1}H and ^{27}Al. Furthermore, ^{29}Si nuclei often exhibits long longitudinal relaxation times, which further reduces the sensitivity. The ^{29}Si isotropic chemical shift in ASA provides information on the second neighbors of silicon atoms, allowing to distinguish the different Q^n units [$Si(OX)_n(OH)_{4-n}$ with X = Si or Al].

5.2. State-of-the-art of solid-state NMR of ASA

In the ^{27}Al spectra of most of the ASA, three major peaks appear at 60, 30 and 0 ppm. The peak at 60 ppm is assigned to tetra-coordinated (AlO_4) aluminum and that at 30 ppm is associated to penta-coordinated alumina (AlO_5) of ASA. De Witte *et al*. found AlO_5 environment at the interface of the alumina and silica-alumina phases in ASA prepared by sol-gel procedure.[126] Conversely, in ASA generated by flame spray pyrolysis, no alumina phase was detected and Al^V sites were found to be accessible to guest molecules and hence, to be dispersed on the surface of ASA.[127] Furthermore, Al^V has been demonstrated to contribute to the Brønsted acidity of ASA through 2D *D*-HMQC NMR experiments.[70] The octahedral aluminum (AlO_6) resonance showed around 0 ppm is often associated with transitional alumina domains or polymeric forms of Al, as it is the dominant coordination in many transitional aluminas.[128] This is why octahedral Al is also known as "extra-framework Al". Although this assumption is largely accurate for alumina-rich ASA, octahedral Al in silica-rich ASA has been found to transform partially or completely to tetrahedral Al upon NH_3 adsorption.[129,130] The alterations in coordination of octahedral Al when exposed to ammonia reveal that these Al are still linked to the aluminosilicate framework. In particular, Omegna *et al*.[129] determined that the flexible coordination is limited to the aluminum atoms that are part of an amorphous silica alumina character, as there is no change in Al coordination following adsorption of NH_3 for γ-alumina.

In aluminosilicates, the silicon sites can be either fully or partially coordinated. The most important active sites are silanol sites. These sites, called Q^3 sites, correspond to silicon atoms connected to three other silicon atoms by oxygen bridges, with the fourth oxygen bonded to a hydroxyl group. They resonate around –95 ppm.[131] Some silanol groups are located near aluminum atoms, but their hydroxyl oxygen are usually not covalently bonded to aluminum (SiOH···Al). These sites are referred to as pseudo-bridging silanols (PBS).[68,132,133] The aluminum atom stabilizes the silanolate anion and hence, increases their Brønsted acidity, which remains lower than that of bridging silanols SiOHAl found in zeolites, in which there is a covalent bond between the oxygen atom of the silanol group and the aluminum atoms. PBS sites have been observed by solid-state NMR experiments probing proximities between ^1H and ^{27}Al and measuring ^1H-^{17}O distances.[70,134,135] In particular, 2D ^1H-^{27}Al heteronuclear correlation demonstrated that PBS associated to both

AlO_4 or AlO_5 sites can act as acid sites and are able to protonate ammonia.[70] Nevertheless, ASA can contain stronger Brønsted acid sites than PBS, which can catalyze propane cracking and H/D exchange. The presence of these strong acid sites was initially evidenced by infrared spectroscopy using probe molecules.[136,137] NMR experiments probing ^{1}H-^{27}Al proximities demonstrated that these strong acid sites are SiOHAl BASs similar to those found in zeolites.[138,139] 2D ^{27}Al-{^{1}H} *D*-HMQC experiments at 35.2 T showed that these BASs in ASA are based both on AlO_4 and AlO_5 sites, contrary to zeolites, in which the BASs are always covalently bonded to AlO_4 moieties.

In addition to the Q^3 sites, ASA contains Q^4 silicon sites, in which silicon atoms are bound to four bridging oxygen atoms ($Si(OSi)_4$) that connect to neighboring silicon or aluminum atoms. These fully linked tetrahedral structures are common in highly polymerized silicate networks and often exhibit isotropic chemical shifts of −100 ppm.[131]

Protons can usually be easily detected by NMR owing to their high natural abundance and high gyromagnetic ratio. In aluminosilicates, ^{1}H NMR spectra allow distinguishing the different types of hydroxyl groups, such as PBS or BAS, based on their isotropic chemical shifts. For instance, protons resonate at 4.2-4.6 ppm in BAS instead of 1.9 ppm in PBS.[138,140] Furthermore, quantitative ^{1}H NMR spectra allows measuring the relative amounts of the different hydrogen environments. Nevertheless, a limitation is often the lack of resolution of 1D ^{1}H NMR spectra, owing to the ^{1}H-^{1}H dipolar interactions, the limited range of ^{1}H isotropic chemical shifts and the amorphous structure of ASAs.

5.3. State-of-the-art of NMR under light irradiation

The use of light irradiation in solid-state NMR has improved greatly over the years, owing mostly to the necessity to investigate photon-induced reactions in materials. The first studies, initiated in 1997 by D. Raftery *et al.*, introduced a home-built setup to perform in situ photo-irradiation MAS NMR on photocatalytic materials.[141,142] Their system employed a quartz rod to direct light through a 10 mm gap in the rf coil and into a 5 mm glass sample tube. However, this device required a bespoke rf coil and was limited to MAS spinning rates below 2.7 kHz. In 2004, M. Hunger *et al*. developed a more advanced configuration by modifying a 7 mm Bruker MAS probe.[143] This design allowed light irradiation during in situ NMR under MAS conditions on continuous flow reaction by

integrating an injection mechanism into the rotor and replacing its bottom with a quartz window that allowed light delivery via a fiber optic cable. This innovation improved the control and accessibility for monitoring reactions under photo-irradiation.

Over time, in situ irradiation setups gradually evolved, allowing light to be introduced either from the rotor walls or from the rotor cap, depending on the experimental requirements. In the following decades, interest in photo-irradiation MAS NMR expanded, notably for studying the light-responsive activity of photoreceptor proteins. Many groups created home-built devices that directed light through the MAS stator, perpendicular to the rotor, to illuminate the rotor walls. Thin-walled zirconia rotors[144] or specially developed transparent rotors were utilized to ensure adequate light penetration.[145,146,147] In parallel, the methodology was expanded to include photo-chemically induced dynamic nuclear polarization (photo-CIDNP), a hyperpolarization method based on spin-correlated radical pair production.[148] This method dramatically improved NMR sensitivity under light irradiation and was used in several experiments with DNP MAS probes. Light was frequently transmitted through microwave waveguides onto the sides of clear sapphire rotors spinning at 8 kHz. De Biasi *et al*. demonstrated that high-field photo-CIDNP may induce bulk hyperpolarization of protons in materials employing a donor-chromophore-acceptor (D-C-A) polarizing agent (PhotoPol-S) under 450 nm laser irradiation.[149] By tuning the electron-electron interaction in the excited state to match the proton Larmor frequency, enhancements of nearly two orders of magnitude were achieved in MAS experiments at 9.4 and 21.1 T.

Since 2011, the group of A. Naito *et al*., has also developed instrumentations for in situ photo-irradiation under MAS, using fiber optics to illuminate materials from within the spinning rotor.[150,151] Their setup involved gluing a tapered glass rod to the end cap of a 4 mm Varian pencil rotor, with the narrow end extending into the sample chamber. Light was then coupled directly into the rod via a fiber optic connection. This design supported MAS frequencies up to 4 kHz and allowed for the analysis of dynamic photo-induced processes such as photopolymerization and photoreceptor activity.

A very recent study made by Thomas J. N. Hooper *et al*., introduced a new, low-cost in situ photo-irradiation MAS NMR system capable of achieving consistent MAS frequencies of up to 15 kHz while exposing samples to UV light.[152] The main innovation was replacing the

rotor's end cap with a tapered quartz glass rod, which increased light dispersion within the sample. This technique eliminates the need for specific rotors or complex coil modifications, making it easier to install and more flexible in terms of light source alternatives. To assess and analyze the configuration, the polymerization of n-butyl acrylate (nBA) initiated by UV light was selected for the experiment. High-resolution magic angle spinning NMR spectra displayed prominent signals for both monomer and polymer components, facilitating an in-depth monitoring of the reaction's progress.

Exploring non-crystalline aluminosilicates deepens our understanding of their acid and structural features which determine their usefulness in many chemical reactions. However, the interaction of ASA with external stimuli such as light irradiation remains unexplored. This is particularly significant for ASAs loaded with gold nanoparticles, which are known for their unique plasmonic properties when exposed to light. Our research aims to bridge these two fields: by applying solid-state NMR to gold-loaded ASA under light irradiation, we aim to understand how plasmonic effects influence catalytic activity and the NMR parameters of Brønsted acid sites. This approach will provide insights on the dynamic behavior of these materials under photonic activation.

6. References

(1) *Technology Vision 2020. The U.S. Chemical Industry*; EERE Publication and Product Library, Washington, D.C. (United States), **1996**. https://www.osti.gov/biblio/1218627 (accessed 2024-06-24).

(2) Cheng, S. From Layer Compounds to Catalytic Materials. *Catal. Today* **1999**, *49* (1), 303–312. https://doi.org/10.1016/S0920-5861(98)00437-4.

(3) Flanigen, E. M.; Lok, B. M.; Patton, R. L.; Wilson, S. T. Aluminophosphate Molecular Sieves and the Periodic Table. Elsevier, **1986**; Vol. 28, pp 103–112. https://doi.org/10.1016/S0167-2991(09)60862-4.

(4) Wu, C.-D. Crystal Engineering of Metal-Organic Frameworks for Heterogeneous Catalysis. In *Selective Nanocatalysts and Nanoscience*; John Wiley & Sons, Ltd, **2011**; pp 271–298. https://doi.org/10.1002/9783527635689.ch8.

(5) Fechete, I.; Wang, Y.; Védrine, J. C. The Past, Present and Future of Heterogeneous Catalysis. *Catal. Today* **2012**, *189* (1), 2–27. https://doi.org/10.1016/j.cattod.2012.04.003.

(6) Hoelderich, W. F. Zeolites: Catalysts for The Synthesis of Organic Compounds. In *Studies in Surface Science and Catalysis*; Jacobs, P. A., van Santen, R. A., Eds.; Zeolites: Facts, Figures, Future Part A - Proceedings of the 8th International Zeolite Conference; Elsevier, **1989**; Vol. 49, pp 69–93. https://doi.org/10.1016/S0167-2991(08)61709-7.

(7) Mizuno, N.; Misono, M. Heterogeneous Catalysis. *Chem. Rev.* **1998**, *98* (1), 199–218. https://doi.org/10.1021/cr960401q.

(8) Ishihara, A.; Mochizuki, H.; Lee, J.; Qian, E. W.; Kabe, T.; Tatsumi, Y.; Umehara, K. Development of Hydrodesulfurization Catalysts Using Molybdenum Complex with Molybdenum-Sulfur Bonds (Part 1) Effect of Activation Method on Catalytic Activity. *J. Jpn. Pet. Inst.* **2005**, *48* (3), 137–144. https://doi.org/10.1627/jpi.48.137.

(9) Luo, N.; Yang, W.; Feng, L.; Huang, S.; Huang, P.; Wei, M. Recent Advances in Utilizing Molybdenum and Tungsten Carbides for Fischer-Tropsch Synthesis. *Mol. Catal.* **2024**, *553*, 113683. https://doi.org/10.1016/j.mcat.2023.113683.

(10) Qian, X.; Fang, J.; Xia, J.; He, G.; Chen, H. Recent Progress and Perspective on Molybdenum-Based Electrocatalysts for Water Electrolysis. *Int. J. Hydrog. Energy* **2023**, *48* (67), 26084–26106. https://doi.org/10.1016/j.ijhydene.2023.03.228.

(11) Wang, Q.; Guo, J.; Chen, P. Complex Transition Metal Hydrides for Heterogeneous Catalysis. *Chem Catal.* **2023**, *3* (3), 100524. https://doi.org/10.1016/j.checat.2023.100524.

(12) Mehdad, A.; Jentoft, R. E.; Jentoft, F. C. Highly Selective Molybdenum-Based Catalysts for Ring Hydrogenation and Contraction. *Appl. Catal. Gen.* **2019**, *569*, 45–56. https://doi.org/10.1016/j.apcata.2018.10.012.

(13) Szymańska, A.; Nitek, W.; Oszajca, M.; Łasocha, W.; Pamin, K.; Połtowicz, J. Molybdenum Complexes as Catalysts for the Oxidation of Cycloalkanes with Molecular Oxygen. *Catal. Lett.* **2016**, *146* (5), 998–1010. https://doi.org/10.1007/s10562-016-1716-7.

(14) Travert, A.; Dujardin, C.; Maugé, F.; Veilly, E.; Cristol, S.; Paul, J.-F.; Payen, E. CO Adsorption on CoMo and NiMo Sulfide Catalysts: A Combined IR and DFT Study. *J. Phys. Chem. B* **2006**, *110* (3), 1261–1270. https://doi.org/10.1021/jp0536549.

(15) Qian, S.; Dai, T.; Feng, K.; Li, Z.; Sun, X.; Chen, Y.; Nie, K.; Yan, B.; Cheng, Y. Design Principle of Molybdenum-Based Metal Nitrides for Lattice Nitrogen-Mediated Ammonia Production. *JACS Au* **2024**, *4* (5), 1975–1985. https://doi.org/10.1021/jacsau.4c00194.

(16) Levy, R. B.; Boudart, M. Platinum-Like Behavior of Tungsten Carbide in Surface Catalysis. *Science* **1973**, *181* (4099), 547–549. https://doi.org/10.1126/science.181.4099.547.
(17) Ma, Y.; Guan, G.; Hao, X.; Cao, J.; Abudula, A. Molybdenum Carbide as Alternative Catalyst for Hydrogen Production – A Review. *Renew. Sustain. Energy Rev.* **2017**, *75*, 1101–1129. https://doi.org/10.1016/j.rser.2016.11.092.
(18) Amigues, P.; Chauvin, Y.; Commereuc, D.; Hong, C. T.; Lai, C. C.; Liu, Y. H. Methathesis of Ethylene-Butene Mixtures to Propylene with Rhenium on Alumina Catalysts. *J. Mol. Catal.* **1991**, *65* (1), 39–50. https://doi.org/10.1016/0304-5102(91)85080-L.
(19) *Rhenium Price - Historical Prices - 2025 Forecast - How to Buy*. https://strategicmetalsinvest.com/rhenium-prices/ (accessed 2025-07-14).
(20) *Molybdenum Price*. https://www.dailymetalprice.com/molybdenum.html?#google_vignette (accessed 2025-07-14).
(21) *Today's Ruthenium Price - Historical Charts - Price Forecast*. Strategic Metals Invest. https://strategicmetalsinvest.com/ruthenium-prices/ (accessed 2025-07-14).
(22) Mike. *Tungsten (APT) price index*. businessanalytiq. https://businessanalytiq.com/procurementanalytics/index/tungsten-price-index/ (accessed 2024-06-26).
(23) Grubbs, R. H. Introduction. In *Handbook of Metathesis*; John Wiley & Sons, Ltd, **2003**; pp 1–3. https://doi.org/10.1002/9783527619481.ch1.
(24) Natta, G.; Dall'Asta, G.; Mazzanti, G. Stereospecific Homopolymerization of Cyclopentene. *Angew. Chem. Int. Ed. Engl.* **1964**, *3* (11), 723–729. https://doi.org/10.1002/anie.196407231.
(25) Schrock, R. R.; Murdzek, J. S.; Bazan, G. C.; Robbins, J.; DiMare, M.; O'Regan, M. Synthesis of Molybdenum Imido Alkylidene Complexes and Some Reactions Involving Acyclic Olefins. *J. Am. Chem. Soc.* **1990**, *112* (10), 3875–3886. https://doi.org/10.1021/ja00166a023.
(26) Astruc, D. The Metathesis Reactions: From a Historical Perspective to Recent Developments. *New J. Chem.* **2005**, *29* (1), 42–56. https://doi.org/10.1039/B412198H.
(27) Ivin, K. J.; Mol, J. C. 17 - Applications of the Olefin Metathesis Reaction. In *Olefin Metathesis and Metathesis Polymerization (Second Edition)*; Ivin, K. J., Mol, J. C., Eds.; Academic Press: London, **1997**; pp 397–410. https://doi.org/10.1016/B978-012377045-5/50018-5.
(28) Olefin Metathesis and Metathesis Polymerization By K. J. Ivin (The Queen's University of Belfast) and J. C. Mol (University of Amsterdam) As a local characterization technique. *J. Am. Chem. Soc*. **1997**. https://pubs.acs.org/doi/10.1021/ja975520h.
(29) Buchmeiser, M. R. Homogeneous Metathesis Polymerization by Well-Defined Group VI and Group VIII Transition-Metal Alkylidenes: Fundamentals and Applications in the Preparation of Advanced Materials. *Chem. Rev.* **2000**, *100* (4), 1565–1604. https://doi.org/10.1021/cr990248a.
(30) Astruc, D. La métathèse : de Chauvin à la chimie verte.
(31) Lehman Jr., S. E.; Wagener, K. B. Admet Polymerization. In *Handbook of Metathesis*; John Wiley & Sons, Ltd, **2003**; pp 283–353. https://doi.org/10.1002/9783527619481.ch38.

(32) Hamilton, J. G. Stereochemistry of Ring-Opening Metathesis Polymerization. In *Handbook of Metathesis*; John Wiley & Sons, Ltd, **2003**; pp 143–179. https://doi.org/10.1002/9783527619481.ch34.
(33) Chatterjee, A. K. Olefin Cross-Metathesis. In *Handbook of Metathesis*; John Wiley & Sons, Ltd, **2003**; pp 246–295. https://doi.org/10.1002/9783527619481.ch20.
(34) Black, G.; Maher, D.; Risse, W. Living Ring-Opening Olefin Metathesis Polymerization. In *Handbook of Metathesis*; John Wiley & Sons, Ltd, **2003**; pp 2–71. https://doi.org/10.1002/9783527619481.ch31.
(35) Ogba, O. M.; Warner, N. C.; O'Leary, D. J.; Grubbs, R. H. Recent Advances in Ruthenium-Based Olefin Metathesis. *Chem. Soc. Rev.* **2018**, *47* (12), 4510–4544. https://doi.org/10.1039/C8CS00027A.
(36) Fürstner, A. Olefin Metathesis and Beyond. *Angew. Chem. Int. Ed.* **2000**, *39* (17), 3012–3043. https://doi.org/10.1002/1521-3773(20000901)39:17<3012::AIDANIE3012>3.0.CO;2-G.
(37) Keim, W. Oligomerization of Ethylene to α-Olefins: Discovery and Development of the Shell Higher Olefin Process (SHOP). *Angew. Chem. Int. Ed Engl.* **2013**, *52* (48), 12492–12496. https://doi.org/10.1002/anie.201305308.
(38) Banks, R. L.; Bailey, G. C. Olefin Disproportionation. A New Catalytic Process. *IEC Prod. Res. Dev.* **1964**, *3* (3), 170–173. https://doi.org/10.1021/i360011a002.
(39) Schrock, R. R. Alkylcarbene Complex of Tantalum by Intramolecular. Alpha. -Hydrogen Abstraction. *J. Am. Chem. Soc.* **1974**, *96* (21), 6796–6797. https://doi.org/10.1021/ja00828a061.
(40) Schrock, R. R. First Isolable Transition Metal Methylene Complex and Analogs. Characterization, Mode of Decomposition, and Some Simple Reactions. *J. Am. Chem. Soc.* **1975**, *97* (22), 6577–6578. https://doi.org/10.1021/ja00855a048.
(41) Calderon, N.; Ofstead, E. A.; Ward, J. P.; Judy, W. A.; Scott, K. W. Olefin Metathesis. I. Acyclic Vinylenic Hydrocarbons. *J. Am. Chem. Soc.* **1968**, *90* (15), 4133–4140. https://doi.org/10.1021/ja01017a039.
(42) Lewandos, G. S.; Pettit, R. Mechanism of the Metal-Catalyzed Disproportionation of Olefins. *J. Am. Chem. Soc.* **1971**, *93* (25), 7087–7088. https://doi.org/10.1021/ja00754a067.
(43) Biefeld, C. G.; Eick, H. A.; Grubbs, R. H. Crystal Structure of Bis(Triphenylphosphine)Tetramethyleneplatinum(II). *Inorg. Chem.* **1973**, *12* (9), 2166–2170. https://doi.org/10.1021/ic50127a046.
(44) Hérisson, J.-L., P.; Chauvin, Y. Catalyse de transformation des oléfines par les complexes du tungstène. II. Télomérisation des oléfines cycliques en présence d'oléfines acycliques. *Makromol. Chem.* **1971**, *141* (1), 161–176. https://doi.org/10.1002/macp.1971.021410112.
(45) Schrock, R. R. Olefin Metathesis by Molybdenum Imido Alkylidene Catalysts. *Tetrahedron* **1999**, *55* (27), 8141–8153. https://doi.org/10.1016/S0040-4020(99)00304-X.
(46) Ho, T.-L. Hard Soft Acids Bases (HSAB) Principle and Organic Chemistry. *Chem. Rev.* **1975**, *75* (1), 1–20. https://doi.org/10.1021/cr60293a001.
(47) Schrock, R. R.; Hoveyda, A. H. Molybdenum and Tungsten Imido Alkylidene Complexes as Efficient Olefin-Metathesis Catalysts. *Angew. Chem. Int. Ed Engl.* **2003**, *42* (38), 4592–4633. https://doi.org/10.1002/anie.200300576.

(48) Alexander, J. B.; La, D. S.; Cefalo, D. R.; Hoveyda, A. H.; Schrock, R. R. Catalytic Enantioselective Ring-Closing Metathesis by a Chiral Biphen−Mo Complex. *J. Am. Chem. Soc.* **1998**, *120* (16), 4041–4042. https://doi.org/10.1021/ja974353i.

(49) Amakawa, K.; Sun, L.; Guo, C.; Hävecker, M.; Kube, P.; Wachs, I. E.; Lwin, S.; Frenkel, A. I.; Patlolla, A.; Hermann, K.; Schlögl, R.; Trunschke, A. How Strain Affects the Reactivity of Surface Metal Oxide Catalysts. *Angew. Chem. Int. Ed.* **2013**, *52* (51), 13553–13557. https://doi.org/10.1002/anie.201306620.

(50) Michorczyk, P.; Węgrzyniak, A.; Węgrzynowicz, A.; Handzlik, J. Simple and Efficient Way of Molybdenum Oxide-Based Catalyst Activation for Olefins Metathesis by Methane Pretreatment. *ACS Catal.* **2019**, *9* (12), 11461–11467. https://doi.org/10.1021/acscatal.9b03714.

(51) Marcilly, C. *Acido-Basic Catalysis: Application to Refining and Petrochemistry*; IFP publications; Editions Technip: Paris, France, 2006.

(52) Kim, J. M.; Ryoo, R. Disintegration of Mesoporous Structures of MCM-41 and MCM-48 in Water. *Bull. Korean Chem. Soc.* **1996**.

(53) Liu, Y.; Zhang, W.; Pinnavaia, T. J. Steam-Stable MSU-S Aluminosilicate Mesostructures Assembled from Zeolite ZSM-5 and Zeolite Beta Seeds. *Angew. Chem. Int. Ed Engl.* **2001**, *40* (7), 1255–1258.

(54) Choi, M.; Cho, H. S.; Srivastava, R.; Venkatesan, C.; Choi, D.-H.; Ryoo, R. Amphiphilic Organosilane-Directed Synthesis of Crystalline Zeolite with Tunable Mesoporosity. *Nat. Mater.* **2006**, *5* (9), 718–723. https://doi.org/10.1038/nmat1705.

(55) Oil Refining and Products. In *Encyclopedia of Energy*; **2004**; Vol. 4, pp 715–729. https://doi.org/10.1016/B0-12-176480-X/00259-X.

(56) Li, Y.; Li, L.; Yu, J. Applications of Zeolites in Sustainable Chemistry. *Chem* **2017**, *3* (6), 928–949. https://doi.org/10.1016/j.chempr.2017.10.009.

(57) Wang, Z.; Jiang, Y.; Baiker, A.; Huang, J. Efficient Acid-Catalyzed Conversion of Phenylglyoxal to Mandelates on Flame-Derived Silica/Alumina. *ACS Catal.* **2013**, *3* (7), 1573–1577. https://doi.org/10.1021/cs400271e.

(58) Mouat, A. R.; George, C.; Kobayashi, T.; Pruski, M.; van Duyne, R. P.; Marks, T. J.; Stair, P. C. Highly Dispersed SiO/Al_2O_3 Catalysts Illuminate the Reactivity of Isolated Silanol Sites. *Angew. Chem. Int. Ed.* **2015**, *54* (45), 13346–13351. https://doi.org/10.1002/anie.201505452.

(59) Huber, G. W.; Cortright, R. D.; Dumesic, J. A. Renewable Alkanes by Aqueous-Phase Reforming of Biomass-Derived Oxygenates. *Angew. Chem. Int. Ed Engl.* **2004**, *43* (12), 1549–1551. https://doi.org/10.1002/anie.200353050.

(60) Busca, G. Acid Catalysts in Industrial Hydrocarbon Chemistry. *Chem. Rev.* **2007**, *107* (11), 5366–5410. https://doi.org/10.1021/cr068042e.

(61) Hensen, E. J. M.; Poduval, D. G.; Degirmenci, V.; Ligthart, D. A. J. M.; Chen, W.; Mauge, F.; Rigutto, M. S.; van Veen, J. A. R. Acidity Characterization of Amorphous Silica-Alumina. *J. Phys. Chem. C* **2012**, *116* (40), 21416–21429. https://doi.org/10.1021/jp309182f.

(62) Van Santen, R. A.; Kramer, G. J. Reactivity Theory of Zeolitic Broensted Acidic Sites. *Chem. Rev.* **1995**, *95* (3), 637–660. https://doi.org/10.1021/cr00035a008.

(63) Carvajal, R.; Chu, P.-J.; Lunsford, J. H. The Role of Polyvalent Cations in Developing Strong Acidity: A Study of Lanthanum-Exchanged Zeolites. *J. Catal.* **1990**, *125* (1), 123–131. https://doi.org/10.1016/0021-9517(90)90083-V.

(64) Li, S.; Zheng, A.; Su, Y.; Zhang, H.; Chen, L.; Yang, J.; Ye, C.; Deng, F. Brønsted/Lewis Acid Synergy in Dealuminated HY Zeolite: A Combined Solid-State NMR and Theoretical

Calculation Study. *J. Am. Chem. Soc.* **2007**, *129* (36), 11161–11171. https://doi.org/10.1021/ja072767y.

(65) Huang, J.; Jiang, Y.; Marthala, V. R. R.; Thomas, B.; Romanova, E.; Hunger, M. Characterization and Acidic Properties of Aluminum-Exchanged Zeolites X and Y. *J. Phys. Chem.* **2008**, *112*. https://doi.org/10.1021/jp7103616.

(66) Góra-Marek, K.; Derewiński, M.; Sarv, P.; Datka, J. IR and NMR Studies of Mesoporous Alumina and Related Aluminosilicates. *Catal. Today* **2005**, *101* (2), 131–138. https://doi.org/10.1016/j.cattod.2005.01.010.

(67) Bevilacqua, M.; Montanari, T.; Finocchio, E.; Busca, G. Are the Active Sites of Protonic Zeolites Generated by the Cavities? *Catal. Today* **2006**, *116* (2), 132–142. https://doi.org/10.1016/j.cattod.2006.01.024.

(68) Chizallet, C.; Raybaud, P. Pseudo-Bridging Silanols as Versatile Brønsted Acid Sites of Amorphous Aluminosilicate Surfaces. *Angew. Chem. Int. Ed Engl.* **2009**, *48* (16), 2891–2893. https://doi.org/10.1002/anie.200804580.

(69) Huang, J.; van Vegten, N.; Jiang, Y.; Hunger, M.; Baiker, A. Increasing the Brønsted Acidity of Flame-Derived Silica/Alumina up to Zeolitic Strength. *Angew. Chem. Int. Ed Engl.* **2010**, *49* (42), 7776–7781. https://doi.org/10.1002/anie.201003391.

(70) Wang, Z.; Jiang, Y.; Lafon, O.; Trébosc, J.; Duk Kim, K.; Stampfl, C.; Baiker, A.; Amoureux, J.-P.; Huang, J. Brønsted Acid Sites Based on Penta-Coordinated Aluminum Species. *Nat. Commun.* **2016**, *7*, 13820. https://doi.org/10.1038/ncomms13820.

(71) Araujo, T. P.; Quiroz, J.; Barbosa, E. C. M.; Camargo, P. H. C. Understanding Plasmonic Catalysis with Controlled Nanomaterials Based on Catalytic and Plasmonic Metals. *Curr. Opin. Colloid Interface Sci.* **2019**, *39*, 110–122. https://doi.org/10.1016/j.cocis.2019.01.014.

(72) Verma, R.; Belgamwar, R.; Polshettiwar, V. Plasmonic Photocatalysis for CO_2 Conversion to Chemicals and Fuels. *ACS Mater. Lett.* **2021**, *3* (5), 574–598. https://doi.org/10.1021/acsmaterialslett.1c00081.

(73) Perras, F. A.; Paterson, A. L. High Field Solid-State Nmr of Challenging Nuclei in Inorganic Systems. **2023**, 138–177. https://doi.org/10.1016/B978-0-12-823144-9.00015-7.

(74) Li, S.; Lafon, O.; Wang, W.; Wang, Q.; Wang, X.; Li, Y.; Xu, J.; Deng, F. Recent Advances of Solid-State NMR Spectroscopy for Microporous Materials. *Adv. Mater.* **2020**, *32* (44), 2002879. https://doi.org/10.1002/adma.202002879.

(75) Gan, Z.; Gor'kov, P.; Cross, T. A.; Samoson, A.; Massiot, D. Seeking Higher Resolution and Sensitivity for NMR of Quadrupolar Nuclei at Ultrahigh Magnetic Fields. *J. Am. Chem. Soc.* **2002**, *124* (20), 5634–5635. https://doi.org/10.1021/ja025849p.

(76) Gan, Z. Perspectives on High-Field and Solid-State NMR Methods of Quadrupole Nuclei. *J. Magn. Reson.* **2019**, *306*, 86–90. https://doi.org/10.1016/j.jmr.2019.07.028.

(77) Hu, J. Z.; Kwak, J. H.; Wang, Y.; Peden, C. H. F.; Zheng, H.; Ma, D.; Bao, X. Studies of the Active Sites for Methane Dehydroaromatization Using Ultrahigh-Field Solid-State ^{95}Mo NMR Spectroscopy. *J. Phys. Chem. C* **2009**, *113* (7), 2936–2942. https://doi.org/10.1021/jp8107914.

(78) Zhang, W.; Hassan, A.; Struppe, J.; Monette, M.; Hung, I.; Gan, Z.; Martins, V.; Terskikh, V.; Huang, Y. Overcoming Challenges in ^{67}Zn NMR: A New Strategy of Signal Enhancement for MOF Characterization. *Chem. Commun. Camb. Engl.* **2023**, *59* (35), 5205–5208. https://doi.org/10.1039/d3cc00716b.

(79) Andrew, E. R.; Bradbury, A.; Eades, R. G. Removal of Dipolar Broadening of Nuclear Magnetic Resonance Spectra of Solids by Specimen Rotation. *Nature* **1959**, *183* (4678), 1802–1803. https://doi.org/10.1038/1831802a0.

(80) Siegel, R.; Nakashima, T. T.; Wasylishen, R. E. Sensitivity Enhancement of NMR Spectra of Half-Integer Spin Quadrupolar Nuclei in Solids Using Hyperbolic Secant Pulses. *J. Magn. Reson.* **2007**, *184* (1), 85–100. https://doi.org/10.1016/j.jmr.2006.09.007.

(81) Perras, F. A.; Viger-Gravel, J.; Burgess, K. M. N.; Bryce, D. L. Signal Enhancement in Solid-State NMR of Quadrupolar Nuclei. *Solid State Nucl. Magn. Reson.* **2013**, *51–52*, 1–15. https://doi.org/10.1016/j.ssnmr.2012.11.002.

(82) Fernandez, C.; Pruski, M. Probing Quadrupolar Nuclei by Solid-State NMR Spectroscopy: Recent Advances. *Top. Curr. Chem.* **2012**, *306*, 119–188. https://doi.org/10.1007/128_2011_141.

(83) Iuga, D.; Schäfer, H.; Verhagen, R.; Kentgens, A. P. M. Population and Coherence Transfer Induced by Double Frequency Sweeps in Half-Integer Quadrupolar Spin Systems. *J. Magn. Reson.* **2000**, *147* (2), 192–209. https://doi.org/10.1006/jmre.2000.2192.

(84) Goswami, M.; van Bentum, P. J. M.; Kentgens, A. P. M. Repetitive Sideband-Selective Double Frequency Sweeps for Sensitivity Enhancement of MAS NMR of Half-Integer Quadrupolar Nuclei. *J. Magn. Reson.* **2012**, *219*, 25–32. https://doi.org/10.1016/j.jmr.2012.04.007.

(85) Larsen, F. H.; Jakobsen, H. J.; Ellis, P. D.; Nielsen, N. Chr. Sensitivity-Enhanced Quadrupolar-Echo NMR of Half-Integer Quadrupolar Nuclei. Magnitudes and Relative Orientation of Chemical Shielding and Quadrupolar Coupling Tensors. *J. Phys. Chem. A* **1997**, *101* (46), 8597–8606. https://doi.org/10.1021/jp971547b.

(86) Dey, K. K.; Ash, J. T.; Trease, N. M.; Grandinetti, P. J. Trading Sensitivity for Information: Carr-Purcell-Meiboom-Gill Acquisition in Solid-State NMR. *J. Chem. Phys.* **2010**, *133* (5), 054501. https://doi.org/10.1063/1.3463653.

(87) Smith, M. E. Recent Progress in Solid-State Nuclear Magnetic Resonance of Half-Integer Spin Low-γ Quadrupolar Nuclei Applied to Inorganic Materials. *Magn. Reson. Chem.* **2021**, *59* (9–10), 864–907. https://doi.org/10.1002/mrc.5116.

(88) Moudrakovski, I. L. Chapter Four - Recent Advances in Solid-State NMR of Alkaline Earth Elements. In *Annual Reports on NMR Spectroscopy*; Webb, G. A., Ed.; Academic Press, **2013**; Vol. 79, pp 129–240. https://doi.org/10.1016/B978-0-12-408098-0.00004-5.

(89) Duong, N. T.; Trébosc, J.; Lafon, O.; Amoureux, J.-P. Improved Sensitivity and Quantification for 29Si NMR Experiments on Solids Using UDEFT (Uniform Driven Equilibrium Fourier Transform). *Solid State Nucl. Magn. Reson.* **2019**, *100*, 52–62. https://doi.org/10.1016/j.ssnmr.2019.03.007.

(90) G.M. Rankin, A.; Pourpoint, F.; Duong, N. T.; Delevoye, L.; Amoureux, J.-P.; Lafon, O. Advances in the Characterization of Inorganic Solids Using NMR Correlation Experiments. In *Comprehensive Inorganic Chemistry III*; Elsevier, **2023**; pp 534–582. https://doi.org/10.1016/B978-0-12-823144-9.00192-8.

(91) Vega, A. J. CPMAS of Quadrupolar S =^{32}S Nuclei. *Solid State Nucl. Magn. Reson.* **1992**, *1* (1), 17–32. https://doi.org/10.1016/0926-2040(92)90006-U.

(92) Venkatesh, A.; Luan, X.; Perras, F. A.; Hung, I.; Huang, W.; Rossini, A. J. T_1-Noise Eliminated Dipolar Heteronuclear Multiple-Quantum Coherence Solid-State NMR Spectroscopy. *Chem. Phys.* **2020**, *22* (36), 20815–20828. https://doi.org/10.1039/D0CP03511D.

(93) Nagashima, H.; Trébosc, J.; Kon, Y.; Lafon, O.; Amoureux, J.-P. Efficient Transfer of DNP-Enhanced ^{1}H Magnetization to Half-Integer Quadrupolar Nuclei in Solids at Moderate Spinning Rate. *Magn. Reson. Chem.* **2021**, *59* (9–10), 920–939. https://doi.org/10.1002/mrc.5121.

(94) Nagashima, H.; Trébosc, J.; Kon, Y.; Sato, K.; Lafon, O.; Amoureux, J.-P. Observation of Low-γ Quadrupolar Nuclei by Surface-Enhanced NMR Spectroscopy. *J. Am. Chem. Soc.* **2020**, *142* (24), 10659–10672. https://doi.org/10.1021/jacs.9b13838.

(95) Freeman, R.; Kempsell, S. P.; Levitt, M. H. Radiofrequency Pulse Sequences Which Compensate Their Own Imperfections. *J. Magn. Reson. 1969* **1980**, *38* (3), 453–479. https://doi.org/10.1016/0022-2364(80)90327-3.

(96) Levitt, M. H.; Freeman, R. NMR Population Inversion Using a Composite Pulse. *J. Magn. Reson. 1969* **1979**, *33* (2), 473–476. https://doi.org/10.1016/0022-2364(79)90265-8.

(97) Nagashima, H.; Trébosc, J.; Kon, Y.; Sato, K.; Lafon, O.; Amoureux, J.-P. Observation of Low-γ Quadrupolar Nuclei by Surface-Enhanced NMR Spectroscopy. *J. Am. Chem. Soc.* **2020**, *142* (24), 10659–10672. https://doi.org/10.1021/jacs.9b13838.

(98) Thomas, L. H. The Calculation of Atomic Fields. *Math. Proc. Camb. Philos. Soc.* **1927**, *23* (5), 542–548. https://doi.org/10.1017/S0305004100011683.

(99) Fermi, E. A Statistical Method for the Determination of Some Atomic Properties and the Application of This Method to the Theory of the Periodic System of Elements; Elsevier, **1975**; pp 205–213. https://doi.org/10.1016/B978-0-08-017819-6.50030-7.

(100) Hohenberg, P.; Kohn, W. Inhomogeneous Electron Gas. *Phys. Rev.* **1964**, *136* (3B), B864–B871. https://doi.org/10.1103/PhysRev.136.B864.

(101) Kohn, W.; Sham, L. J. Self-Consistent Equations Including Exchange and Correlation Effects. *Phys. Rev.* **1965**, *140* (4A), A1133–A1138. https://doi.org/10.1103/PhysRev.140.A1133.

(102) Monkhorst, H. J.; Pack, J. D. Special Points for Brillouin-Zone Integrations. *Phys. Rev. B* **1976**, *13* (12), 5188–5192. https://doi.org/10.1103/PhysRevB.13.5188.

(103) Liu, P. Low Scaling GW Method: Implementation and Applications, 2017.

(104) Blöchl, P. E. Projector Augmented-Wave Method. *Phys. Rev. B* **1994**, *50* (24), 17953–17979. https://doi.org/10.1103/PhysRevB.50.17953.

(105) Petrilli, H. M.; Blöchl, P. E.; Blaha, P.; Schwarz, K. Electric-Field-Gradient Calculations Using the Projector Augmented Wave Method. *Phys. Rev. B* **1998**, *57* (23), 14690–14697. https://doi.org/10.1103/PhysRevB.57.14690.

(106) Kresse, G.; Furthmüller, J. Efficiency of Ab-Initio Total Energy Calculations for Metals and Semiconductors Using a Plane-Wave Basis Set. *Comput. Mater. Sci.* **1996**, *6* (1), 15–50. https://doi.org/10.1016/0927-0256(96)00008-0.

(107) Kresse, G.; Furthmüller, J. Efficient Iterative Schemes for Ab Initio Total-Energy Calculations Using a Plane-Wave Basis Set. *Phys. Rev. B* **1996**, *54* (16), 11169–11186. https://doi.org/10.1103/PhysRevB.54.11169.

(108) Ceperley, D. M.; Alder, B. J. Ground State of the Electron Gas by a Stochastic Method. *Phys. Rev. Lett.* **1980**, *45* (7), 566–569. https://doi.org/10.1103/PhysRevLett.45.566.

(109) Blöchl, P. E.; Jepsen, O.; Andersen, O. K. Improved Tetrahedron Method for Brillouin-Zone Integrations. *Phys. Rev. B* **1994**, *49* (23), 16223–16233. https://doi.org/10.1103/PhysRevB.49.16223.

(110) Davidson, E. R. The Iterative Calculation of a Few of the Lowest Eigenvalues and Corresponding Eigenvectors of Large Real-Symmetric Matrices. *J. Comput. Phys.* **1975**, *17* (1), 87–94. https://doi.org/10.1016/0021-9991(75)90065-0.

(111) Pulay, P. Convergence Acceleration of Iterative Sequences. the Case of Scf Iteration. *Chem. Phys. Lett.* **1980**, *73* (2), 393–398. https://doi.org/10.1016/0009-2614(80)80396-4.
(112) Johnson, D. D. Modified Broyden's Method for Accelerating Convergence in Self-Consistent Calculations. *Phys. Rev. B* **1988**, *38* (18), 12807–12813. https://doi.org/10.1103/PhysRevB.38.12807.
(113) Hsieh, Y.-C.; Leißing, M.; Nowak, S.; Hwang, B.-J.; Winter, M.; Brunklaus, G. Quantification of Dead Lithium via *In Situ* Nuclear Magnetic Resonance Spectroscopy. *Cell Rep. Phys. Sci.* **2020**, *1* (8), 100139. https://doi.org/10.1016/j.xcrp.2020.100139.
(114) Peach, A.; Fabregue, N.; Gajan, D.; Mentink-Vigier, F.; Scott, F.; Gervais, C.; Laurencin, D. Experimental and Computational 17O Solid-State NMR Investigation of Na- and K-(Bi)Carbonate Salts. *Solid State Nucl. Magn. Reson.* **2025**, *139*, 102020. https://doi.org/10.1016/j.ssnmr.2025.102020.
(115) Cheng, W.-C.; Luthra, N. P. NMR Study of the Adsorption of Phosphomolybdates on Alumina. *J. Catal.* **1988**, *109* (1), 163–169. https://doi.org/10.1016/0021-9517(88)90194-7.
(116) Gomes, Y. H. F.; Lograd o, M.; Inoue, T.; Nakane, S.; Kato, Y.; Yamazaki, H.; Yamada, A.; Eckert, H. Structural Aspects of Ambient-Temperature Densification of Highly Crack-Resistant Borosilicate and Aluminoborosilicate Glasses: Two Case Studies Examined by Solid-State NMR. *J. Phys. Chem. B* **2024**, *128* (14), 3508–3520. https://doi.org/10.1021/acs.jpcb.4c00560.
(117) Moran, R. F.; McKay, D.; Tornstrom, P. C.; Aziz, A.; Fernandes, A.; Grau-Crespo, R.; Ashbrook, S. E. Ensemble-Based Modeling of the NMR Spectra of Solid Solutions: Cation Disorder in $Y_2(Sn,Ti)_2O_7$. *J. Am. Chem. Soc.* **2019**, *141* (44), 17838–17846. https://doi.org/10.1021/jacs.9b09036.
(118) Machida, N.; Eckert, H. FT-IR, FT-Raman and ^{95}Mo MAS–NMR Studies on the Structure of Ionically Conducting Glasses in the System $AgI–Ag_2O–MoO_3$. *Solid State Ion.* **1998**, *107* (3), 255–268. https://doi.org/10.1016/S0167-2738(98)00009-5.
(119) Yasui, Y.; Tansho, M.; Fujii, K.; Sakuda, Y.; Goto, A.; Ohki, S.; Mogami, Y.; Iijima, T.; Kobayashi, S.; Kawaguchi, S.; Osaka, K.; Ikeda, K.; Otomo, T.; Yashima, M. Hidden Chemical Order in Disordered $Ba_7Nb_4MoO_{20}$ Revealed by Resonant X-Ray Diffraction and Solid-State NMR. *Nat. Commun.* **2023**, *14* (1), 2337. https://doi.org/10.1038/s41467-023-37802-4.
(120) Zheng, H.; Ma, D.; Bao, X.; Hu, J. Z.; Kwak, J. H.; Wang, Y.; Peden, C. H. F. Direct Observation of the Active Center for Methane Dehydroaromatization Using an Ultrahigh Field ^{95}Mo NMR Spectroscopy. *J. Am. Chem. Soc.* **2008**, *130* (12), 3722–3723. https://doi.org/10.1021/ja7110916.
(121) Cuny, J.; Cordier, S.; Perrin, C.; Pickard, C. J.; Delevoye, L.; Trébosc, J.; Gan, Z.; Pollès, L. L.; Gautier, R. ^{95}Mo Solid-State Nuclear Magnetic Resonance Spectroscopy and Quantum Simulations: Synergetic Tools for the Study of Molybdenum Cluster Materials. *Inorg. Chem.* **2013**, *52* (2), 617–627. https://doi.org/10.1021/ic301648s.
(122) Edwards, J. C.; Adams, R. D.; Ellis, P. D. A Molybdenum-95 Solid-State NMR Study of Hydrodesulfurization Catalysts. 1. Formation of Fresh HDS Catalyst Precursors by Adsorption of Polyoxomolybdates onto Gamma Alumina. *J. Am. Chem. Soc.* **1990**, *112* (23), 8349–8364. https://doi.org/10.1021/ja00179a020.
(123) d'Espinose de Lacaillerie, J.-B.; Gan, Z. MAS NMR Strategies for the Characterization of Supported Molybdenum Catalysts. *Appl. Magn. Reson.* **2007**, *32*, 499–511. https://doi.org/10.1007/s00723-007-0033-0.

(124) Berkson, Z. J.; Zhu, R.; Ehinger, C.; Lätsch, L.; Schmid, S. P.; Nater, D.; Pollitt, S.; Safonova, O. V.; Björgvinsdóttir, S.; Barnes, A. B.; Román-Leshkov, Y.; Price, G. A.; Sunley, G. J.; Copéret, C. Active Site Descriptors from ^{95}Mo NMR Signatures of Silica-Supported Mo-Based Olefin Metathesis Catalysts. *J. Am. Chem. Soc.* **2023**, *145* (23), 12651–12662. https://doi.org/10.1021/jacs.3c02201.

(125) Jakobsen, H. J.; Bildsøe, H.; Bondesgaard, M.; Iversen, B. B.; Brorson, M.; Larsen, F. H.; Gan, Z.; Hung, I. Exciting Opportunities for Solid-State ^{95}Mo NMR Studies of MoS_2 Nano-Structures in Materials Research from Low to Ultra-High Magnetic Field (35.2 T). *J. Phys. Chem. C Nanomater. Interfaces* **2021**, *125* (14), 7824–7838. https://doi.org/10.1021/acs.jpcc.0c10522.

(126) De Witte, B. M.; Grobet, P. J.; Uytterhoeven, J. B. Pentacoordinated Aluminum in Noncalcined Amorphous Aluminosilicates, Prepared in Alkaline and Acid Mediums. *J. Phys. Chem.* **1995**, *99* (18), 6961–6965. https://doi.org/10.1021/j100018a031.

(127) Wang, Z.; Jiang, Y.; Yi, X.; Zhou, C.; Rawal, A.; Hook, J.; Liu, Z.; Deng, F.; Zheng, A.; Hunger, M.; Baiker, A.; Huang, J. High Population and Dispersion of Pentacoordinated AlV Species on the Surface of Flame-Made Amorphous Silica-Alumina. *Sci. Bull.* **2019**, *64* (8), 516–523. https://doi.org/10.1016/j.scib.2019.04.002.

(128) MacKenzie, K. J. D.; Temuujin, J.; Smith, M. E.; Angerer, P.; Kameshima, Y. Effect of Mechanochemical Activation on the Thermal Reactions of Boehmite (γ-AlOOH) and γ-Al_2O_3. *Thermochim. Acta* **2000**, *359* (1), 87–94. https://doi.org/10.1016/S0040-6031(00)00513-X.

(129) Omegna, A.; Van Bokhoven, J. A.; Prins, R. Flexible Aluminum Coordination in Alumino−Silicates. Structure of Zeolite H−USY and Amorphous Silica−Alumina. *J. Phys. Chem. B* **2003**, *107* (34), 8854–8860. https://doi.org/10.1021/jp030094+.

(130) Wouters, B. H.; Chen, T.-H.; Grobet, P. J. Reversible Tetrahedral−Octahedral Framework Aluminum Transformation in Zeolite Y. *J. Am. Chem. Soc.* **1998**, *120* (44), 11419–11425. https://doi.org/10.1021/ja982082l.

(131) Valla, M.; Rossini, A. J.; Caillot, M.; Chizallet, C.; Raybaud, P.; Digne, M.; Chaumonnot, A.; Lesage, A.; Emsley, L.; van Bokhoven, J. A.; Copéret, C. Atomic Description of the Interface between Silica and Alumina in Aluminosilicates through Dynamic Nuclear Polarization Surface-Enhanced NMR Spectroscopy and First-Principles Calculations. *J. Am. Chem. Soc.* **2015**, *137* (33), 10710–10719. https://doi.org/10.1021/jacs.5b06134.

(132) Trombetta, M.; Busca, G.; Rossini, S.; Piccoli, V.; Cornaro, U.; Guercio, A.; Catani, R.; Willey, R. J. FT-IR Studies on Light Olefin Skeletal Isomerization Catalysis: III. Surface Acidity and Activity of Amorphous and Crystalline Catalysts Belonging to the SiO_2–Al_2O_3System. *J. Catal.* **1998**, *179* (2), 581–596. https://doi.org/10.1006/jcat.1998.2251.

(133) Chizallet, C. Toward the Atomic Scale Simulation of Intricate Acidic Aluminosilicate Catalysts. *ACS Catal.* **2020**, *10* (10), 5579–5601. https://doi.org/10.1021/acscatal.0c01136.

(134) Crépeau, G.; Montouillout, V.; Vimont, A.; Mariey, L.; Cseri, T.; Maugé, F. Nature, Structure and Strength of the Acidic Sites of Amorphous Silica Alumina: An IR and NMR Study. *J. Phys. Chem. B* **2006**, *110* (31), 15172–15185. https://doi.org/10.1021/jp062252d.

(135) A. Perras, F.; Wang, Z.; Kobayashi, T.; Baiker, A.; Huang, J.; Pruski, M. Shedding Light on the Atomic-Scale Structure of Amorphous Silica–Alumina and Its Brønsted Acid Sites. *Chem. Phys.* **2019**, *21* (35), 19529–19537. https://doi.org/10.1039/C9CP04099D.

(136) Poduval, D. G.; Veen, J. A. R. van; Rigutto, M. S.; Hensen, E. J. M. Brønsted Acid Sites of Zeolitic Strength in Amorphous Silica-Alumina. *Chem. Commun.* **2010**, *46* (20), 3466–3468. https://doi.org/10.1039/C000019A.

(137) Xu, B.; Sievers, C.; Lercher, J. A.; van Veen, J. A. R.; Giltay, P.; Prins, R.; van Bokhoven, J. A. Strong Brønsted Acidity in Amorphous Silica−Aluminas. *J. Phys. Chem. C* **2007**, *111* (32), 12075–12079. https://doi.org/10.1021/jp073677i.

(138) Wang, Z.; Chen, K.; Jiang, Y.; Trébosc, J.; Yang, W.; Amoureux, J.-P.; Hung, I.; Gan, Z.; Baiker, A.; Lafon, O.; Huang, J. Revealing Brønsted Acidic Bridging SiOHAl Groups on Amorphous Silica–Alumina by Ultrahigh Field Solid-State NMR. *J. Phys. Chem. Lett.* **2021**, *12* (47), 11563–11572. https://doi.org/10.1021/acs.jpclett.1c02975.

(139) Salvia, W. S.; Zhao, T. Y.; Chatterjee, P.; Huang, W.; Perras, F. A. Are the Brønsted Acid Sites in Amorphous Silica–Alumina Bridging? *Chem. Commun.* **2023**, *59* (94), 13962–13965. https://doi.org/10.1039/D3CC04237E.

(140) Jiang, Y.; Huang, J.; Dai, W.; Hunger, M. Solid-State Nuclear Magnetic Resonance Investigations of the Nature, Property, and Activity of Acid Sites on Solid Catalysts. *Solid State Nucl. Magn. Reson.* **2011**, *39* (3), 116–141. https://doi.org/10.1016/j.ssnmr.2011.03.007.

(141) Hwang, S.-J.; Petucci, C.; Raftery, D. *In Situ* Solid-State NMR Studies of Trichloroethylene Photocatalysis: Formation and Characterization of Surface-Bound Intermediates. *J. Am. Chem. Soc.* **1998**, *120* (18), 4388–4397. https://doi.org/10.1021/ja974192i.

(142) Pilkenton, S.; Raftery, D. Solid-State NMR Studies of the Adsorption and Photooxidation of Ethanol on Mixed TiO_2–SnO_2 Photocatalysts. *Solid State Nucl. Magn. Reson.* **2003**, *24* (4), 236–253. https://doi.org/10.1016/S0926-2040(03)00030-4.

(143) Hunger, M.; Wang, W. Formation of Cyclic Compounds and Carbenium Ions by Conversion of Methanol on Weakly Dealuminated Zeolite H-ZSM-5 Investigated via a Novel in Situ CF MAS NMR/UV-Vis Technique. *Chem. Commun.* **2004**, No. 5, 584–585. https://doi.org/10.1039/B315779B.

(144) Concistrè, M.; Gansmüller, A.; McLean, N.; Johannessen, O. G.; Marín Montesinos, I.; Bovee-Geurts, P. H. M.; Verdegem, P.; Lugtenburg, J.; Brown, R. C. D.; DeGrip, W. J.; Levitt, M. H. Double-Quantum ^{13}C Nuclear Magnetic Resonance of Bathorhodopsin, the First Photointermediate in Mammalian Vision. *J. Am. Chem. Soc.* **2008**, *130* (32), 10490–10491. https://doi.org/10.1021/ja803801u.

(145) Hu, J. G.; Sun, B. Q.; Bizounok, M.; Hatcher, M. E.; Lansing, J. C.; Raap, J.; Verdegem, P. J. E.; Lugtenburg, J.; Griffin, R. G.; Herzfeld, J. Early and Late M Intermediates in the Bacteriorhodopsin Photocycle: A Solid-State NMR Study. *Biochemistry* **1998**, *37* (22), 8088–8096. https://doi.org/10.1021/bi973168e.

(146) Bajaj, V. S.; Mak-Jurkauskas, M. L.; Belenky, M.; Herzfeld, J.; Griffin, R. G. Functional and Shunt States of Bacteriorhodopsin Resolved by 250 GHz Dynamic Nuclear Polarization–Enhanced Solid-State NMR. *Proc. Natl. Acad. Sci.* **2009**, *106* (23), 9244–9249. https://doi.org/10.1073/pnas.0900908106.

(147) Petkova, A. T.; Hatanaka, M.; Jaroniec, C. P.; Hu, J. G.; Belenky, M.; Verhoeven, M.; Lugtenburg, J.; Griffin, R. G.; Herzfeld, J. Tryptophan Interactions in Bacteriorhodopsin: A Heteronuclear Solid-State NMR Study. *Biochemistry* **2002**, *41* (7), 2429–2437. https://doi.org/10.1021/bi012127m.

(148) Matysik, J.; Ding, Y.; Kim, Y.; Kurle, P.; Yurkovskaya, A.; Ivanov, K.; Alia, A. Photo-CIDNP in Solid State. *Appl. Magn. Reson.* **2022**, *53* (3), 521–537. https://doi.org/10.1007/s00723-021-01322-5.

(149) De Biasi, F.; Karthikeyan, G.; Visegrádi, M.; Levien, M.; Hope, M. A.; Brown, P. J.; Wasielewski, M. R.; Ouari, O.; Emsley, L. Light-Induced ^{1}H NMR Hyperpolarization in Solids at 9.4 and 21.1 T. *J. Am. Chem. Soc.* **2024**, *146* (29), 19667–19672. https://doi.org/10.1021/jacs.4c06151.

(150) Tomonaga, Y.; Hidaka, T.; Kawamura, I.; Nishio, T.; Ohsawa, K.; Okitsu, T.; Wada, A.; Sudo, Y.; Kamo, N.; Ramamoorthy, A.; Naito, A. An Active Photoreceptor Intermediate Revealed by In Situ Photo irradiated Solid-State NMR Spectroscopy. *Biophys. J.* **2011**, *101* (10), L50–L52. https://doi.org/10.1016/j.bpj.2011.10.022.

(151) Naito, A.; Makino, Y.; Shigeta, A.; Kawamura, I. Photoreaction Pathways and Photo intermediates of Retinal-Binding Photoreceptor Proteins as Revealed by in Situ Photoirradiation Solid-State NMR Spectroscopy. *Biophys. Rev.* **2019**, *11* (2), 167–181. https://doi.org/10.1007/s12551-019-00501-w.

(152) N. Hooper, T. J.; Oliveira-Silva, R. de; Sakellariou, D. High-Resolution in Situ Photo-Irradiation MAS NMR: Application to the UV-Polymerization of n-Butyl Acrylate. *J. Mater. Chem. A* **2025**, *13* (2), 933–939. https://doi.org/10.1039/D4TA06729K.

Chapter 2.
Study of molybdenum-based catalysts for olefin's metathesis reaction: ^{95}Mo solid-state NMR and DFT calculations

Chapter 2. Study of molybdenum-based catalysts for Olefin's metathesis reaction: ^{95}Mo Solid-State NMR and DFT calculations

Part I: ^{95}Mo NMR of molybdenum-based molecular complexes

1. Introduction

In today's industry, molybdenum-based catalysts have shown excellent catalytic activity. This transition metal can have many oxidation states and strong metal-ligand interactions, making it highly adaptable in several catalytic mechanisms. In particular, these catalysts are employed in industrial processes, such as olefin metathesis and selective oxidation reactions.

2. Types of Olefin metathesis catalysts

2.1. Molecular Metathesis Catalysts

In 1974, Schrock discovered the well-defined high-valent Mo molecular metathesis catalysts inspired by tantalum chemistry.[1] These systems are called "Schrock alkylidene complexes" with a general formula of:

$$\mathrm{M}(=\mathrm{CHR})(\mathrm{X})(\mathrm{E})_n$$

where M is an early transition metal, CHR, an alkylidene ligand, X, an electron-withdrawing ligands (e.g., alkoxides, halides) and L, a supporting ligand. The X ligands make the metal more electrophilic and increase its reactivity. Commonly employed X ligands include the fluorinated alkoxides, such as $-\mathrm{OCMe}(\mathrm{CF_3})_2$. The bulkiness of these ligands also provides steric protection and prevent deactivation pathways. The E ligand also stabilizes the Mo complex, but is not directly involved in its catalytic activity. In particular, large imido ligands, such as 2,6-disubstituted arylimido groups, are commonly employed to enhance stability of Mo complexes (see Figure 15).[2,3] Oxo groups can also be used as supporting ligand. Nevertheless, these complexes are less stable than the imido counterparts since the oxo

ligand are smaller and hence, they are more susceptible to bimolecular decomposition.[4] However, highly active Mo-oxo alkylidenes have been produced by the addition of water to alkylidyne complexes.[5,6]

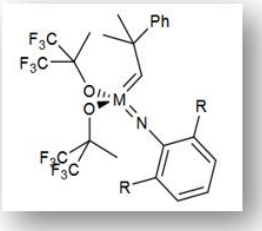

***Figure 15**. Example of molecular Schrock-type metathesis catalysts.*

2.2. SOMC-based metathesis catalysts

Nowadays, chemical industries fall back on processes relying on heterogenous catalysts rather than their homogeneous counterparts. The heterogeneous catalysts have the advantages that they can be easily separated from reaction products and reemployed. Heterogeneous catalysts are synthesized by distributing a metal molecular complex onto an oxide support. These materials to be activated are typically heated under a gas flow (e.g., air), which allows the metal (M) to be dispersed on the support surface. Nevertheless, this procedure leads to a variable number of M-O bonds and then ill-defined surface sites.[7] Among these different environments, only a small percentage is typically active in catalysis (< 5%) and processes using these catalysts often require high temperatures (> 200 °C). The distribution of surface sites make the characterization of these catalysts challenging and limits their rational development.[8–10]

This limitation can be circumvented by surface organometallic chemistry (SOMC).[11] This approach uses the surface of the solid support as a ligand to graft molecular metal complexes, thus generating a well-defined active site. Silica (SiO_2) and alumina (Al_2O_3) are the most commonly used supports in SOMC reactions since both of which have surface hydroxyl groups. Those supports can be heat-treated to adjust the density of surface OH moieties. These hydroxyl groups can undergo protonolysis, in such way that they replace ligands in the molecular complex and the metal center is grafted to the surface. If this reaction occurs on a support with a low surface hydroxyl density, the resulting oxide

support contains isolated organometallic complexes, which improves control over the catalyst structure. This approach modulates the electronic and steric properties of the grafted metal complex. Thanks to their heterogenization, the resulting catalysts exhibit improved stability, as the anchored active sites ensure better accessibility of the reactants.[12–15]

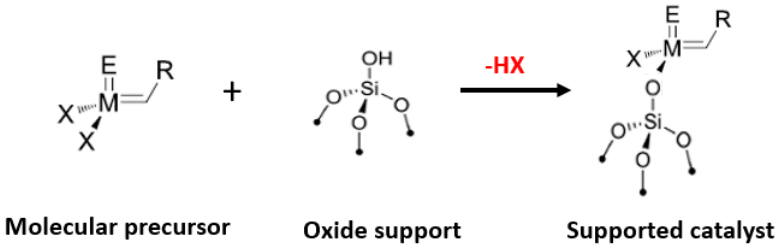

***Figure 16**. SOMC general process for the synthesis of well-defined supported alkylidenes where M = Mo, X = OR or NR, and E = NR or O.*

3. Well-defined Silica Supported Catalysts

Many types of materials whether amorphous or crystalline can function as solid supports. They must possess high surface area, since this parameter determines the number of active surface sites per unit mass. Amorphous silica is one of the most used supports in heterogeneous catalysis given its stability and high specific surface area (i.e., 50 – 1000 $m^2 g^{-1}$).[16,17] It is mainly composed of siloxane bridges and terminated with silanol groups, which can have different concentrations depending on the thermal treatment temperature.[18]. The thermal treatment also affects the local environments of silanol groups, which can be classified as (i) isolated, i.e. a single hydroxyl group attached to a silicon atom, which is not involved in hydrogen bonds, (ii) vicinal, i.e. hydroxyl groups on adjacent silicon atoms, which are close enough to form a hydrogen bond, (iii) or geminal, i.e. $Si(OH)_2$ (see). Upon heat treatment up to 700 °C, the density of OH groups begin to decrease by a dehydroxylation mechanism. This process increases the concentration of isolated Si–OH groups on the surface while retaining up to 10% of geminal silanols.[19] At such temperature, the protonolysis of M-X moiety, where M is the metal center and X = C, Cl, H, etc., from the molecular precursor by the isolated surface OH groups will form M–O–Si covalent linkage and release HX as side product (Figure 18a). The catalyst formed is so called “isolated grafted monopodal complex”. Lower dehydroxylation temperatures

produce supports with a higher density of vicinal silanols, resulting in a greater number of bipodal species, meaning that the metal of the molecular complex forms two M–O–Si covalent bonds with the silica support (Figure 18b). The maximal density of bipodal species was found for silica treated at temperatures around 200 °C.[20]

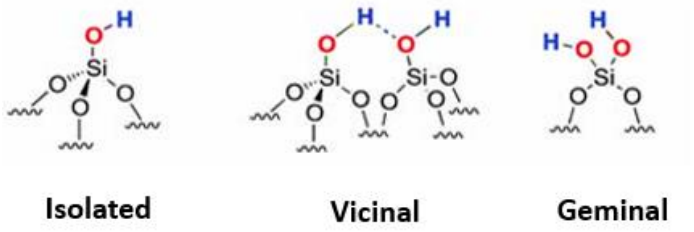

***Figure 17**. Types of silanols groups formed upon the dehydroxylation of oxide support.*

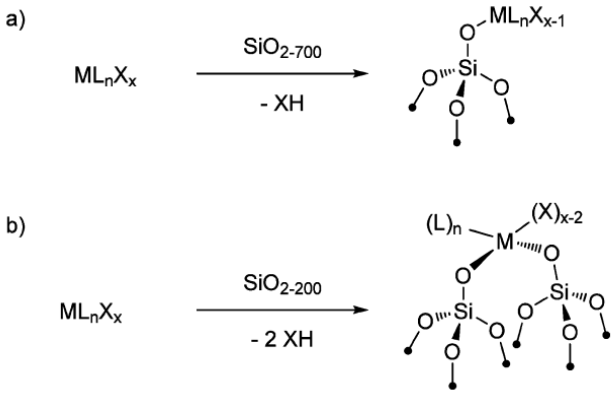

***Figure 18.** Synthesis of (a) monopodal and (b) bipodal grafted complexes.*

4. Well Defined Molybdenum-Based Silica-Supported Catalysts

4.1. Characteristics of Mo Transition Metal

Molybdenum is a transition metal with an electronic structure of [Kr] $5s^1$ $4d^5$. It can have several oxidation states ranging from +II to +VI, with the most catalytically active being +IV, +V, and +VI. The oxidation state of molybdenum has a direct impact on its electronic properties and hence, affects its reactivity, coordination environment, and catalytic performance. Mo^{VI} is the highest oxidation state observed in catalysis with a d^0 electronic

configuration, making it exceptionally electrophilic and able to coordinate with electron-rich substrates and ligands. The molecular complexes discussed in this manuscript all have the metal Mo with an empty d orbital and low energy. This feature is particularly important in olefin metathesis catalysis, as Mo^{VI} metal center efficiently forms metal carbene intermediates, that is an important step in the olefin's metathesis cycle.[21] Furthermore, Mo has the ability to cycle between different oxidation states, promoting therefore the redox reaction (e.g., Mo^{VI} undergoes reduction to Mo^{V}) before being re-oxidized, thus regenerating the active species and completing the catalytic cycle.

Complementary to the oxidation state, the coordination environment of molybdenum influences as well its catalytic performance. The olefin metathesis catalysts employ two main types of supporting ligand, oxo (Mo=O) or imido (Mo=NR), which influence the electronic properties. The Mo=O bond has a high polarization because of the high electronegativity of oxygen, which produces a partial positive charge on Mo atom, further increasing its electrophilicity and lowering the energy of its lowest unoccupied molecular orbital (LUMO). As a result, this low electron density near Mo facilitates alkene coordination. Nevertheless, the small size of oxo ligand decreases the stability of these complexes, which tend to decompose. The lower electronegativity of N atom also results in lower electrophilicity of the Mo complex, which affects its reactivity.[22]

4.2. Grafting of Molybdenum-Based Molecular Complexes on SiO_2

One of the most important features making molybdenum-based catalysts important in large-scale olefin metathesis industrial processes is their high activity and selectivity at low temperatures. The most famous are MoO_3 supported on Al_2O_3 synthesized through impregnation method and used in Shell Higher Olefin Process (SHOP) and operating at 100 to 200 °C.[23] SHOP process allow the formation of olefins with long chains from ethylene following three main parts: oligomerization, isomerization and olefin metathesis. However, for supported catalysts it is necessary to study the structure of the metal active sites as well as their dispersion on the surface. Many spectroscopic techniques (e.g., Raman, UV-Visible) have been used to characterize the MoO_3/Al_2O_3 and found that at low Mo loading only

monomeric Mo bis-oxo are observed, while at higher loadings (> 1 Mo/nm^2) oligomeric mono-oxo are dominant and easily activated.[24,25]

Recently, silica supported molybdenum-based catalysts generated through SOMC reaction have gained a considerable attention having a similar surface structure as the alumina supported counterparts but with lower activity.[7] So far, well-defined metal catalysts based on molybdenum and tungsten have proven more efficient than rhenium alkylidene catalysts in several olefin metathesis reactions. The best synthesized SOMC catalyst for propene metathesis is shown in Figure 19: it is the silica supported [(≡Si −O−)Mo(≡NAd)(=CH^{t}Bu)(2,5−dimethyl pyrrolyl)]. This catalyst showed a turnover number (TON) of 231.000, compared to 11.000 for the tungsten-based catalyst[26–28], where the TON is the number of moles of substrate that a mole of catalyst can convert before becoming inactivated. Additionally, Mo-oxo catalysts have demonstrated superior efficiency in terminal olefin metathesis over tungsten oxides. The grafting of oxo complex Mo(=O)($CH_2{}^tBu)_3$Cl on silica-700 and silica-200 generates mainly monopodal (Figure 20 a) and bipodal complexes (Figure 20 b), respectively, where the bipodal catalyst shows better tolerance toward functional groups in different olefin metathesis reactions but with the monopodal complex being more efficient in propene metathesis showing a TON of 90,000.[29]

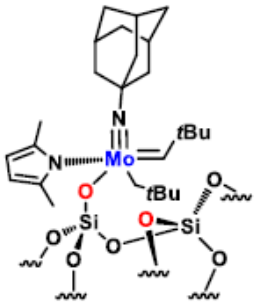

***Figure 19**. SOMC-generated catalyst for propene metathesis.*

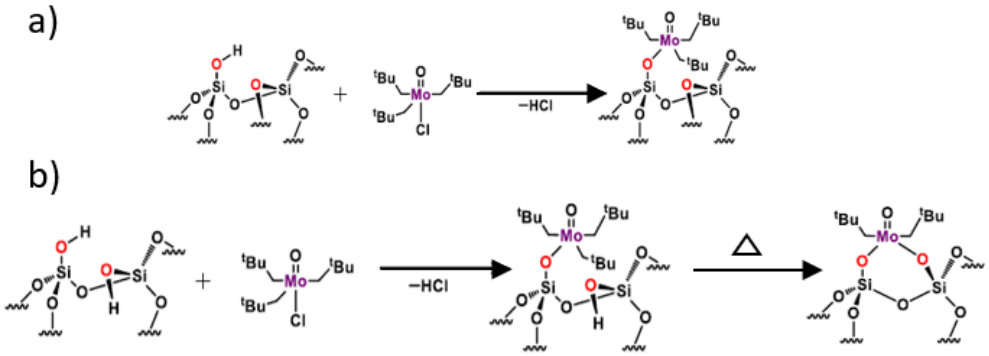

***Figure 20**. Grafted oxide complex Mo(=O)($CH_2{}^tBu$)$_3$Cl on a) $SiO_{2\text{-}700}$ and b) $SiO_{2\text{-}200}$.*

The above examples show that the local environment of the molybdenum atom strongly influences the reactivity of the grafted complexes. Therefore, the rational optimization of these complexes requires to characterize their atomic-level structure. Nevertheless, as the grafted complexes lack long-range order, their structure cannot be determined using diffraction techniques, contrary to molecular complexes. Furthermore, several commonly employed spectroscopic techniques, such as Raman and UV-visible spectroscopies, do not provide direct insight into the local environment of the molybdenum atom. Therefore, ^{95}Mo NMR spectroscopy represents a promising approach to fill that gap. Linking the ^{95}Mo NMR parameters to Mo local environment requires to record ^{95}Mo NMR spectra of molybdenum molecular complexes.

5. Solid-State NMR Experiments on Mo molecular complexes

5.1. Rationale for using multiple magnetic field strengths (18.8 T and 28.2 T)

In solid-state NMR of quadrupolar nuclei, obtaining spectra at multiple magnetic field strengths is useful to determine the magnitude of both quadrupolar interaction and chemical shift anisotropy since the relative contributions of these interactions to overall linewidth vary with the applied magnetic field. As mentioned above, MAS averages the first-order quadrupolar interaction. However, the second-order quadrupolar interaction exhibits a more complex angular dependence and it is only partially averaged under MAS

conditions. Consequently, second-order broadening persists under MAS and increases with the larger quadrupolar coupling constant, C_Q, but decreases with increasing external magnetic field strength, B_0. This makes high-field NMR particularly beneficial for the study of quadrupolar nuclei. According to the second order perturbation theory, the total central transition linewidth under MAS, $\Delta\nu_{CT}$, is given by the equation below[30]

(Eq. 34)

$$\Delta\nu_{CT} = \frac{a(6+\eta_Q)^2}{504} \quad \text{where} \quad a = \frac{\nu_Q^2}{\nu_0} I(I+1) - \frac{3}{4}$$

where ν_0 denotes the Larmor frequency and $\nu_Q = 3C_Q/[2I(2I-1)]$ the quadrupolar frequency.

In contrast, the magnitude of CSA (in Hz) scales linearly with B_0. Therefore, faster spinning rates are required to suppress spinning sidebands due to CSA at high B_0.[31,32] However, higher spinning rates require smaller rotor diameters, thus reducing sample volume. This is a challenge for acquiring high quality spectra of ^{95}Mo, which has low receptivity.

Thus, ^{95}Mo NMR at multiple fields experiments are often required to accurately determine NMR parameters. On a one hand, lower field allows a better estimation of C_Q and the asymmetry parameter (η_Q), as their effects are more pronounced. On the other hand, higher field allows for more precise determination of CSA and its asymmetry parameter (η_{CSA}). Spectra acquired at two different fields are simulated simultaneously using ssNake software, to extract the most reliable set of NMR parameters.[33]

5.2. Studied molybdenum-based molecular complexes: mono/bis -Oxo & -Imido

In this section, we present our study of well-defined molybdenum-based molecular complexes with different supporting ligands: oxo (complexes 1-3), bis-oxo (complex 4), imido (complexes 5-6) and bis-imido (complex 7). These ligands are of great importance in catalysis, particularly in olefin metathesis. These model compounds, which are representatives of catalyst precursors, were selected to understand how the different supporting ligands affect the ^{95}Mo NMR parameters. Depending on the stability, these complexes can be grafted onto silica or alumina supports via different bonds. For example,

complex 1 may graft via either the oxo bond or the N=P bond and complex 2 via the oxo or Mo-Cl bond. This knowledge is crucial before addressing the structurally more complex and diverse systems encountered in industrial catalysts supported on amorphous supports.

In their study, Berkson *et al.* [34] used ^{95}Mo solid-state NMR to investigate how ligands like fluorinated alkoxides and silanolates, impact the electronic environment of molybdenum alkylidyne complexes. Their findings revealed that increasing fluorination lowered the HOMO and LUMO energies of complexes, which correlates with changes in the ^{95}Mo chemical shift tensors. The δ_{iso} range of the complexes varies between 610 and 190 ppm depending on the amount of fluorine present, and the C_Q range from 2 to 4.5 MHz. Importantly, the selected systems were relatively structurally simple, well-defined molecular complexes that can be supported and already prevalent in industrial applications.

Our work extends this approach to more complex molecular pre-catalysts. Unlike Berkson *et al.*,[34] who focused on the influence of fluorinated ligands, located further from the molybdenum center, we investigate variations of ^{95}Mo parameters arising from changes induced by the ligands directly coordinated to Mo(VI), i.e., within the first coordination sphere, since grafting will subsequently anchor Mo to the oxygen atoms of the support, thereby altering the geometry of the first coordination sphere. This strategy aims to establish clearer correlations between the electronic structure and variation of NMR descriptors that probe the local environment of molybdenum. To ensure accurate spectral assignment and reliable determination of anisotropic parameters, ^{95}Mo NMR spectra were acquired at two magnetic field strengths, 18.8 and 28.2 T. Figure 21 displays the molecular structures of the complexes examined in this study and table 3 shows their structural characteristics.

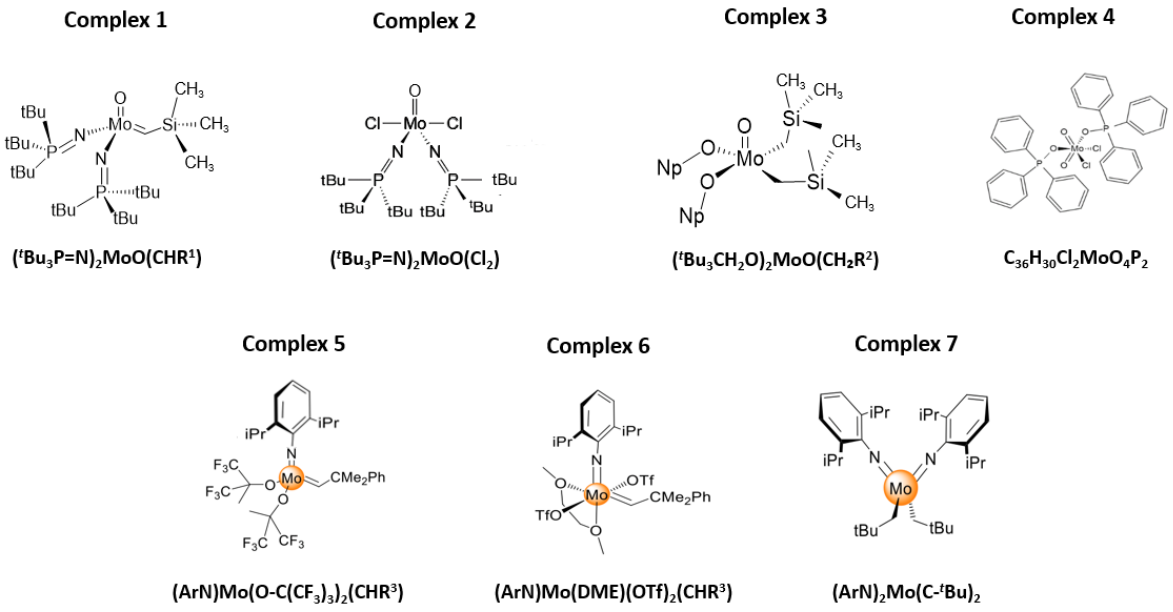

***Figure 21**. Molecular structures of oxo and imido complexes studied by solid-state NMR.*

***Table 3.** Structural details of oxo and imido molecular complexes studied.*

Molecular Complexes	Supporting Ligands	Other Ligands	Coordination Number	Local Geometry
Complex 1 ($(^tBu_3P{=}N)_2MoO(CHR^1)$)	Oxo	Phosphinimides, carbene	4	Distorted tetrahedron
Complex 2 ($(^tBu_3P{=}N)_2Mo{=}O{-}Cl_2$)	Oxo	Phosphinimides, chloride	5	Square-pyramidal
Complex 3 ($(^tBu_3CH_2O)_2MoO(CH_2R^2)$)	Oxo	Alkoxide, neosilyl	5	Square-pyramidal
Complex 4 $C_{36}H_{30}Cl_2MoO_4P_2$	Bis-oxo	Chloride, alkoxide	6	Distorted octahedral
Complex 5 ($(ArN)Mo(O{-}C(CF_3)_3)_2(CHR^3)$)	Imido	trifluoromethoxy, carbene	4	Distorted tetrahedron
Complex 6 ($(ArN)Mo(DME)(OTf)_2(CHR^3)$)	Imido	Triflate(CF_3SO^{3-}), DME, carbene	6	Distorted octahedral
Complex 7 ($(ArN)_2Mo(C{-}^tBu)_2$)	Bis-imido	Alkyl	4	Distorted tetrahedron

5.3. Experimental Conditions for NMR Analysis

Molybdenum possesses two NMR-active isotopes, ^{97}Mo and ^{95}Mo. In this study, we observed ^{95}Mo owing to its higher natural abundance (15.9 %) and small electric quadrupolar moment. NMR spectra were recorded at two magnetic fields, 18.8 and 28.2 T, under MAS conditions. These conditions allow, in the most favorable case, the extraction of both isotropic and anisotropic NMR parameters, δ_{iso}, δ_{CSA}, η_{CS}, C_Q and η_Q, as well as the

Euler angles (α, β, γ), which describe the orientation between the quadrupolar coupling tensor and the chemical shift tensor.

The first set of experiments were carried out at B_0 = 18.8 T, with a ^{95}Mo Larmor frequency is −52.6 MHz, at room temperature, on a narrow-bore magnet equipped with Bruker AVANCE NEO NMR console and a 3.2 mm double-resonance (HX) low-γ MAS probe. Powder samples were packed in a JACOMEX glove box, into a zirconia rotor closed with a Kel-F driving cap. In the probe, the rotors were spun at a MAS frequency of ν_R = 20 kHz under nitrogen gas.

The second set of experiments was carried out at B_0 = 28.2 T, with a ^{95}Mo Larmor frequency is −78.9 MHz. The spectrometer is equipped with standard Bruker AVANCE NEO console. All spectra were acquired at room temperature using a 3.2 mm double resonance (HX) MAS probe. The samples were packed in rotors under the same conditions as for previous experiments at 18.8 T and ν_R = 20 kHz.

A DFS-QCPMG sequence was used to improve sensitivity. The spectra were processed using Topspin 4.1.4 software. In some cases, a Fourier transform was applied directly to the recorded train of echoes (FID), resulting in spectra featuring a comb of spikelets. In other cases, the different acquired echoes were summed and the Fourier transform of this sum yields the envelope of the signal. All spectra were referenced to the ^{95}Mo signal of liquid Na_2MoO_4, which resonates at 0 ppm. Given the expected large width of the spectra due to combined quadrupolar and CSA interactions, the QCPMG sequence was essential to improve signal-to-noise ratios. Depending the decay rate of the echo envelope (T_2'), 20 to 2000 echoes were acquired and refocusing pulses were repeated with cycle times ranging from 470 to 2000 µs.

For imido and bisimido complexes, 1D ^{95}Mo DFS-QCPMG spectra at 18.8 T were obtained with a CT selective pulse of 8.5 µs and ν_1 = 29.4 kHz. For oxo complexes, QCPMG pulses lasted 3.2 µs with ν_1 = 78.1 kHz. No ^{1}H heteronuclear decoupling was applied during acquisition.

One-dimensional ^{95}Mo DFS-QCPMG spectra at 28.2 T were all acquired using QCPMG pulses that lasted 3.2 µs with ν_1 = 78.1 kHz. No ^{1}H heteronuclear decoupling was applied during the acquisition.

The DFS pulses are usually applied prior to selective 90° pulses. DFS parameters were optimized using a molybdenum reference compound and applied uniformly across all experiments. The duration of the frequency sweep was set to 1000 µs with an RF power of 22 W. For efficient DFS convergence, the starting sweep frequency was set to the extreme value of ST range i.e., 150 kHz, and the final sweep frequency was kept relatively far from the central transition (CT), at 80 kHz.

5.4. Results of ^{95}Mo DFS-QCPMG for oxo and bisoxo complexes

Ligands play a central role in modulating the electronic properties of the Mo center. Strong σ- and π-donating ligands influence the energy levels of the metal's frontier molecular orbitals, especially the LUMO, and thereby affect both the ^{95}Mo NMR chemical shifts and the quadrupolar coupling constant.[34,35] As a result, solid-state ^{95}Mo NMR serves as an effective tool for probing subtle variations in electronic structure and predicting catalytic reactivity.[21,34,35]

This section describes solid-state ^{95}Mo NMR data for compounds featuring oxo and bis-oxo coordination. Each molecule has a unique set of surrounding ligands, resulting in diverse local electronic environment around the molybdenum center. These differences are expected to considerably impact the ^{95}Mo NMR parameters, which will be examined in details in the following subsections. Figure 22 shows the ^{95}Mo spectrum of molecular complex 1, recorded at two different high magnetic fields. The 1D spectra were simultaneously deconvoluted using the ssNake software to extract the NMR parameters listed in Table 4. At both fields, the most intense peak corresponds to the central transition, and a single set of parameters is sufficient to reproduce the spectra at both fields. This is consistent with the presence of a single Mo site in compound 1. Asterisks indicate the spinning sidebands. The comparison of both spectra for complex 1 reveals a noticeable line narrowing at 28.2 T, reflecting the reduction of second-order quadrupolar broadening with increasing magnetic field strength.

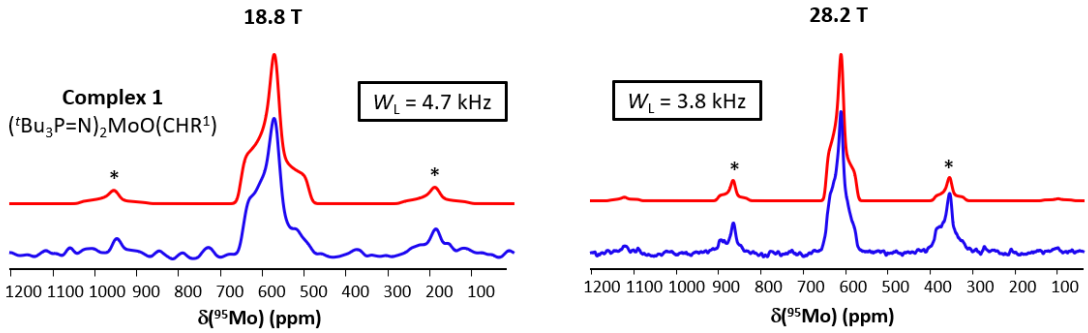

Figure 22: *Comparison of the 1D ^{95}Mo NMR experimental (blue) and simulated (red) spectra of complex 1 acquired at 18.8 and 28.2 T with ν_R = 20 kHz. W_L represents the full width at half-maximum. *Spinning sidebands*

Complex 1, beside the oxo ligand, has strongly electron-donating ligands: two phosphinimides and a carbene attached to TMS group (denoted R^1). All the ligands are π donors. The Mo atom occupies a distorted tetrahedral geometry with a high degree of asymmetry owing especially to the two double bonds, Mo=O and Mo=C. Complex 2 resembles complex 1 but with the carbene replaced by two chlorides increasing the coordination number to 5 and changing the geometry to square pyramidal. The Mo-chloride bonds have a higher ionic character than Mo=C bond. Complex 3 has a mono-oxo Mo(VI) core, coordinated by two alkoxide ligands (OR) and two neosilyl groups (R^2) giving rise to a coordination number of 5 with a square pyramidal local geometry. The Mo-O bond has a strong ionic character[36], whereas Mo-C bonds are highly covalent. In contrast, complex 4 has a bis-oxo Mo(VI) core with two chlorides, two phosphine oxide ligands arranged symmetrically around the Mo, this complex adopts octahedral coordination. Because each bond type is located symmetrically in opposite planes of the octahedron, this arrangement gives molybdenum a more regular coordination geometry. After presenting the compounds and their geometries, Table 4 summarizes the measured ^{95}Mo NMR parameters. We will now discuss how the structural properties of these complexes affect their NMR parameters.

Table 4. *^{95}Mo ssNMR parameters of oxo complexes (1-3) and bisoxo complex (4) determined by simulating ^{95}Mo NMR spectra.*

	NMR Data	δ_{iso} (ppm)	C_Q (MHz)	η_Q	δ_{CSA} (ppm)	η_{CSA}	Euler Angles α β γ (°)	LW 18.8 T (kHz)	LW 28.2 T (kHz)
Complex 1	$(^tBu_3P{=}N)_2MoO(CHR^1)$	650	5	1	261	1	90 36 0	**4.7**	**3.8**
Complex 2	$(^tBu_3P{=}N)_2MoO(Cl_2)$	230	8.2	0.75	950	0.5	90 0 30	-	**8**
Complex 3	$(^tBu_3CH_2O)_2MoO(CH_2R^2)$	1145	12.3	0	1000	0.23	0 16 64	**25**	**22**
Complex 4	$C_{36}H_{30}Cl_2MoO_4P_2$	130	4.5	0.5	300	0	0	**4.5**	**3.7**

The chemical shifts of the four complexes fall within the positive range and differ significantly from one complex to another. The complex 1 has a deshielded chemical shift of 650 ppm falling above the rang of the fluorinated complexes studied in Berkson *et al.* [34]. This may be due to the stronger π donation by phosphinimides and alkylidene ligands compared to alkoxydes and the stronger covalent character of Mo−N and Mo=C bonds compared to Mo-O counterpart. Replacing the alkylidene group by two chloride ligands in complex 2 strongly shields the ^{95}Mo signal, owing to the ionic character of Mo-Cl bonds (see figure 23)

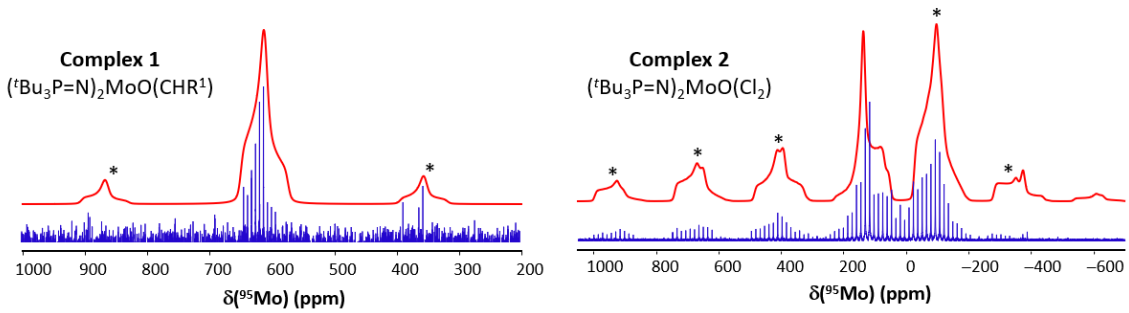

Figure 23*. 1D DFS-QCPMG ^{95}Mo ssNMR spectra acquired at 28.2 T with ν_R = 20 kHz of oxo molecular complexes (1) and (2). Blue: experimental spectra; red: simulated spectra using ssNake software. *Spinning sidebands*

Complex 3 has a strongly deshielded ^{95}Mo resonance at 1145 ppm. Grekov *et al.*[37] have previously shown that neosilyl ligands have a considerable electronic and steric influence on tungsten oxo complexes, improving stability and activity in propylene metathesis compared to analogous neopentyl ligands. By example, the dramatic deshielding observed here implies that neosilyl substitution also has a significant influence on Mo's electrical environment, validating its role as a highly effective auxiliary ligand. The higher ^{95}Mo isotropic chemical shift of complex 3 with respect to complex 1 may stem from (i) the coordination by two carbene ligands instead of one alkylidene ligand and (ii) the stronger

covalent character of Mo-C bond compared to Mo=C counterpart since sp^3-hybridized carbon atoms are less electronegative than sp^2-hybridized carbon atoms.

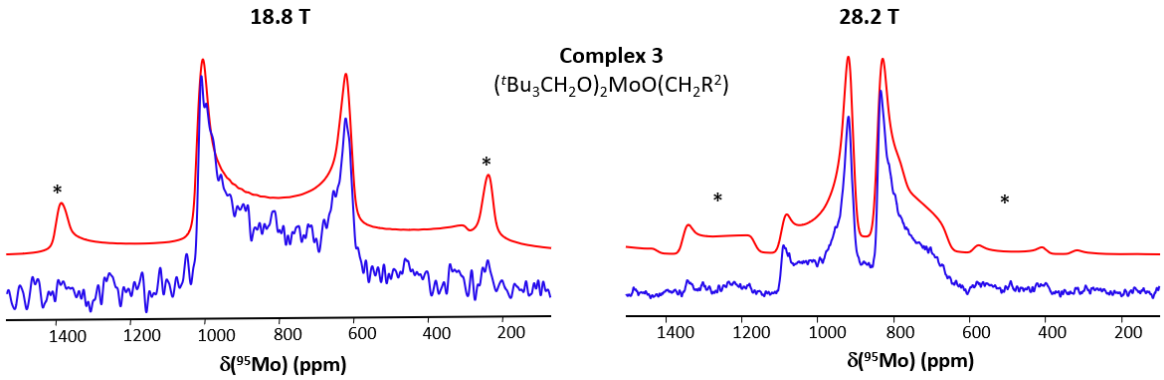

***Figure 24**. 1D DFS-QCPMG ^{95}Mo ssNMR spectrum of complex 3 acquired at 18.8 (left) and 28.2 T (right) with ν_R = 20 kHz. Blue: experimental spectra; red: simulated spectra using ssNake. *Spinning sidebands*

Complex 4 exhibits low isotropic chemical shifts because of the ionic character of Mo-Cl and Mo-O bonds. The measured isotropic chemical shift, δ_{iso}= 130 ppm, is similar to that observed for a complex with similar ligands in benzene solvent (see Figure 25b).[35] Notably, from complex 2 to complex 4, the addition of three oxygen atoms in the coordination sphere of Mo shifts the resonance progressively to lower values (i.e.; to the right).

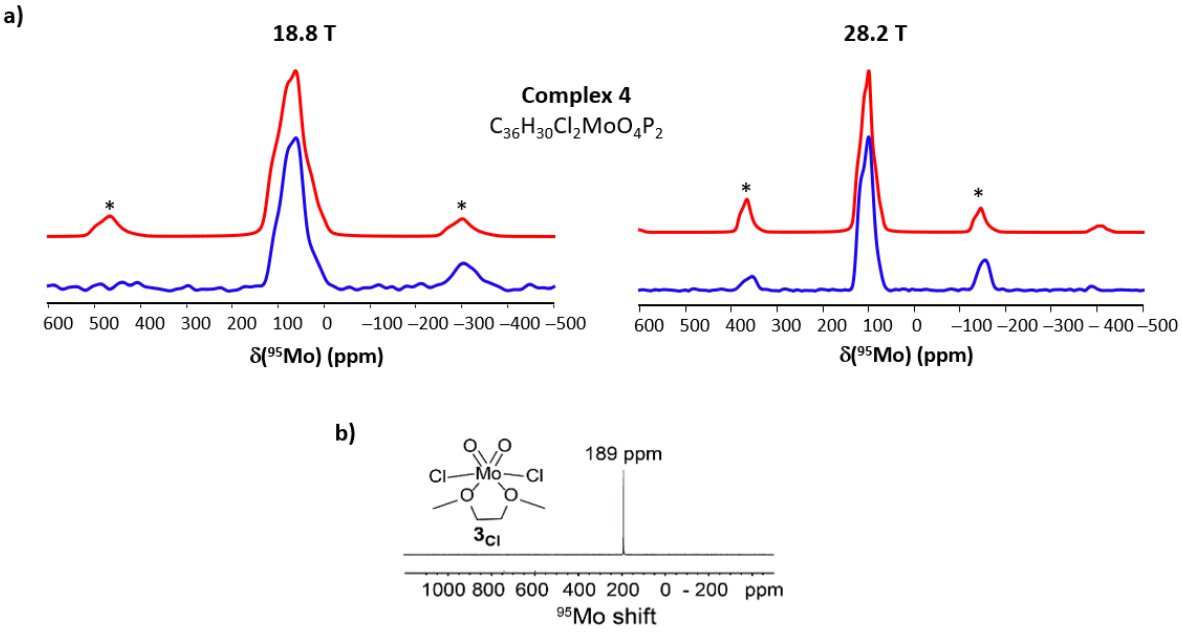

***Figure 25.** 1D DFS-QCPMG ^{95}Mo ssNMR spectra of complex 4 acquired at 18.8 (left) and 28.2 T (right) with ν_R = 20 kHz. Blue: experimental spectra; red: simulated spectra using ssNake software. *Spinning side bands b) solution-state ^{95}Mo NMR spectrum of the complex shown above the spectrum. Figure adapated from ref. 35.*

The comparison between the isotropic chemical shifts of complexes 1, 2 and 4 also shows that the ^{95}Mo nuclei with higher coordination number are more shielded. Nevertheless, the three complexes have different ligands and complex 3 has higher isotropic chemical shift than complex 1, even if it is higher coordination number. This counterexample shows the influence of the nature of the ligands.

Having discussed the isotropic chemical shifts, we now consider the anisotropic parameters, namely the quadrupolar coupling constant (C_Q) that spans from 4.5 to 12.3 MHz, and the chemical shift anisotropy (CSA) ranging from 261 to 1485 ppm. We observe that tetrahedral and octahedral complexes 1 and 4 with higher symmetry exhibit lower CSA and C_Q constant than square-pyramidal complexes 2 and 3. Furthermore, the C_Q value of 4.5 MHz measured for complex 4 is comparable to that of 3.3 MHz reported for the complex shown figure 25b.[35]

In conclusion, given the diversity of ligands and the structural differences among the complexes studied, it is challenging to establish a universal trend that applies to all of them. A broader set of complexes (more than seven) would be required to draw more general conclusions. Nevertheless, certain tendencies are evident: a higher coordination number leads to a more symmetrical environment around the metal center, which in turn results in lower C_Q and CSA values as well as more shielded chemical shifts.

Another observable trend is that the more oxygen ligands directly coordinated to Mo (i.e., in the first coordination sphere), the lower the isotropic chemical shift (more shielded signal). In contrast, an increase in carbon-based ligands, particularly carbenes and bulky neosilyl groups, leads to higher chemical shifts (deshielded signal).

A noticeable trend as well is that greater distortion from ideal geometry, as in square-pyramidal complexes, leads to higher C_Q and CSA due to the uneven distribution of the electronic environment around Mo.

5.5. Results of ^{95}Mo DFS-QCPMG for imido and bisimido complexes

The isotropic chemical shifts and anisotropic NMR parameters for the series of Mo(VI) complexes 5 (ArN)Mo(O-C(CF_3)$_3$)$_2$(CHR^3), 6 (ArN)Mo(DME)(OTf)$_2$(CHR^3) and 7 (ArN)$_2$Mo(C-^{t}Bu)$_2$ show strong variations between the different complexes (see table 5).

In complex 5, the Mo center is coordinated by two strongly electron-withdrawing tris(trifluoromethoxy) (O(CF_3)$_3$) ligands and a carbene ligand (CHR^3), resulting in a distorted tetrahedral geometry and coordination number of 4. In line with the data reported by Berkson *et al.*,[34] a pronounced deshielding is observed in such complexes containing fluor alkoxide ligands, reflecting their strong electron-withdrawing character. The degree of fluorination of this complex (12 F) is close to that of complex 1F$_3$ (9 F) and both complexes exhibit similar isotropic chemical shifts and CSA (δ_{iso} = 330 ppm and $|\delta_{CSA}|$ = 600 ppm for 1F$_3$ as shown in table S3.1 of ref.[34]). The C_Q constant of tetrahedral complex 5 (4.45 MHz) is similar with that of complex 1, which is also tetrahedral.

In complex 6, the coordination of Mo atom by triflate ligands containing electron-withdrawing groups CF_3 further reduces the electron density near molybdenum and hence, increases the isotropic chemical shift of this nucleus, which reaches 545 ppm.[38] The octahedral geometry of the complex 6 leads to moderate quadrupolar coupling (C_Q = 4.0 MHz).

Table 5. *^{95}Mo ssNMR parameters for imido complexes 5 and 6 and bisimido complex 7 determined by the simulation of NMR spectra using ssNake software.*

	NMR Data	δ_{iso} (ppm)	C_Q (MHz)	η_Q	δ_{CSA} (ppm)	η_{CSA}	Euler Angles α β γ (°)	W_L 18.8 T (kHz)	W_L 28.2 T (kHz)
Complex 5	(ArN)Mo(O-C(CF_3)$_3$)$_2$(CHR^3)	330	4.45	0.97	690	0.8	0 20 0	**4.6**	**3.2**
Complex 6	(ArN)Mo(DME)(OTf)$_2$(CHR^3)	545	4	0.2	577	1	0 55 35	**2.9**	**1.8**
Complex 7	(ArN)$_2$Mo(C-^{t}Bu)$_2$	892	7.6	0.4	1485	0	0 81 10	**10.5**	-

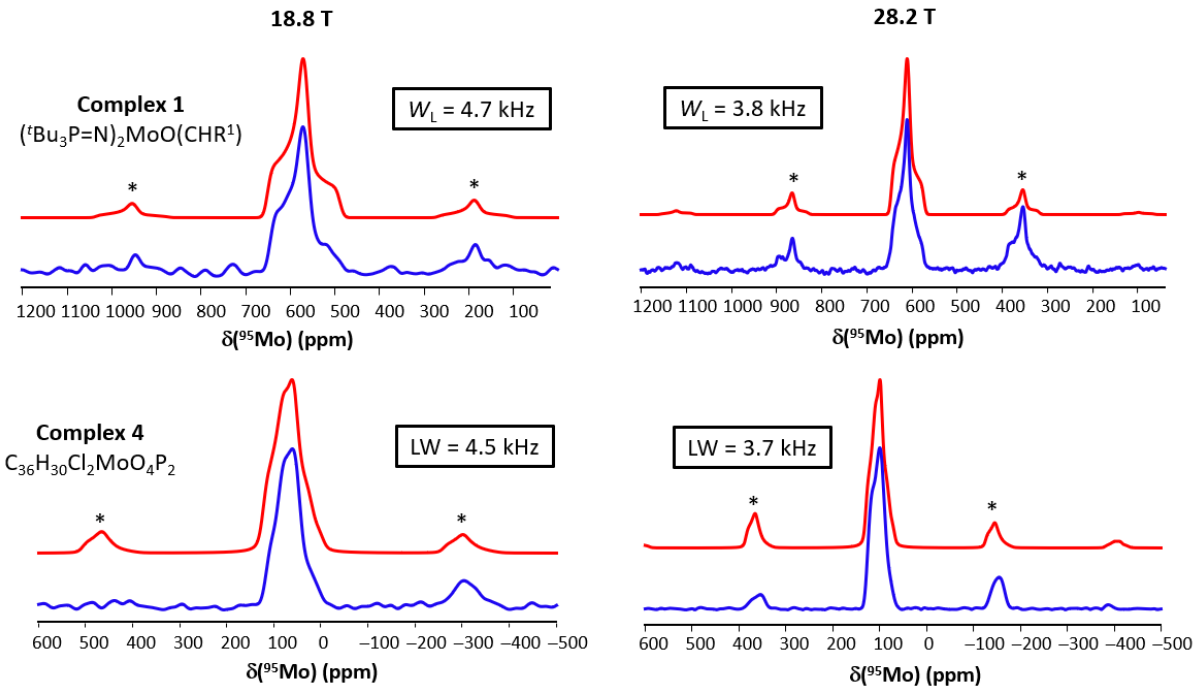

***Figure* 26.** *1D DFS-QCPMG ^{95}Mo ssNMR spectra of complexes 5 (top) and 6 (bottom) acquired at 18.8 (left) and 28.2 T (right) with ν_R = 20 kHz. Blue: experimental spectra; red: simulated spectra using ssNake software. *Spinning side bands*

In bis-imido complex 7, the two imido ligands, which are strong π-donors, and the two carbene ligands yield larger deshielding with δ_{iso} = 892 ppm (see figure 27). Large C_Q constant (7.6 MHz) and CSA (1485 ppm) are also consistent with those measured for complex 3 with carbene ligands.

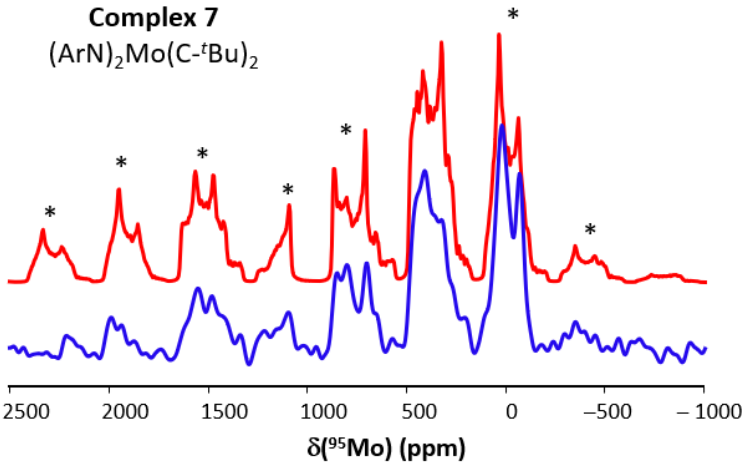

***Figure 27**. 1D DFS-QCPMG ^{95}Mo ssNMR spectra of bis-imido complex 7 acquired at 18.8 T with ν_R = 20 kHz.* Blue: experimental spectra; red: simulated spectra using ssNake. **Spinning side bands*

As a conclusion, we were able to extract NMR parameters from ^{95}Mo NMR spectra for a diverse set of complexes. Notably, the isotropic and anisotropic chemical shifts span a very wide range, from about 100 up to 1500 ppm, while the quadrupole coupling constants range between 4 and 13 MHz, with most values centered between 4 and 8 MHz. These broad distributions highlight the significant influence of ligand environments on the electronic structure of the molybdenum center. While these results demonstrate the wide variation of ^{95}Mo NMR parameters accessible through ligand modification, they also reveal the complexity of drawing correlations between NMR parameters and the coordination of Mo atom.

6. Calculation of NMR parameters using DFT: periodic approach

6.1. Calculation of ^{95}Mo NMR parameters using GIPAW method

To link the ^{95}Mo NMR parameters to the local environment of Mo metal, it is useful to be able to predict these parameters from a structural model. For that purpose, we calculated the ^{95}Mo NMR parameters of the investigated molecular complexes determined by diffraction and compared these calculated parameters to those measured experimentally. Initially we employed density functional theory (DFT) and a periodic approach to calculate the ^{95}Mo NMR parameters of molecular complexes. This approach relies on the GIPAW method[39], which is suitable for crystalline compounds. The VASP calculation code uses pseudopotentials to reconstruct the all-electron response, which reduces the computational cost and time and maintains high accuracy.

At first, a geometry optimization was performed for all the structures. The calculations were carried out with the VASP 6.4.1 software[40] and the PAW pseudopotentials[41] used are listed in Table 6 The optimization took up to approximately 24 hours for systems with a number of atoms between 400 to 800 and 48 hours for systems including atoms in the range of 800 to 1100 (because of their higher numbers of electrons). Similar computation times were necessary to calculate NMR parameters. In our calculations, the GGA-type functional developed by Perdew, Burke and Ernzerhof (PBE) was used.[42] The calculations

were performed from the .cif files from The Cambridge Structural Database (CCDC) or directly from experimental XRD. The accuracy of the crystallographic data depends on the diffraction methods, such as X-rays or neutrons, and the type of sample, either powder or single crystal. The relaxation of the positions of the atoms allowed us to find the most stable, lowest-energy structure. The conjugate gradient algorithm was adopted to relax the position of the atoms. The convergence criteria were set at 0.02 eV/Å for the force acting on the atoms, and the stress tensor components must be less than 0.005 eV/Å^3.

Table 6. *List of pseudopotentials used for each atom.*

Atoms	Pseudopotential	Notation (VASP 6.4.1)
Mo	PAW	Mo_sv
O	PAW	O
C	PAW	C
H	PAW	H
Cl	PAW	Cl
P	PAW	P
N	PAW	N
Si	PAW	Si
Br	PAW	Br

The GIPAW algorithm developed by Pickard and Mauri allows the calculation of chemical shift and electric field gradient (EFG) tensors. The VASP software uses the Herzfeld-Berger convention (See Eq. 35 - 37) for chemical shift (δ_{iso}), span (Ω) and chemical shift asymmetry (κ). [43]

$$\delta_{iso} = \frac{1}{3}(\delta_{11} + \delta_{22} + \delta_{33}) \quad \text{(Eq. 35)}$$

$$\Omega = (\delta_{11} - \delta_{33}) \quad \text{(Eq.(36)}$$

$$\kappa = 3\frac{(\delta_{22} - \delta_{iso})}{\Omega} \quad \text{(Eq. 37)}$$

where the principal components of chemical shift tensor, {δ_{11}, δ_{22}, δ_{33}}, are labeled by decreasing chemical shift order, *i.e.* $\delta_{11} \geq \delta_{22} \geq \delta_{33}$. The results are then converted from the Herzfeld-Berger convention to the Haeberlen convention (Eq. 38 - 40) since the ssNake software uses this convention to simulate NMR spectra. (Eq. 38)

(Eq. 40)

$$\delta_{iso} = \frac{1}{3}(\delta_{XX} + \delta_{YY} + \delta_{ZZ})$$

$$\delta_{CSA} = (\delta_{ZZ} - \delta_{iso})$$

$$\eta_{CS} = \frac{(\delta_{YY} - \delta_{XX})}{\delta_{CSA}}$$

where the principal components of the chemical shift tensor $\{\delta_{XX}, \delta_{YY}, \delta_{ZZ}\}$ are ordered according to their separation from the isotropic value: $|\delta_{ZZ}-\delta_{iso}| \geq |\delta_{XX}-\delta_{iso}| \geq |\delta_{YY}-\delta_{iso}|$.

According to Bloch's theorem,[44] the calculations can be restricted to the first Brillouin zone whose dimensions depend on the lattice parameters and the symmetry elements of the crystal. Monkhorst-Pack grids allow sampling the Brillouin zone and the point density *k* was tested between 1x1x1 and 1x5x1 fixed according to the lattice parameters of each compound.[45]

The wave function is defined by plane waves having kinetic energy less than the cut-off energy ($E_{cut\text{-}off}$). For all model compounds, the electric field gradient and chemical shift tensors converge for a cut-off energy between 600 eV to 1000 eV. For most systems, a plane-wave cutoff energy of 600 eV was sufficient to ensure that the electrical and geometric improvements converged consistently. However, for a few complexes, convergence of total energy and forces did not meet expectations at this value, most likely due to the existence of harsher PAW potentials and shorter metal-ligand bond lengths. For these complexes, the cutoff energy was raised to 800 or 1000 eV, ensuring smooth convergence of the optimizations. Table 7 below presents the lattice parameters for each complex with the corresponding *k*-points grid and $E_{cut\text{-}off}$ used during the calculation.

Table 7. *Set of parameters used for each complex for the periodic approach calculation using VASP software.*

Molecular Complexes	Lattice Parameters	*k*-point Grid	$E_{cut\text{-}off}$ (eV)
Complex 1 $(^tBu_3P{=}N)_2MoO(CHR^1)$	*a* = 12.7 A° *b* = 16.7 A° *c* = 16.3 A°	1 x 1 x 1	1000
Complex 2 $(^tBu_3P{=}N)_2Mo{=}O\text{-}Cl_2$	*a* = 13 A° *b* = 13.4 A° *c* = 16.6 A°	1 x 1 x 1	600
Complex 3 $(^tBu_3CH_2O)_2MoO(CH_2R^2)$	*a* = 21 A° *b* = 6 A° *c* = 21 A°	1x 5 x 1	800
Complex 4 $C_{36}H_{30}Cl_2MoO_4P_2$	*a* = 19 A° *b* = 10 A° *c* = 18 A°	1 x 3 x 1	600
Complex 5 $(ArN)Mo(O\text{-}C(CF_3)_3)_2(CHR^3)$	*a* = 7 A° *b* = 19 A° *c* = 18 A°	3 x 1 x 1	600
Complex 6 $(ArN)Mo(DME)(OTf)_2(CHR^3)$	*a* = 17.5 A° *b* = 19 A° *c* = 10 A°	1 x 1 x 3	600
Complex 7 $(ArN)_2Mo(C\text{-}^tBu)_2$	*a* = 18 A° *b* = 11 A° *c* = 17 A°	1 x 3 x 1	1000

6.2. Correlation curves between experimental and calculated δ_{iso} and C_Q

6.2.1. Phosphomolybdates and simple systems

A first study of the calculation of ^{95}Mo NMR parameters using DFT and periodic approach was carried out in our team in 2019 for crystalline phosphomolybdates, in which molybdenum adopts octahedral or tetrahedral coordination. The motivation to study these phophomolybdates is that phosphate glasses incorporating MoO_3 are potential candidates for nuclear waste storage or solid electrolytes. It has been shown that the incorporation of MoO_3 leads to the formation of a more rigid mixed glass network containing P–O–Mo and/or Mo–O–Mo bonds besides P–O–P linkage. In particular, Bridge *et al.*[46] showed that, in the $MoO_3P_2O_5$ system, the elastic modulus varies with the degree of polymerization of the phosphate network. These variations have been correlated with the local structure of the crystallized compounds, and more particularly with the size of the rings formed by the chaining of the MoO_6 and PO_4 polyhedra. The evolution of properties is therefore closely

linked to the local structure of molybdenum: when the available oxygens become insufficient to maintain isolated units, Mo–O–Mo bonds are formed, influencing network connectivity and electronic transfers.[47] This increased connectivity results in a reduction of the coefficient of thermal expansion and a non-linear evolution of mechanical properties. The improvement of the thermal and electrical properties of these materials requires a thorough understanding of the local structure of molybdenum. The structure of phosphomolybdates glass has been studied by nuclear magnetic resonance by combining a spin 1/2 nucleus, ^{31}P, and a quadrupolar nucleus, ^{95}Mo. However, the local coordination of molybdenum remains uncertain and continues to be debated. Therefore, to link the ^{95}Mo NMR parameters to the local coordination of Mo atom, DFT calculations on crystalline phosphomolybdates were carried out in our team.

A large set of crystalline phosphomolybdates were studied, including $CsMoO_2PO_4$ and $KMoO_2PO_4$ containing octahedral Mo environments as well as $Zr_2MoO_4(PO_4)_2$ and Rb_2MoO_4 with tetrahedral Mo environments. The experimental and calculated NMR parameters of ^{95}Mo nuclei in these phosphomolybdates were compared by plotting correlation curves. These correlation curves allow us to determine the references for calculating the isotropic chemical shift. In addition, the slope of the curve, which should theoretically be equal or close to 1, gives an estimate of the accuracy of the calculations.

As seen in Figure 28, the regression curves between calculated and experimental isotropic chemical shifts differ between MoO_6 and MoO_4 local environments:

MoO_6: $\delta_{iso}^{calc} = 0.88\ \delta_{iso}^{exp} + 944$ (Eq. 41)

MoO_4: $\delta_{iso}^{calc} = 1.02\ \delta_{iso}^{exp} + 877$ (Eq. 42)

The slopes of the curves are close to 1, which confirms the precision of the method in describing the electronic density around the molybdenum atom in these crystalline materials. The good correlation between the calculated and experimental chemical shift anisotropy (CSA) with a coefficient of determination $R^2 = 0.99$ proves that the total mesh optimization accurately describes the local structure.

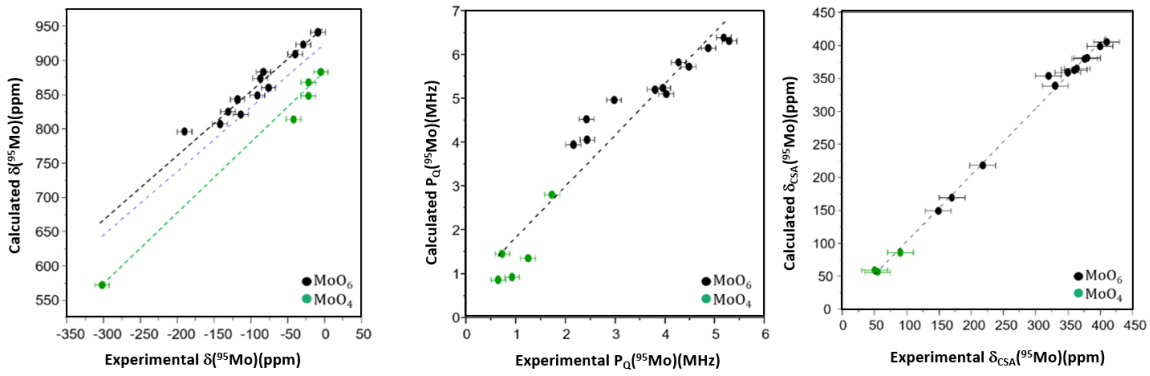

Figure 28. *Correlation curves between the experimental and calculated ^{95}Mo isotropic chemical shift (left), P_Q (middle) and C_Q (right) from the optimized structures using periodic approach*

The quadrupolar product $P_Q = \left(C_Q\sqrt{1+\frac{\eta_Q}{3}}\right)$ determines the quadrupolar-induced shift (QIS). It constitutes a very precise imprint of the local environment of the nucleus. The correlation curve between calculated and experimental quadrupolar product shows that the components of the EFG tensor are slightly overestimated by the calculations, as indicated by the slope of the regression curve below:

$$P_Q^{calc} = 1.17\ P_Q^{exp} + 0.65. \qquad \text{(Eq. 43)}$$

Therefore, the different correlation curves show that after optimization of the structure, the periodic approach calculations allow to predict accurately the NMR parameters of ^{95}Mo nuclei in phosphomolybdates, in particular the isotropic chemical shift and the CSA, whereas the quadrupole products are slightly overestimated. However, the variation of NMR parameters in such materials occurs over a relatively narrow range of a few hundred ppm (i.e., −350 to 0 ppm for δ_{iso}). The following section, carried out during my thesis, presents this approach was applied to molybdenum molecular complexes.

6.2.2. Molecular Complexes

Building on this foundation, we expanded our research to the molybdenum-based precursors that can be afterwards grafted on amorphous supports. The diversity of ligands surrounding the metal center gives these systems a more complex structural environment. As a result, their NMR spectra show more complicated line shapes caused by both quadrupolar interaction and chemical shift anisotropy. The performance of a potential can be affected by the chemical environment of the atom in the crystal.

From the experimental values, we observed greater variations in the NMR parameters of the complex systems compared to the phosphomolybdates, indicating a wider range of values and therefore a more complex behavior to interpret. The coefficient of determination of the chemical shift regression line of the molecular complexes is low and equal to $R^2 = 0.688$. The equation of the regression is the following:

$$\delta_{\mathrm{iso}}^{\mathrm{calc}} = 0.75\ \delta_{\mathrm{iso}}^{\mathrm{exp}} + 1036 \qquad \text{(Eq. 44)}$$

The slope of the curve, 0.75, significantly deviates from the theoretical value of 1. This deviation means that while there may still be correlation, the scaling between theory and experiment is not perfect. The plane wave cutoff energy, *k*-point sampling, and convergence of atomic geometries have a significant impact on the reliability of the results; they must be properly optimized. Inadequate cutoff values or *k*-point grids can lead to inaccuracies in the electrical structure and, consequently, in the calculated shielding. However, different cutoff energies and *k*-point grids were used in order to obtain the best values which are listed in Table 7. The quality of PAW pseudopotentials must also be carefully evaluated, especially when describing core and semi-core states, because errors can propagate into the predicted NMR properties.

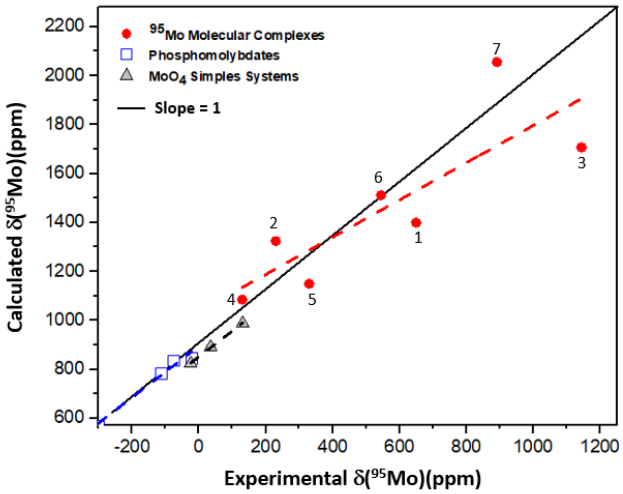

Figure 29. *Correlation curves between the experimental and calculated ^{95}Mo isotropic chemical shifts for different Mo-containing solids. The calculations were carried out on optimized structures using periodic approach. The complexes are identified by their number in the figure.*

The regression equations of C_Q and δ_{CSA} for molecular complexes are the following:

$$C_{\mathrm{Q}}^{\mathrm{calc}} = 0.45\ C_{Q}^{\mathrm{exp}} + 5.7 \qquad \text{(Eq. 45)}$$

$$\delta_{CSA}^{calc} = 0.27\,\delta_{CSA}^{exp} + 520 \qquad \text{(Eq. 46)}$$

Although these results show some correlation between the experimental and calculated values, the poor slope (far from 1) and the low coefficient of determination R^2 = 0.09 and 0.4 for C_Q and δ_{CSA} respectively indicate that the model does not adequately describe the anisotropy around the Mo in the systems.

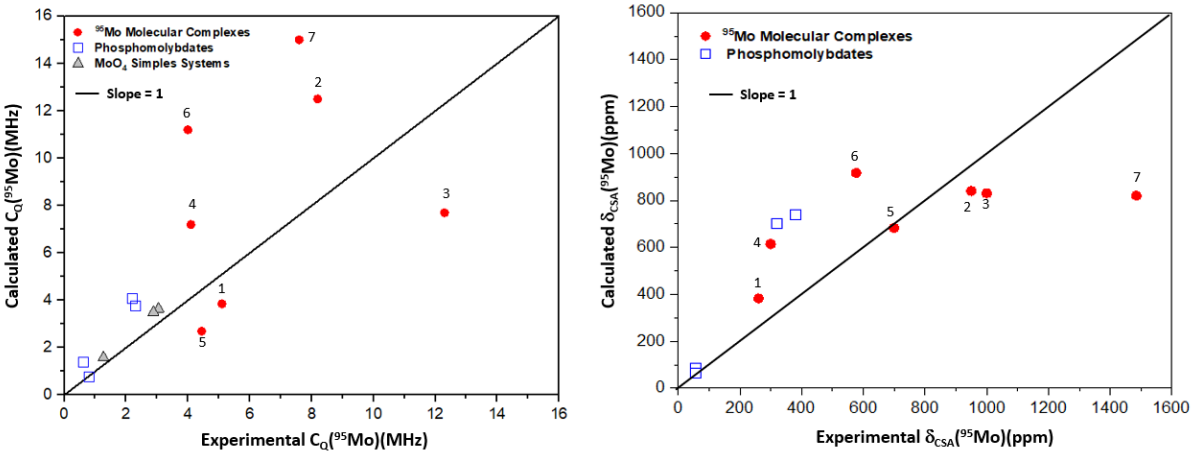

Figure 30. *Correlation curves between the experimental and calculated ^{95}Mo C_Q and δ_{CSA} for different Mo-containing solids. The calculations were carried out on the optimized structures using periodic approach.*

The chemical shielding tensor and hence δ_{iso} is a ground-state feature with a sum-over-states response function that relies on precise virtual orbital energies. C_Q is obtained from the electric field gradient, a ground-state observable that is very sensitive to electron charge density distributions around the nucleus. According to Autschbach and Srebro,[48] EFGs and NMR shielding constants reveal different aspects of electron density, with EFGs being more immediately affected by any delocalization error (DE) in the functional. The PBE functional belongs to the Generalized Gradient Approximation (GGA) family, which is known to suffer from DE that is an over delocalization of electron density, particularly in transition metal complexes. This results in an inaccurate description of the bonds especially when strong σ and π donor ligands are attached to the metal center. DE has a significant impact on quadrupolar couplings due to its reliance on anisotropic electron density distributions. This is consistent with the lower slope (e.g., 0.45) shown for the C_Q regression line. As pointed in the Cuny *et al.* paper,[49] PAW-based periodic computations can reasonably match chemical shielding but frequently fall short of quadrupolar couplings,

particularly for d^0 metals. The pseudopotentials may not fully reflect core-core and core-valence relativistic interactions, which are required for exact EFG computations.

The isotropic chemical shift is in better agreement with experimental results, as evidenced by a regression slope of approximately 0.75. This better agreement can be attributed to a lower sensitivity to relativistic effects. According to Cuny *et al.*,[49,50] δ_{iso} represents an averaged value across the entire shielding tensor. This averaging makes it less sensitive to minor structural perturbations, such as ligand distortions or thermal fluctuations around a fixed geometry. However, although relativistic effects are essential, they have a limited impact on the isotropic shielding of d metals. They found also that the scalar and spin-orbit corrections had only a minimal impact on the estimated δ_{iso} and their effect is cancelled out when the shifts are referenced to a common standard, these features are tested in the next section. The use of periodic boundary conditions (as implemented in VASP) improves the accuracy and reliability of anticipated δ_{iso} values by accounting for solid-state intermolecular interactions.[49] Despite these improvements, the slope of the regression remains less than one, showing that PAW pseudopotentials generated does not describe perfectly the electronic structure of atoms hence, inhibiting full quantitative agreement with experiment. [50]

Given the limitations of the periodic DFT calculations, particularly the poor correlation of quadrupolar coupling constants, we decided to switch to a molecular approach using the Amsterdam Density Functional (ADF) package.

7. Structural study by DFT calculation: Molecular approach

Calculations of the ^{95}Mo magnetic shielding tensors were performed using the gauge-including atomic orbital (GIAO) approach,[51] as available in the Amsterdam Modeling Suite (AMS 2024.106),[52,53] with the tetrahedral $[MoO_4]^{2-}$ unit employed as the reference molecule. A single molecule derived from the energy-optimized solid-state geometry (as obtained from VASP) served as the structural input. Both the generalized gradient approximation functional PBE [42] and the hybrid functional PBE0 [54] were applied in conjunction with the zeroth-order regular approximation (ZORA) relativistic Hamiltonian,

at the scalar (SR) and scalar plus spin–orbit (SO) levels.[55–57] The PBE0 mixes the PBE exchange energy and Hartree–Fock (HF) exchange energy with 25% HF exchange, along with the full PBE correlation energy. Furthermore, the fraction of HF exchange with respect to PBE exchange was modified and calculations were carried out also for 15 and 40% of HF exchange. For PBE and PBE0 calculations including ZORA/SO, the exchange–correlation response kernel was corrected.[58] Slater-type basis sets were employed, specifically triple-ζ plus two polarization functions (TZ2P) for molybdenum, double-ζ polarized basis (DZP) for non-hydrogen atoms, and double-ζ basis (DZ) for hydrogen.[59] In order to enhance the accuracy, an extended scheme was also tested, combining quadruple--ζ with four polarization functions (QZ4P) on Mo with TZ2P for the remaining elements. Such levels of theory have been shown to yield reliable results for ^{95}Mo NMR calculations.[60,34] The correlations between experimental and estimated ^{95}Mo isotropic chemical shift values were tested, within both scalar and spin-orbit frameworks. The former stems both from (i) the mass-velocity correction, i.e., fact that for heavy elements, such as Mo, the velocities of core and inner-valence electrons become a significant fraction of the speed of light and hence, their relativistic mass increases, which affects their motion and (ii) very rapid quantum fluctuations in the position of the electrons due to Darwin term. The spin-orbit term arises from the interaction between electrons' spin angular momentum and their orbital motion in the electric field of the nucleus, which generates a magnetic field. The results of the regression curves using TZ2P/DZP/DZ basis sets are displayed in figure 31.

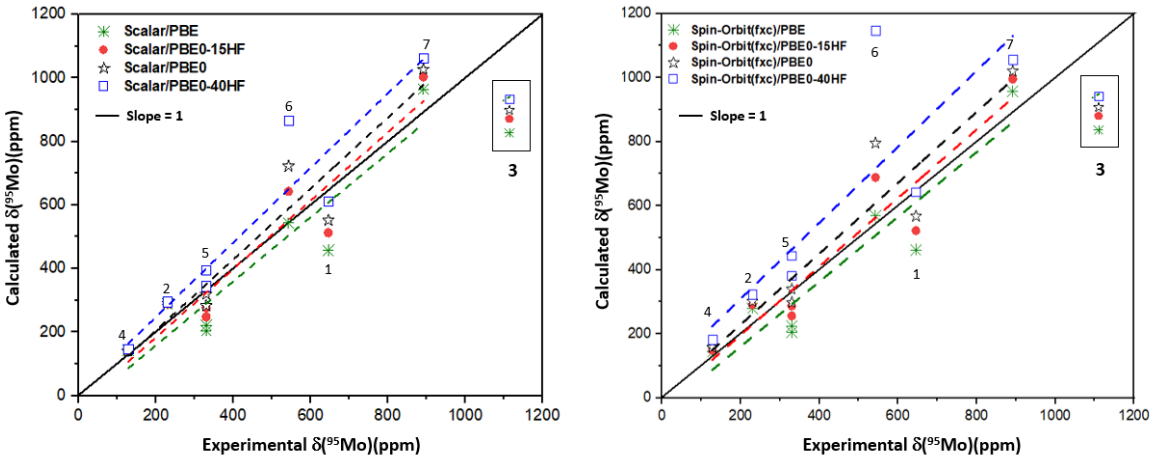

Figure 31. *Correlation curves between experimental and calculated ^{95}Mo isotropic chemical shifts of the investigated Mo molecular complexes. The calculations were carried out on optimized structures using molecular approach with TZ2P/DZP/DZ basis sets considering scalar effects (left) and spin-orbit (right)*

The ADF computations took into account both scalar and spin-orbit relativistic effects. The scalar relativistic approach allows for mass-velocity and Darwin corrections,[54] which are required for heavy elements like molybdenum.[61] The spin-orbit treatment expands on this by explicitly incorporating spin-orbit coupling via the two-component ZORA formalism, which can have a considerable impact on magnetic properties such as NMR chemical shifts.[62] Overall, the calculated chemical shifts from ADF showed a reasonable correlation with the experimental data in terms of the observed trends (with the exception of compound 3). Incorporating spin–orbit relativistic effects did not lead to a noticeable improvement compared with the scalar relativistic treatment. This is likely related to the nature of a second-row transition metal such as Mo^{6+} with d^0 configuration. Among the tested functionals, PBE0 with 15% HF exchange provided the closest match to the experimental shifts, whereas increasing the HF contribution to 40% gave no benefit. Consequently, the ^{95}Mo isotropic chemical shifts were re-examined using only the scalar relativistic Hamiltonian at the higher QZ4P/TZ2P level of theory (See Figure 32). Across both basis set combinations (TZ2P/DZP/DZ and QZ4P/TZ2P), PBE0 with 15% HF exchange again gave the most reliable agreement with experimental shifts. Nonetheless, the improvement over the GGA PBE functional was marginal, supporting the use of PBE as a practical choice for periodic VASP calculations.

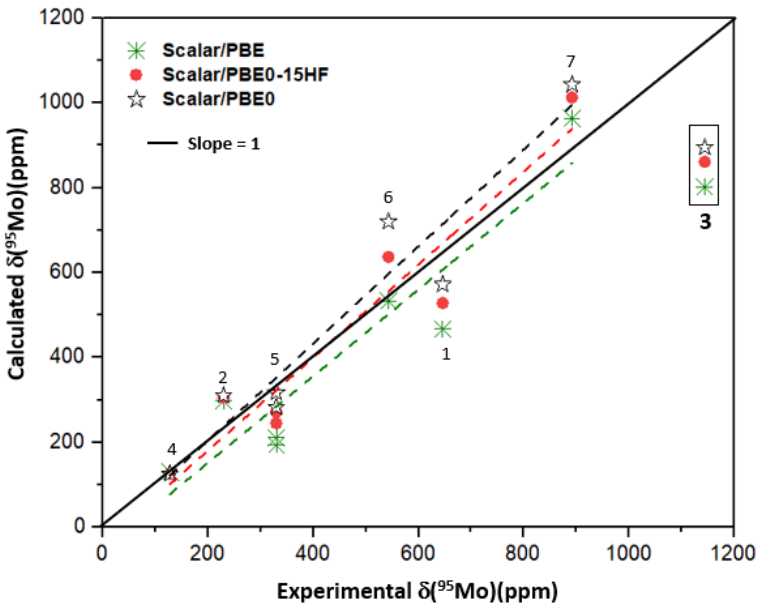

Figure 32. *Correlation curves between experimental and calculated ^{95}Mo isotropic chemical shifts of the investigated Mo molecular complexes. The calculations were carried out on the optimized structures using molecular approach with QZ4P/TZ2P basis sets considering scalar relativistic effects.*

Table 8. *Correlation equations of isotropic chemical shift relative to each functional employing TZ2P/DZP/DZ and QZ4P/TZ2P basis sets considering scalar and spin-orbit effects*

Functionals	Correlation equations	Coefficient of determination
TZ2P/DZP/DZ basis sets		
Scalar PBE	$\delta_{iso}^{calc} = 1.01\ \delta_{iso}^{exp} - 43$	R^2 = 0.85
Scalar PBE0	$\delta_{iso}^{calc} = 1.1\ \delta_{iso}^{exp} - 18$	R^2 = 0.91
Scalar PBE0 – 15 % HF	$\delta_{iso}^{calc} = 1.07\ \delta_{iso}^{exp} - 31$	R^2 = 0.90
Scalar PBE0 – 40 % HF	$\delta_{iso}^{calc} = 1.17\ \delta_{iso}^{exp} + 13$	R^2 = 0.88
Spin-orbit PBE	$\delta_{iso}^{calc} = 1.01\ \delta_{iso}^{exp} - 42$	R^2 = 0.88
Spin-orbit PBE0	$\delta_{iso}^{calc} = 1.1\ \delta_{iso}^{exp} + 7$	R^2 = 0.88
Spin-orbit PBE0 – 15 % HF	$\delta_{iso}^{calc} = 1.06\ \delta_{iso}^{exp} - 13$	R^2 = 0.89
Spin-orbit PBE0 – 40 % HF	$\delta_{iso}^{calc} = 1.18\ \delta_{iso}^{exp} + 71$	R^2 = 0.71
QZ4P/TZ2P basis sets		
Scalar PBE	$\delta_{iso}^{calc} = 1.01\ \delta_{iso}^{exp} - 43$	R^2 = 0.85
Scalar PBE0	$\delta_{iso}^{calc} = 1.1\ \delta_{iso}^{exp} - 18$	R^2 = 0.91
Scalar PBE0 – 15 % HF	$\delta_{iso}^{calc} = 1.07\ \delta_{iso}^{exp} - 31$	R^2 = 0.90

The regression curves of the chemical shift anisotropy are represented in figure 33 and regression equations are given in table 9. Overall, all calculation tests provided better agreement compared to the periodic approach. At the QZ4P/TZ2P level of theory, the comparison between computed and experimental scalar PBE0 functional yields the most reliable agreement, characterized by a slope approaching unity (1.06), high coefficient of correlation (0.92), and the lower overall error values. The PBE0 functional with 15% HF exchange resulted in almost the same amount of agreement. For the lower level of theory (TZ2P/DZP/DZ), spin-orbit coupling shows only a minimal impact on overall correlation.

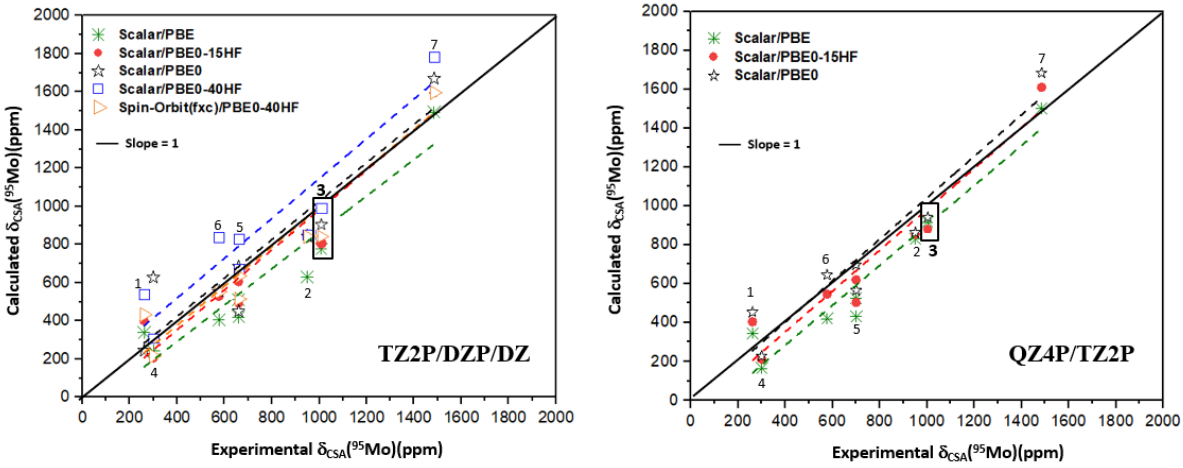

***Figure 33**. Correlation curves between the experimental and calculated ^{95}Mo chemical shift anisotropy of the investigated Mo molecular complexes. The calculations were carried out on the optimized structures using molecular approach employing TZ2P/DZP/DZ and QZ4P/TZ2P basis sets considering scalar and spin-orbit effects*

***Table 9:** Correlation equations of chemical shift anisotropy relative to each functional employing TZ2P/DZP/DZ basis sets and QZ4P/TZ2P basis sets*

Functionals	Correlation equations	Coefficient of determination
TZ2P/DZP/DZ basis sets		
Scalar PBE	$\delta_{CSA}^{calc} = 0.95\ \delta_{CSA}^{exp} - 89$	R^2 = 0.89
Scalar PBE0	$\delta_{CSA}^{calc} = 1.0\ \delta_{CSA}^{exp} + 21$	R^2 = 0.84
Scalar PBE0 – 15 % HF	$\delta_{CSA}^{calc} = 1.04\ \delta_{CSA}^{exp} - 65$	R^2 = 0.93
Scalar PBE0 – 40 % HF	$\delta_{CSA}^{calc} = 1.04\ \delta_{CSA}^{exp} + 102$	R^2 = 0.88
Spin-orbit PBE0 – 15 % HF	$\delta_{CSA}^{calc} = 1.02\ \delta_{CSA}^{exp} - 33$	R^2 = 0.93
QZ4P/TZ2P basis sets		
Scalar PBE	$\delta_{CSA}^{calc} = 1.02\ \delta_{CSA}^{exp} - 126$	R^2 = 0.92
Scalar PBE0	$\delta_{CSA}^{calc} = 1.06\ \delta_{CSA}^{exp} - 23$	R^2 = 0.92
Scalar PBE0 – 15 % HF	$\delta_{CSA}^{calc} = 1.04\ \delta_{CSA}^{exp} - 67$	R^2 = 0.92

A good correlation is observed between calculated and experimental data when considering both scalar and spin orbit effects for isotropic chemical shift. However, the introduction of the latter one only causes modest differences. This is consistent with Cuny *et al.*[49,50] results since the isotropic chemical shifts are referenced to a common standard. The slopes of correlation equations and coefficients of determination (R^2 values ranging from 0.85 to 0.99) are comparable between the two approaches. The absolute isotropic shielding value of the reference showed minimal sensitivity to variations in the functional, particularly with respect to the %HF exchange.[63] For chemical shift anisotropy, this level of

theory appears to accurately represent the local electrical environment of Mo(VI) centers, allowing for the reproduction of experimental values.

The C_Q results obtained from the molecular approach are significantly better than those obtained from the periodic calculations, although there is still room for improvement since they remained poor at both levels of theory.[34,35] At the QZ4P/TZ2P level of theory, the comparison between computed and experimental C_Q indicates that the scalar PBE0 functional yields the most reliable agreement, characterized by a slope approaching unity (1.09) and the highest coefficient of correlation (0.64). The scalar PBE0 with 15% HF exchange provides slightly reduced accuracy, whereas the scalar PBE functional systematically overestimates C_Q values, resulting in the weakest correlation. Like the periodic approach, the molecular counterpart used in this section fails to predict accurately the isotropic chemical shift and C_Q constant of complex 3. For this reason, we chose to remove the data for this compound from the regression analysis, even if the corresponding data points are displayed in figures 32 to 34 to show the discrepancy observed. However, to assess whether this deviation arises from model limitations, calculations were carried out for a three-unit cluster model along the Mo=O axis. The central fragment was computed at the same level of theory (TZ2P/DZP/DZ), while the two terminal units were simplified using the SZ basis set.[64,65] This extended model did not produce any substantial improvement. These results indicate that further refinement of the computational approach is required to predict NMR parameters of complex 3.

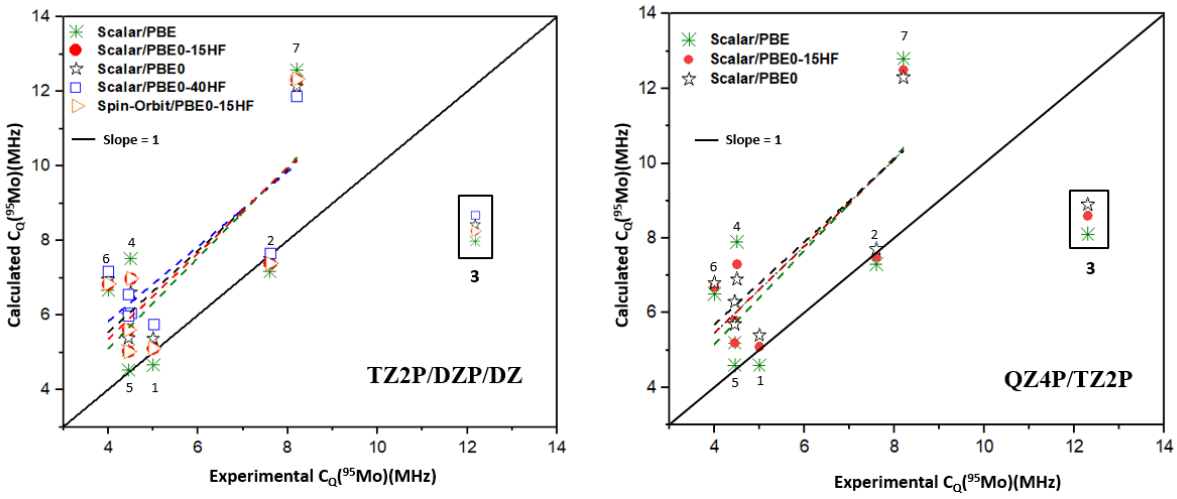

Figure 34. *Correlation curves between the experimental and calculated ^{95}Mo C_Q constants of the investigated Mo molecular complexes. The calculations were carried out on the optimized structures using molecular*

approach considering scalar and spin-orbit effects employing TZ2P/DZP/DZ basis sets and QZ4P/TZ2P basis sets

Table 10. *Correlation equations of quadrupole coupling constant relative to each functional employing TZ2P/DZP/DZ basis sets and QZ4P/TZ2P basis sets.*

Functionals	Correlation equations	Coefficient of determination
TZ2P/DZP/DZ basis sets		
Scalar PBE	$C_Q^{calc} = 1.21\, C_Q^{exp} + 0.22$	R^2 = 0.55
Scalar PBE0	$C_Q^{calc} = 1.09\, C_Q^{exp} + 1.17$	R^2 = 0.63
Scalar PBE0 – 15 % HF	$C_Q^{calc} = 1.17\, C_Q^{exp} + 0.77$	R^2 = 0.60
Scalar PBE0 – 40 % HF	$C_Q^{calc} = 1.0\, C_Q^{exp} + 1.8$	R^2 = 0.62
Spin-orbit PBE0 – 15 % HF	$C_Q^{calc} = 1.14\, C_Q^{exp} + 0.77$	R^2 = 0.60
QZ4P/TZ2P basis sets		
Scalar PBE	$C_Q^{calc} = 1.25\, C_Q^{exp} + 1.2$	R^2 = 0.55
Scalar PBE0	$C_Q^{calc} = 1.09\, C_Q^{exp} + 0.6$	R^2 = 0.64
Scalar PBE0 – 15 % HF	$C_Q^{calc} = 1.12\, C_Q^{exp} + 0.8$	R^2 = 0.60

8. Conclusion

This first part of this chapter shows the difficulties of precisely predicting ^{95}Mo NMR parameters in molybdenum-based compounds. Both ligand identity and coordination geometry have a significant impact on isotropic chemical shift, quadrupolar coupling constant, and chemical shift anisotropy.

Periodic computations accurately predict isotropic chemical shifts in well-ordered systems like phosphomolybdates (R^2 = 0.98). However, constraints in pseudopotentials and delocalization error in GGA functionals impeded accurate prediction of quadrupolar parameters (C_Q) in the diverse molecular complexes we investigated. As a conclusion, to isolate and understand the impact of specific ligand changes on NMR parameters, research should ideally use well-defined and simplified model systems, since it is not that easy for industrially relevant molybdenum precursors. These compounds have diverse coordination environments, making them more difficult to model. To improve accuracy, we adopted an all-electron molecular approach based on the ADF package, which allows for more control over relativistic treatments and electron localization. Although employing the larger QZ4P basis set for molybdenum improves the theoretical treatment, a systematic overestimation persists.

Part II: Synthesis and characterization of grafted molybdenum-based catalyst

After the study of molecular-based catalysts and their well-defined coordination environments, we now shift our focus to supported systems that better reflect industrial realities. While molecular models provide insights into the electronic structure of active sites, they cannot capture the heterogeneity and surface interactions that characterize supported catalysts. In industrial procedures, olefin metathesis is often carried out utilizing oxide-supported transition metal oxides, such as MoO_3/SiO_2 or WO_3/SiO_2. The following section delves into these grafted systems, with a particular emphasis on their structural characterization and reactivity in olefin metathesis.

9. Overview on the ^{17}O MAS NMR structural characterization of W(VI) and Mo(VI)-oxo species active in olefin's metathesis

The aim of this section is to revisit previous efforts to characterize the local environment of tungsten and molybdenum centers after grafting onto silica supports. In this context, ^{17}O MAS NMR has proven to be a powerful technique for probing the geometry and electronic structure of terminal oxo ligands, a key feature for many surface organometallic species. In particular, ^{17}O NMR parameters, namely the chemical shift, C_Q and CSA, provide insight into the nature of the grafting mode, whether mono- or bis-grafted, by revealing specific interactions between the oxo sites and the surface, including silanol groups.

9.1. The case of tungsten-based catalysts

Tungsten-based catalysts, specifically WO_3 dispersed on silica (WO_3/SiO_2), are commonly employed as pre-catalysts in olefin metathesis processes.[66] Mononuclear tungsten oxo species supported on silica have been identified as suitable analogs for the active sites in industrial WO_3/SiO_2 catalysts. Initially, pre-formed tungsten alkyl compounds such as $[W(=O)(CH_2{}^tBu)_3Cl]$ were used for grafting, but their complex synthesis limited broader application.[67]

A more practical approach includes selectively grafting commercially available [$WOCl_4$] onto partially dehydroxylated silica SiO_2, forming $WOCl_4$-SiO_2. These grafted pre-catalyst species are afterwards alkylated to form a catalytically active metal-carbene complex. Surface species have been comprehensively characterized using a combination of analytical techniques. However, for ^{17}O solid-state NMR, isotopic labelling with ^{17}O is required due to the very low natural abundance of this isotope (0.038%), in order to detect W=^{17}O NMR signal. Back in 2014, ^{17}O-labelled $WOCl_4$ was synthesized from the reaction of WCl_6 with ^{17}O-labelled $(Me_3Si)_2O$).[68] The resulting ^{17}O-enriched molecular precursor [$WOCl_4$] exhibited a single, well-defined resonance at 671 ppm with a C_Q of 1.0 MHz and CSA of −330 ppm, confirming the presence of a symmetric terminal W=O group in the molecular molecule. Grafting [$WOCl_4$] onto dehydroxylated SiO_2 at 700 °C resulted in the mono-grafted species [(≡SiO)$WOCl_3$]. The ^{17}O MAS NMR spectrum of this sample revealed a prominent resonance at 829 ppm with a C_Q value below 2.0 MHz, consistent with a square pyramidal geometry around tungsten, with the oxo ligand at the apical position. Grafting onto partly dehydroxylated silica $SiO_{2\text{-}200}$, which contains vicinal silanol groups, facilitates bipodal anchoring.[69] The W(VI)-Cl bonds undergo silanolysis, resulting in mostly bis-grafted tungsten oxo dichloride species [$(≡SiO)_2WOCl_2$], with a minor fraction of mono-grafted sites [(≡SiO)$WOCl_3$] in a 4:1 ratio.[66] The ^{17}O MAS NMR spectrum showed a broad signal composed of three components: a peak at 829 ppm corresponding to the mono-grafted species, a sharp minor signal at 480 ppm for an unidentified impurity, and a dominant resonance at 810 ppm assigned to the bis-grafted species [$(≡SiO)_2WOCl_2$]. The latter exhibited a large CSA of −650 ppm and a low estimated C_Q constant of 2.5 MHz, suggesting a square pyramidal structure with the oxo ligand at the apical position as well.[66] These results highlight the efficiency of the ^{17}O NMR approach in precisely probing the local geometric environment of the tungsten oxo moiety.

9.2. $MoOCl_4$ supported on $SiO_{2\text{-}200}$ and $SiO_{2\text{-}700}$

The analysis was extended to Mo(VI) oxo complexes to examine the applicability and robustness of ^{17}O NMR as a local probe in related systems. Schelimov suggested that bipodal Mo(VI)-oxo carbene molecules serve as active sites in industrial MoO_3/SiO_2 catalysts.[70] Therefore, it is proposed that [$MoOCl_4$], similar to [$WOCl_4$], could serve as a viable molecular precursor for generating Mo-based surface organometallic complexes.[70]

The oxygen NMR spectra of $MoOCl_4$ showed greater isotropic δ_{iso} and anisotropic δ_{CSA} chemical shifts compared to W(VI), with an increase of about 200 ppm. Theoretical NMR values calculated for the isolated [$MoOCl_4$] molecule, using a square-pyramidal geometry, differ only slightly from those derived using the periodic structure. After grafting on $SiO_{2\text{-}200}$ and $SiO_{2\text{-}700}$, both silica samples are deep green, indicating the presence of Mo complexes on the surface. However, the ^{17}O MAS NMR spectra did not reveal any distinct signal in the oxo region. Only weak signals, barely above noise, were observed between 500 and 1200 ppm, but no definitive assignments could be made. The absence of a clear signal in the oxo region could imply that, after grafting, molybdenum undergoes a change in oxidation state and becomes paramagnetic, interfering with the detection of surrounding atoms (particularly oxygen) in NMR. It is also possible that significant exchange mechanisms may lead to the dilution of the ^{17}O introduced with the precursor, rendering its concentration too low to be detected in the oxo region.

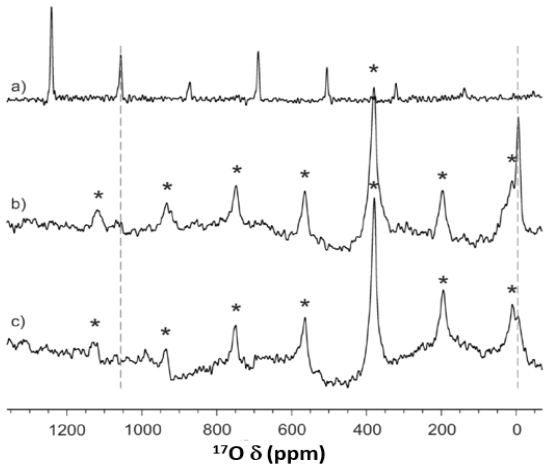

Figure 35. *1D ^{17}O MAS NMR spectra of (a) molecular $MoOCl_4$ complex and (b,c) identical complex supported on (b) $SiO_{2\text{-}700}$ and (c) $SiO_{2\text{-}200}$ acquired at 18.8 T with ν_R = 20 kHz. Dashed lines represent the position of the oxo ligand (high δ) and the silica domain (low δ).*

Overall, the absence of a clear oxo signal in the ^{17}O NMR spectra of supported $MoOCl_4$ reflects the limitations of the technique for surface-grafted Mo species and highlights the intrinsic complexity of molybdenum chemistry.

10. Synthesis of labelled $^{95}MoOCl_4$ grafted on SiO_2 supports

10.1. Reaction Conditions and synthesis of $^{95}MoOCl_4$

To overcome the limitations of probing the Mo=O environment via ^{17}O NMR spectroscopy, we used an alternative strategy based on direct observation of the metal center by ^{95}Mo NMR. Due to the low natural abundance (15.9%) and low gyromagnetic ratio of ^{95}Mo isotope ($|\gamma(^{95}Mo)/\gamma(^{1}H)| \approx 6.5\%$), isotopic enrichment was necessary. ^{95}Mo-enriched [$MoOCl_4$] was synthesized and then grafted onto activated silica and the resulting complexes were studied using ^{95}Mo MAS NMR spectroscopy, to assess the electrical and geometric environments of the active species. This approach should provide direct information into Mo-based frameworks relevant to grafted metathesis catalysts.

The synthesis was carried out in collaboration with colleagues from the CP2M-CPE Lyon laboratory. ^{95}Mo-labelled complexes are not commercially available. After negotiations with several suppliers, we obtained 278 mg of isotopically enriched molybdenum trioxide ($^{95}MoO_3$) from CortecNet, labelled with 94.3 atom % of molybdenum-95. This compound was used as the starting material to prepare $^{95}MoOCl_4$, which was then grafted and activated by alkylation. Due to the limited quantity of labeled material, most optimizations of the synthetic steps were carried out with non-labeled commercial MoO_3 to validate each step before using the labeled material.

The first step consisted of the reaction between $^{95}MoO_3$ and an excess of anhydrous $SOCl_2$ (thionyl chloride) placed in a spherical Schlenk flask under argon. The mixture was then heated to the boiling temperature of $SOCl_2$ (i.e.; 80 $\pm$ 20 °C) for 6 hours. The goal is to break two of the oxo ligands of the molybdenum trioxide, forming molybdenum oxytetrachloride. However, beyond 6 hours, the third oxo ligand might also be replaced by Cl, yielding $MoCl_6$ instead of tetrachloride molybdenum oxide.[71,72] This reaction time was optimized on unlabeled and commercial MoO_3 to avoid wasting the costly labeled precursor. The reaction occurring is the following: [73]

$$^{95}MoO_3 + 2\ SOCl_2 \rightarrow {}^{95}MoOCl_4 + 2\ SO_2$$

During this first step reaction, a color change to green-brown color with the presence of insoluble black residue is observed, suggesting the formation of impurities or reduced molybdenum species. Normally, $MoOCl_4$ should be dark green, a sign for the presence of Mo(VI). A first possibility is the formation of molybdenum hexachloride ($MoCl_6$) due to overheating of molybdic acid and thionyl chloride under anhydrous conditions and refluxing for several hours.[71] This may produce several molybdenum-containing chlorides, such as $MoCl_6$ that is unstable and may degrade into $MoCl_5$, and $MoCl_4$. $MoCl_6$ like molybdenum pentachloride, appears as a black powder or silver-grey single crystals.[71] A second possibility is the incomplete molybdenum oxidation during the synthesis of $^{95}MoO_3$, leading to MoO_2 impurities. When MoO_2 combines with excess $SOCl_2$, a redox chlorination pathway may develop a side solid black product $MoCl_4$ that is paramagnetic. XPS analysis was carried out to confirm the presence of paramagnetic species (see discussion below).

To reduce material loss and address experimental constraints during synthesis, a purification step was necessary to remove impurities and residual by-products. This operation, essential before the silica grafting step, was carried out under an inert atmosphere using a double Schlenk. The solid product was placed in toluene, a solvent chosen for its ability to selectively solubilize the $MoOCl_4$ complex. The impurities remained insoluble in this solvent. The mixture was stirred to promote the dissolution of $MoOCl_4$ in the organic phase. Then, it was filtered by transfer into a second Schlenk tube, allowing the liquid phase containing the purified $MoOCl_4$ to be separated from the solid residue impurities. The toluene was then evaporated under vacuum to recover the complex in solid form. This double Schlenk purification method yields to dark-green powder notably characteristic of $MoOCl_4$. Only 100 mg of complex was obtained after purification.

10.2. Solid-Solid Grafting on $SiO_{2\text{-}200}$ and $SiO_{2\text{-}700}$

Solid-solid grafting of the $^{95}MoOCl_4$ complex onto silica was performed to immobilize the metal species on a solid support. In some cases, this solid-solid grafting was proven more efficient than conventional grafting methods, provided the complex exhibits sufficient mobility. This is the case for complexes that can sublime, such as $MoOCl_4$. Two types of silica, dehydroxylated at 200 °C and 700 °C respectively (see Part I, section 0) were used as supports. For both grafting, 370 mg of the support was mixed with 40 mg of the

molecular complex. The $^{95}MoOCl_4/SiO_2$ mixture was heated at 80 °C for 4 hours in a sand bath, with static stirring, inside a glove box, to allow the anchoring of the metal complex onto the silica surface. After the reaction, the complexes were washed several times with toluene to remove the excess of unreacted $MoOCl_4$ complex. The samples obtained, after filtration and drying, correspond to the $^{95}MoOCl_4/SiO_{2\text{-}200}$ and $^{95}MoOCl_4/SiO_{2\text{-}700}$.

Grafting the $^{95}MoOCl_4$ complex onto silica consists of the reaction between the Mo metal and the surface hydroxyl groups (≡Si–OH), present in different amounts depending on the silica pretreatment temperature. Two anchoring modes are possible: monopodal and bipodal. The reactions involved on both supports are the following:

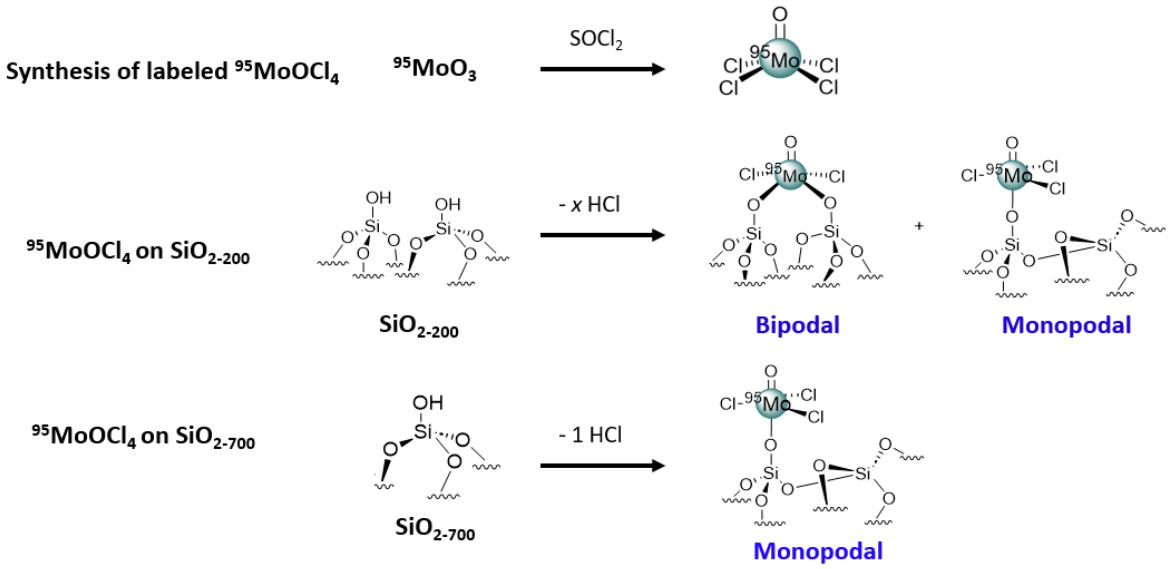

Scheme 1. *Synthesis of $^{95}MoOCl_4$ and grafting onto $SiO_{2\text{-}200}$ and $SiO_{2\text{-}700}$.*

11. Results and discussion

11.1. DRIFT analysis

To evidence the grafting of the molecular precursor on the support, diffuse reflectance infrared Fourier transform spectroscopy (DRIFT) was performed on both types of untreated silica as well as on the grafted complexes to assess the concentration of the surface hydroxyl groups. Figure 36 shows the stretching band of OH groups at 3747 cm^{-1} for the pure supports. This band disappears upon grafting of $^{95}MoOCl_4$, evidencing the consumption of nearly all free surface silanols of $SiO_{2\text{–}200}$ and almost all OH groups of

SiO_{2-700}.[29] Additionally, a stretching band is observed between 2850 and 3030 cm^{-1} corresponding to CH groups. This signal is attributed to traces of toluene used during the washing steps. [29,66,74]

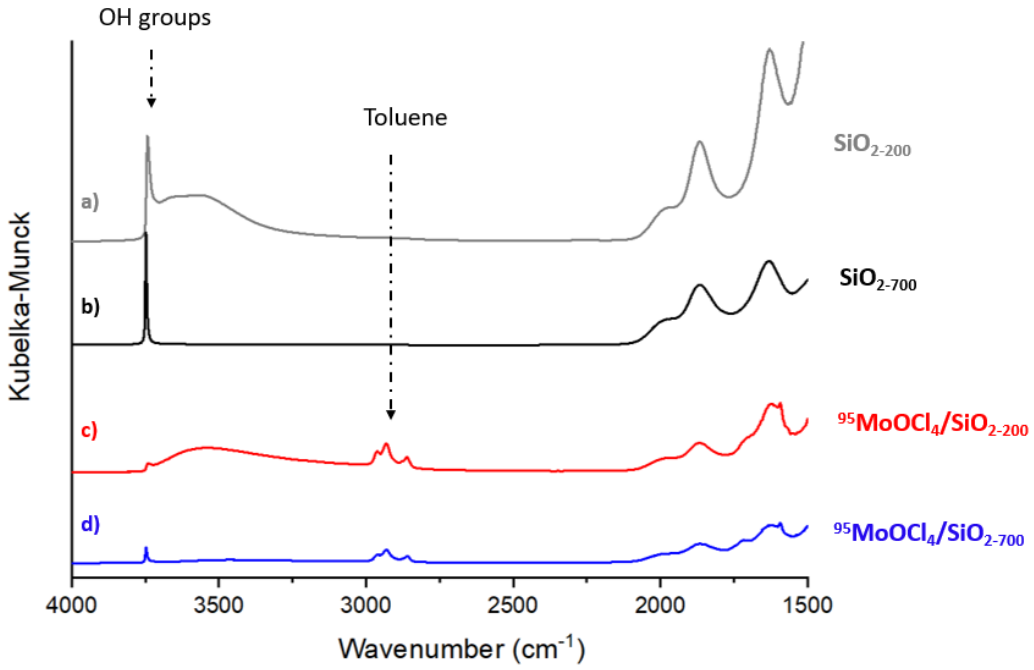

Figure 36. *DRIFT spectra of a) SiO_{2-200}, b) SiO_{2-700}, c) grafted $^{95}MoOCl_4/SiO_{2-200}$ and d) grafted $^{95}MoOCl_4/SiO_{2-700}$.*

11.2. Experimental conditions for NMR analysis

All experiments were carried out at a high magnetic field strength of B_0 = 28.2 T, corresponding to a ^1H Larmor frequency of 1200 MHz and a ^{95}Mo Larmor frequency of −78.9 MHz. The spectrometer is equipped with standard Bruker AVANCE NEO console. All spectra were acquired at room temperature using a 3.2 mm double-resonance (HX) MAS probe. The powder samples were packed under inert conditions in a JACOMEX glove box, into zirconia rotors sealed with Kel-F drive caps and spun at a MAS frequency of ν_R = 20 kHz under nitrogen gas.

The 1D ^1H DEPTH spectra were recorded with 16 transients using a 90° pulse of 3 µs at a RF field strength with ν_1 = 83.3 kHz. The 1D ^{95}Mo DFS-QCPMG spectra at 28.2 T were all acquired using CT selective QCPMG pulses that lasted 9.5 µs with ν_1 = 26.3 kHz. No ^1H heteronuclear decoupling was applied during acquisition. The DFS parameters were consistent with those used for molecular complexes. However, to overcome the effect of

the mobility of the support that induced a very fast decay of the echo enveloppe, a short echo time of 50 µs was used with 200 echoes forming the echo train. The experimental time was approximately 20 hours.

11.2.1. ^{1}H ssNMR of the grafted systems

Proton spectra were acquired to evaluate the purity of the grafted samples, specifically to assess the amount of residual surface OH groups and detect any potential moisture contamination that may have occurred during sample transportation from Lyon to Lille.

As shown in figure 37, both samples show a tiny peak at 1.8 ppm characteristic of isolated silanol groups remaining after grafting. However, the intensity of the signal is small, indicating that these OH groups were almost completely consumed, in agreement with DRIFT results.[75,76,77] A broad, low-intensity peak at 3.5 ppm is assigned to physisorbed water.[75] Additionally, a very weak signal at 2.1 ppm corresponds to traces of toluene due to several washing processes.[78]

Interestingly, an intense peak at 0.7 ppm is observed. In these material, such signal is assigned to a metal bonded to hydroxyl group, which may correspond in our case to a terminal Mo-OH species.[77,79] However, based on scheme 1, this type of bond should not be observed in the grafted materials. Moreover, the spectra showed as well another intense peak at 1.2 ppm with a higher relative integrated intensity of 48% for $^{95}MoOCl_4/SiO_{2\text{-}700}$ versus 34% for $^{95}MoOCl_4/SiO_{2\text{-}200}$. This additional peak could correspond to additional hydroxyl groups interacting with Mo atom. These observations suggest that the samples may have been exposed to air, either during transportation, inside the glove box, or inside the spectrometer, resulting in hydrolysis of Mo–Cl bonds to Mo–OH.

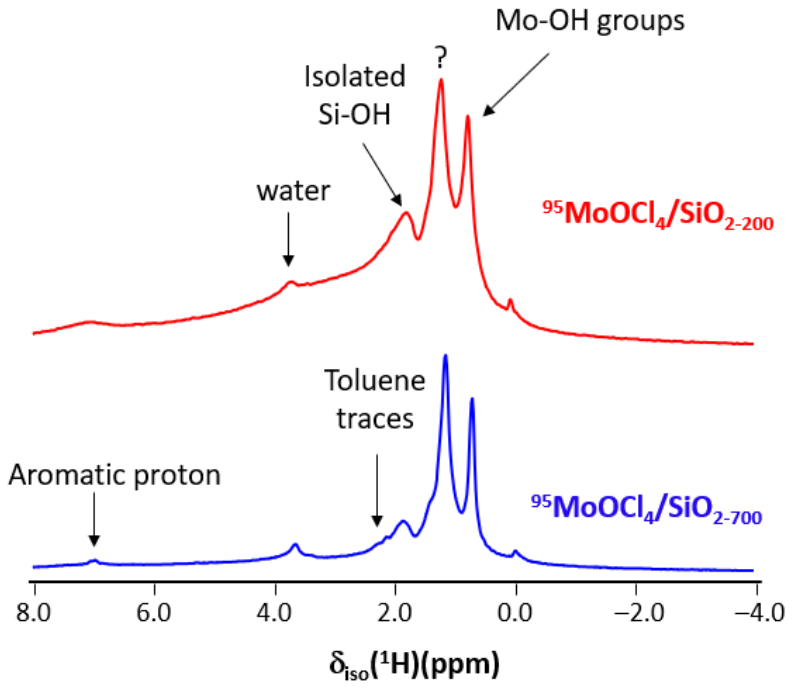

Figure 37. *1D ^1H MAS DEPTH spectra of $^{95}MoOCl_4/SiO_{2\text{-}200}$ (red) and $^{95}MoOCl_4/SiO_{2\text{-}700}$ (blue) acquired at 28.2 T with ν_R = 20 kHz using 3.2 mm HX probe spinning under N_2 gas.*

During the synthesis of $^{95}MoOCl_4$, fine black particles were detected, indicating the existence of reduced molybdenum species (e.g., Mo^{+IV}). The presence of these reduced species may lead to a significant broadening of the ^1H resonances. To confirm the presence of reduced species, X-ray photoelectron spectroscopy (XPS) analysis were performed. Based on the spin–orbit constraints applied during the fitting of the XPS Mo 3d core levels ($3d_{5/2}$ and $3d_{3/2}$), two different oxidation states of molybdenum were identified: Mo^{+VI} and Mo^{+IV}. The deconvolution of the spectra, taking into account the characteristic doublet splitting, yields the relative contributions of each oxidation state (see figure 38). The spectral lines at 229.5 and 233 eV are assigned to the spin components $3d_{5/2}$ of Mo^{+IV} in MoO_2 and Mo^{+VI} in MoO_3.[80,81] These results evidenced the presence of paramagnetic species in the complex, indicating that not all Mo have an oxidation number of (+VI), even after purification. For the $SiO_{2\text{-}200}$ sample, the Mo(VI) species dominate with 93.8%, while the Mo(IV) contribution is 6.14%. For the $SiO_{2\text{-}700}$ sample, the proportion of Mo(VI) decreases to 87.84%, with a corresponding increase in Mo(IV) to 12.7%.

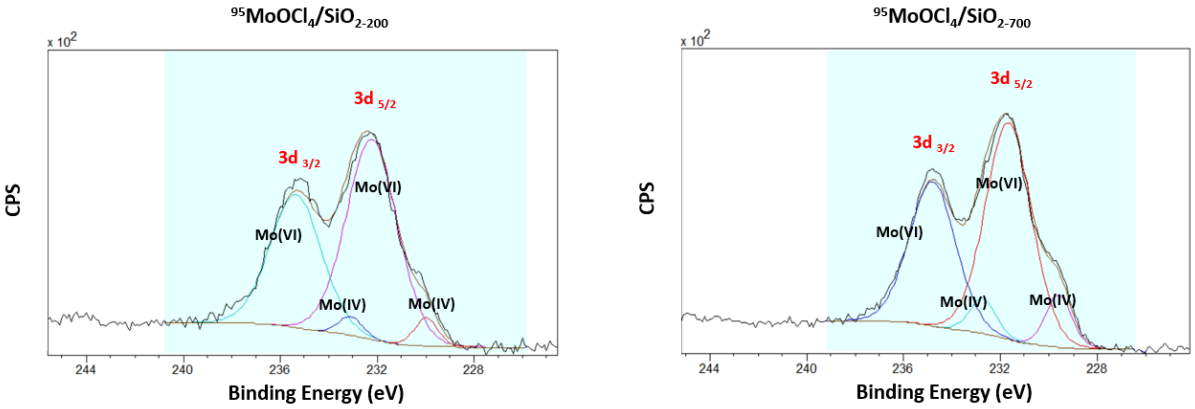

Figure 38. *XPS spectra of $^{95}MoOCl_4/SiO_{2\text{-}200}$ (left) and $^{95}MoOCl_4/SiO_{2\text{-}700}$ (right).*

11.2.2. ^{95}Mo ssNMR of the grafted systems

Solid-state ^{95}Mo NMR experiments started with the grafted complex onto $SiO_{2\text{-}700}$, which is expected to yield a single dominant Mo site. This strategy would allow us to directly determine the chemical shift of the monopodal species. Then, ^{95}Mo acquisition was performed on $^{95}MoOCl_4/SiO_{2\text{-}200}$, where the signal from bipodal and monopodal should coexist, the latter appearing at the same chemical shift as observed for $^{95}MoOCl_4/SiO_{2\text{-}700}$. The MAS ^{95}Mo spectra in figure 39 reveal two distinct line shapes. Interestingly, the fullwidth at half maxima (FWHM) of $^{95}MoOCl_4/SiO_{2\text{-}700}$ signal is 90 kHz, nearly twice that of $^{95}MoOCl_4/SiO_{2\text{-}200}$, which is 55 kHz. This broadening raises the question of whether the signal corresponds to a single site or to several environments on the surface. Based on the reaction in Scheme 1, the grafting on $SiO_{2\text{-}700}$ should lead to a single peak, whereas $^{95}MoOCl_4/SiO_{2\text{-}200}$ is expected to produce a dominant signal from bipodal species with possibly a minor contribution from monopodal species. At this stage, the broad peaks observed prevented reliable extraction of the NMR parameters using ssNake deconvolution, especially without any clue from DFT calculations. To interpret these spectral features, we considered insights from recent studies combining experimental and theoretical approaches.

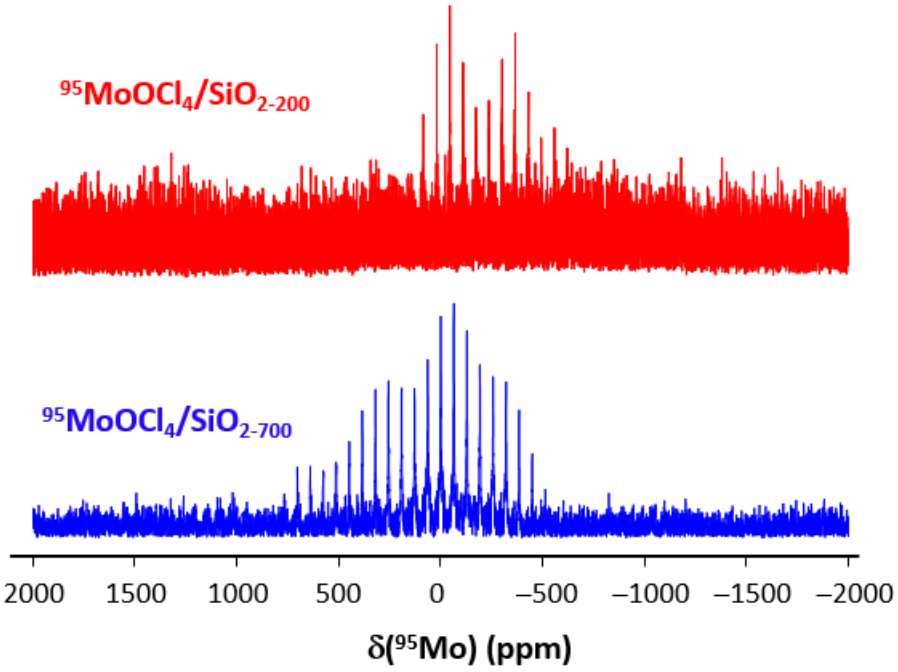

Figure 39. *1D ^{95}Mo DFS-QCPMG spectra of $^{95}MoOCl_4/SiO_{2\text{-}200}$ (red) and $^{95}MoOCl4/SiO_{2\text{-}700}$ (blue) acquired at 28.2 T with ν_R = 20 kHz using 3.2 mm HX probe spinning under N_2 gas.*

The supporting information from ref. [35] provides valuable insight into the influence of the local chemical environment on the ^{95}Mo chemical shift. For example, $MoOCl_4$ in solution resonates at 1015 ppm (figure 40a), while the commercial solid $MoOCl_4$ powder resonates at 850 ppm (see Figure 41). This indicates that chlorine ligands impose a strong deshielding effect on the Mo center. Upon removal of Cl ligands, the resonance shifts to lower chemical shifts, as observed for complexes 3_{Cl} and 1_{F9}, which exhibit δ_{iso} values of 189 and 150 ppm, respectively (see figure 40b). Conversely, reference complexes containing only oxygen ligands (i.e., no chlorine) show lower isotropic chemical shifts, in the negative region, such as for complexes 2_{F0} and 3_{F9}. Furthermore, MoO_3 exhibits an isotropic chemical shift of −150 ppm, confirming the hypothesis that Cl ligands significantly deshield the ^{95}Mo signal.[82]

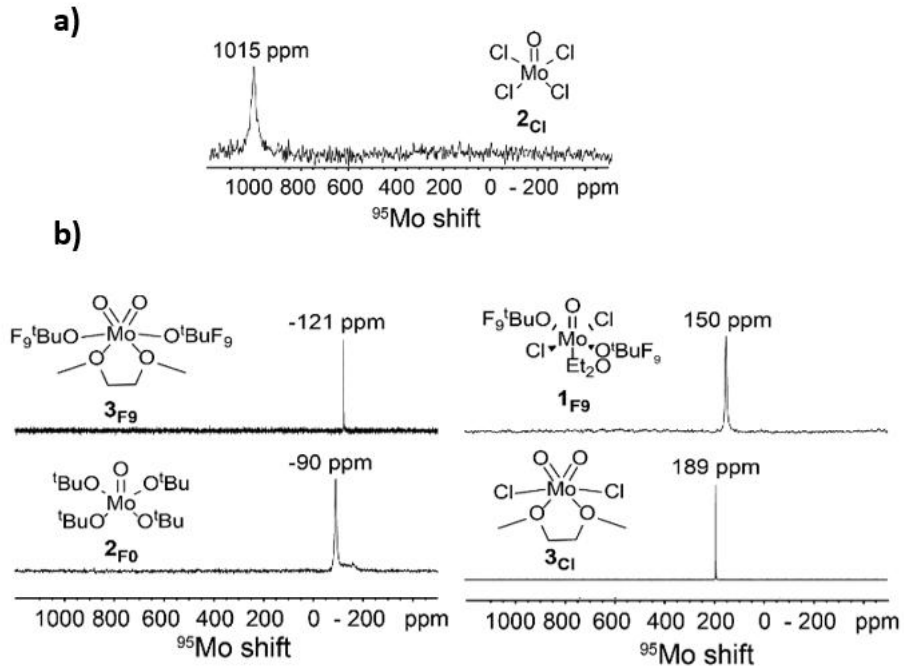

Figure 40. *1D ^{95}Mo solution state NMR of (a) $MoOCl_4$ and (b) reference complexes.*[35]

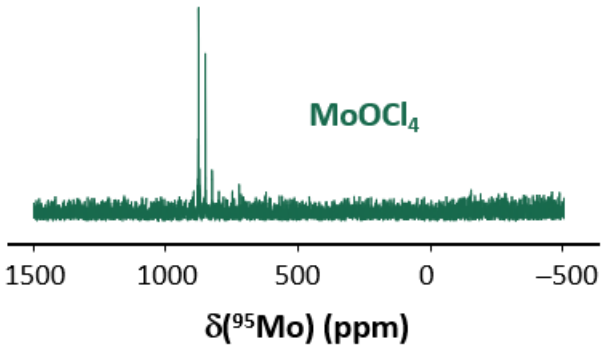

Figure 41. *1D ^{95}Mo DFS-QCPMG spectrum of $MoOCl_4$ powder acquired at 28.2 T with ν_R = 20 kHz using 3.2 mm HX probe.*

Based on the results discussed in the ref. [35], the isotropic chemical shifts of Mo species bonded to oxygen atoms and grafted on silica typically span from –80 to –200 ppm. In our study, the observed resonances range from 150 to –200 ppm for $^{95}MoOCl_4/SiO_{2\text{-}200}$, while they extend from 500 to –200 ppm for $^{95}MoOCl_4/SiO_{2\text{-}700}$. These results suggest that, rather than considering a classical mono- or bis-grafting process involving one or two Cl atoms, the molybdenum precursor has experienced hydrolysis leading to the progressive replacement of one or more Cl ligands by OH groups (Scheme 2). The increasing substitution of Cl by OH results in a strong shielding of the Mo center, moving chemical shifts towards more negative values. Signals in the negative region are therefore attributed

to fully hydroxylated species where two OH have replaced two Cl ligands. Signals in the positive chemical shift region is likely to correspond to partially hydroxylated complexes where one Cl ligand remains.

The increased reactivity of $SiO_{2\text{-}700}$ may account for a greater diversity of complexes on the surface as well as the broader linewidths observed. On this basis, the resonances observed in the positive region may be assigned to monopodal species of the type $MoOCl_2(OH)/SiO_{2\text{-}700}$, $MoOCl(OH)_2/SiO_{2\text{-}700}$, and $MoO(OH)_3/SiO_{2\text{-}700}$, appearing respectively from high to low chemical shifts as the degree of hydrolysis increases.

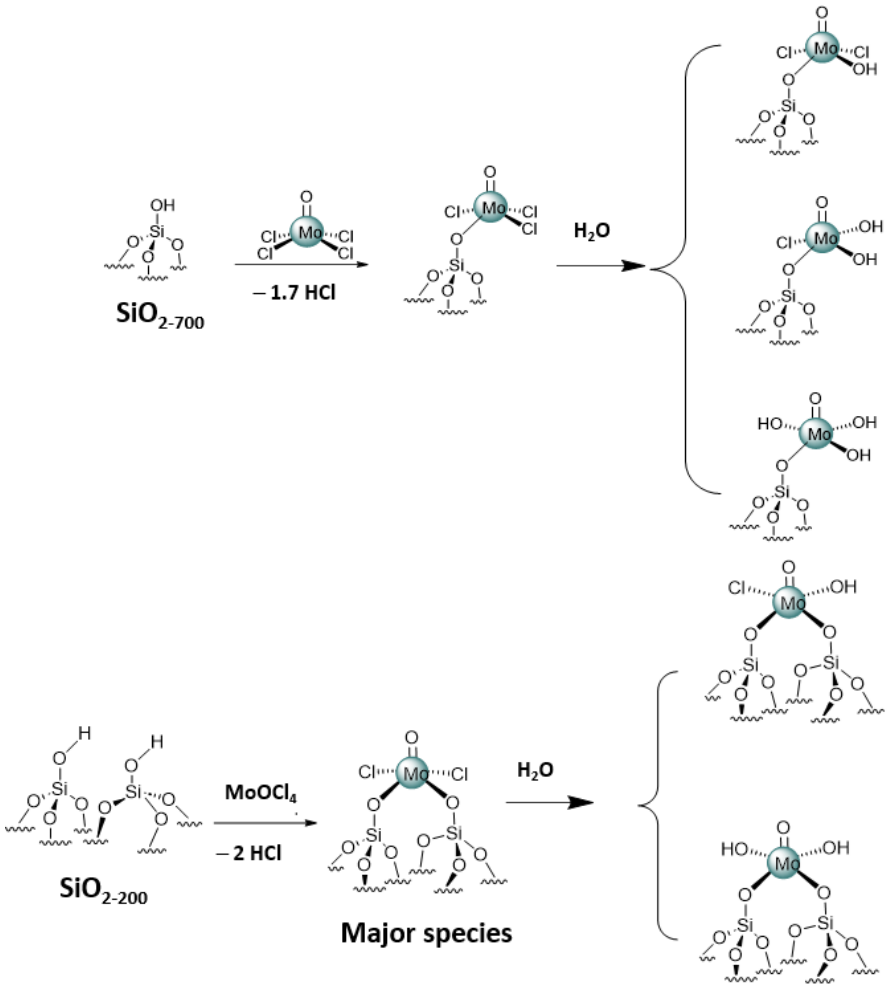

Scheme 2. *Possible reaction schemes of $MoOCl_4$ with silica dehydroxylated at 200 °C and 700 °C*

12. Calculation of NMR parameters using a molecular approach ADF

Chemical shift calculations were carried out using the ADF 2014 code and the improved Perdew-Burke-Ernzerhof functionals. The high level of theory was used for molybdenum employing QZ4P basis set, DZP basis set for all other atoms, and protons at DZ. The all-electron relativistic zeroth-order regular approximation (ZORA) was used as well allowing to treat the relativistic problem with a reformulation of the Schrödinger equation. The functionals used are PBE and PBE0 and PBE0 with 15% Hartree-Fock exchange.

The ADF calculations for $MoOCl_4/SiO_{2\text{-}200}$ were carried out considering both *cis* and *trans* configurations of the chloride ligands.[66] The calculated NMR parameters are displayed in Table 11.

Table 11. *NMR parameters obtained from molecular approach using high level of theory QZ4P/TZ2P basis set for* $MoOCl_4/SiO_{2\text{-}200}$ *where Cl ligands are either in cis or trans configuration.*

Functionals	δ_{iso} (ppm)	δ_{CSA} (ppm)	C_Q (MHz)
Cis configuration $MoOCl_4/SiO_{2\text{-}200}$			
Scalar PBE	309	750	5.3
Scalar PBE0	323	980	6.1
Scalar PBE0 – 15 % HF	319	880	5.8
Trans configuration $MoOCl_4/SiO_{2\text{-}200}$			
Scalar PBE	612	306	4.5
Scalar PBE0	685	464	4.9
Scalar PBE0 – 15 % HF	642	390	4.8

Experimentally, the ^{95}Mo NMR spectrum of $MoOCl_4/SiO_{2\text{-}200}$ spans the region from −200 to 150 ppm, with no detectable signals around 300 ppm. According to Berkson *et al.*[35] grafted molybdenum species on $SiO_{2\text{-}200}$ without chlorine ligands, display chemical shifts in the range of –80 to –200 ppm, with a maximum C_Q value of 7 MHz. However, as analyzed in the previous sections, the presence of chlorine ligands leads to increased isotropic chemical shift, which explains the frequencies in the positive region of the spectra. The ^{95}Mo spectrum of $MoOCl_4/SiO_{2\text{-}700}$ exhibits signal between 200 and 130 ppm, which may stem from ^{95}Mo nuclei bonded to two Cl atoms based on the isotropic chemical shifts measured for complexes 1_{F9} and 3_{Cl} (see b) and 2 and 4 (see).

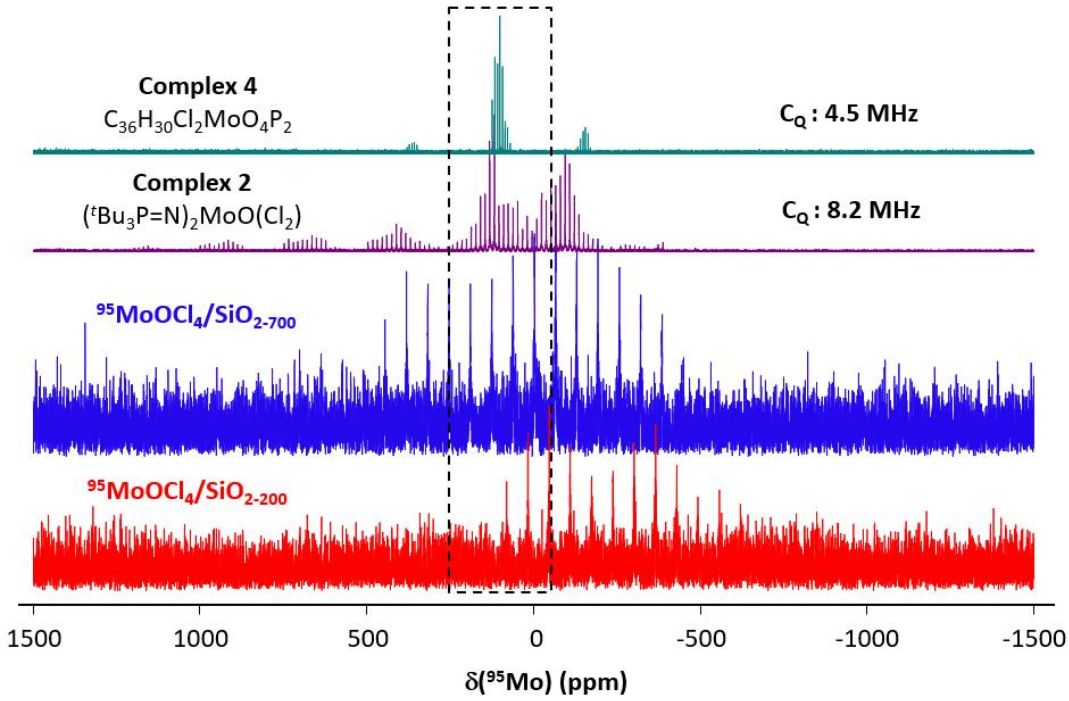

Figure 42. *Comparison of 1D ^{95}Mo DFS-QCPMG spectra of grafted and molecular complexes acquired at 28.2 T with ν_R = 20 kHz using 3.2 mm HX probe spinning under N_2 gas. The dashed region highlights the superposition of the central transitions of molecular complexes with C_Q close to those computed for the grafted systems.*

On $SiO_{2\text{-}700}$, the chemical shift is further shifted towards positive values, likely due to the higher chlorine content. In contrast, $SiO_{2\text{-}200}$ exhibits lower isotropic chemical shifts. To assign the 1D ^{95}Mo NMR spectrum of $MoOCl_4/SiO_{2\text{-}200}$ sample, we compare it with other experimental and simulated spectra (see Figure 43).

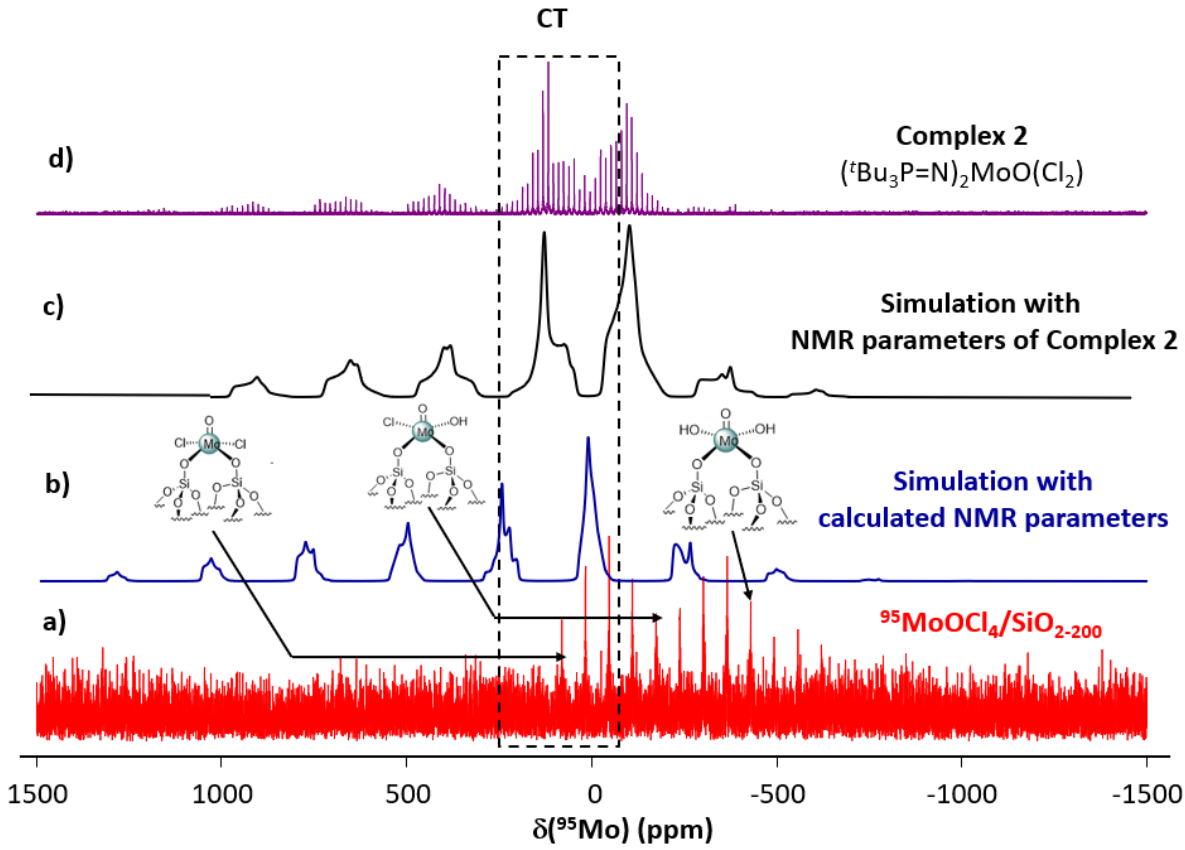

Figure 43. *(a, d) Experimental 1D ^{95}Mo DFS-QCPMG spectra of ^{95}MoOCl$_4$/SiO$_{2\text{-}200}$ and molecular complex 2 acquired at 28.2 T with ν_R = 20 kHz using a 3.2 mm HX probe spinning under N_2 gas. The dashed region highlights the superposition of the central transitions of complex 2 and the grafted complexes. (b, c) Simulated 1D ^{95}Mo DFS-QCPMG spectra of (b) grafted MoCl$_2$(=O)(OSi)$_2$ complex with cis configuration (in blue) using NMR parameters calculated using PBE0 functional and scalar relativistic effects and for the cis configuration and of (c) complex 2 using experimental NMR parameters obtained using ssNake software. The structures of the identified grafted complexes are also displayed.*

As seen in b, the 1D ^{95}Mo NMR spectrum of MoOCl$_4$/SiO$_{2\text{-}200}$ sample exhibits signal at the same isotropic chemical shifts as the central transitions of penta-coordinated MoCl$_2$(=O)(OSi)$_2$ with *cis* configuration grafted on silica surface and complex 2. This result suggests the presence of grafted penta-coordinated oxo Mo complexes bound to two chloro ligands in MoOCl$_4$/SiO$_{2\text{-}200}$ sample. Nevertheless, these complexes cannot account for signals resonating below −200 ppm.

These signals with negative isotropic chemical shifts must correspond to grafted Mo complexes bound to more oxygen atoms. In particular, the grafted bis-oxo bipodal Mo complex have ^{95}Mo isotropic chemical shift of −135 ppm (see Figure 44).[35] Therefore, we can assume that MoOCl$_4$/SiO$_{2\text{-}200}$ sample contains grafted MoCl(=O)OH(OSi)$_2$ and MoCl(=O)(OH)$_2$(OSi)$_2$ complexes.

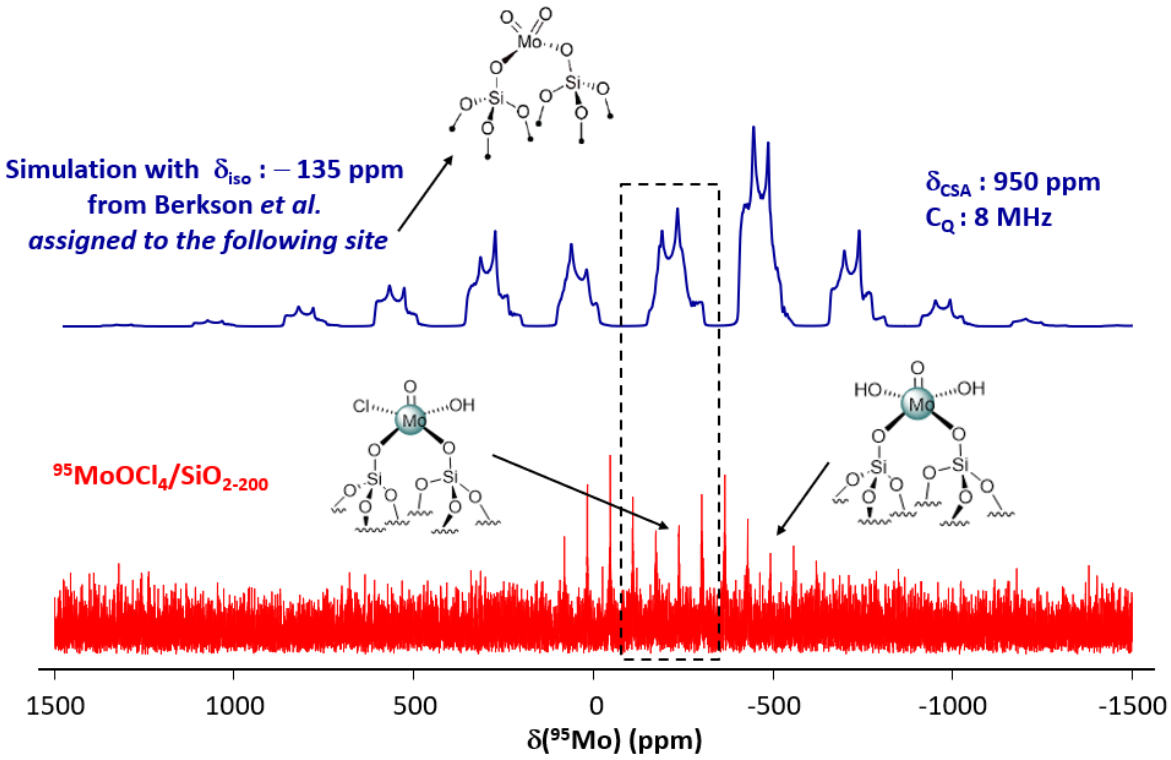

Figure 44. *Experimental 1D ^{95}Mo DFS-QCPMG spectrum of $^{95}MoOCl_4/SiO_{2\text{-}200}$ (red) acquired at 28.2 T with ν_R = 20 kHz using 3.2 mm HX probe and spinning under N_2 gas along with simulated 1D ^{95}Mo NMR spectrum (blue) of bis-oxo bipodal species (structure displayed on the top) using NMR parameters reported in ref. [35]. The structures of the grafted complexes yielding signals with negative isotropic chemical shifts are displayed above the experimental spectrum. The dashed region corresponds to signals produced by Mo species bound to four O atoms.*

13. Conclusion

The ^{95}Mo NMR study of molybdenum-based catalysts for olefin metathesis proved to be particularly challenging, reflecting the inherent complexity of Mo chemistry. For the molecular complexes, we managed to record 1D ^{95}Mo NMR spectra with good sensitivity and resolution through the combination of very high magnetic fields and the DFS-QCPMG pulse sequence. NMR parameters were extracted at two different fields to ensure accuracy. Periodic DFT calculations, however, did not provide a satisfactory description of the systems. ADF calculations, which explicitly include relativistic effects, yielded more reliable results, with chemical shifts and C_Q values in better agreement with experiment and a regression slope approaching unity. The inclusion of spin–orbit effects did not bring significant changes. We were unable to develop a theoretical framework that specifies how NMR parameters vary depending on the nature of the ligands in molybdenum's initial coordination sphere. Nonetheless, establishing such a link remains difficult due to the

intricate interaction of electronic structure, distortions, ligand field effects, and relativistic contributions, all of which having a substantial impact on computed chemical shifts and quadrupolar couplings.

The investigation of the grafted systems proved to be far more complex. Both the synthesis and the acquisition of ^{95}Mo spectra presented major challenges. The $^{95}MoO_3$ precursor was found to contain reduced molybdenum species and was therefore not fully oxidized. Given the high cost of labeled $^{95}MoO_3$, we were unable to obtain additional material and the synthesis had to be done on such small quantities. We observed the formation of fine black particles during synthesis, i.e., an impure $^{95}MoOCl_4$, as evidenced by ^{1}H NMR and XPS analyses. Despite these constraints, the NMR study performed on grafted systems yielded valuable insights. The hydrolysis observed, even accidental in our present study and probably due to a non-optimized synthesis protocol, introduced additional hydroxylated sites that are consistent with the few examples reported in the literature. These new environments complicated the spectral interpretation but they represent an encouraging first step towards the study of a larger family of surface species. The ^{95}Mo spectra of our grafted systems reflect a mixture of environments. This underlines the need for improved synthetic strategies to obtain well-defined grafted precursors and, ultimately, to enable a more straightforward interpretation of ^{95}Mo NMR signatures in these heterogeneous catalytic systems.

14. Statement of contribution

The molecular pre-catalysts and grafted systems studied in Chapter 2 were synthesized by **Nicolas Merle** (Maître de conférences, CADICOM team, UCCS–UMR 8181, University of Lille), **Mostafa Taoufik** (Research Scientist, CP2M–UMR 5128, CPE Lyon), **Kai Chung Szeto** (Research Engineer, CP2M–UMR 5128, CPE Lyon), and myself (for the part carried out in Lyon). I performed the ssNMR experiments and analyzed the experimental data. I also carried out the periodic-approach simulations. The ADF molecular-approach simulations were performed by **Pr. Jochen Autschbach** and **Soumya Ranjan Dash** (Postdoctoral Fellow) both working in Jochen Autschbach's group, department of Chemistry, SUNY Buffalo. **Laurent Delevoye** provided supervision and contributed to the analysis and interpretation of the results.

15. References

(1) Schrock, R. R. Alkylcarbene Complex of Tantalum by Intramolecular. Alpha. -Hydrogen Abstraction. *J. Am. Chem. Soc.* **1974**, *96* (21), 6796–6797. https://doi.org/10.1021/ja00828a061.

(2) Schrock, R. R.; Hoveyda, A. H. Molybdenum and Tungsten Imido Alkylidene Complexes as Efficient Olefin-Metathesis Catalysts. *Angew. Chem. Int. Ed Engl.* **2003**, *42* (38), 4592–4633. https://doi.org/10.1002/anie.200300576.

(3) Schrock, R. R. Recent Advances in High Oxidation State Mo and W Imido Alkylidene Chemistry. *Chem. Rev.* **2009**, *109* (8), 3211–3226. https://doi.org/10.1021/cr800502p.

(4) Peryshkov, D. V.; Schrock, R. R.; Takase, M. K.; Müller, P.; Hoveyda, A. H. Z-Selective Olefin Metathesis Reactions Promoted by Tungsten Oxo Alkylidene Complexes. *J. Am. Chem. Soc.* **2011**, *133* (51), 20754–20757. https://doi.org/10.1021/ja210349m.

(5) Bukhryakov, K. V.; Schrock, R. R.; Hoveyda, A. H.; Tsay, C.; Müller, P. Syntheses of Molybdenum Oxo Alkylidene Complexes through Addition of Water to an Alkylidyne Complex. *J. Am. Chem. Soc.* **2018**, *140* (8), 2797–2800. https://doi.org/10.1021/jacs.8b00499.

(6) De Jesus Silva, J.; Pucino, M.; Zhai, F.; Mance, D.; Berkson, Z. J.; Nater, D. F.; Hoveyda, A. H.; Copéret, C.; Schrock, R. R. Boosting the Metathesis Activity of Molybdenum Oxo Alkylidenes by Tuning the Anionic Ligand σ Donation. *Inorg. Chem.* **2021**, *60* (10), 6875–6880. https://doi.org/10.1021/acs.inorgchem.0c03173.

(7) Lwin, S.; Wachs, I. E. Olefin Metathesis by Supported Metal Oxide Catalysts. *ACS Catal.* **2014**, *4* (8), 2505–2520. https://doi.org/10.1021/cs500528h.

(8) Copéret, C.; Comas-Vives, A.; Conley, M. P.; Estes, D. P.; Fedorov, A.; Mougel, V.; Nagae, H.; Núñez-Zarur, F.; Zhizhko, P. A. Surface Organometallic and Coordination Chemistry toward Single-Site Heterogeneous Catalysts: Strategies, Methods, Structures, and Activities. *Chem. Rev.* **2016**, *116* (2), 323–421. https://doi.org/10.1021/acs.chemrev.5b00373.

(9) Groppo, E.; Lamberti, C.; Bordiga, S.; Spoto, G.; Zecchina, A. The Structure of Active Centers and the Ethylene Polymerization Mechanism on the Cr/SiO_2 Catalyst: A Frontier for the Characterization Methods. *Chem. Rev.* **2005**, *105* (1), 115–184. https://doi.org/10.1021/cr040083s.

(10) Wachs, I. E.; Roberts, C. A. Monitoring Surface Metal Oxide Catalytic Active Sites with Raman Spectroscopy. *Chem. Soc. Rev.* **2010**, *39* (12), 5002–5017. https://doi.org/10.1039/C0CS00145G.

(11) Copéret, C.; Chabanas, M.; Petroff Saint-Arroman, R.; Basset, J.-M. Homogeneous and Heterogeneous Catalysis: Bridging the Gap through Surface Organometallic Chemistry. *Angew. Chem. Int. Ed Engl.* **2003**, *42* (2), 156–181. https://doi.org/10.1002/anie.200390072.

(12) Candy, J.-P.; Copéret, C.; Basset, J.-M. Analogy between Surface and Molecular Organometallic Chemistry. In *Surface and Interfacial Organometallic Chemistry and Catalysis*; Copéret, C., Chaudret, B., Eds.; Springer: Berlin, Heidelberg, **2005**; pp 151–210. https://doi.org/10.1007/b138076.

(13) Marks, T. J. Surface-Bound Metal Hydrocarbyls. Organometallic Connections between Heterogeneous and Homogeneous Catalysis. *Acc. Chem. Res.* **1992**, *25* (2), 57–65. https://doi.org/10.1021/ar00014a001.

(14) Serna, P.; Gates, B. C. Molecular Metal Catalysts on Supports: Organometallic Chemistry Meets Surface Science. *Acc. Chem. Res.* **2014**, *47* (8), 2612–2620. https://doi.org/10.1021/ar500170k.

(15) Rimoldi, M.; Mezzetti, A. Site Isolated Complexes of Late Transition Metals Grafted on Silica: Challenges and Chances for Synthesis and Catalysis. *Catal. Sci. Technol.* **2014**, *4* (9), 2724–2740. https://doi.org/10.1039/C4CY00450G.

(16) Rascón, F.; Wischert, R.; Copéret, C. Molecular Nature of Support Effects in Single-Site Heterogeneous Catalysts: Silicavs.Alumina. *Chem. Sci.* **2011**, *2* (8), 1449–1456. https://doi.org/10.1039/C1SC00073J.

(17) Conley, M. P.; Copéret, C. State of the Art and Perspectives in the "Molecular Approach" Towards Well-Defined Heterogeneous Catalysts. *Top. Catal.* **2014**, *57* (10), 843–851. https://doi.org/10.1007/s11244-014-0245-0.

(18) Morrow, B. A.; McFarlan, A. J. Chemical Reactions at Silica Surfaces. *J. Non-Cryst. Solids* **1990**, *120* (1), 61–71. https://doi.org/10.1016/0022-3093(90)90191-N.

(19) Liu, C. C.; Maciel, G. E. The Fumed Silica Surface: A Study by NMR. *J. Am. Chem. Soc.* **1996**, *118* (21), 5103–5119. https://doi.org/10.1021/ja954120w.

(20) Ballard, D. G. H. Pi and Sigma Transition Metal Carbon Compounds as Catalysts for the Polymerization of Vinyl Monomers and Olefins. In *Advances in Catalysis*; Elsevier, 1973; Vol. 23, pp 263–325. https://doi.org/10.1016/S0360-0564(08)60303-X.

(21) Poater, A.; Solans-Monfort, X.; Clot, E.; Copéret, C.; Eisenstein, O. Understanding D0-Olefin Metathesis Catalysts: Which Metal, Which Ligands? *J. Am. Chem. Soc.* **2007**, *129* (26), 8207–8216. https://doi.org/10.1021/ja070625y.

(22) Solans-Monfort, X.; Copéret, C.; Eisenstein, O. Oxo vs Imido Alkylidene D^0-Metal Species: How and Why Do They Differ in Structure, Activity, and Efficiency in Alkene Metathesis? *Organometallics* **2012**, *31* (19), 6812–6822. https://doi.org/10.1021/om300576r.

(23) Mol, J. C. Industrial Applications of Olefin Metathesis. *J. Mol. Catal. Chem.* **2004**, *213* (1), 39–45. https://doi.org/10.1016/j.molcata.2003.10.049.

(24) Chakrabarti, A.; Wachs, I. E. Molecular Structure–Reactivity Relationships for Olefin Metathesis by Al_2O_3-Supported Surface MoOx Sites. *ACS Catal.* **2018**, *8* (2), 949–959. https://doi.org/10.1021/acscatal.7b03598.

(25) Chakrabarti, A.; Wachs, I. E. Activation Mechanism and Surface Intermediates during Olefin Metathesis by Supported $MoOx/Al_2O_3$ Catalysts. *J. Phys. Chem. C* **2019**, *123* (19), 12367–12375. https://doi.org/10.1021/acs.jpcc.9b02426.

(26) Le Roux, E.; Taoufik, M.; Copéret, C.; de Mallmann, A.; Thivolle-Cazat, J.; Basset, J.-M.; Maunders, B. M.; Sunley, G. J. Development of Tungsten-Based Heterogeneous Alkane Metathesis Catalysts Through a Structure–Activity Relationship. *Angew. Chem. Int. Ed.* **2005**, *44* (41), 6755–6758. https://doi.org/10.1002/anie.200501382.

(27) Blanc, F.; Salameh, A.; Thivolle-Cazat, J.; Basset, J.-M.; Copéret, C.; Sinha, A.; Schrock, R. R. Grafting mechanism and olefin metathesis activity of well-defined silica-supported Mo imido alkyl alkylidene complexes. *Comptes Rendus Chim.* **2008**, *11* (1–2), 137–146. https://doi.org/10.1016/j.crci.2007.02.017.

(28) Blanc, F.; Berthoud, R.; Salameh, A.; Basset, J.-M.; Copéret, C.; Singh, R.; Schrock, R. R. Dramatic Improvements of Well-Defined Silica Supported Mo-Based Olefin Metathesis Catalysts by Tuning the N-Containing Ligands. *J. Am. Chem. Soc.* **2007**, *129* (27), 8434–8435. https://doi.org/10.1021/ja073095e.

(29) Merle, N.; Quéméner, F. L.; Barman, S.; Samantaray, M. K.; Szeto, K. C.; Mallmann, A. D.; Taoufik, M.; Basset, J.-M. Well-Defined Silica Supported Bipodal Molybdenum Oxo Alkyl Complexes: A Model of the Active Sites of Industrial Olefin Metathesis Catalysts. *Chem. Commun.* **2017**, *53* (82), 11338–11341. https://doi.org/10.1039/C7CC06041F.

(30) Amoureux, J. P.; Fernandez, C.; Granger, P. Interpretation of Quadrupolar Powder Spectra: Static and MAS Experiments. In *Multinuclear Magnetic Resonance in Liquids and Solids — Chemical Applications*; Granger, P., Harris, R. K., Eds.; Springer Netherlands: Dordrecht, 1990; pp 409–424. https://doi.org/10.1007/978-94-009-2149-8_22.

(31) Hodgkinson, P. Heteronuclear Decoupling in the NMR of Solids. *Prog. Nucl. Magn. Reson. Spectrosc.* **2005**, *46* (4), 197–222. https://doi.org/10.1016/j.pnmrs.2005.04.002.

(32) Hu, B.; Delevoye, L.; Lafon, O.; Trébosc, J.; Amoureux, J. P. Double-Quantum NMR Spectroscopy of 31P Species Submitted to Very Large CSAs. *J. Magn. Reson.* **2009**, *200* (2), 178–188. https://doi.org/10.1016/j.jmr.2009.06.020.

(33) van Meerten, S. G. J.; Franssen, W. M. J.; Kentgens, A. P. M. ssNake: A Cross-Platform Open-Source NMR Data Processing and Fitting Application. *J. Magn. Reson. San Diego Calif 1997* **2019**, *301*, 56–66. https://doi.org/10.1016/j.jmr.2019.02.006.

(34) Berkson, Z. J.; Lätsch, L.; Hillenbrand, J.; Fürstner, A.; Copéret, C. Classifying and Understanding the Reactivities of Mo-Based Alkyne Metathesis Catalysts from ^{95}Mo NMR Chemical Shift Descriptors. *J. Am. Chem. Soc.* **2022**, *144* (33), 15020–15025. https://doi.org/10.1021/jacs.2c06252.

(35) Berkson, Z. J.; Zhu, R.; Ehinger, C.; Lätsch, L.; Schmid, S. P.; Nater, D.; Pollitt, S.; Safonova, O. V.; Björgvinsdóttir, S.; Barnes, A. B.; Román-Leshkov, Y.; Price, G. A.; Sunley, G. J.; Copéret, C. Active Site Descriptors from ^{95}Mo NMR Signatures of Silica-Supported Mo-Based Olefin Metathesis Catalysts. *J. Am. Chem. Soc.* **2023**, *145* (23), 12651–12662. https://doi.org/10.1021/jacs.3c02201.

(36) Groysman, S.; Grass, A. Alkoxide Ligands. In *Reference Module in Chemistry, Molecular Sciences and Chemical Engineering*; 2021. https://doi.org/10.1016/B978-0-08-102688-5.00113-6.

(37) Grekov, D.; Bouhoute, Y.; Szeto, K. C.; Merle, N.; De Mallmann, A.; Lefebvre, F.; Lucas, C.; Del Rosal, I.; Maron, L.; Gauvin, R. M.; Delevoye, L.; Taoufik, M. Silica-Supported Tungsten Neosilyl Oxo Precatalysts: Impact of the Podality on Activity and Stability in Olefin Metathesis. *Organometallics* **2016**, *35* (13), 2188–2196. https://doi.org/10.1021/acs.organomet.6b00220.

(38) Hayashida, T.; Kondo, H.; Terasawa, J.; Kirchner, K.; Sunada, Y.; Nagashima, H. Trifluoromethanesulfonate (Triflate) as a Moderately Coordinating Anion: Studies from Chemistry of the Cationic Coordinatively Unsaturated Mono- and Diruthenium Amidinates. *J. Organomet. Chem.* **2007**, *692* (1), 382–394. https://doi.org/10.1016/j.jorganchem.2006.08.069.

(39) Pickard, C. J.; Mauri, F. All-Electron Magnetic Response with Pseudopotentials: NMR Chemical Shifts. *Phys. Rev. B* **2001**, *63* (24), 245101. https://doi.org/10.1103/PhysRevB.63.245101.

(40) Kresse, G.; Furthmüller, J. Efficient Iterative Schemes for Ab Initio Total-Energy Calculations Using a Plane-Wave Basis Set. *Phys. Rev. B* **1996**, *54* (16), 11169–11186. https://doi.org/10.1103/PhysRevB.54.11169.

(41) Blöchl, P. E. Projector Augmented-Wave Method. *Phys. Rev. B* **1994**, *50* (24), 17953–17979. https://doi.org/10.1103/PhysRevB.50.17953.

(42) Perdew, J. P.; Burke, K.; Ernzerhof, M. Generalized Gradient Approximation Made Simple. *Phys. Rev. Lett.* **1996**, *77* (18), 3865–3868. https://doi.org/10.1103/PhysRevLett.77.3865.

(43) Herzfeld, J.; Berger, A. E. Sideband Intensities in NMR Spectra of Samples Spinning at the Magic Angle. *J. Chem. Phys.* **1980**, *73* (12), 6021–6030. https://doi.org/10.1063/1.440136.

(44) Harris, R. K.; Hodgkinson, P.; Pickard, C. J.; Yates, J. R.; Zorin, V. Chemical Shift Computations on a Crystallographic Basis: Some Reflections and Comments. *Magn. Reson. Chem.* **2007**, *45* (S1), S174–S186. https://doi.org/10.1002/mrc.2132.

(45) Monkhorst, H. J.; Pack, J. D. Special Points for Brillouin-Zone Integrations. *Phys. Rev. B* **1976**, *13* (12), 5188–5192. https://doi.org/10.1103/PhysRevB.13.5188.

(46) Bridge, B.; Patel, N. D. The Elastic Constants and Structure of the Vitreous System Mo-P-O. *J. Mater. Sci.* **1986**, *21* (4), 1187–1205. https://doi.org/10.1007/BF00553251.

(47) Hoppe, U. A Structural Model for Phosphate Glasses. *J. Non-Cryst. Solids* **1996**, *195* (1), 138–147. https://doi.org/10.1016/0022-3093(95)00524-2.

(48) Autschbach, J.; Srebro, M. Delocalization Error and "Functional Tuning" in Kohn–Sham Calculations of Molecular Properties. *Acc. Chem. Res.* **2014**, *47* (8), 2592–2602. https://doi.org/10.1021/ar500171t.

(49) Cuny, J.; Sykina, K.; Fontaine, B.; Pollès, L. L.; Pickard, C. J.; Gautier, R. ^{95}Mo Nuclear Magnetic Resonance Parameters of Molybdenum Hexacarbonyl from Density Functional Theory: Appraisal of Computational and Geometrical Parameters. *Phys. Chem. Chem. Phys.* **2011**, *13* (43), 19471–19479. https://doi.org/10.1039/C1CP22289A.

(50) Cuny, J.; Furet, E.; Gautier, R.; Le Pollès, L.; Pickard, C. J.; d'Espinose De Lacaillerie, J. Density Functional Theory Calculations of ^{95}Mo NMR Parameters in Solid-State Compounds. *ChemPhysChem* **2009**, *10* (18), 3320–3329. https://doi.org/10.1002/cphc.200900586.

(51) O'Dell, L. A.; Rossini, A. J.; Schurko, R. W. Acquisition of Ultra-Wideline NMR Spectra from Quadrupolar Nuclei by Frequency Stepped WURST–QCPMG. *Chem. Phys. Lett.* **2009**, *468* (4), 330–335. https://doi.org/10.1016/j.cplett.2008.12.044.

(52) Rodriguez-Fortea, A.; Alemany, P.; Ziegler, T. Density Functional Calculations of NMR Chemical Shifts with the Inclusion of Spin−Orbit Coupling in Tungsten and Lead Compounds. *J. Phys. Chem. A* **1999**, *103* (41), 8288–8294. https://doi.org/10.1021/jp9912004.

(53) Krykunov, M.; Ziegler, T.; Lenthe, E. van. Hybrid density functional calculations of nuclear magnetic shieldings using Slater-type orbitals and the zeroth-order regular approximation. *Int. J. Quantum Chem.* **2009**, *109* (8), 1676–1683. https://doi.org/10.1002/qua.21985.

(54) Lenthe, E. van; Baerends, E. J.; Snijders, J. G. Relativistic Regular Two-component Hamiltonians. *J. Chem. Phys.* **1993**, *99* (6), 4597–4610. https://doi.org/10.1063/1.466059.

(55) van Lenthe, E.; Baerends, E. J.; Snijders, J. G. Relativistic Total Energy Using Regular Approximations. *J. Chem. Phys.* **1994**, *101* (11), 9783–9792. https://doi.org/10.1063/1.467943.

(56) Adamo, C.; Barone, V. Toward Chemical Accuracy in the Computation of NMR Shieldings: The PBE_0 Model. *Chem. Phys. Lett.* **1998**, *298* (1), 113–119. https://doi.org/10.1016/S0009-2614(98)01201-9.

(57) Visscher, L.; van Lenthe, E. On the Distinction between Scalar and Spin–Orbit Relativistic Effects. *Chem. Phys. Lett.* **1999**, *306* (5), 357–365. https://doi.org/10.1016/S0009-2614(99)00458-3.

(58) Autschbach, J. The Role of the Exchange-Correlation Response Kernel and Scaling Corrections in Relativistic Density Functional Nuclear Magnetic Shielding Calculations with the Zeroth-Order Regular Approximation. *Mol. Phys.* **2013**, *111* (16–17), 2544–2554. https://doi.org/10.1080/00268976.2013.796415.

(59) Van Lenthe, E.; Baerends, E. J. Optimized Slater-Type Basis Sets for the Elements 1–118. *J. Comput. Chem.* **2003**, *24* (9), 1142–1156. https://doi.org/10.1002/jcc.10255.

(60) Adamo, C.; Barone, V. Toward Reliable Density Functional Methods without Adjustable Parameters: The PBE0 Model. *J Chem Phys* **1999**, *110*. https://doi.org/10.1063/1.478522.

(61) Pyykko, P. Relativistic Effects in Structural Chemistry. *Chem. Rev.* **1988**, *88* (3), 563–594. https://doi.org/10.1021/cr00085a006.

(62) Lenthe, E.; Ehlers, A.; Baerends, E. Geometry Optimization in the Zero Order Regular Approximation for Relativistic Effects. *J. Chem. Phys.* **1999**, *110*, 8943–8953. https://doi.org/10.1063/1.478813.

(63) Staemmler, V.; Hättig, C.; Marx, D. Editorial. *Mol. Phys.* **2013**, *111* (16–17), 2375–2376. https://doi.org/10.1080/00268976.2013.835150.

(64) Becke, A. D. A Multicenter Numerical Integration Scheme for Polyatomic Molecules. *J. Chem. Phys.* **1988**, *88* (4), 2547–2553. https://doi.org/10.1063/1.454033.

(65) Franchini, M.; Philipsen, P. H. T.; Visscher, L. The Becke Fuzzy Cells Integration Scheme in the Amsterdam Density Functional Program Suite. *J. Comput. Chem.* **2013**, *34* (21), 1819–1827. https://doi.org/10.1002/jcc.23323.

(66) Bouhoute, Y.; Garron, A.; Grekov, D.; Merle, N.; Szeto, K.; Mallmann, A. de; Del rosal, I.; Maron, L.; Girard, G.; Gauvin, R. M.; Delevoye, L.; Taoufik, M. Well-Defined Supported Mononuclear Tungsten Oxo Species as Olefin Metathesis Pre-Catalysts. *ACS Catal.* **2014**, *4* (11), 4232.

(67) Merle, N.; Girard, G.; Popoff, N.; De Mallmann, A.; Bouhoute, Y.; Trébosc, J.; Berrier, E.; Paul, J.-F.; Nicholas, C. P.; Del Rosal, I.; Maron, L.; Gauvin, R. M.; Delevoye, L.; Taoufik, M. On the Track to Silica-Supported Tungsten Oxo Metathesis Catalysts: Input from 17O Solid-State NMR. *Inorg. Chem.* **2013**, *52* (17), 10119–10130. https://doi.org/10.1021/ic401521m.

(68) Gibson, V. C.; Kee, T. P.; Shaw, A. New, Improved Syntheses of the Group 6 Oxyhalides, $W(O)Cl_4$, $W(O)_2Cl_2$ and $Mo(O)_2Cl_2$. *Polyhedron* **1988**, *7* (7), 579–580. https://doi.org/10.1016/S0277-5387(00)86336-6.

(69) Tosin, G.; Delgado, M.; Baudouin, A.; Santini, C. C.; Bayard, F.; Basset, J.-M. Surface Organometallic Chemistry of $Hf(CH2^tBu)_4$ on Silica and Silica−Alumina: Reaction of the Resulting Grafted Hafnium Neopentyl with Dihydrogen. *Organometallics* **2010**, *29* (6), 1312–1322. https://doi.org/10.1021/om900258q.

(70) Shelimov, B. N.; Elev, I. V.; Kazansky, V. B. Spectroscopic Study of Formation of Active Metal-Carbene Species in Photoreduced Silica-Molybdena Catalysts for Olefin Metathesis. *J. Mol. Catal.* **1988**, *46* (1), 187–200. https://doi.org/10.1016/0304-5102(88)85093-4.

(71) Mercer, M. Molybdenum Hexachloride. *Chem. Commun. Lond.* **1967**, No. 3, 119–119. https://doi.org/10.1039/C19670000119.

(72) Colton, R.; Tomkins, I.; Wilson, P. The Preparation of Molybdenum Oxidetetrachloride. *Aust. J. Chem.* **1964**, *17* (4), 496. https://doi.org/10.1071/ch9640496.

(73) Nam, T.; Colleran, T. A.; Partridge, J. L.; Cavanagh, A. S.; George, S. M. Thermal Atomic Layer Etching of Molybdenum Using Sequential Oxidation and Deoxychlorination Reactions. *Chem. Mater.* **2024**, *36* (3), 1449–1458. https://doi.org/10.1021/acs.chemmater.3c02606.

(74) Merle, N.; Le Quéméner, F.; Bouhoute, Y.; Szeto, K. C.; De Mallmann, A.; Barman, S.; Samantaray, M. K.; Delevoye, L.; Gauvin, R. M.; Taoufik, M.; Basset, J.-M. Well-Defined Molybdenum Oxo Alkyl Complex Supported on Silica by Surface Organometallic Chemistry: A Highly Active Olefin Metathesis Precatalyst. *J. Am. Chem. Soc.* **2017**, *139* (6), 2144–2147. https://doi.org/10.1021/jacs.6b11220.

(75) Kim, H. N.; Lee, S. K. Atomic Structure and Dehydration Mechanism of Amorphous Silica: Insights from 29Si and 1H Solid-State MAS NMR Study of SiO_2 Nanoparticles. *Geochim. Cosmochim. Acta* **2013**, *120*, 39–64. https://doi.org/10.1016/j.gca.2013.05.047.

(76) Grünberg, B.; Emmler, T.; Gedat, E.; Shenderovich, I.; Findenegg, G. H.; Limbach, H.-H.; Buntkowsky, G. Hydrogen Bonding of Water Confined in Mesoporous Silica MCM-41 and SBA-15 Studied by 1H Solid-State NMR. *Chem. Weinh. Bergstr. Ger.* **2004**, *10* (22), 5689–5696. https://doi.org/10.1002/chem.200400351.

(77) Herrera, J. E.; Kwak, J. H.; Hu, J. Z.; Wang, Y.; Peden, C. H. F. Synthesis of Nanodispersed Oxides of Vanadium, Titanium, Molybdenum, and Tungsten on Mesoporous Silica Using Atomic Layer Deposition. *Top. Catal.* **2006**, *39* (3), 245–255. https://doi.org/10.1007/s11244-006-0063-0.

(78) *TOLUENE-D8(2037-26-5) 1H NMR spectrum*. https://www.chemicalbook.com/SpectrumEN_2037-26-5_1HNMR.htm (accessed 2025-07-23).

(79) Amakawa, K.; Kröhnert, J.; Wrabetz, S.; Frank, B.; Hemmann, F.; Jäger, C.; Schlögl, R.; Trunschke, A. Active Sites in Olefin Metathesis over Supported Molybdena Catalysts. *ChemCatChem* **2015**, *7* (24), 4059–4065. https://doi.org/10.1002/cctc.201500725.

(80) *Molybdenum | XPS Periodic Table - FR*. https://www.thermofisher.com/fr/fr/home/materials-science/learning-center/periodic-table/transition-metal/molybdenum.html (accessed 2025-07-22).

(81) Wagner, C. D.; Wagner, C. D. *Handbook of X-Ray Photoelectron Spectroscopy: A Reference Book of Standard Data for Use in X-Ray Photoelectron Spectroscopy*; Perkin-Elmer, 1979.

(82) Mastikhin, V. M.; Lapina, O. B.; Maximovskaya, R. I. 95Mo Solid-State NMR Spectra of Molybdates. *Chem. Phys. Lett.* **1988**, *148* (5), 413–416. https://doi.org/10.1016/0009-2614(88)87197-5.

Chapter 3.
Solid-State NMR study under light irradiation of new acidic amorphous aluminosilicates (AAS) functionalized with gold nanoparticles.

Chapter 3: Solid-State NMR study under light irradiation of new acidic amorphous aluminosilicates (AAS) functionalized with gold nanoparticles

1. Introduction

Amorphous silica-alumina (ASAs) are popular solid-acid catalysts, which are widely employed in petroleum refining, biomass conversion and organic synthesis.[1,2] ASAs exhibit milder acidity than zeolites. Despite extensive studies, the structure of Brønsted acid sites (BAS) in ASA is still highly debated. Compared to zeolites, the amorphous structure of ASAs makes it difficult to determine the atomic-level structure of their BAS. On the basis of molecular modelling studies, it has been proposed that the acidity of ASAs is mainly due to silanol groups in the proximity of aluminum atoms, which stabilizes the silanolate anion and, hence, increase the Brønsted acidity of these pseudo-bridging silanol (PBS) groups.[3,4] In contrast with BAS based on bridging silanol (BS) groups, Si−O(H)−Al, found in zeolites, there is a lack of covalent bonds between O and Al atoms in PBS. Solid-state NMR experiments, which allowed to probe proximities between ^{1}H and ^{27}Al nuclei and to measure ^{1}H–^{17}O distances in ASA, provided experimental evidence for the existence of PBS in these catalysts and their ability to protonate ammonia.[5–7]

Nevertheless, the existence of BAS based on BS in ASA was suggested by their catalytic activity for the propane cracking and H/D exchange and the presence of sites with distinct acidities, as detected by infrared spectroscopy using probe molecules.[8,9] Recently, solid-state NMR experiments were conducted at an ultra-high magnetic field (35.2 T), i.e., a ^{1}H Larmor frequency of 1.5 GHz, to observe the proximity between ^{1}H and ^{27}Al nuclei and provided the first direct spectral evidence for the existence of BAS based on BS in ASA.[10] The presence of these BS in ASA was later confirmed by the measurement of ^{1}H–^{27}Al distance in deuterated ASA selectively protonated in the strong BAS.[11]

Furthermore, recently, the group of Vivek Polshettiwar has introduced nanosponges made of amorphous acidic aluminosilicate (AAS), which possess BAS based on BS similar to those found in zeolites but textural properties and high mesoporosity like ASAs which have weak

acidic sites.[12] AAS catalyst has a high surface area and large pore volume. This unique combination of acidity and accessibility is able to catalyse various challenging reactions more effectively than zeolites. These new materials differ from conventional ASA first by their texture and morphology. AAS are nanoparticles with a distinctive dendritic porous sponge-like morphology and high, tunable microporosity (with a BET surface of 436–588 $m^2.g^{-1}$ and of pore volume 0.7–1.5 $cm^3.g^{-1}$). This arises from a microemulsion soft-templating route. Furthermore, comparable hydrolysis rates between Si and Al precursor (which are tetra ethyl Orthosilicate for the former and Al-acetylacetonate for the latter) avoid homo condensation and the formation of distinct phases. It was shown that Al is homogeneously distributed across the nanosponges. AAS contains more BS than conventional ASAs since the 1D ^1H NMR spectrum of AAS exhibits, besides the signal of PBS at 1.9 ppm, intense signals at 4.7 ppm assigned to BS.[13] It is this combination of high acidity and high mesoporosity that makes AAS materials different from other conventional solid acids. This combination achieved through a tailored synthesis method with controlled hydrolysis and condensation of Al and Si precursors preserves Brønsted acidity and mesoporosity, differentiating AAS from conventional zeolites or ASAs.

AAS catalyzes different reactions that require strong acidity, including styrene oxide ring-opening, Friedel–Crafts alkylation, *m*-xylene isomerization, and cumene cracking, with better performance than state-of-the-art zeolites and amorphous aluminosilicates. Notably, AAS also efficiently converts a range of waste plastics to hydrocarbons at significantly lower temperatures. Last year, the group of Vivek Polshettiwar had shown that oxygen vacancies can be introduced into AAS to further enhance the Brønsted acidity of AAS.[13] The catalytic performances of these defective AAS in acid-catalyzed reactions outperform those of conventional AAS. However, certain reactions require even stronger acidity hence there is a need to improve the acidity of these Bronsted acidic sites in AAS. Recently, it has also been observed that the Brønsted acidity of AAS can be increased by functionalizing them with gold nanoparticles and irradiating them with light. This represents an unexplored area of research with significant potential. To investigate this, AAS coated with Au nanoparticles was synthesised (Au-AAS). The localized surface plasmon resonance (LSPR) of gold nanoparticles is known to enhance the electric field in its vicinity. This electric near-field enhancement can induce elongation in the polar bonds near the Au

NPs, which can lead to enhanced polarisation of those bonds. These Au/AAS materials represent promising solid-acid photocatalysts, which could use sunlight as the energy source to drive chemical reactions. A significant improvement in the conversion percentage and the rate of reaction was observed in the Au/AAS catalyst. Attempts were made to understand the role of gold nanoparticles and their SPR in the enhancement of the catalytic activity of the catalyst through intensity-dependent and wavelength-dependent studies. It has been hypothesized that this acidity enhancement stems from localized surface plasmon resonance (LSPR) process, which produces localized electric fields near gold nanoparticles in the presence of light.[14] These electric near-field enhancement can induce elongation in the O−H bonds of silanol groups, thus enhancing their Brønsted acidity and better catalytic activity of the catalyst. Nevertheless, this structural modification in the presence of light has not been evidenced so far.

During my PhD, we tried to investigate this bond elongation, the corresponding increase in acidity and characterize structural changes of AAS functionalized by gold nanoparticles in the presence of light using advanced solid-state NMR experiments.

2. Synthesis of AAS with zeolite-like acidity

2.1. Synthesis of AAS via controlled hydrolysis-condensation

The synthesis of AAS is described below and schematically displayed in Scheme 3. First, a round flask was filled with cetyltrimethylammonium bromide (CTAB)-500 mg, urea-600 mg, and water-5 mL, which was then agitated at room temperature (RT) at 1400 revolutions per minutes (rpm) for 30 min. Following this, a freshly prepared solution of 2.8 mmol aluminum acetylacetonate ($Al(acac)_3$) and 2.8 mmol tetraethyl orthosilicate (TEOS), both freshly dissolved in 45 mL *p*-xylene was added dropwise and stirred for 30 min at 1000 rpm at RT. The reaction mixture was then refluxed at 120 °C for 12 h while stirring continuously at 1000 rpm. This stage facilitated the components to self-assemble into an ordered lamellar phase structure in the water/*p*-xylene mixture. After the reaction, the solid product was separated by centrifugation. It was extensively rinsed three times with ethanol (EtOH) and three times with deionized (DI) water to eliminate any remaining

surfactants and byproducts. The material was dried at 80 °C for 12 h to eliminate any leftover solvents. The dried product was calcined at 750 °C (at a rate of 5 °C/min) for 6 h. This thermal treatment eliminates the organic template while stabilizing the porous framework, resulting in the creation of nano-sponge-like AAS.

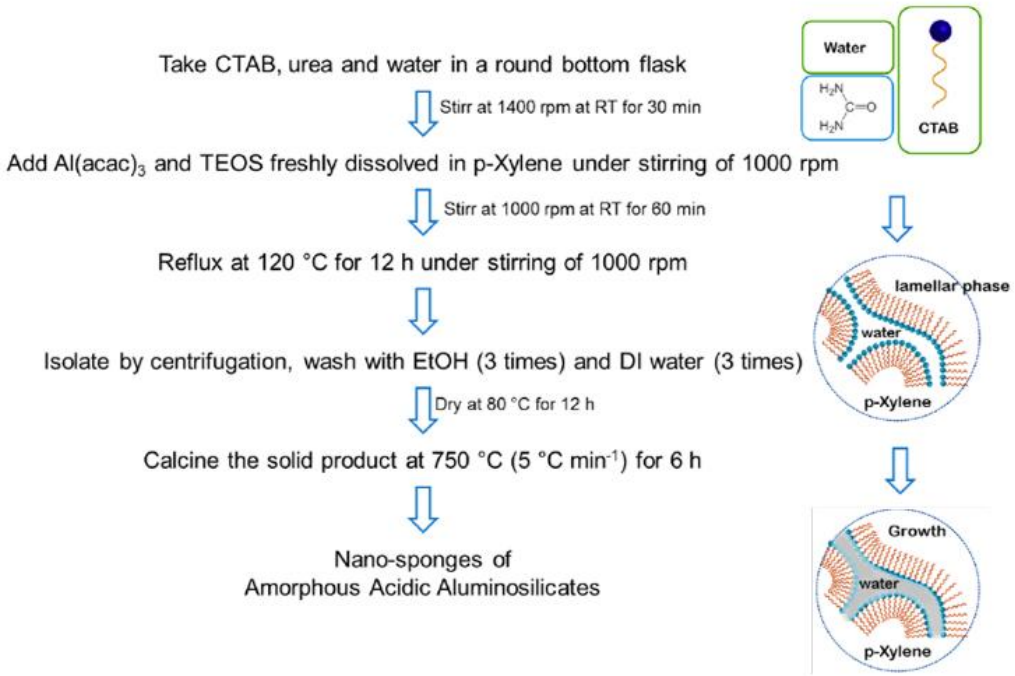

Scheme 3: *Step by step synthesis protocol of AAS from Verma et al.*[13]

2.2. Functionalization of AAS with Au nanoparticles

The synthesis of Au/AAS material requires 100 mg of AAS dispersed in 10 mL of deionised water in a conical flask and sonicated for 15 min to ensure uniform dispersion. Then, 200 µL of an aqueous $HAuCl_4$ stock solution (100 $mg.mL^{-1}$) was added, followed by another 15 min of sonication. The resulting suspension was then stirred at room temperature at 4000 rpm for 15 min. For reduction of Au^{3+} ions, a freshly prepared $NaBH_4$ solution was prepared by dissolving 30 mg of $NaBH_4$ in 60 mL of water. This reducing solution was added dropwise to the gold precursor suspension under vigorous stirring, and the reaction mixture was further stirred for 3 h at room temperature. The solid product was isolated by centrifugation (without additional washing) and subsequently dried overnight at 80 °C to obtain the final Au/AAS material.

The prepared AAS and Au/AAS samples were initially characterized using conventional techniques, such as X-ray diffraction (XRD), scanning electron microscopy (SEM), transmission electron microscopy (TEM), energy-dispersive X-ray spectroscopy (EDX), UV-visible diffuse reflectance spectroscopy (UV-Vis DRS), and thermogravimetric analysis (TGA), as explained in the next section.

3. Characterization of structural and optical properties of AAS and Au/AAS

3.1. SEM, TEM, EDS and PXRD

All SEM images were acquired with a Zeiss Ultra microscope at 5 kV and a working distance of 3-5 mm. TEM analysis were carried out at an accelerating voltage of 300 kV using an FEI Titan microscope. Elemental mapping was performed using energy-dispersive X-ray spectroscopy (EDS). Samples were prepared by dispersing a small amount of solid powder in ethanol by sonication for 10 s, and the dispersion was drop-casted onto a holey carbon-coated 200 mesh copper TEM grid. Powder XRD (PXRD) patterns were obtained using a Panalytical X'Pert Pro powder X-ray diffractometer with Cu-Kα radiation. Prior to all of the characterization techniques, samples were degassed at 120 °C for 2 h.

Both SEM and TEM images show that AAS and Au/AAS samples have a sponge-like porous structure. This morphology is retained in the Au/AAS sample under SEM (Figure 45b), with bright contrasting spots suggesting gold nanoparticle deposition. Gold, as a heavy metal, scatters electrons and hence, appears brighter. This sponge-like structure is also observed in TEM images, shown in Figures 45 c and d. Again, Au/AAS samples exhibit brilliant spots evenly dispersed throughout the matrix, corresponding to gold nanoparticles.

We also employed EDS coupled with TEM to determine the elemental composition of materials, i.e., the mass fractions of the different element (Si, Al, O, and Au) (see Figure 46 and Table 12). This technique indicates a gold fraction of 4.5 wt.% in Au/AAS. This loading was further confirmed by ICP-MS. Particle size distribution analysis was also done using multiple TEM images and indicated the presence of small Au NPs ranging from 5 to 70 nm.

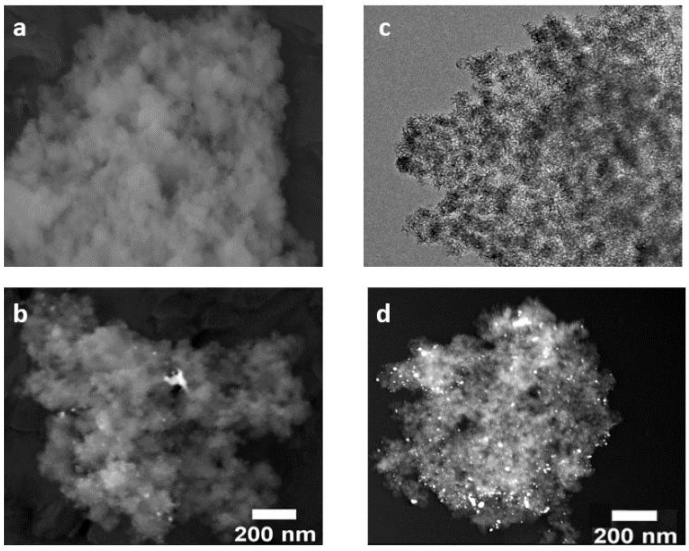

Figure 45: *(a, b) SEM and (c, d) TEM images of (a, c) AAS and (b, d) Au/AAS.*

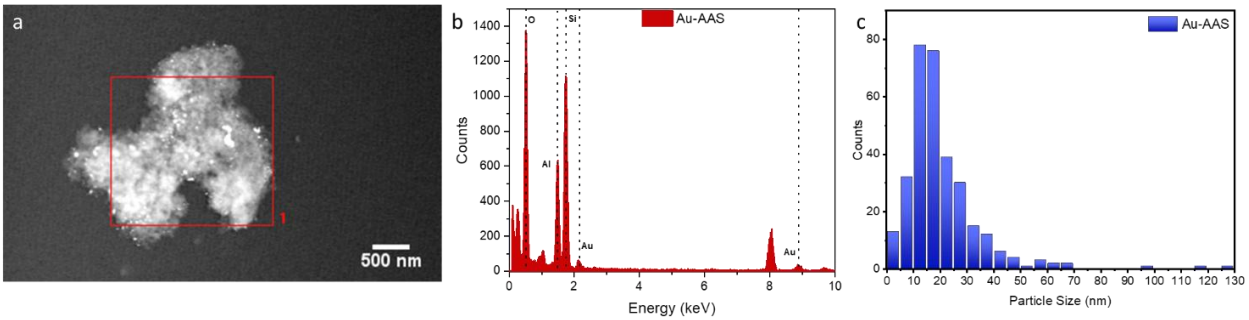

Figure 46: *EDS coupled to TEM of Au/ASA. (a) The TEM image is shown, while (b) X-rays emission as function of energy allows the determination of the elemental composition (c) Particle size distribution of Au NPs loaded on AAS.*

Table 12: *Quantitative results of EDS showing the elemental composition of AAS and Au/AAS in weight percent.*

Sample	Si	O	Al	Au
AAS	30.8 ± 1.2	55.7 ± 1.0	13.4 ± 0.8	N.A.
Au/AAS	29.2 ± 3.6	53.5 ± 5.1	12.9 ± 1.3	4.5 ± 0.8

PXRD was employed to probe the formation of crystalline phase. For AAS, a purely amorphous phase is observed (a hump at around 22° due to the amorphous AAS support). However, for Au/AAS, reflections observed at 38.21°, 44.51° and 64.5° are produced by crystallographic planes, (111), (200) and (220) of gold nanoparticles, corresponding to the diffraction pattern of the gold cubic lattice, confirming their crystallinity (Figure 47).[15]

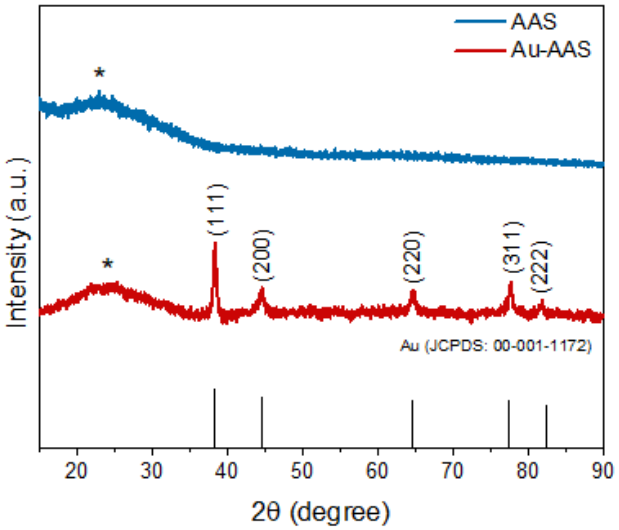

Figure 47: *Experimental PXRD patterns of AAS (blue) and Au/AAS (red) along with simulated pattern of gold crystalline phase. Reflections of Au/AAS are assigned to Miller indices of gold crystalline planes.*

3.2. TGA

The thermal stability of AAS and Au/AAS was investigated using TGA. The analysis was conducted with a Mettler Toledo TGA TGA-DSC2/LF/1100, in an air flow of 40 mL/min and the chamber was heated from 100 to 800 °C at a rate of 10 °C per minute.

The TGA results showed a first mass loss of 19 wt.% for AAS at 100 °C attributed to the desorption of adsorbed water from the catalyst surface. For Au/AAS, a loss of 13 wt.% is observed at the same temperature, indicating that the presence of gold nanoparticles lowers the material's ability to adsorb water, most likely due to partial pore blockage. As the temperature increased, a second weight loss occurred above 120 °C. This stage marks the removal of surface hydroxyl groups within the material's structure. The loss is about 6 wt.% for AAS and 7 wt.% for the Au/AAS, showing that both samples have same amount of hydroxyl groups.

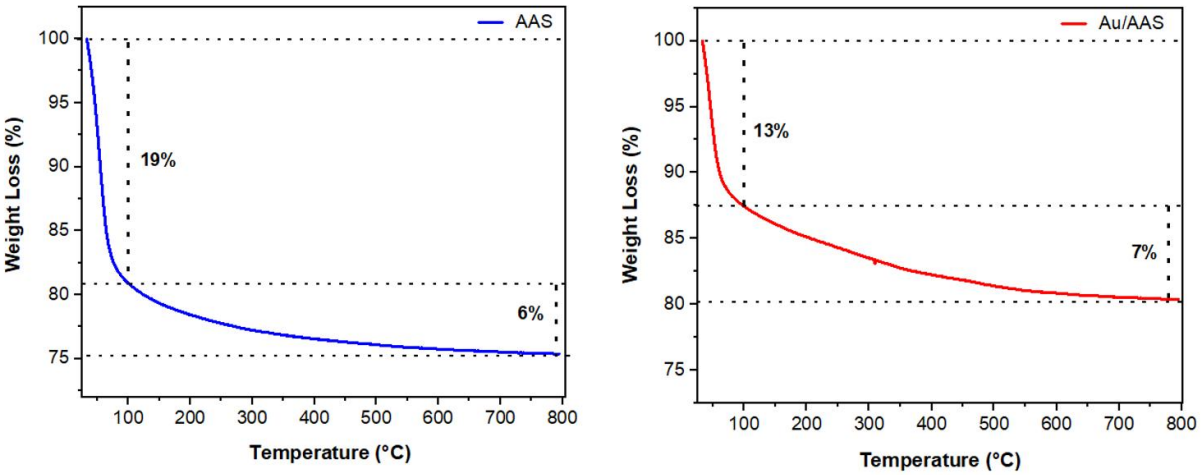

Figure 48: *TGA of AAS (left) and Au/AAS (right) showing two successive mass losses, at 100 °C and above 120 °C attributed to loss of absorbed water and hydroxyl groups, respectively.*

3.3. UV-Vis-DRS

Au/AAS are expected to be highly acidic photocatalysts with potential applications in chemical manufacturing, energy storage and environmental remediation. So far, zeolites have been tested as photocatalysts for the breakdown of pollutants using UV radiation.[16] However, UV radiation accounts for only 5% of sunlight energy at Earth's surface, which limits the applicability of photocatalysts relying on UV light. A promising approach to boost light absorption consists in the incorporation of plasmonic nanostructures, which leads to LSPR phenomenon, *i.e.*, when metallic nanoparticles are exposed to light, their surface free conduction electrons collectively oscillate, enhancing the electric field of the incident light. The amplification can be significant, reaching a factor of roughly 10^3 near the surface of a single isolated nanoparticle and up to 10^6 at the junctions between closely spaced particles. The optical absorption of Au/AAS was characterized using UV-Vis DRS (see Figure 49). UV–Vis–DRS measurements of Au/AAS and AAS were carried out using a JASCO UV–Vis/NIR spectrophotometer. With respect to AAS, the UV-Vis spectra of Au/AAS show an increased absorbance at around 519 nm ascribed to LSPR effects. This wavelength falls in the green region within the visible spectrum.[17]

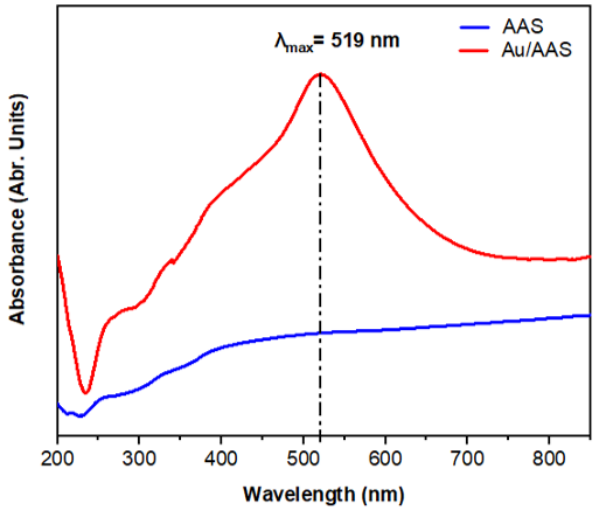

Figure 49: *UV-visible spectra of AAS (blue) and Au/AAS (red).*

3.4. N_2 sorption isotherms

Nitrogen sorption isotherms are commonly used to evaluate the textural features of porous materials, including surface area, pore volume, and pore size distribution. Measurements are typically performed at 77 K using nitrogen gas as the adsorbate. The Brunauer-Emmett-Teller (BET) method is commonly employed for quantitative surface area analysis.[18] The total surface area is calculated from the adsorption data obtained in P/P_0 range of 0.05 to 0.3. In addition to surface area, the total pore volume is commonly determined from the quantity of nitrogen adsorbed at high relative pressure (e.g., P/P_0 = 0.98). Pore size distribution can be obtained further utilizing methods, such as Barrett-Joyner-Halenda (BJH) [19] for mesopores.

Adsorption isotherms are often categorized into six groups depending on porosity properties, as displayed in Figure 50. Type I are common isotherms of microporous materials. Adsorption in this situation is confined to a monolayer because the pores are so small that they quickly get saturated. When the micropores are full, there is no more available surface area for more gas to adsorb. Type II are typically found in nonporous or macroporous materials having pores larger than ~100 nm exhibiting multilayer adsorption. Type III isotherms describe multilayer adsorption on nonporous surfaces. However, unlike Type II, they lack a strong initial gas uptake implying a weak contact of the adsorbate with the adsorbent's surface. Type IV materials are mesoporous, with pore diameters ranging from 1.5 to 100 nm. These isotherms show a rapid increase in gas adsorbed volume at

intermediate pressures due to capillary condensation within the pores. A significant feature of type IV isotherms is the hysteresis loop that arises between the adsorption and desorption branches. Type V, like Type III, exhibits modest adsorbate-adsorbent interactions. They are, nonetheless, linked to mesoporous materials and show hysteresis loops, albeit less obvious than those in Type IV. Type VI isotherms correspond to stepwise multilayer adsorption on a uniform, non-porous surface.

N_2 sorption isotherms were measured for AAS and Au/AAS samples. These studies were performed using a Micromeritics 3-Flex surface analyzer. Before the analysis samples were degassed at 120 °C for 12 h under 0.18 mmHg vacuum, followed by in-situ degassing at 120 °C for another 2 h under 0.000119 mmHg vacuum. BET and BJH calculations are applied to determine the surface area and the pore volume respectively (see Figure 50 b-e).

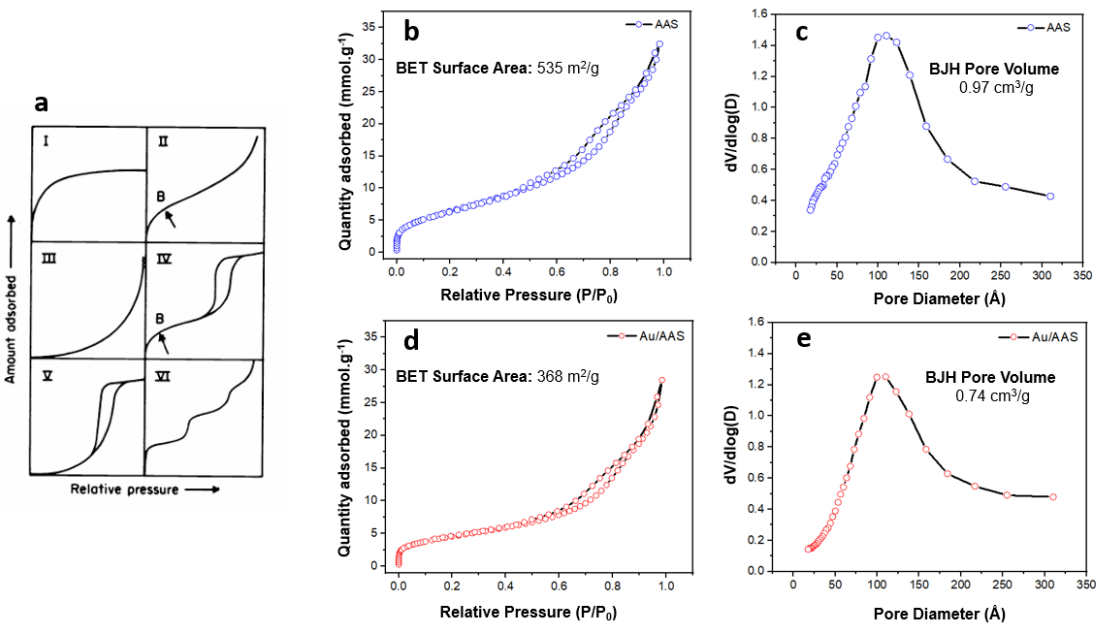

Figure 50: *(a) Different types of physisorption isotherms.[20] (b, d) Experimental nitrogen sorption isotherms of (b) AAS and (d) Au/AAS. BET surface areas are written in the plots. BJH adsorption pore-size distributions of (c) AAS and (e) Au/AAS for textural characterization.*

The isotherms of both AAS and Au/AAS correspond to the type IV family. The surface area shows a decrease from 535 to 365 $m^2.g^{-1}$ after the deposition of Au NPs. The same trend is observed for the pore volume, which drops from 0.97 $cm^3.g^{-1}$ to AAS to 0.74 $cm^3.g^{-1}$ for Au/AAS. The reduced surface and pore volume of Au/AAS stem from the pore blockage by gold nanoparticles.[15] The size of gold nanoparticles can be measured on TEM image. The diameter of these pseudospherical nanoparticles ranges from 5 to 70 nm. Therefore, the

smaller pores of AAS can be blocked or partially filled by these gold nanoparticles, leaving reduced surface area and pore space available for nitrogen during physisorption tests.[21]

4. Acid-catalysed styrene oxide ring opening reaction

4.1. Catalytic Conversion

In a recent publication on AAS, A. Maity *et al.* demonstrated that AASs contain zeolite-like BS groups and proved their good catalytic activity in reactions that require strong acidic catalysts with large pores size.[12] These materials are efficient catalysts for processes, such as styrene oxide ring-opening, vesidryl and jasminaldehyde synthesis, Friedel-Crafts alkylation, *m*-xylene isomerization, and cumene cracking. Furthermore, they outperformed typical zeolites and conventional amorphous aluminosilicates, demonstrating a high activity and greater accessibility to active areas due to their nanosponge shape and mesoporosity. AASs are found also to be efficient at degrading plastic waste into hydrocarbons at lower temperatures.

Herein, the catalytic activities of Au/AAS and pure AAS were compared for the styrene oxide ring opening reaction. These reactions were carried out with and without light irradiation to see if plasmonic stimulation of Au NPs increases the acidity of Brønsted sites and, therefore, the catalytic efficiency. This comparative study provides a straightforward method for evaluating the effect of LSPR on acid strength and reaction kinetics.

In this reaction, an acidic site protonates the epoxide oxygen, activating the strained three-membered ring by increasing the electrophilicity of the neighboring carbon atoms. This protonation step produces a reactive oxonium intermediate. The opening of the epoxide ring leads to a carbocation with a positive charge on the benzylic carbon. This benzylic carbon is attached by methanol, acting as a nucleophile. Finally, the system deprotonates to renew the acidic site and produce the end product, 2-methoxy-2-phenylethanol as displayed on Figure 51.

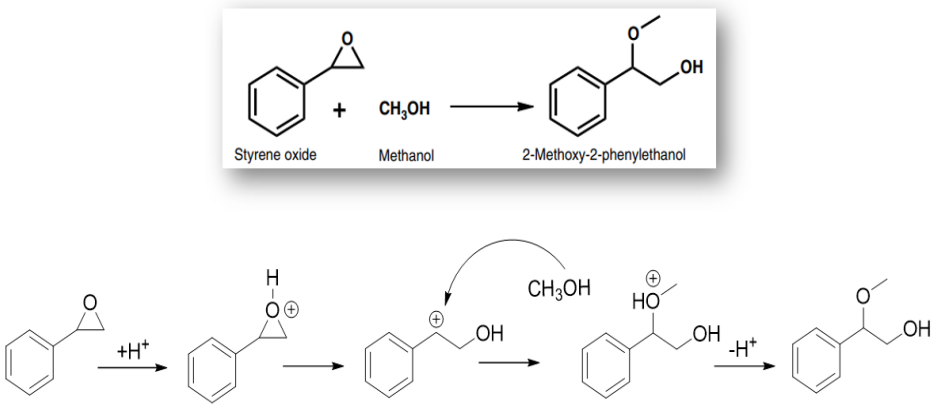

Figure 51: *Styrene oxide ring opening reaction mechanism*

Catalytic reactions were carried out in a Schlenk tube with 15 mg of Au/ASA catalyst. The catalyst was first degassed at 120 °C for 1 h before cooling to room temperature. Before the reaction, the system was purged with nitrogen and the temperature was set to 40 °C. Then, 5 mL of methanol was added to the Schlenk tube, and the suspension was sonicated for 5-10 s to ensure uniform dispersion of the catalyst. Next step consists of the addition of 500 μL of styrene oxide and the collection of an initial sample (0 min). During photocatalytic tests, the light intensity was kept at 1.04 W cm^{-2} and the reaction mixture was stirred at 500 rpm. Aliquots were collected at predetermined time intervals and examined with gas chromatography-mass spectrometry. The solution temperature was measured using a thermocouple and recorded at the end of the reaction. Furthermore, control tests were carried out. These tests included reactions under dark conditions at the same temperatures as those measured during photocatalytic reaction to account for simply thermal contributions, as well as reactions under light irradiation but without a catalyst to exclude direct photolysis of the substrate.

For reaction under light irradiation, the illumination was done with a Newport light source at 1.04 W/cm^2. The reaction profiles show a significant variance in conversion rates depending on the catalyst and the presence of light, as shown in Figure 52. The catalytic activity of pure AAS increased moderately when exposed to light. After 180 minutes, conversion reached 65% under light, compared to 45% in the dark. In contrast, the activity of the Au/AAS increased dramatically when exposed to light. Under illumination, conversion reached about 100% in just 2 h, whereas in darkness, conversion slowed and plateaued at around 40%, almost similar to AAS in the dark. Therefore, we can conclude

that light irradiation boosts the catalytic performance by photo-excitation of the catalysts in the presence of Au NPs.

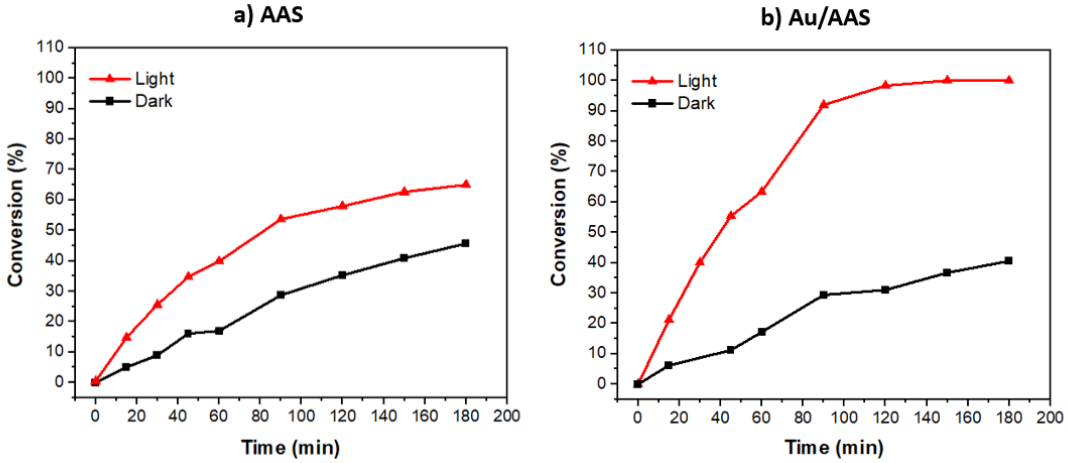

Figure 52: *Catalytic activity of (a) AAS and (b) Au/AAS in styrene oxide ring-opening reaction in the dark and under visible light irradiation of λ = 519 nm.*

4.2. Light intensity and wavelength dependence

As seen in Figure 53, The catalytic activity of the photocatalysts in ring opening reaction is strongly influenced by light intensity (see plot on the left side of Figure 53). Higher light intensities excite more electrons in Au NPs, leading to a stronger electromagnetic field in their vicinity and higher conversion rate. Light wavelength also influences the photoconversion measured with Au/AAS, as seen on the plot at the right side of Figure 53. AAS has very limited light absorption at wavelength greater than 200 nm, while Au/AAS exhibits an absorption peak at 525 nm in the visible light range (Figure 53, right plot). The wavelength-dependent study shown in the figure demonstrates a clear correlation between the catalytic conversion and the absorption profile of gold.[15] The highest conversion is observed at 450 nm, which corresponds closely to the LSPR peak of Au nanoparticles, indicating that the reaction is strongly influenced by plasmonic excitation. Interestingly, when comparing the results at 637 nm and 808 nm, the conversion is significantly higher at 637 nm, even though the bulk temperature at 808 nm is higher. This suggests that the catalytic activity is not merely a result of macroscopic heating but is instead governed by the localized plasmonic effects of gold. While local temperatures near the nanoparticle surface could be higher than the measured bulk temperature, the strong correlation between the absorption maximum and conversion strongly points toward an

electric-field–driven mechanism associated with LSPR. Thus, these results indicate that plasmon-induced electric field enhancement, rather than simple photothermal heating, plays the dominant role in enhancing the catalytic activity of the Au-AAS system.

Since the conversion closely follows the trend of light intensity and correlates with the optical absorption of Au (as shown in the wavelength-dependent study), it suggests that plasmon-induced electric field enhancement is playing the dominant role. This intensity dependence indicates that the reaction is primarily driven by LSPR mediated activation rather than bulk thermal effects.

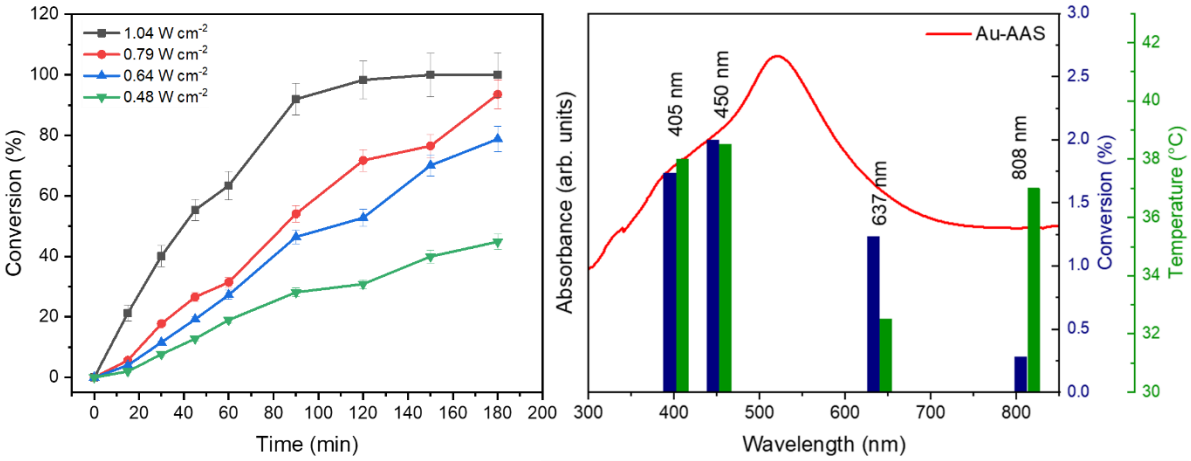

Figure 53: *Effects of the light intensity (left) and light wavelength (right) on the photoconversion of styrene oxide into 2-methoxy-2-phenylethanol in the presence of Au/AAS catalyst.*

4.3. Reaction mechanism and hypothesis

The ring-opening of styrene oxide over D-AAS-12 proceeds via a Brønsted acid catalysed mechanism (as shown in Figure 7 and 10). Initially, styrene oxide is adsorbed near a Si–OH–Al Brønsted acid site, where the acidic proton of the BAS protonates the epoxide oxygen, forming a highly activated oxonium intermediate. This protonation weakens the C–O bond, generating partial positive character at the benzylic carbon, which is then attacked by methanol as a nucleophile, leading to epoxide ring opening. The resulting β-alkoxy alcohol intermediate subsequently undergoes deprotonation, regenerating the BAS and releasing the final product. To achieve higher catalytic activity for the ring-opening reaction, it is essential to enhance the Brønsted acidity of the catalyst. This can be

effectively accomplished through the LSPR of gold nanoparticles, which can modulate the acidity of nearby active sites under light excitation.

LSPR is a collective oscillation of conduction electrons in a metal nanoparticle that occurs when the frequency of incident light matches the natural frequency of these electrons. Because the nanoparticle is much smaller than the wavelength of light, this oscillation becomes confined or localized to the nanoparticle surface, creating intense, highly localized electromagnetic fields near the particle. Illumination of Au/AAS at the LSPR wavelength hence produces very strong, highly localized electric fields. This enhanced electric field polarizes and transiently lengthens O–H bonds of nearby Si–OH–Al (BS) Brønsted acid sites located in the proximity of gold nanoparticles (as depicted in Figure 54), increasing proton acidity in the presence of light. When the light is turned off, the field vanishes hence, the bond should return to its ground geometry. This lengthening increases their Brønsted acidity and hence, their catalytic activity for the ring opening of styrene oxide. As the carriers in collective oscillation motion interact with the surrounding environment (electron-phonon coupling), the stored energy gradually dissipates, eventually transforming into heat, causing the heating of the nanoparticle itself. This subsequent heat can then disperse into the surrounding environment, resulting in what is termed the photothermal effect near Au nanoparticles. This local heating can induce bond breaking, elongation, or reorganisation at the silica–alumina interface. Those structural rearrangements can remain after illumination and therefore produce permanent changes in the catalyst. Both pathways can act simultaneously; the net effect depends on local energy deposition exposure time, and local chemical susceptibility.

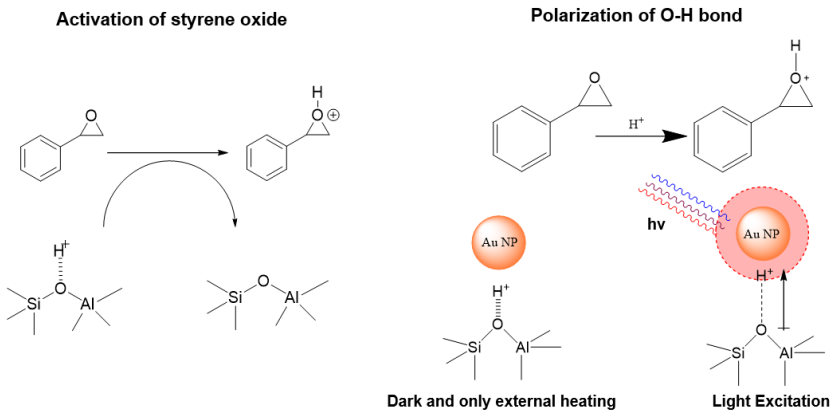

Figure 54: *Protonation and activation of styrene oxide by BAS based on BS (left) and enhancement of O–H bond polarization of BS near gold nanoparticle under light irradiation owing to LSPR phenomenon (right).*

During my PhD, we tried to characterize the atomic-level structure of BAS in Au/AAS using multinuclear (^{1}H, ^{27}Al, ^{29}Si) solid-state NMR (ssNMR) spectroscopy and specially to observe structural modifications under light irradiation. These NMR results are presented and discussed in the following sections.

5. ssNMR without light irradiation

5.1. Experimental conditions at 9.4 T in zirconia rotors

The first experiments were carried out on the first batch of samples synthesized by our colleagues at the Tata Institute of Fundamental Research (TIFR), in Mumbai. The samples were simply dried in oven at 120 °C for 12 h and shipped in vacuumed vials to avoid contamination with air and moisture. It should be noted that dehydration temperature must remain below 200 °C to preserve the Brønsted acidity of AAS. At Lille NMR facility, the samples were stored in Jacomex glove box.

NMR spectra were acquired using a Bruker Avance II spectrometer equipped with a 9.4 T widebore magnet operating at Larmor frequencies of 400 MHz for ^{1}H, 104.22 MHz for ^{27}Al, and 79.46 MHz for ^{29}Si. Powdered samples were packed into 4 mm ZrO_2 rotors in the glove box and rotated at magic angle spinning (MAS) frequency, ν_R = 10 kHz, using a conventional 4 mm HXY probe in double resonance mode.

The 1D ^{1}H MAS NMR spectra were acquired using DEPTH sequence[22] to suppress background signal using a 90° pulse that lasted 3.5 µs with a radiofrequency (rf) field amplitude, ν_1 = 71.4 kHz. The 1D ^{1}H NMR spectra resulted from averaging 16 transients with a recovery delay of 5 s, i.e., a total experimental time of 2 min. The 1D ^{29}Si MAS NMR spectra were recorded using UDEFT pulse sequence[23] to improve sensitivity and quantification. The ^{29}Si π/2 pulse applied lasted 5 µs at ν_1 = 50 kHz. The 1D ^{29}Si NMR spectra resulted from averaging 2048 transients with a recovery delay τ_{RD} = 10 s, i.e., an experimental time of 8 h.

For the 2D ^{1}H→^{29}Si CP-HETCOR experiment, the initial ^{1}H π/2 pulse lasted 3.5 µs and was followed by a CP contact time equal to 5 ms. During the CP transfer, the rf nutation

frequency on the ^{29}Si channel was constant and equal to 59.5 kHz, while the ^{1}H nutation frequency was linearly ramped from 35.7 to 71.4 kHz. SPINAL-64 ^{1}H decoupling[24] with ν_1 = 71 kHz was applied during acquisition. The Hartmann-Hahn condition was calibrated using octakis(trimethylsiloxy)silsesquioxane (Q_8M_8) powder presented in scheme 4. This sample is an ideal compound for such calibration since it contains eight mobile and equivalent trimethylsiloxy groups, which yields narrow and intense ^{29}Si signal. The 2D ^{1}H→^{29}Si CP-HETCOR spectra were recorded using a recovery delay τ_{RD} = 3 s and resulted from averaging 4096 transients for each of 18 t_1 increments, corresponding to a total experimental time of 24 h.

The 1D NMR spectra were simulated using ssNake software.[25] The ^{1}H isotropic chemical shifts, $\delta_{iso}(^{1}H)$, were referenced to 1 vol% tetramethylsilane (TMS) in $CDCl_3$ using the signal of the CH_2 group of adamantane at 1.735 ppm as a secondary reference. ^{29}Si isotropic chemical shift were referenced with respect to a solution of 1% tetramethylsilane (TMS) in $CDCl_3$ using the resonance of $OSi(OMe)_3$ group of Q_8M_8 at 11.35 ppm as a secondary reference.[26]

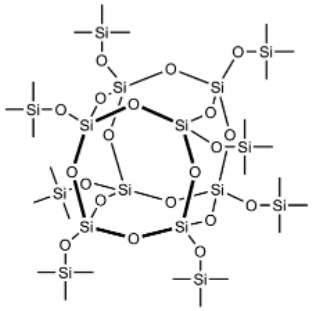

Scheme 4: *Structure of Q_8M_8.*

5.1.1. ^{29}Si MAS UDEFT

As explained in Chapter 1, UDEFT pulse sequence actively brings back the remaining ^{29}Si transverse magnetization at the end of acquisition, which improves the sensitivity and quantification of 1D NMR spectra of ^{29}Si isotope, which generally exhibits slow longitudinal relaxation, T_1, in solids. Figure 55 displays the 1D ^{29}Si MAS NMR spectra of AAS and Au/AAS.

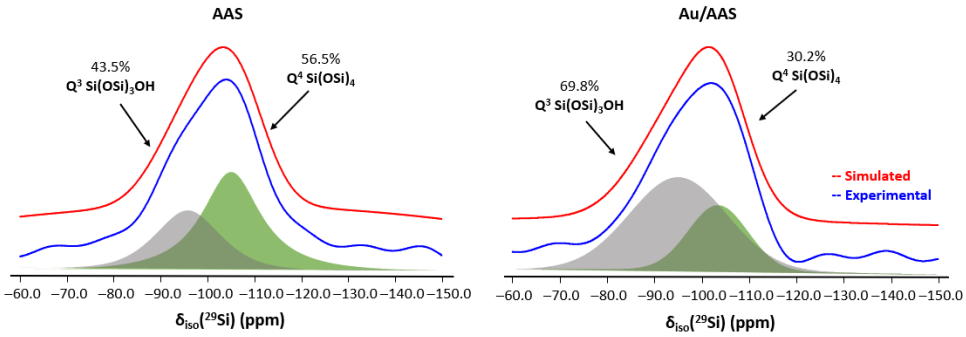

Figure 55: *Experimental (blue) and simulated (red) 1D ^{29}Si MAS UDEFT spectra (blue) for AAS and Au/AAS samples acquired at 9.4 T with ν_R = 10 kHz. The contributions of individual Q^3 sites to simulated spectra are shown in grey and that of Q^4 in green.*

Table 13: *Best-fit NMR parameters to simulate the 1D ^{29}Si MAS UDEFT spectra of AAS and Au/AAS. These spectra were simulated as the sum of two Gaussian lineshapes ascribed to Q^3 and Q^4 sites. W_L represents the Lorentzian full-width at half maximum (FWHM).*

^{29}Si sites	AAS			Au/AAS		
	δ_{iso} (^{29}Si) (ppm)	Integrated Intensity (%)	W_L (ppm)	δ_{iso} (^{29}Si) (ppm)	Integrated Intensity (%)	W_L (ppm)
Q^3 $Si(OSi)_3OH$	−96	43.5	17	−96	69.8	24
Q^4 $Si(OSi)_4$	−105	56.5	15	−105	30.2	15

The ^{29}Si spectra of both samples can be simulated as the sum of two Gaussian lineshapes centered at −96 and −105 ppm assigned to $Si(OSi)_3OH$ and $Si(OSi)_4$ local environments, denoted Q^3 and Q^4 sites, respectively, hereafter. The relative amount of Q^3 sites is higher in Au/AAS than in AAS (69.8% instead of 43.5%). This increased fraction of Q^3 sites must stem from the use of $NaBH_4$ as reducing agent during the deposition of gold nanoparticles. The reaction of AAS with $NaBH_4$ results in a partial cleavage of Si−O−Si linkages. The signal of Q^3 environments is also broader for Au/AAS than for AAS. This broadening of these sites located near the surface and hence, the gold nanoparticle stems from inhomogeneous local magnetic field near the surface of gold nanoparticles, which have magnetic susceptibility distinct from AAS.[27] Conversely, the signal of Q^4 sites is not significantly broadened by the deposition of gold nanoparticles since they are mainly located in the bulk region of the AAS particles and hence, are more distant from gold nanoparticles.

5.1.2. ^{1}H MAS NMR

The 1D ^{1}H NMR spectra of AAS and Au/AAS are compared in Figure 56. The signal at 1.8 ppm is assigned to PBS sites (Si-μ^1-OH···Al), whereas that at 1.4 ppm stems from other

terminal Si-μ^1-OH groups, which are non-acidic.[7,28–31] Protons resonating around 4.2-4.5 ppm are assigned to Si(μ^2-OH)Al BAS.[10] Finally, the signals at 0.85, 3.8 and 7.7 ppm are produced by terminal Al-μ^1-OH groups,[30,7] doubly-bridging Al(μ^2-OH)Al[10] and water adsorbed on Al-containing Lewis acid sites.[32] Furthermore, the ^{1}H NMR resonances of Au/AAS sample are significantly broader than those of AAS. This broadening stems from the inhomogeneous local magnetic field near the surface of gold nanoparticles.[27]

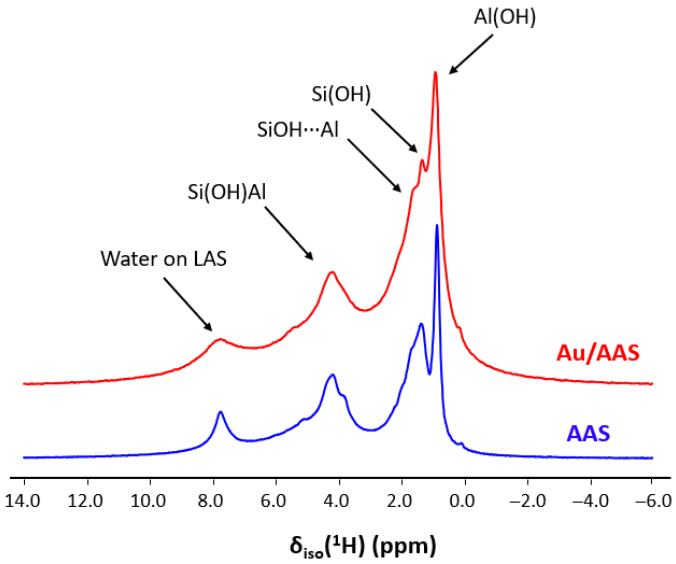

Figure 56: *Experimental 1D ^{1}H MAS DEPTH spectra of AAS (blue) and Au/AAS (red) acquired at 9.4 T with ν_R = 10 kHz*

5.1.3. ^{1}H→^{29}Si CP-HETCOR

To confirm the assignment of 1D ^{1}H NMR spectra, proximities between ^{1}H and ^{29}Si nuclei were also probed by two-dimensional (2D) ^{1}H→^{29}Si CP-HETCOR experiments. Figure 57 compares the 2D ^{1}H→^{29}Si CP HETCOR spectra of AAS and Au/AAS. Both spectra are dominated by a broad cross-peaks at $\delta_{iso}(^{29}Si)$ = –95 ppm and $\delta_{iso}(^1H)$ = 4.2 ppm, which is produced by BS connected to Q^3 Si site. The width along F_2 dimension of this cross-peak is larger for Au/AAS owing to the deposition gold nanoparticles, which increases atomic-level disorder and also creates inhomogeneous local magnetic field because of its different magnetic susceptibility.[27]

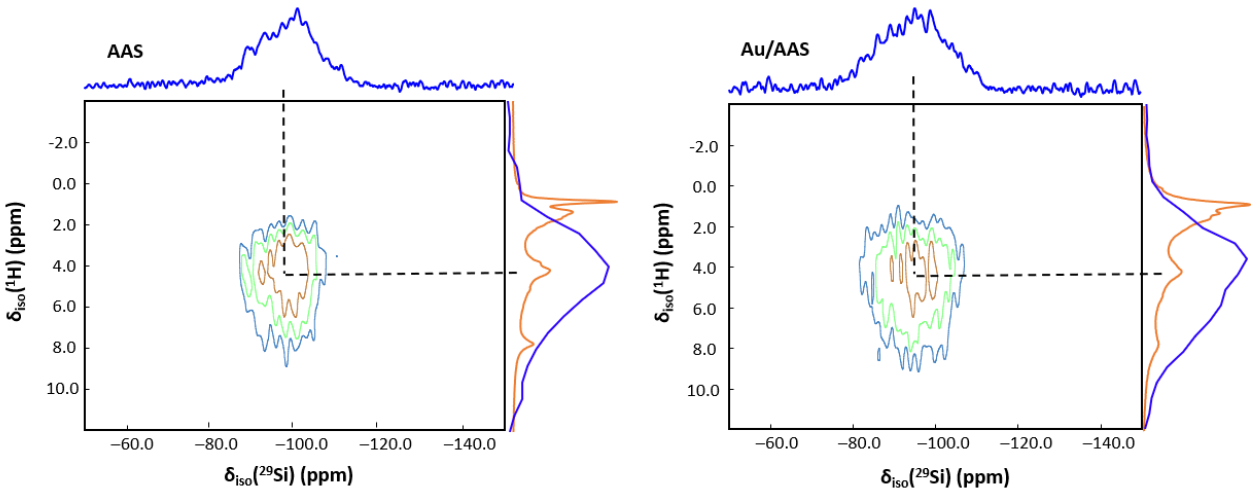

Figure 57: *2D $^{1}H \rightarrow ^{29}Si$ CP-HETCOR 2D spectrum of AAS (left) and Au/AAS (right). The samples were dehydrated at 120 °C for 2 h under vacuum and recorded at 9.4 T with ν_R = 10 kHz and contact time of 5 ms. The skyline projections for both indirect (^{1}H) and direct (^{29}Si) dimensions are displayed in blue, whereas the 1D ^{1}H DEPTH spectra are also shown in orange for the sake of comparison.*

5.2. ssNMR experiments at 18.8 T using zirconia rotors

This set of experiments is performed on the second batch of samples dried in an oven at 100 °C for 12 h at TIFR and shipped in vacuumed vials. At Lille NMR facility, the samples were dehydrated again using a high-vacuum Schlenk line (i.e., 10^{-4} mbar) with the Schlenk flask placed in a 120 °C water bath for 2 h. The samples were then stored in Jacomex glove box.

The 1D ^{1}H and ^{27}Al as well as 2D $^{27}Al\{^{1}H\}$ *D*-HMQC-SR4_1^2 MAS NMR spectra were recorded at room temperature on a Bruker AVANCE NEO NMR spectrometer at B_0 = 18.8 T equipped with double-resonance Bruker 3.2 mm HX MAS probe. The Larmor frequencies at this field are of 800 MHz for ^{1}H and 208.45 MHz for ^{27}Al. The powdered samples were packed in the glove box into a 3.2 mm outer diameter zirconia rotor with a Kel-F driving cap and spun at a MAS frequency of ν_R = 20 kHz.

The 1D ^{1}H DEPTH spectra were acquired using a 90° pulse that lasted 5.25 µs using ν_1 = 47.6 kHz. They resulted from averaging 16 transients with a recovery delay τ_{RD} = 5 s, i.*e.* T_{exp} = 2 min. The 1D ^{27}Al MAS NMR spectra were recorded using a single pulse experiment with low flip angle pulse lasting 1 µs and using ν_1 = 250 kHz and a recycle delay τ_{RD} = 2 s. The spectra resulted from averaging 1024 transients corresponding to an experimental time of 30 min.

The 2D ^{27}Al{^{1}H} *D*-HMQC MAS NMR experiments with ^{27}Al direct detection were carried out by reintroducing the ^{1}H-^{27}Al dipolar couplings under MAS conditions through the application of $SR4_1^2$ scheme on the ^{1}H channel during the defocusing and refocusing delays. The lengths of each $SR4_1^2$ recoupling block applied during the defocusing and refocusing delays were both equal to 0.5 ms. The ^{1}H RF nutation frequencies during the π/2 pulses and $SR4_1^2$ recoupling were equal to ν_1 = 47.6 and 40 kHz, respectively. ^{27}Al CT selective pulses were applied with $\nu_1 \approx 30$ kHz. The spectra result from averaging 2048 transients for each of 20 t_1-increments with a recovery delay of 1 s, i.e. a total experimental time of 12 h. The States-TPPI procedure was used to achieve quadrature detection along the indirect dimension.[33]

The ^{1}H isotropic chemical shifts, $\delta_{iso}(^{1}H)$, were referenced to 1 vol% tetramethylsilane (TMS) in $CDCl_3$ using the signal of the CH_2 group of adamantane at 1.735 ppm as a secondary reference. ^{27}Al chemical shifts were referenced at 0 ppm to 1 mol/L $[Al(H_2O)_6]^{3+}$ solution.[26] The ^{27}Al 1D spectra were simulated using DmFit software.[34]

5.2.1. ^{27}Al MAS NMR

Figure 58 compares the 1D ^{27}Al direct excitation MAS NMR spectra of AAS and Au/AAS. The spectra were acquired with short excitation pulse to ensure a reliable quantification of the different ^{27}Al local environments. Both samples exhibit three Al resonances assigned to tetra-, penta- and hexa-coordinated Al sites (denoted hereafter Al^{IV}, Al^{V} and Al^{VI}, respectively) near 62, 37 and 9 ppm, respectively.[5,7] The resonances of these sites tail towards low shifts and can be simulated assuming a Gaussian isotropic distribution of the EFG tensor also called the Czjzek model.[35] These lineshapes betray a distribution of local Al environments consistent with the amorphous nature of the AAS.

The comparison of 1D ^{27}Al NMR spectra shown in Figure 58b shows a reduced intensity of Al^{V} and Al^{VI} signals after the deposition of gold nanoparticles, whereas that of Al^{IV} signal is barely affected. This observation is consistent with the reduced relative integrated intensities of Al^{V} and Al^{VI} sites in the simulated spectra (see Figure 58a). It suggests a leaching of Al^{V} and Al^{VI} sites during the deposition of gold nanoparticles, may be because of a partial hydrolysis of AAS support by reaction with $NaBH_4$ reducing agent. The Al^{IV} local environments appear to be more stable, may be because most of them are located below the surface.

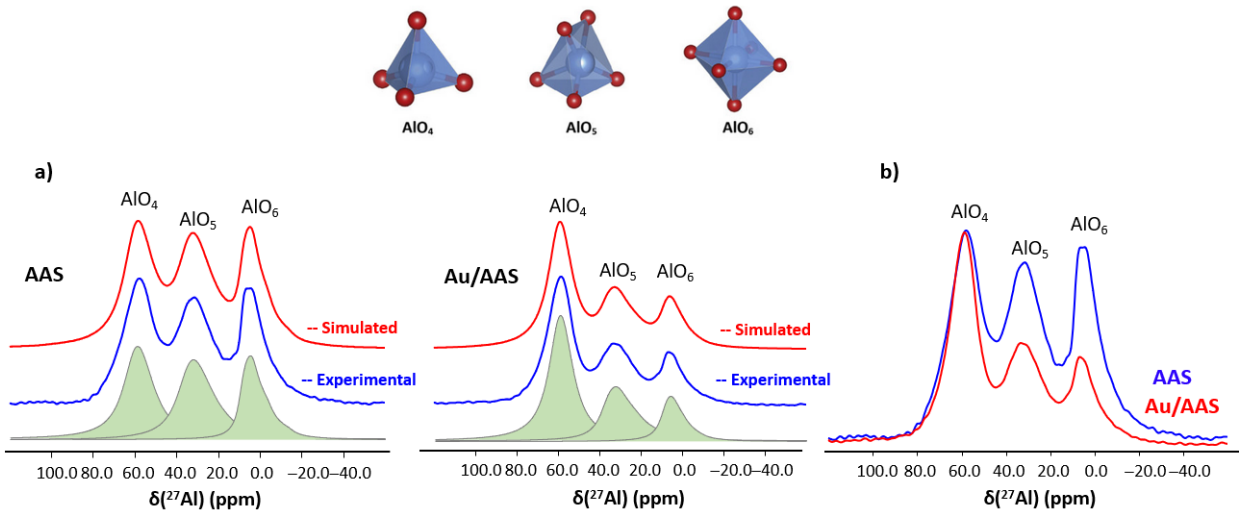

Figure 58: a) *Experimental (blue) and simulated (red) 1D ^{27}Al direct excitation MAS NMR spectra of AAS and Au/AAS samples acquired at 18.8 T with ν_R = 20 kHz. The contributions of individual sites to simulated spectra are shown as green lines. The top structures represent tetra-, penta- and hexa-coordinated alumina local environment.* ***b)*** *Comparison of 1D ^{27}Al direct excitation MAS spectra of AAS and Au/AAS samples acquired at 18.8 T with ν_R = 20 kHz.*

Table 14: *The best-fit NMR parameters for the three sites for AAS and Au/AAS simulated on DmFit software. W_L represents the Lorentzian full-width at half maximum (FWHM).*

^{27}Al sites	AAS				Au/AAS			
	δ_{iso}(^{27}Al) (ppm)	Integrated Intensity (%)	$\sqrt{\langle C_Q^2 \rangle}$ (MHz)	W_L (ppm)	δ_{iso}(^{27}Al) (ppm)	Integrated Intensity (%)	$\sqrt{\langle C_Q^2 \rangle}$ (MHz)	W_L (ppm)
Al(IV)	62	38	4.7	12	61	55	3.5	13
Al(V)	37	38	6.5	14	38	29	7.4	10
Al(VI)	9	24	6.7	5	9	16	5.7	8

5.2.2. ^{1}H MAS NMR

We also acquired 1D ^{1}H MAS NMR spectra of AAS and Au/AAS at 18.8 T with a MAS frequency of 20 kHz. These spectra are similar to those acquired at 9.4 T with ν_R = 10 kHz. Higher magnetic field and MAS frequencies do not enhance the spectral resolution since the ^{1}H linewidth for these amorphous materials is dominated by the distribution of isotropic chemical shift.

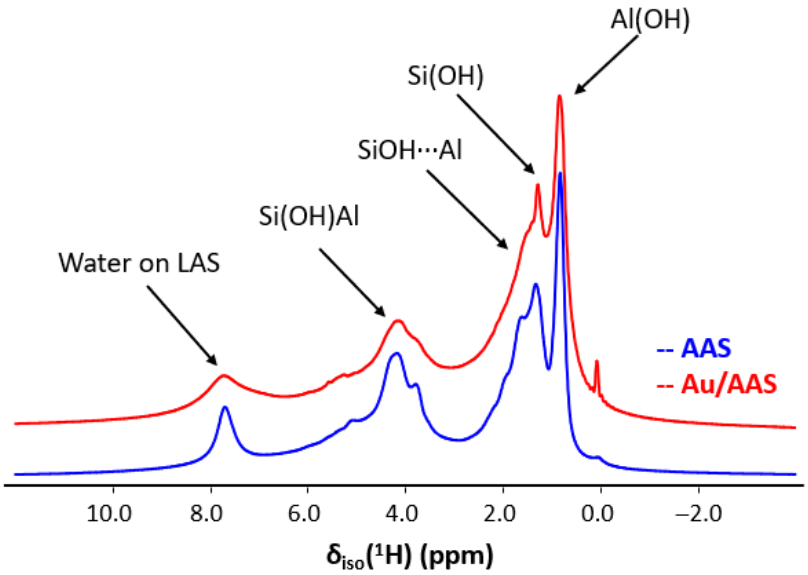

Figure 59: *Experimental 1D ^{1}H MAS DEPTH spectra of AAS (blue) and Au/AAS (red) acquired at 18.8 T with ν_R = 20 kHz.*

5.2.3. ^{27}Al{^{1}H} *D*-HMQC

The proximities between ^{1}H and ^{27}Al nuclei in AAS and Au/AAS were probed using 2D ^{27}Al{^{1}H} *D*-HMQC experiments. The obtained spectra are shown in Figure 60.

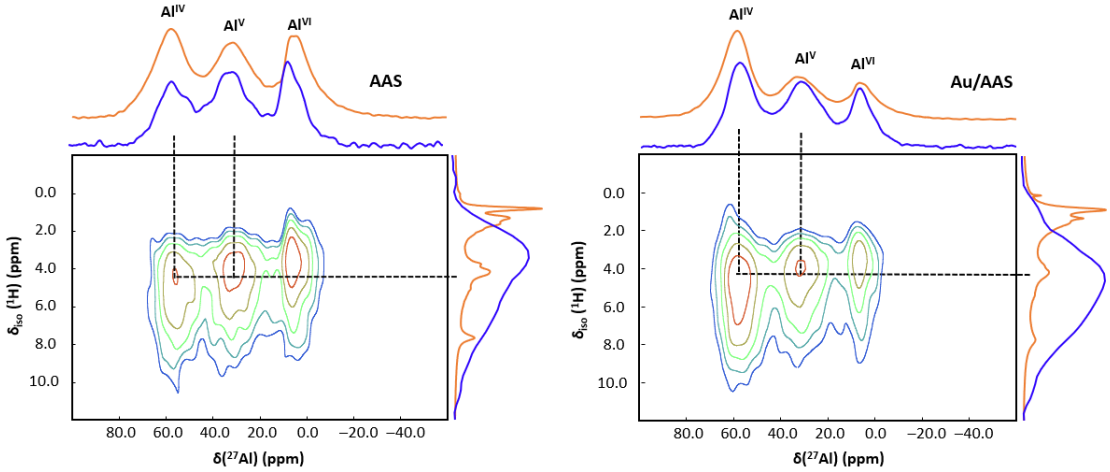

Figure 60: *2D ^{27}Al{^{1}H} D-HMQC 2D spectra of AAS (left) and Au/AAS (right) acquired at 18.8 T with ν_R = 20 kHz and $SR4_1^2$ recoupling block lasting 0.5 ms during both defocusing and refocusing delays. The positive projections along both indirect (^{1}H) and direct (^{27}Al) dimensions are displayed in blue, whereas the 1D ^{1}H and ^{27}Al MAS NMR spectra are shown in orange for the sake of comparison.*

The spectra of these two samples exhibit cross peaks between the BS proton at 4.2 ppm and Al^{IV} and Al^{V} signals. These two cross-peaks confirm the presence of $Si(OH)Al^{IV}$ and $Si(OH)Al^{V}$ sites in these samples, which are BAS.[10] Furthermore, for both samples, an additional cross-peak is observed between Al^{VI} signal and $Al(\mu^2\text{-}OH)Al$ [10] protons at 3.8 ppm.

For Au/AAS, another cross-peaks between Al^{IV} resonance and AlOH peaks near 1-2 ppm is detected. It is assigned to $Al^{IV}OH$ species formed by the partial hydrolysis of AAS during the deposition of gold nanoparticles.[36–38] In addition, the intensity of cross peaks with Al^{V} and Al^{VI} signals are reduced for Au/AAS because of the leaching of the species during the functionalization with gold nanoparticles.

After the ssNMR characterization of AAS and Au/AAS in the absence of light, we wanted to test whether similar experiments can be performed in the presence of light to evidence structural modifications induced by light irradiation. These experiments require the use of rotors transparent to light. For that purpose, we employed sapphire rotors.

5.3. ssNMR at 18.8 T in sapphire rotors

This set of experiments is performed on the third batch of samples dried in an oven at 120°C at TIFR institute and shipped in vacuumed vials. At Lille NMR facility, the samples were dehydrated again using a high-vacuum Schlenk line (i.e., 10^{-4} mbar) with the Schlenk flask placed in a 120 °C water bath. The samples were then stored in Jacomex glove box.

The 1D ^{1}H and ^{27}Al and 2D MAS NMR experiments were recorded at room temperature on a Bruker AVANCE NEO NMR spectrometer at B_0 = 18.8 T equipped with double resonance Bruker 3.2 mm low gamma MAS probe. The Larmor frequencies at this field are of 800 MHz for ^{1}H and 208.45 MHz ^{27}Al. The powdered samples were packed in the glove box into a 3.2 mm outer diameter sapphire rotor with a zirconia driving cap and spun at a MAS frequency of ν_R = 15 kHz.

The 1D ^{1}H DEPTH spectra were acquired using a 90° pulse that lasted 3.77 µs with ν_1 = 66 kHz. They resulted from averaging 16 transients with a recovery delay τ_{RD} = 5 s, i.*e.* T_{exp} = 2min. The 1D ^{27}Al spectra were recorded using a single pulse experiment. The low flip angle (π/10) pulse applied lasted 1 µs at ν_1 = 250 kHz, with a recycle delay τ_{RD} = 10 s. The spectra were acquired for 16 transients corresponding to an experimental time of 3min.

The 2D $^{1}H\{^{27}Al\}$ *D*-HMQC-$SR4_1^2$ and $^{27}Al\{^{1}H\}$ *D*-HMQC-$SR4_1^2$ MAS NMR experiments using sapphire rotors were carried out with ^{1}H and ^{27}Al detection, respectively. The ^{1}H-^{27}Al dipolar couplings were reintroduced during the defocusing and refocusing delays by applying $SR4_1^2$ scheme built from single π pulses on the ^{1}H channel for both experiments.

The lengths of each $SR4_1^2$ recoupling block applied during the defocusing and refocusing delays were both equal to 0.53 ms. The ^{1}H RF nutation frequency during the π/2 pulses and central refocusing π pulse was equal to ν_1 = 66 kHz, whereas we employed $\nu_1 = 2\ \nu_R$ = 30 kHz during $SR4_1^2$ recoupling. ^{27}Al CT-selective pulses were applied with $\nu_1 \approx 50$ kHz. The spectra result from averaging 1024 transients for each of 30 t_1-increments with a recovery delay of 3 s, i.e., a total experimental time is 7 h. The States-TPPI procedure was used to achieve along the indirect dimension.[33]

The 2D ^{1}H{^{27}Al} TONE-*D*-HMQC MAS NMR experiment [39] using sapphire rotor was carried out with ^{1}H detection. The ^{1}H-^{27}Al dipolar couplings were reintroduced by applying $SR4_1^2$ scheme built from 270_090_{180} composite inversion pulses [40] (denoted $SR4_1^2(270_090_{180})$ hereafter) on the ^{1}H channel. This composite pulse improves the robustness to ^{1}H-^{1}H dipolar couplings, RF field inhomogeneity and offset. The lengths of each $SR4_1^2$ recoupling block applied during the defocusing and refocusing delays were both equal to 0.8 ms. The ^{1}H RF nutation frequency during the π/2 pulses and central refocusing π pulse was equal to ν_1 = 66 kHz, whereas we employed $\nu_1 = 4\nu_R$ = 60 kHz during $SR4_1^2(270_090_{180})$ recoupling. ^{27}Al CT selective pulses were applied with $\nu_1 \approx 50$ kHz. The spectrum results from averaging 256 transients for each of 40 slices t_1-increments with a recovery delay of 2.5 s, *i.e.,* a total experimental time is 7 hours. Pre-saturation pulses with an RF field of 66 kHz (number of pulses = 11) are applied on ^{27}Al channel to eliminate ^{27}Al magnetization, which is not transferred from protons. The States-TPPI procedure was used to achieve quadrature detection along the indirect dimension.[33]

The ^{27}Al{^{1}H} *D*-RINEPT experiments are performed on the fourth batch of sample dried in an oven at 120 °C at TIFR and shipped in vacuumed vials. At Lille NMR facility, the samples were dehydrated again using a high-vacuum Schlenk line (i.e., 10^{-4} mbar) with the Schlenk placed in a tube furnace at 200 °C. The ^{1}H-^{27}Al dipolar couplings were reintroduced by applying $SR4_1^2$ scheme built from tanh/tan (tt) adiabatic pulse[41,42] (denoted $SR4_1^2$(tt) hereafter) on the ^{1}H channel during defocusing and refocusing delays. As this recoupling scheme is not γ-encoded, the $SR4_1^2$(tt) blocks applied during defocusing and refocusing delays must be rotor-synchronized. Continuous wave irradiation is applied during the delays separating the $SR4_1^2$(tt) blocks to limit the losses due to ^{1}H-^{1}H dipolar interactions. Furthermore, composite π/2 and π pulses are also applied on the ^{1}H channel to improve

the robustness to RF inhomogeneities of the sequence. The lengths of each $SR4_1^2$ recoupling block applied during the defocusing and refocusing delays were both equal to 0.8 ms. The ^{1}H RF nutation frequency was equal to ν_1 = 75 kHz during $SR4_1^2$(tt) recoupling and 66 kHz during other pulses. ^{27}Al CT selective pulses were applied with $\nu_1 \approx 50$ kHz. Pre-saturation pulses are applied on ^{27}Al channel with an RF field of 83 kHz. The spectrum results from averaging 1024 transients for each of t_1-increments with a recovery delay of 1 s, i.e., a total experimental time of 10 h. The States-TPPI procedure was used to achieve quadrature detection along the indirect dimension.

The ^{1}H isotropic chemical shifts, $\delta_{iso}(^1H)$, were referenced to 1 vol% tetramethylsilane (TMS) in $CDCl_3$ using the signal of the CH_2 group of adamantane at 1.735 ppm as a secondary reference. ^{27}Al chemical shifts were referenced at 0 ppm to 1 mol/L $[Al(H_2O)_6]^{3+}$ solution.[26]

5.3.1. ^{27}Al{^{1}H} D-HMQC- $SR4_1^2$

Sapphire rotors are transparent to light but made of aluminum oxide, which results in large ^{27}Al background signal, which masks those of AAS and Au/AAS (see 1D spectra on the left of Figure 61). Differences between the 1D spectra shown in Figure 61 stem from the use of different sapphire rotors with different orientation of crystalline domains with respect to the rotor axis.[43]

As seen in Figure 61, this background signal due to the sapphire rotor results in large t_1-noise in 2D ^{27}Al{^{1}H} *D*-HMQC 2D spectrum, even if sapphire does not contain protons. Such noise overlaps with the desired cross-peaks. These artefacts are produced by the incomplete elimination of the sapphire ^{27}Al signals by the phase cycle since ^{27}Al nuclei in crystalline sapphire exhibits slow longitudinal relaxation.

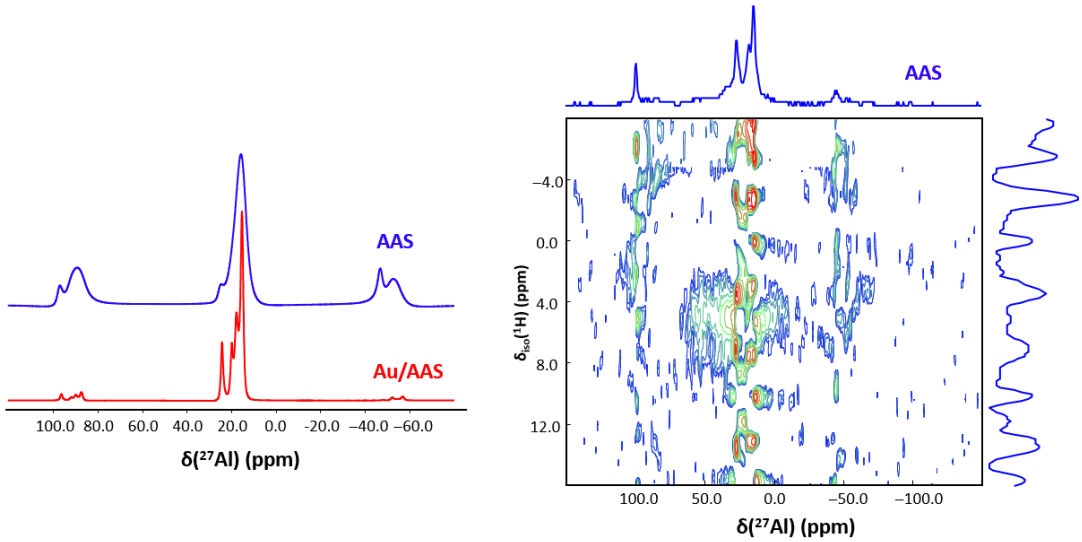

Figure 61: *1D ^{27}Al MAS NMR spectra (left) of AAS and Au/AAS packed in sapphire rotors. ^{27}Al{^{1}H} D-HMQC 2D spectrum of AAS packed in the same rotor (right). The skyline projections along both indirect (^{1}H) and direct (^{27}Al) dimensions are displayed in blue.*

5.3.2. ^{1}H{^{27}Al} *D*-HMQC- SR4$_1^2$

An alternative to correlate ^{27}Al and ^{1}H signals for a sample packed in sapphire rotor consists in the use of ^{1}H{^{27}Al} *D*-HMQC pulse sequence, in which ^{1}H signal is detected during the acquisition. The spectra acquired using this pulse sequence are displayed in figure 62. In these spectra, we observe the same cross-peaks as those of Figure 60 acquired with ^{27}Al detection. Nevertheless, they still exhibit some t_1-noise. This noise results from MAS fluctuations, which leads to imperfect refocusing of ^{1}H CSA and hence, variation of signal amplitude between scans.[39] These variations prevent a total suppression of the uncorrelated ^{1}H signal, which is not encoded by ^{27}Al frequencies during t_1 period and produces t_1-noise.

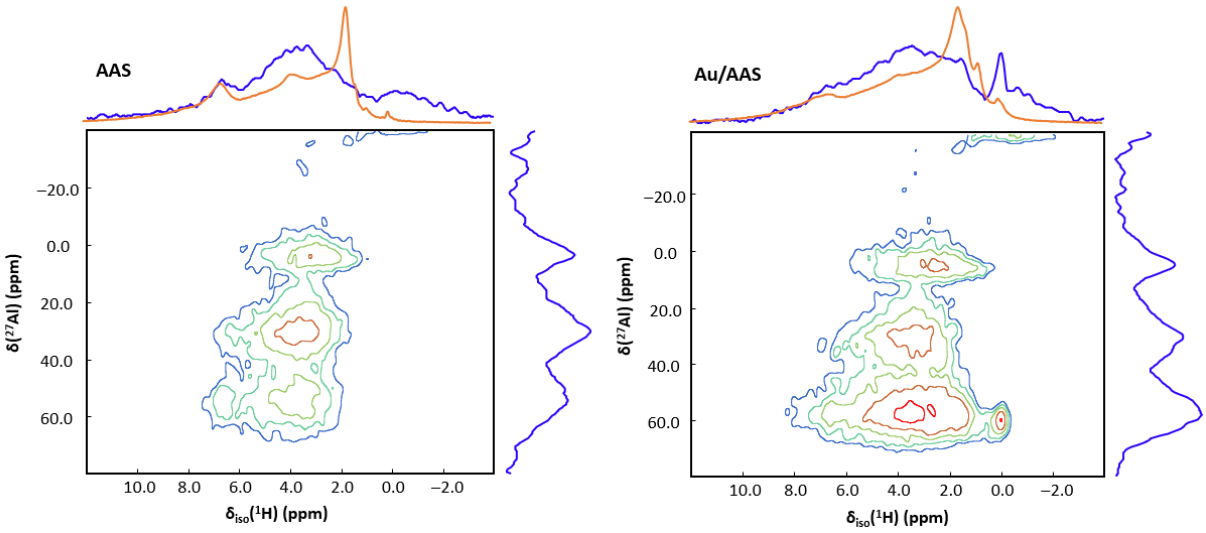

Figure 62: *2D $^{1}H\{^{27}Al\}$ D-HMQC 2D spectra of AAS (left) and Au/AAS (right) packed in sapphire rotor acquired at 18.8 T with ν_R = 20 kHz and $SR4_1^2$ recoupling block lasting 0.5 ms during both defocusing and refocusing delays. The positive projections along both indirect (^{1}H) and direct (^{27}Al) dimensions are displayed in blue, whereas the 1D ^{1}H MAS NMR spectra are shown in orange for the sake of comparison.*

5.3.3. $^{1}H\{^{27}Al\}$ TONE D-HMQC- $SR4_1^2$

A variant of $^{1}H\{^{27}Al\}$ *D*-HMQC sequence, called TONE *D*-HMQC, has been introduced to reduce the t_1-noise.[39] In this variant, π pulses are applied on ^{1}H and ^{27}Al channels in the middle of defocusing and refocusing delays to refocus the evolution due to ^{1}H CSA. This refocusing limits the variation of signal amplitude due to MAS fluctuations and hence, the t_1-noise. Figure 63 shows the 2D $^{1}H\{^{27}Al\}$ TONE *D*-HMQC spectrum of Au/AAS, which exhibits the same cross-peaks as those observed in the spectrum of Figure 60 without TONE. Nevertheless, the sensitivity, defined as the signal-to-noise ratio per square root of unit time, calculated for the TONE *D*-HMQC spectrum is equal to 5.5 $h^{-1/2}$, instead of 6.6 $h^{-1/2}$ for the variant without TONE. This lower sensitivity stems from incorporation of additional π pulses.

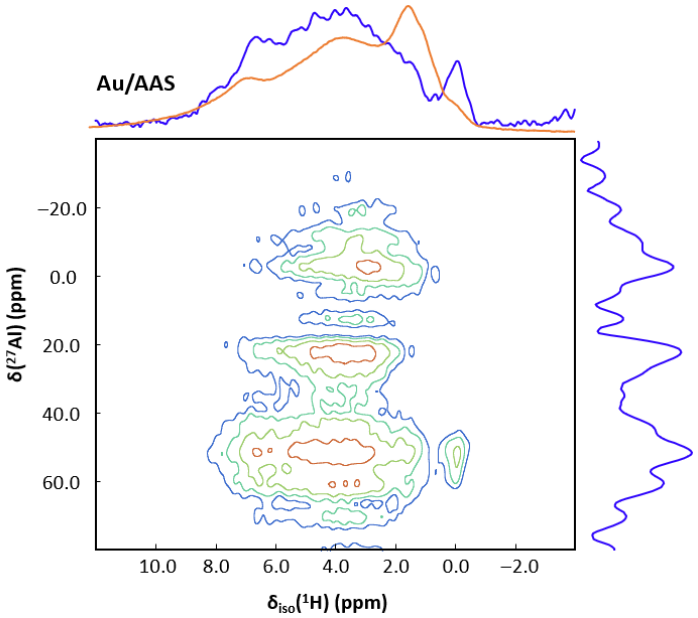

Figure 63: *2D $^{1}H\{^{27}Al\}$ TONE D-HMQC 2D spectrum of Au/AAS acquired at 18.8 T with ν_R=15 kHz and $SR4_1^2$ recoupling blocks lasting 0.8 ms during both defocusing and refocusing delays. The skyline projections along both indirect (^{1}H) and direct (^{27}Al) dimensions are displayed in blue, whereas the 1D ^{1}H MAS NMR spectrum is shown in orange for the sake of comparison.*

5.3.4. $^{27}Al\{^{1}H\}$ *D*-INEPT- $SR4_1^2$(tt)

A last technique, which was tested to correlate ^{1}H and ^{27}Al NMR signals when using sapphire rotors, is $^{27}Al\{^{1}H\}$ *D*-RINEPT[41,42] sequence using $SR4_1^2$(tt) recoupling built from adiabatic pulses, as well as composite pulses and continuous wave irradiation on ^{1}H channel to minimize the losses due to ^{1}H-^{1}H dipolar interactions and to improve the robustness to RF field inhomogeneity. The 2D $^{27}Al\{^{1}H\}$ *D*-RINEPT[41,42] spectra of AAS and Au/AAS are shown in Figure 64. They contain the same cross-peaks as those detected using *D*-HMQC pulse sequence. However, the sensitivity of this experiment is equal to 12 $h^{-1/2}$, which is almost two-fold higher than that of $^{1}H\{^{27}Al\}$ *D*-HMQC variant. Therefore, the $^{27}Al\{^{1}H\}$ *D*-RINEPT pulse sequence was selected to probe ^{1}H-^{27}Al proximities under light irradiation.

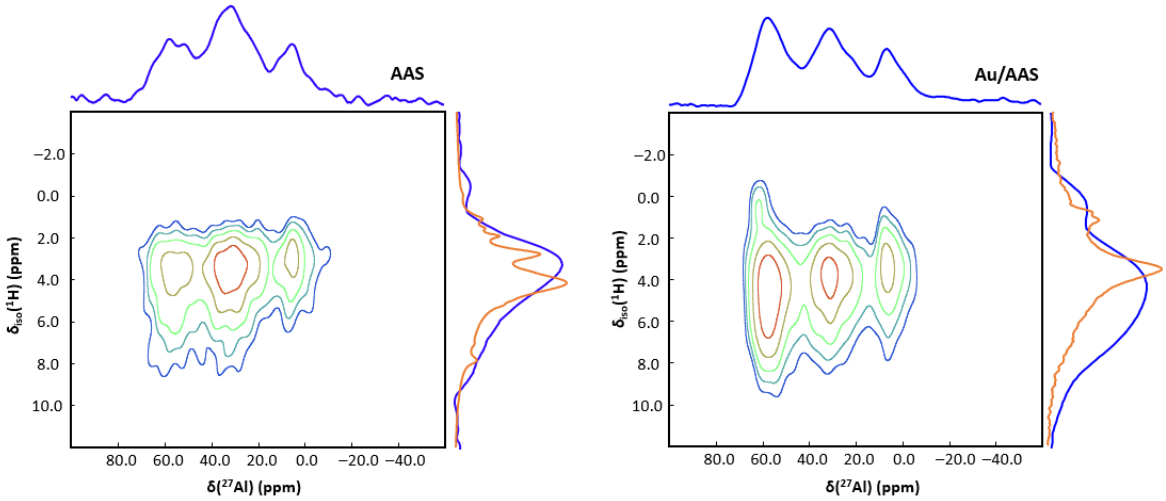

Figure 64: *2D $^{27}Al\{^{1}H\}$ D-RINEPT-SR4_1^2(tt) 2D spectra of AAS (left) and Au/AAS (right) acquired at 18.8 T with ν_R = 15 kHz and SR4_1^2(tt) recoupling blocks lasting 0.53 ms during both defocusing and refocusing delays. The positive projections along both indirect (^{1}H) and direct (^{27}Al) dimensions are displayed in blue, whereas the 1D ^{1}H MAS NMR spectrum is shown in orange for the sake of comparison*

6. Brønsted acid sites characterization by SSNMR with light irradiation in situ

6.1. Experimental conditions for NMR at 19.9 T

This set of experiments is performed on the **fourth** batch of samples dried in an oven at 120 °C at TIFR institute and shipped in vacuumed vials. At Lille NMR facility, the samples were dehydrated again using a high-vacuum Schlenk line (i.e., 10^{-4} mbar) with the Schlenk placed in a tube furnace at 200 °C and stored inside a Jacomex glove box. To improve the penetration of light into the sample, 33 mg of dehydrated Au/AAS were mixed inside the glove box with 17 mg of glass beads with a diameter of 106 µm supplied by Sigma-Aldrich and packed into a sapphire rotor with an outer diameter of 3.2 mm closed with zirconia caps. NMR experiments on the mixture of Au/AAS and glass beads were initially tested without light irradiation at Lille NMR facility to ensure that NMR spectra can be recorded within a reasonable time despite the reduction in sample volume.

The comparison between NMR spectra acquired with and without light irradiation was performed at the Biomolecular Magnetic Resonance Center (BMRZ) of Goethe University Frankfurt on Bruker AVANCE II NMR spectrometer at B_0 = 19.9 T equipped with double

resonance Bruker 3.2 mm HX MAS probe spinning at ν_R = 12 kHz using nitrogen gas. For the purpose, NMR rotors were transported to Frankfurt in vacuumed vials. The Larmor frequencies at this field are of 850 MHz for ^{1}H and 221.51 MHz for ^{27}Al. The probe incorporates an optical fiber bundle so that the sample can be illuminated inside the NMR rotor by light with a wavelength of 525 nm produced by LED. This wavelength is close to the absorption maximum at 519 nm in the UV-visible spectrum of Au/AAS (see Figure 49).

The 1D ^{1}H DEPTH spectra were acquired using a 90° pulse that lasted 2.8 µs using ν_1 = 89 kHz. The spectra resulted from averaging 16 transients with a recycle delay, τ_{RD} = 5 s, *i.e.* an experimental time of 2 min. In 2D ^{27}Al{^{1}H} *D*-RINEPT-SR4_1^2(tt) experiments, the ^{1}H-^{27}Al dipolar couplings were reintroduced by applying SR4_1^2(tt) scheme on the ^{1}H channel during defocusing and refocusing delays. As the two-spin order recoupling schemes are non-γ-encoded, these SR4_1^2(tt) recoupling blocks must be rotor-synchronized. The lengths of SR4_1^2 recoupling block during both defocusing and refocusing delays were equal to 0.66 ms. The ^{1}H RF nutation frequencies of the π/2 pulses and SR4_1^2(tt) recoupling were equal to ν_1 = 89 and 66 kHz, respectively. Composite π/2 and π pulses were applied on the ^{1}H channel to improve the robustness to RF inhomogeneities of the sequence. To limit the losses due to ^{1}H-^{1}H dipolar interactions, continuous wave irradiation with ν_1 = 90 kHz was applied between the pulses. CT selective pulses on ^{27}Al channel employed ν_1 ≈ 28 kHz. The ^{27}Al magnetization before *D*-RINEPT transfer was eliminated by the application of a train of 11 pre-saturation pulses with an RF field of 100 kHz. The 2D ^{27}Al{^{1}H} *D*-RINEPT spectra result from averaging 2048 transients for each of 26 t_1-increments with a recycle delay of 1 s, leading to a total experimental time of 16 h. The States-TPPI procedure was used to achieve quadrature detection along the indirect dimension.

6.1.1. ^{1}H MAS NMR

As seen in Figure 65, we observe a broadening of the ^{1}H NMR resonances after the illumination of the sample (compare Exp. 1 and 2). This broadening indicates an increased disorder at atomic level after light irradiation. The electric field generated by LSPR can modify the length of O−H bonds leading to a greater distribution of local environment. As seen in Figure 21, the 1D ^{1}H NMR spectrum remains identical after the cessation of light irradiation (compare Exp. 2 and 3). This observation suggests that structural modifications triggered by light are irreversible.

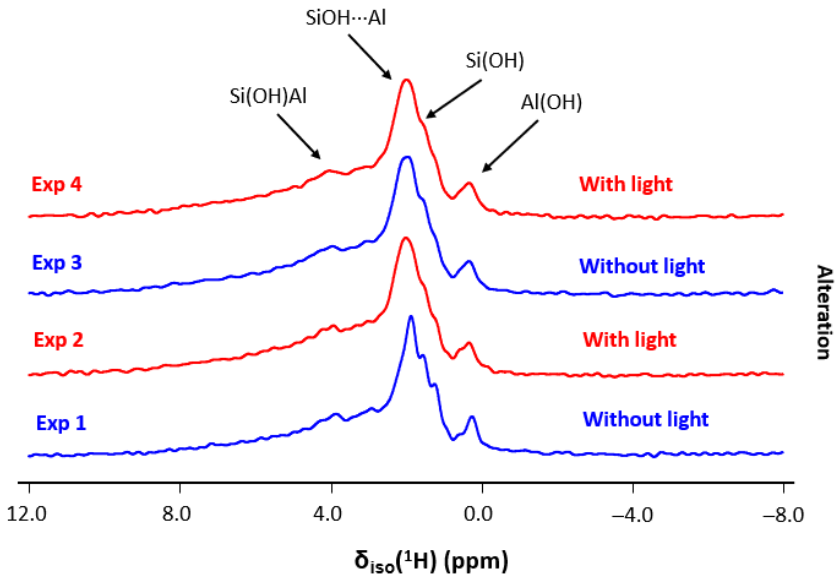

Figure 65: *Experimental 1D ^{1}H MAS DEPTH spectra of Au/AAS (blue) acquired at 19.9 T with ν_R = 12 kHz. The first spectrum (Exp. 1) was acquired before light irradiation, whereas the second one (Exp. 2) was acquired after 2 min of illumination. These experiments were repeated to test their reversibility. The spectrum of Exp. 3 was acquired after Exp. 2 and 2 min without illumination. After this experiment, the sample was finally illuminated during 2 min before the acquisition of the spectrum labeled as Exp. 4.*

6.1.2. ^{27}Al{^{1}H} *D*-INEPT- SR4$_1^2$(tt)

After the 1D ^{1}H MAS spectra of Figure 65, we acquired 1D ^{27}Al{^{1}H} *D*-RINEPT-SR4$_1^2$(tt) spectra of Au/AAS with and without light irradiation (see Figure 66 left). These spectra are both dominated by the signal of AlO_4 site. Furthermore, in that case, no major difference is detected between 1D ^{27}Al{^{1}H} *D*-RINEPT spectra acquired with and without light. This observation confirms that structural changes produced by light irradiation are irreversible.

Figure 66 (right) also shows the 2D ^{27}Al{^{1}H} *D*-RINEPT-SR4$_1^2$(tt) spectrum of Au/AAS acquired under illumination. This spectrum exhibits a cross-peak between AlO_4 site and ^{1}H resonating at 4 ppm, which was already observed before illumination (see Figure 64) and is assigned to Si(OH)Al^{IV} site. However, the cross-peak between ^{1}H signal at 4 ppm and AlO_5 site is no longer detected under light irradiation. Conversely, in the presence of light, novel cross-peaks are detected between ^{1}H resonances at 6-7 ppm and AlO_4 and AlO_5 sites. The increased isotropic chemical shift of protons is consistent with the elongation of OH bonds.[30,44,45] Hence, these novel cross-peaks must stem from Si(OH)Al^{IV} and Si(OH)Al^{V} sites with OH bonds polarized by electric field produced by LSPR and this result represents the first experimental evidence of structural modifications of Brønsted acid sites at atomic level by LSPR.

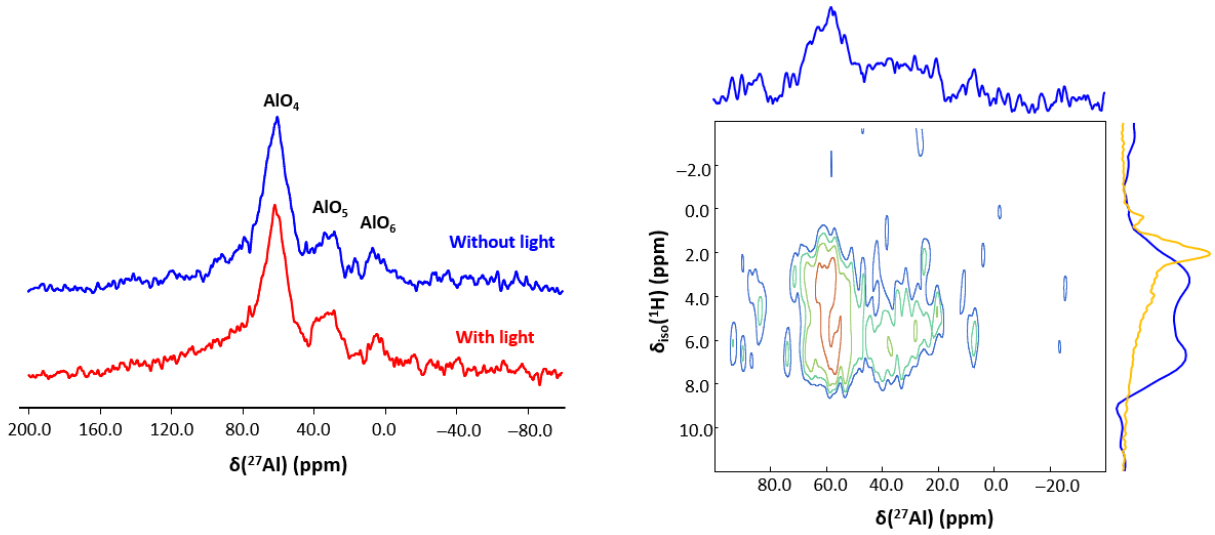

Figure 66: *1D $^{27}Al\{^{1}H\}$ D-RINEPT-SR4_1^2(tt) spectra of Au/AAS with and without light (left) and 2D $^{27}Al\{^{1}H\}$ D-RINEPT-SR4_1^2(tt) spectrum under light irradiation (right) acquired at 19.9 T with ν_R = 12 kHz and SR4_1^2(tt) recoupling blocks lasting 0.66 ms during both defocusing and refocusing delays. The skyline projection along both indirect (^{1}H) and direct (^{27}Al) dimensions are displayed in blue, whereas the 1D ^{1}H MAS NMR spectrum is shown in orange for the sake of comparison.*

7. Brønsted acid sites characterization by SSNMR with light irradiation ex situ

To verify the presence of deshielded Brønsted acid sites (between ^{1}H resonances at 6-7 ppm) and assess the irreversibility of the light effect, another set of experiments was conducted at the Lille facility under the same experimental conditions at 18.8 T described in Section 5.3. However, in this case, no *in situ* irradiation was applied during the 12 hours of the 2D experiment. Instead, the sample was irradiated *ex situ* using a 525 nm xenon lamp for 20 minutes prior to performing the 2D experiment in the dark. This approach will allow us to determine whether these sites persist after irradiation.

As shown in Figure 67, the correlation peaks with the ^{1}H resonance at 6–7 ppm are no longer observed. This indicates that the effect of light is reversible, and once the illumination is turned off, the changes occurring in the O–H elongation are no longer detected. Therefore, we can conclude that the light-induced effects arise from the localized surface plasmon resonance phenomenon of the gold nanoparticles rather than from irreversible photothermal effects.

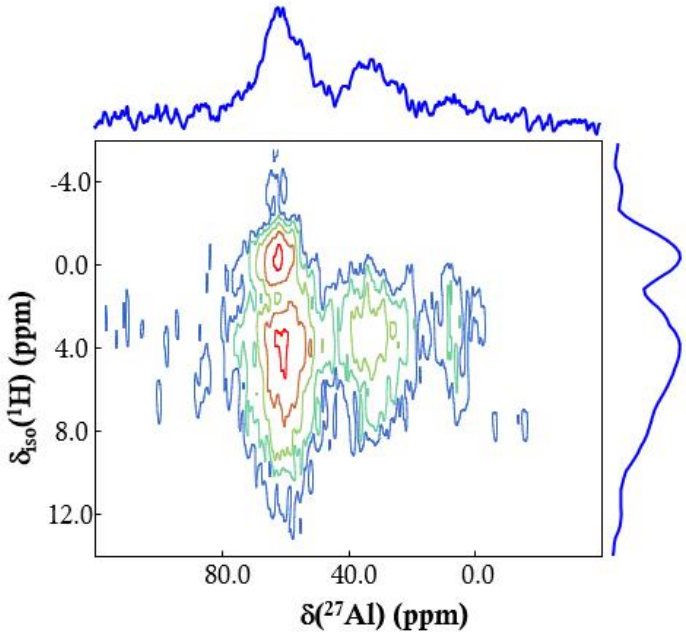

Figure 67: *2D $^{27}Al\{^1H\}$ D-RINEPT-SR4_1^2(tt) spectrum under light irradiation acquired at 18.8 T with ν_R = 20 kHz and SR4_1^2(tt) recoupling blocks lasting 0.66 ms during both defocusing and refocusing delays. The skyline projection along both indirect (^1H) and direct (^{27}Al) dimensions are displayed in blue. The sample was irradiated during 20min before the deposition of the rotor in the probe.*

8. Conclusion

In this chapter, we have shown how multinuclear (^1H, ^{27}Al and ^{29}Si) solid-state NMR spectroscopy can provide unique insights into the atomic-level structure of Au/AAS. In particular, we have demonstrated that the reaction between $NaBH_4$ and AAS during the deposition of gold nanoparticles leads to the partial hydrolysis of AAS support, which results in an increased amount of Q^3 sites and the partial leaching of AlO_5 and AlO_6 sites. Furthermore, the presence of gold nanoparticles produces inhomogeneous local magnetic fields near AAS surface, which broaden their ^1H NMR signals. Furthermore, 2D ^1H-^{29}Si and ^1H-^{27}Al through-space heteronuclear correlation experiments show the presence of $Si(OH)Al^{IV}$ and $Si(OH)Al^{V}$ sites in Au/AAS, which are similar to those detected before gold deposition. Nevertheless, solid-state NMR experiments under illumination indicates that light irradiation modifies the local environment of protons, resulting in a broadening of ^1H resonances. This structural modification is irreversible and persists after the light irradiation has ceased. In addition, 2D ^1H-^{27}Al through-space heteronuclear correlation spectra acquired under light irradiation exhibits cross-peaks between between ^1H

resonances at 6-7 ppm and AlO_4 and AlO_5 sites. These signals are ascribed to $Si(OH)Al^{IV}$ and $Si(OH)Al^{V}$ sites with elongated OH bonds. This elongation stems from the strong electric fields near gold nanoparticles in the presence of light. However, as discussed above, under light irradiation, the enhanced near-field generated by LSPR can only transiently polarise and elongate the O–H bonds of BAS, increasing their acidity and catalytic activity in a reversible manner. This electric-field–driven effect occurs only in the presence of light and disappears immediately once the illumination is switched off. In contrast, nonradiative decay of the plasmon can generate hot carriers that relax via electron–phonon coupling, leading to localized heating. If this local temperature rise is sufficiently high, it can induce irreversible structural changes. To determine which pathway is dominant, the catalyst can first be analyzed in the dark, then under illumination, and finally again in the dark. If the catalytic or spectroscopic changes observed during illumination vanish once the light is turned off, the effect is reversible and can be attributed to near-field polarization. However, if the changes persist even after the light is removed, this indicates a photothermal origin. Nevertheless, this result represents the first experimental observation of atomic-level structural modifications of Brønsted acid sites by LSPR. These modifications explain the enhanced Brønsted acidity of Au/AAS photocatalysts in the presence of light.

9. Statement of contribution

All samples used in this chapter were synthesized and their structures were characterized by the **Prof. Vivek Polshettiwar** and his student **Ms. Charvi Singhvi** in the Department of Chemical Sciences (DCS), Tata Institute of Fundamental Research (TIFR), Homi Bhabha Road, Colaba, Mumbai 400005, India. All NMR experiments without light irradiation were performed by myself at the Lille NMR facility. The NMR experiments under light irradiation were also carried out by myself at the Biomolecular Magnetic Resonance Center (BMRZ) of Goethe University Frankfurt, with the assistance of **Dr. Johanna Baldus**, head of the NMR facility. All NMR data were simulated and analyzed by myself under the supervision of **Prof. Olivier Lafon** who provided supervision and contributed to the analysis and interpretation of the results.

10. References

(1) Busca, G. Silica-Alumina Catalytic Materials: A Critical Review. *Catal. Today* **2020**, *357*, 621–629. https://doi.org/10.1016/j.cattod.2019.05.011.

(2) Wang, Z.; Jiang, Y.; Baiker, A.; Huang, J. Pentacoordinated Aluminum Species: New Frontier for Tailoring Acidity-Enhanced Silica–Alumina Catalysts. *Acc. Chem. Res.* **2020**, *53* (11), 2648–2658. https://doi.org/10.1021/acs.accounts.0c00459.

(3) Chizallet, C.; Raybaud, P. Pseudo-Bridging Silanols as Versatile Brønsted Acid Sites of Amorphous Aluminosilicate Surfaces. *Angew. Chem. Int. Ed.* **2009**, *48* (22), 3896–3896. https://doi.org/10.1002/anie.200990114.

(4) Trombetta, M.; Busca, G.; Rossini, S.; Piccoli, V.; Cornaro, U.; Guercio, A.; Catani, R.; Willey, R. J. FT-IR Studies on Light Olefin Skeletal Isomerization Catalysis: III. Surface Acidity and Activity of Amorphous and Crystalline Catalysts Belonging to the SiO_2–Al_2O_3System. *J. Catal.* **1998**, *179* (2), 581–596. https://doi.org/10.1006/jcat.1998.2251.

(5) Crépeau, G.; Montouillout, V.; Vimont, A.; Mariey, L.; Cseri, T.; Maugé, F. Nature, Structure and Strength of the Acidic Sites of Amorphous Silica Alumina: An IR and NMR Study. *J. Phys. Chem. B* **2006**, *110* (31), 15172–15185. https://doi.org/10.1021/jp062252d.

(6) Perras, F. A.; Wang, Z.; Kobayashi, T.; Baiker, A.; Huang, J.; Pruski, M. Shedding Light on the Atomic-Scale Structure of Amorphous Silica–Alumina and Its Brønsted Acid Sites. *Chem. Phys.* **2019**, *21* (35), 19529–19537. https://doi.org/10.1039/C9CP04099D.

(7) Wang, Z.; Jiang, Y.; Lafon, O.; Trébosc, J.; Duk Kim, K.; Stampfl, C.; Baiker, A.; Amoureux, J.-P.; Huang, J. Brønsted Acid Sites Based on Penta-Coordinated Aluminum Species. *Nat. Commun.* **2016**, *7*, 13820. https://doi.org/10.1038/ncomms13820.

(8) Xu, B.; Sievers, C.; Lercher, J. A.; van Veen, J. A. R.; Giltay, P.; Prins, R.; van Bokhoven, J. A. Strong Brønsted Acidity in Amorphous Silica−Aluminas. *J. Phys. Chem. C* **2007**, *111* (32), 12075–12079. https://doi.org/10.1021/jp073677i.

(9) Poduval, D. G.; Veen, J. A. R. van; Rigutto, M. S.; Hensen, E. J. M. Brønsted Acid Sites of Zeolitic Strength in Amorphous Silica-Alumina. *Chem. Commun.* **2010**, *46* (20), 3466–3468. https://doi.org/10.1039/C000019A.

(10) Wang, Z.; Chen, K.; Jiang, Y.; Trébosc, J.; Yang, W.; Amoureux, J.-P.; Hung, I.; Gan, Z.; Baiker, A.; Lafon, O.; Huang, J. Revealing Brønsted Acidic Bridging SiOHAl Groups on Amorphous Silica–Alumina by Ultrahigh Field Solid-State NMR. *J. Phys. Chem. Lett.* **2021**, *12* (47), 11563–11572. https://doi.org/10.1021/acs.jpclett.1c02975.

(11) Salvia, W. S.; Zhao, T. Y.; Chatterjee, P.; Huang, W.; Perras, F. A. Are the Brønsted Acid Sites in Amorphous Silica–Alumina Bridging? *Chem. Commun.* **2023**, *59* (94), 13962–13965. https://doi.org/10.1039/D3CC04237E.

(12) Maity, A.; Chaudhari, S.; Titman, J. J.; Polshettiwar, V. Catalytic Nanosponges of Acidic Aluminosilicates for Plastic Degradation and CO_2 to Fuel Conversion. *Nat. Commun.* **2020**, *11* (1), 3828. https://doi.org/10.1038/s41467-020-17711-6.

(13) Verma, R.; Singhvi, C.; Venkatesh, A.; Polshettiwar, V. Defects Tune the Acidic Strength of Amorphous Aluminosilicates. *Nat. Commun.* **2024**, *15* (1), 6899. https://doi.org/10.1038/s41467-024-51233-9.

(14) Xingguang Zhang, 张兴光; Du, A.; Zhu, H.; Jia, J.; Wang, J.; Ke, X. Surface Plasmon-Enhanced Zeolite Catalysis under Light Irradiation and Its Correlation with Molecular Polarity of Reactants. *Chem. Commun. Camb. Engl.* **2014**, *50*. https://doi.org/10.1039/c4cc03225j.

(15) Zhang, X.; Ke, X.; Zhu, H. Zeolite-Supported Gold Nanoparticles for Selective Photooxidation of Aromatic Alcohols under Visible-Light Irradiation. *Chem. – Eur. J.* **2012**, *18* (26), 8048–8056. https://doi.org/10.1002/chem.201200368.

(16) Yang, X.; Qiao, J.; Deng, J.; Jia, R.; Wang, Q. Role of H-Beta Zeolite on Photocatalytic Pollutant Degradation and H_2 Production Enhancement of g-C_3N_4/H-Beta Composite. *J. Environ. Chem. Eng.* **2023**, *11* (5), 110828. https://doi.org/10.1016/j.jece.2023.110828.

(17) Haiss, W.; Thanh, N. T. K.; Aveyard, J.; Fernig, D. G. Determination of Size and Concentration of Gold Nanoparticles from UV−Vis Spectra. *Anal. Chem.* **2007**, *79* (11), 4215–4221. https://doi.org/10.1021/ac0702084.

(18) Brunauer, S.; Emmett, P. H.; Teller, E. Adsorption of Gases in Multimolecular Layers. *J. Am. Chem. Soc.* **1938**, *60* (2), 309–319. https://doi.org/10.1021/ja01269a023.

(19) Barrett, E. P.; Joyner, L. G.; Halenda, P. P. The Determination of Pore Volume and Area Distributions in Porous Substances. I. Computations from Nitrogen Isotherms. *J. Am. Chem. Soc.* **1951**, *73* (1), 373–380. https://doi.org/10.1021/ja01145a126.

(20) Sing, K. S. W. Reporting Physisorption Data for Gas/Solid Systems with Special Reference to the Determination of Surface Area and Porosity (Recommendations 1984). *Pure Appl. Chem.* **1985**, *57* (4), 603–619. https://doi.org/10.1351/pac198557040603.

(21) Li, G.; Enache, D. I.; Edwards, J.; Carley, A. F.; Knight, D. W.; Hutchings, G. J. Solvent-Free Oxidation of Benzyl Alcohol with Oxygen Using Zeolite-Supported Au and Au–Pd Catalysts. *Catal. Lett.* **2006**, *110* (1), 7–13. https://doi.org/10.1007/s10562-006-0083-1.

(22) Cory, D. G.; Ritchey, W. M. Suppression of Signals from the Probe in Bloch Decay Spectra. *J. Magn. Reson.* **1988**, *80* (1), 128–132. https://doi.org/10.1016/0022-2364(88)90064-9.

(23) Duong, N. T.; Trébosc, J.; Lafon, O.; Amoureux, J.-P. Improved Sensitivity and Quantification for ^{29}Si NMR Experiments on Solids Using UDEFT (Uniform Driven Equilibrium Fourier Transform). *Solid State Nucl. Magn. Reson.* **2019**, *100*, 52–62. https://doi.org/10.1016/j.ssnmr.2019.03.007.

(24) Fung, B. M.; Khitrin, A. K.; Ermolaev, K. An Improved Broadband Decoupling Sequence for Liquid Crystals and Solids. *J. Magn. Reson.* **2000**, *142* (1), 97–101. https://doi.org/10.1006/jmre.1999.1896.

(25) van Meerten, S. G. J.; Franssen, W. M. J.; Kentgens, A. P. M. ssNake: A Cross-Platform Open-Source NMR Data Processing and Fitting Application. *J. Magn. Reson. San Diego Calif 1997* **2019**, *301*, 56–66. https://doi.org/10.1016/j.jmr.2019.02.006.

(26) Rk, H.; Ed, B.; Sm, C. de M.; R, G.; P, G. NMR Nomenclature: Nuclear Spin Properties and Conventions for Chemical Shifts. IUPAC Recommendations 2001. *Solid State Nucl. Magn. Reson.* **2002**, *22* (4). https://doi.org/10.1006/snmr.2002.0063.

(27) Slichter, C. P. Probing Phenomena at Metal Surfaces by NMR. *Annu. Rev. Phys. Chem.* **1986**, *37*, 25–51. https://doi.org/10.1146/annurev.pc.37.100186.000325.

(28) Gay, I. D. A Magic-Angle Spinner for Vacuum-Sealed Samples. *J. Magn. Reson. 1969* **1984**, *58* (3), 413–420. https://doi.org/10.1016/0022-2364(84)90145-8.

(29) Hunger, M.; Ernst, S.; Steuernagel, S.; Weitkamp, J. High-Field ^{1}H MAS NMR Investigations of Acidic and Non-Acidic Hydroxyl Groups in Zeolites H-Beta, H-ZSM-5, H-ZSM-58 and H-MCM-22. *Microporous Mater.* **1996**, *6* (5), 349–353. https://doi.org/10.1016/0927-6513(96)00043-0.

(30) Jiang, Y.; Huang, J.; Dai, W.; Hunger, M. Solid-State Nuclear Magnetic Resonance Investigations of the Nature, Property, and Activity of Acid Sites on Solid Catalysts. *Solid*

State Nucl. Magn. Reson. **2011**, *39* (3), 116–141. https://doi.org/10.1016/j.ssnmr.2011.03.007.

(31) Wang, Z.; Jiang, Y.; Jin, F.; Stampfl, C.; Hunger, M.; Baiker, A.; Huang, J. Strongly Enhanced Acidity and Activity of Amorphous Silica–Alumina by Formation of Pentacoordinated Al^{V} Species. *J. Catal.* **2019**, *372*, 1–7. https://doi.org/10.1016/j.jcat.2019.02.007.

(32) Li, S.; Zheng, A.; Su, Y.; Fang, H.; Shen, W.; Yu, Z.; Chen, L.; Deng, F. Extra-Framework Aluminium Species in Hydrated Faujasite Zeolite as Investigated by Two-Dimensional Solid-State NMR Spectroscopy and Theoretical Calculations. *Chem. Phys.* **2010**, *12* (15), 3895–3903. https://doi.org/10.1039/B915401A.

(33) Marion, D.; Ikura, M.; Tschudin, R.; Bax, A. Rapid Recording of 2D NMR Spectra without Phase Cycling. Application to the Study of Hydrogen Exchange in Proteins. *J. Magn. Reson. 1969* **1989**, *85* (2), 393–399. https://doi.org/10.1016/0022-2364(89)90152-2.

(34) Massiot, D.; Fayon, F.; Capron, M.; King, I.; Le Calvé, S.; Alonso, B.; Durand, J.-O.; Bujoli, B.; Gan, Z.; Hoatson, G. Modelling One- and Two-Dimensional Solid-State NMR Spectra. *Magn. Reson. Chem.* **2002**, *40* (1), 70–76. https://doi.org/10.1002/mrc.984.

(35) d'Espinose de Lacaillerie, J.-B.; Fretigny, C.; Massiot, D. MAS NMR Spectra of Quadrupolar Nuclei in Disordered Solids: The Czjzek Model. *J. Magn. Reson.* **2008**, *192* (2), 244–251. https://doi.org/10.1016/j.jmr.2008.03.001.

(36) Chen, K.; Horstmeier, S.; Nguyen, Vy. T.; Wang, B.; Crossley, S. P.; Pham, T.; Gan, Z.; Hung, I.; White, J. L. Structure and Catalytic Characterization of a Second Framework Al(IV) Site in Zeolite Catalysts Revealed by NMR at 35.2 T. *J. Am. Chem. Soc.* **2020**, *142* (16), 7514–7523. https://doi.org/10.1021/jacs.0c00590.

(37) Thomas, N.; Dhainaut, J.; Moissette, A.; Lafon, O.; Manjunatha Reddy, G. N. Resolving Transformative Reactions in Zeolites under Catalytic Hydrothermal Conditions. *J. Phys. Chem. C* **2024**, *128* (25), 10428–10439. https://doi.org/10.1021/acs.jpcc.4c02929.

(38) Chen, K.; Gan, Z.; Horstmeier, S.; White, J. L. Distribution of Aluminum Species in Zeolite Catalysts: ^{27}Al NMR of Framework, Partially-Coordinated Framework, and Non-Framework Moieties. *J. Am. Chem. Soc.* **2021**, *143* (17), 6669–6680. https://doi.org/10.1021/jacs.1c02361.

(39) Venkatesh, A.; Luan, X.; Perras, F.; Hung, I.; Huang, W.; Rossini, A. T1-Noise Eliminated Dipolar Heteronuclear Multiple-Quantum Coherence Solid-State NMR Spectroscopy. **2020**. https://doi.org/10.26434/chemrxiv.12591629.v1.

(40) Gómez, J. S.; Rankin, A. G. M.; Trébosc, J.; Pourpoint, F.; Tsutsumi, Y.; Nagashima, H.; Lafon, O.; Amoureux, J.-P. Improved NMR Transfer of Magnetization from Protons to Half-Integer Spin Quadrupolar Nuclei at Moderate and High Magic-Angle Spinning Frequencies. *Magn. Reson.* **2021**, *2* (1), 447–464. https://doi.org/10.5194/mr-2-447-2021.

(41) Nagashima, H.; Trébosc, J.; Kon, Y.; Sato, K.; Lafon, O.; Amoureux, J.-P. Observation of Low-γ Quadrupolar Nuclei by Surface-Enhanced NMR Spectroscopy. *J. Am. Chem. Soc.* **2020**, *142* (24), 10659–10672. https://doi.org/10.1021/jacs.9b13838.

(42) Nagashima, H.; Trébosc, J.; Kon, Y.; Lafon, O.; Amoureux, J.-P. Efficient Transfer of DNP-Enhanced ^{1}H Magnetization to Half-Integer Quadrupolar Nuclei in Solids at Moderate Spinning Rate. *Magn. Reson. Chem.* **2021**, *59* (9–10), 920–939. https://doi.org/10.1002/mrc.5121.

(43) Osborn Popp, T. M.; Alaniva, N. H.; Barnes, A. B. Setting the Magic Angle Using Single Crystal Sapphire Rotors. *J. Magn. Reson. Open* **2021**, *8–9*, 100019. https://doi.org/10.1016/j.jmro.2021.100019.

(44) Dib, E.; Costa, I. M.; Vayssilov, G. N.; Aleksandrov, H. A.; Mintova, S. Complex H-Bonded Silanol Network in Zeolites Revealed by IR and NMR Spectroscopy Combined with DFT Calculations. *J. Mater. Chem. A* **2021**, *9* (48), 27347–27352. https://doi.org/10.1039/D1TA06908J.

(45) Schroeder, C.; Siozios, V.; Mück-Lichtenfeld, C.; Hunger, M.; Hansen, M. R.; Koller, H. Hydrogen Bond Formation of Brønsted Acid Sites in Zeolites. *Chem. Mater.* **2020**, *32* (4), 1564–1574. https://doi.org/10.1021/acs.chemmater.9b04714.

General Conclusion

In this PhD thesis, we investigated using solid-state NMR spectroscopy two types of heterogeneous catalysts: molybdenum-based catalysts for olefin metathesis and new solid-acid photocatalysts. For the molybdenum-based catalysts, we successfully demonstrated that strong magnetic fields (18.8 and 28.2 T) paired with DFS-QCPMG experiments enable the acquisition of high-resolution ^{95}Mo spectra of molecular complexes with sufficient signal-to-noise ratio, overcoming the intrinsic limits of the low-γ quadrupolar nucleus. Furthermore, the simulation of these ^{95}Mo NMR spectra yielded reliable NMR parameters. We related those parameters to the structure of the molybdenum complexes determined by X-ray diffraction. A larger coordination number around Mo atom typically results in a more symmetrical environment leading to lower C_Q and CSA values and lower isotropic chemical shifts. In addition, larger fraction of oxygen ligands in the first coordination sphere also reduces isotropic chemical shift, whereas carbon-based ligands, particularly carbenes and bulky neosilyl groups, causes deshielding. Finally, deviations from ideal geometries, such as square-pyramidal complexes, results in high C_Q and CSA values. Even if it would be desirable to study a larger number of molecular complexes to generalize these findings, the obtained structure-NMR relationships will be useful for the interpretation of ^{95}Mo NMR spectra. We also conducted ADF calculations of NMR parameters including relativistic effects. The calculated NMR parameters agreed reasonably well with those measured experimentally, which validates the use of theoretical calculations for the prediction of ^{95}Mo NMR parameters. The study of grafted molybdenum complexes proved highly challenging, both in terms of synthesis and the NMR detection of ^{95}Mo nuclei. The $^{95}MoO_3$ precursor contained reduced Mo species leading to the formation of impure $^{95}MoOCl_4$ as confirmed by ^{1}H NMR and XPS. Despite these limitations, the NMR study provided valuable insights: accidental hydrolysis likely introduced additional hydroxylated sites, consistent with literature examples but complicating spectral interpretation. The resulting ^{95}Mo spectra revealed a mixture of environments, inducing broad signal and highlighting the need for improved synthetic strategies to obtain well-defined grafted precursors and clearer ^{95}Mo NMR signatures. Nevertheless, the results discussed clearly demonstrated how strongly ^{95}Mo NMR parameters respond to variations in the local environment, confirming its power as a tool for probing the structure of heterogeneous catalytic systems.

Perspectives for this project will include the preparation of novel grafted molybdenum complexes enriched in ^{95}Mo nuclei using purified precursor. Furthermore, to detect ^{95}Mo isotope in this grafted molybdenum complexes in natural abundance, it would be useful to test techniques to enhance NMR signals, such as the use of low temperature or dynamic nuclear polarization.

In parallel, solid-state NMR was used to probe the atomic-level structure of acid sites in Au/AAS nanosponges, a promising type of solid-acid photocatalyst, and the structural modifications under light irradiation. Using 2D ^{1}H-^{29}Si and ^{1}H-^{27}Al through-space heteronuclear correlation experiments, we observed the presence of Si(OH)Al^{IV} and Si(OH)Al^{V} sites in Au/AAS, which are similar to those detected before gold deposition. Nevertheless, the reaction between $NaBH_4$ and AAS during the deposition of gold nanoparticles leads to the partial hydrolysis of AAS support, which results in an increased amount of Q^3 sites and the partial leaching of AlO_5 and AlO_6 sites. We also carried 1D and 2D NMR experiments under light irradiation. We observed that light irradiation modifies the local environment of protons, resulting in a broadening of ^{1}H resonances. This broadening is irreversible and persists after the light irradiation has ceased. In addition, 2D ^{1}H-^{27}Al through-space heteronuclear correlation spectra acquired under light irradiation exhibits cross-peaks between between ^{1}H resonances at 6-7 ppm and AlO_4 and AlO_5 sites. These signals are ascribed to Si(OH)Al^{IV} and Si(OH)Al^{V} sites with elongated OH bonds. This elongation of OH bonds in bridging silanol under illumination explains the enhanced Brønsted acidity and catalytic activity of Au/AAS under light irradiation. In the future, 2D ^{1}H-^{27}Al through-space heteronuclear correlation spectra will have to be acquired before, during and after light irradiation to determine whether this elongation persists or vanishes after light irradiation. The former result would indicate an elongation due to photothermal activation, whereas the latter would point to LSPR phenomenon. Moreover, these results demonstrate the potential of MAS NMR under light irradiation for the structural characterization of photocatalysts.

These advances confirm that solid-state NMR is not only a powerful tool for probing complex heterogeneous catalysts but also an essential bridge between local structure and macroscopic reactivity. By shedding light on both the successes and limitations

encountered, this work opens new perspectives for the rational design of more efficient, selective, and sustainable catalytic systems.